Growth and Characterisation of III–V Semiconductor Nanowires for Optoelectronic Device Applications

A thesis submitted for the degree of
Doctor of Philosophy
of
The Australian National University

Hannah Jane Joyce

July 2010

Certificate

This thesis, to the best of my knowledge and belief, does not contain any results previously published by another person or submitted for a degree or diploma at any university except where due reference is made in the text.

Hannah J. Joyce

Acknowledgements

The acknowledgements are my favourite part of all the theses I have ever read or written. Nevertheless, so many people have contributed to this work and I cannot possibly list you all, nor thank you enough. Please know that, even if you do not find yourself named here, I have not forgotten your contribution; it has just slipped my mind for the moment.

Firstly, I sincerely thank my principal supervisors, Prof. Jagadish and Dr. Hoe Tan, for their constant support, guidance and encouragement throughout my PhD. Their enthusiasm for science is inspirational. Jagadish has always been there armed with excellent advice and wisdom, to help me through the most difficult times. Hoe has always been there too, but instead, armed with his sense of humour and a bottle of red. I could not imagine two better supervisors.

I am deeply grateful to Dr. Yong Kim. Yong arrived in our group only a month before I arrived, and he had already become the local expert on nanowire growth. He was an excellent support in those first few months of my PhD, and remained an excellent supervisor and collaborator even after he returned to Korea. It was a great pleasure working with Yong.

I am extremely thankful to Dr. Michael Gao, who has helped greatly with my experiments, particularly with the micro-PL measurements. His kind and friendly nature make the lab a wonderful place to work.

Dr. Jenny Wong-Leung deserves very special thanks. Jenny has taught me almost everything I know about TEM. We have had some of the best conversations during our TEM sessions. She has made a mammoth effort performing TEM for this dissertation.

I am also very grateful to our collaborators at the University of Queensland, Prof. Jin Zou, Dr. Xin Zhang, Dr. Mohan Paladugu and Yanan Guo, for performing TEM measurements, for many fruitful discussions, and for sharing their knowledge with me.

The technical staff in the Research School of Physics and Engineering have provided excellent support and I am extremely grateful. In particular I would like to thank Michael Aggett, Craig Saint, David Llewellyn, Dr. John Fitzgerald and Dr. Kidane Belay. I also wish to thank Scott Yates for his tireless work as Department Administrator, and for his kindness and friendship. I am very grateful to all the other administrative and academic staff for their support and companionship, especially Liz Micallef, Josephine

Ivanic, Laura Walmsley, Susie Radovanovic, Belinda Barbour, Prof. Neil Manson, Luda Mangos, Heeok Kyung, Anna Cirjak, Dr. Jodie Bradby, Dr. Lan Fu, Prof. Neville Fletcher, Prof. Jim Williams, Dr. Fouad Karouta, Dr. Haroldo Hattori, Prof. Rob Elliman, Dr. Leandro Araujo, Dr. Avi Shalav, Dr. Dinesh Venkatachalam and Dr. Simon Ruffell.

I am deeply grateful to our collaborators at the University of Cincinnati: Prof. Leigh Smith, Prof. Howard Jackson and Prof. Jan Yarrison-Rice. To say these people were excellent scientists, supervisors and collaborators would not be enough. They were excellent hosts, and made my two month visit to Cincinnati an absolute joy. I also wish to thank the students there: Thang Hoang, Melodie Fickenscher, Saranga Perera and Mohammad Montazeri. I gratefully acknowledge the Australian Research Council Nanotechnology Network for providing travel support for this visit.

I also wish to thank our collaborators, and my future co-workers, at the University of Oxford: Dr. Michael Johnston, Dr. Laura Herz and Patrick Parkinson. I really enjoyed my brief visit to their lab in Oxford, and it has been a great pleasure working with such excellent people.

I wish to thank all my friends here in Canberra, back home in Perth, and overseas, who have all given me unwavering support throughout my studies. I have found some of my best friends amongst the students and staff in the Department of Electronic Materials Engineering, including the people already mentioned. There has rarely been a dull moment at work, with lunches, morning and afternoon tea, beer club, drinks at University House, frisbee matches, spectacular chess games, how-to-host-a-murder evenings, student barbecues and pancake breakfasts, all spent with good friends. My fellow nanowire students and my good friends, Su Paiman, Jordan Kang, Tim Burgess, Shriniwas Deshpande and Vidya Ramesh, have been a great pleasure to work with. The remaining students within the Department of Electronic Materials Engineering, too, are some of the best people I have ever known. I particularly would like to thank Bianca Haberl, Daniel Pyke, Dave Sprouster, Ian McKerracher, Raquel Giulian, Taehyun Kim, Sup Charnvanichborikarn, Peter Kuffner, Mykhaylo Lysevych, Jenn Zhu, Sothia Toch and Adeline Mouzard, for being such firm friends throughout my PhD. I would like to thank my friends in other departments and administration, who make the Research School of Physics and Engineering the most fun, vibrant and happy work environment, especially Sarah Beavan, Morgan Hedges, Elena Nobleza, Lachlan Rogers, Khu Vu, Paula Micallef, Alan Heays, Lesa Byron, Ramin Rafiei, Shaun Howard, Myf Evans, Ksawery Kalinowski, Steve Lade, Trevor Lafleur, Jesse Reid, Jess Hudspeth, David Byrne, Wes Cox, James Dedrick and Julia Ling. My gym mates have helped keep me motivated, fit and happy, and my friends from church have kept me happy and spiritually healthy. My friends at University and Graduate House have become my Canberra siblings, especially Matt

Harrison, Drew Ninnis, Tory Ludowici, Amir Hadad, Laura de la Cruz, Pietro Abate, Lan Wei, Ying Xu, Charis Teh, Moses Lee, Sean Perera, Dulamanie Wanninayake, Junghye Park, Ochini Madanayake and Elissa Sutcliffe. I am very grateful to the Master of University and Graduate House, Prof. John Richards, and Mrs. Glenda Richards, for making Graduate House such a warm and friendly place to live. Very importantly, I thank my Saturday night dinner friends for all the food, fun times, picnics and bushwalks: Ivana Kuo, Anthie Ellis, Patrice Yee, Annie Carroll, Evelyn Chia, Michele Bannister, Michael Jasonsmith, Desmond Chik, Chloe Lim and Steph Cheung. I especially wish to thank my best friend, David Oliver, who crosses into almost all these friendship groups, and has been an immense support throughout my PhD.

Lastly, and most importantly, I thank my family: Mum, Dad, my sister Cerys and my brother Rohan, my grandparents Dan, Papa, Peggy and Ray, and my uncles and aunties, especially my aunties Chris and Mary. Without your unconditional love and support, I could not have managed this work. I love you all.

Abstract

III–V semiconductor nanowires have recently emerged as a new class of nanoscale materials exhibiting outstanding potential as nano-components of future electronic and optoelectronic devices and systems. The development of III–V nanowire-based devices depends on the ability to fabricate nanowires with tight control over properties such as morphology, crystal structure, composition, doping and quantum efficiency. Arguably, the most promising growth technique for III–V nanowires is metalorganic chemical vapour deposition (MOCVD) using Au nanoparticles to drive nanowire growth via the vapour–liquid–solid or vapour–solid–solid mechanism. This fabrication process offers a number of growth parameters which can be tailored for optimum nanowire growth, including the growth temperature, the input V/III ratio and the absolute flow rates of group III and group V precursor species. Nevertheless, a number of growth issues must be controlled if nanowires are to be useful in device applications. These include nanowire kinking and irregular growth directions, nanowire tapering, intrinsic dopant and impurity incorporation, non-radiative recombination at defects and surfaces, and crystallographic defects such as twin defects, stacking faults and zinc-blende–wurtzite polytypism.

This dissertation examines the Au-assisted growth of GaAs, InAs and InGaAs nanowires by MOCVD, and how this growth process can be tailored to produce nanowires suitable for applications in electronics and optoelectronics. A number of experimental techniques have been employed in this work to investigate nanowire properties. Scanning electron microscopy was employed to identify the general morphology of the nanowires, including growth direction, height, diameter, tapering and facet planes. Transmission electron microscopy (TEM) was used to identify the crystal structures (zinc-blende or wurtzite) and the presence of twin phase boundaries and stacking faults. Energy dispersive X-ray spectroscopy (EDS) was used to study the composition of the nanowires and the alloyed Au-nanoparticles. Continuous-wave and time-resolved photoluminescence (PL) spectroscopy provided insight into a number of key optical and electronic nanowire qualities, including excitonic structure, intrinsic carbon doping and carrier dynamics.

Growth temperature is found to profoundly affect the morphology, crystal structure and optical properties of GaAs nanowires. A two-temperature growth procedure was designed to achieve exceptionally high quality GaAs nanowires. This procedure con-

sists of a brief initial high-temperature growth step followed by prolonged growth at a lower temperature. The initial high-temperature step is essential for obtaining straight, vertically-aligned epitaxial nanowires on the GaAs substrate. The lower temperature employed for subsequent growth imparts superior nanowire morphology and crystallographic quality by minimising radial growth and eliminating twin plane defects in these zinc-blende nanowires. PL measurements revealed the low carbon impurity incorporation and the long exciton lifetime of these two-temperature grown nanowires, confirming that the two-temperature procedure achieves excellent nanowire optical quality.

The input V/III ratio was also found to have a significant effect on GaAs nanowire properties. A high V/III ratio dramatically reduced planar crystallographic defects and reduced intrinsic carbon dopant incorporation. Increasing the V/III ratio further, however, instigated nanowire kinking, increased nanowire tapering, and markedly reduced the exciton lifetime. An intermediate V/III ratio is chosen as a compromise, to achieve uniform, vertically aligned GaAs nanowires, with few planar crystallographic defects, reasonable optical properties and relatively low carbon impurity incorporation.

Growth rate had a very unexpected effect on GaAs nanowire growth. In conventional planar growth of bulk III–V materials, a slow growth rate favours high crystallographic quality, optical quality and purity of the resulting material. Surprisingly, exactly the opposite effect was observed for Au-assisted GaAs nanowire growth. By employing a rapid growth rate, the resulting nanowires were markedly less tapered, were free of planar crystallographic defects, and featured very high purity with minimal intrinsic dopant incorporation.

InAs nanowire morphology, too, was highly sensitive to growth temperature, V/III ratio and growth rate. InAs nanowires exhibit similar growth dependencies to GaAs nanowires, although InAs is more strongly influenced by diffusion of reaction species adsorbed on the substrate surface. As a result, InAs nanowires show a marked dependence of height and tapering on nanowire density, with more sparsely distributed InAs nanowires exhibiting enhanced axial and radial growth rates.

Ternary InGaAs nanowires of high In composition also exhibited a strong dependence of height and tapering on nanowire density. This dependency is attributed to the large diffusion length of In compared to Ga species. PL spectra exhibited a red-shift with decreasing nanowire density, suggesting higher In incorporation in more sparsely distributed InGaAs nanowires. EDS analysis revealed a large In/Ga compositional variation along the nanowire length.

TEM studies of GaAs and InAs nanowires found that phase-perfect nanowires, of arbitrary diameter, could be achieved simply by tailoring basic growth parameters: temperature and V/III ratio. Pure zinc-blende nanowires, free of twin defects, were achieved

using a low growth temperature coupled with a high V/III ratio. Conversely, a high growth temperature coupled with a low V/III ratio produced pure wurtzite nanowires free of stacking faults. These growth techniques achieved phase purity without sacrificing important specifications of diameter and dopant levels. A comprehensive nucleation model is developed to explain the formation of these markedly different crystal phases under these growth conditions. Critical to achieving phase purity are changes in the surface energy of the nanowire side-facets, which in turn are controlled by the basic growth parameters of temperature and V/III ratio.

This work presents significant advances in the growth of exceptionally high quality GaAs, InAs and InGaAs nanowires, and reveals intriguing behaviour in the growth of nanoscale materials. These findings will greatly assist the development of future GaAs, InAs and InGaAs nanowire-based electronic and optoelectronic devices, and are expected to be more broadly relevant to the rational synthesis of other III–V nanowire materials.

Publications

1. Y. Kim, H. J. Joyce, Q. Gao, H. H. Tan, C. Jagadish, M. Paladugu, J. Zou, and A. A. Suvorova, "Influence of nanowire density on the shape and optical properties of ternary InGaAs nanowires," *Nano Lett.*, vol. 6, pp. 599–604, 2006.

2. L. V. Titova, T. B. Hoang, H. E. Jackson, L. M. Smith, J. M. Yarrison-Rice, Y. Kim, H. J. Joyce, H. H. Tan, and C. Jagadish, "Temperature dependence of photoluminescence from single core–shell GaAs–AlGaAs nanowires," *Appl. Phys. Lett.*, vol. 89, pp. 173126, 2006.

3. J. Zou, M. Paladugu, H. Wang, G. J. Auchterlonie, Y. Guo, Y. Kim, Q. Gao, H. J. Joyce, H. H. Tan, and C. Jagadish, "Growth mechanism of truncated triangular III–V nanowires," *Small*, vol. 3, pp. 389–393, 2007.

4. H. J. Joyce, Q. Gao, H. H. Tan, C. Jagadish, Y. Kim, X. Zhang, Y. Guo, and J. Zou, "Twin-free uniform epitaxial GaAs nanowires grown by a two-temperature Process," *Nano Lett.*, vol. 7, pp. 921–926, 2007.

5. T. B. Hoang, L. V. Titova, J. M. Yarrison-Rice, H. E. Jackson, A. O. Govorov, Y. Kim, H. J. Joyce, H. H. Tan, C. Jagadish, and L. M. Smith, "Resonant excitation and imaging of nonequilibrium exciton spins in single core–shell GaAs–AlGaAs nanowires," *Nano Lett.*, vol. 7, pp. 588–595, 2007.

6. M. Paladugu, J. Zou, Y.-N. Guo, G. J. Auchterlonie, H. J. Joyce, Q. Gao, H. H. Tan, C. Jagadish, and Y. Kim, "Novel growth phenomena observed in axial InAs/GaAs nanowire heterostructures," *Small*, vol. 3, pp. 1873–1877, 2007.

7. A. Mishra, L. V. Titova, T. B. Hoang, H. E. Jackson, L. M. Smith, J. M. Yarrison-Rice, Y. Kim, H. J. Joyce, Q. Gao, H. H. Tan, and C. Jagadish, "Polarization and temperature dependence of photoluminescence from zincblende and wurtzite InP nanowires," *Appl. Phys. Lett.*, vol. 91, pp. 263104, 2007.

8. M. Paladugu, J. Zou, G. J. Auchterlonie, Y. N. Guo, Y. Kim, H. J. Joyce, Q. Gao, H. H. Tan, and C. Jagadish, "Evolution of InAs branches in InAs/GaAs nanowire heterostructures," *Appl. Phys. Lett.*, vol. 91, pp. 133115, 2007.

9. L. V. Titova, T. B. Hoang, J. M. Yarrison-Rice, H. E. Jackson, Y. Kim, H. J. Joyce, Q. Gao, H. H. Tan, C. Jagadish, X. Zhang, J. Zou, and L. M. Smith, "Dynamics of strongly degenerate electron–hole plasmas and excitons in single InP nanowires," *Nano Lett.*, vol. 7, pp. 3383–3387, 2007.

10. M. S. Song, J. H. Jung, Y. Kim, Y. Wang, J. Zou, H. J. Joyce, Q. Gao, H. H. Tan, and C. Jagadish, "Vertically standing Ge nanowires on GaAs(110) substrates," *Nanotechnology*, vol. 19, pp. 125602, 2008.

11. S. Perera, M. A. Fickenscher, H. E. Jackson, L. M. Smith, J. M. Yarrison-Rice, H. J. Joyce, Q. Gao, H. H. Tan, C. Jagadish, X. Zhang, and J. Zou, "Nearly intrinsic exciton lifetimes in single twin-free GaAs/AlGaAs core–shell nanowire heterostructures," *Appl. Phys. Lett.* vol. 93, pp. 053110, 2008.

12. M. Paladugu, J. Zou, Y.-N. Guo, X. Zhang, Y. Kim, H. J. Joyce, Q. Gao, H. H. Tan, and C. Jagadish, "Nature of heterointerfaces in GaAs/InAs and InAs/GaAs axial nanowire heterostructures," *Appl. Phys. Lett.*, vol. 93, pp. 101911, 2008.

13. H. J. Joyce, Q. Gao, H. H. Tan, C. Jagadish, Y. Kim, M. A. Fickenscher, S. Perera, T. B. Hoang, L. M. Smith, H. E. Jackson, J. M. Yarrison-Rice, X. Zhang, and J. Zou, "High purity GaAs nanowires free of planar defects: growth and characterization," *Adv. Funct. Mater.*, vol. 18, pp. 3794–3800, 2008.

14. M. Paladugu, J. Zou, Y.-N. Guo, X. Zhang, H. J. Joyce, Q. Gao, H. H. Tan, C. Jagadish, and Y. Kim, "Polarity driven formation of InAs/GaAs hierarchical nanowire heterostructures," *Appl. Phys. Lett.*, vol. 93, pp. 201908, 2008.

15. H. J. Joyce, Q. Gao, H. H. Tan, C. Jagadish, Y. Kim, M. A. Fickenscher, S. Perera, T. B. Hoang, L. M. Smith, H. E. Jackson, J. M. Yarrison-Rice, X. Zhang, and J. Zou, "Unexpected benefits of rapid growth rate for III–V nanowires," *Nano Lett.*, vol. 9, pp. 695–701, 2009.

16. M. Paladugu, J. Zou, Y.-N. Guo, X. Zhang, H. J. Joyce, Q. Gao, H. H. Tan, C. Jagadish, and Y. Kim, "Formation of hierarchical InAs nanoring/GaAs nanowire heterostructures," *Angew. Chem.*, vol. 121, pp. 794–797, 2009.

17. X. Zhang, J. Zou, M. Paladugu, Y. Guo, Y. Wang, Y. Kim, H. J. Joyce, Q. Gao, H. H. Tan, and C. Jagadish, "Evolution of epitaxial InAs nanowires on GaAs (111)B," *Small*, vol. 5, pp. 366-369, 2009.

18. M. Paladugu, J. Zou, Y.-N. Guo, X. Zhang, H. J. Joyce, Q. Gao, H. H. Tan, C. Jagadish, and Y. Kim, "Crystallographically driven Au catalyst movement during

growth of InAs/GaAs axial nanowire heterostructures," *J. Appl. Phys.*, vol. 105, pp. 073503, 2009.

19. P. Parkinson, H. J. Joyce, Q. Gao, H. H. Tan, X. Zhang, J. Zou, C. Jagadish, L. M. Herz, M. B. Johnston, "Carrier lifetime and mobility enhancement in nearly defect-free core–shell nanowires measured using time-resolved terahertz spectroscopy," *Nano Lett.*, vol. 9, pp. 3349–3353, 2009.

20. M. Paladugu, J. Zou, Y. Guo, X. Zhang, H. J. Joyce, Q. Gao, C. Jagadish, Y. Kim, "Evolution of wurtzite structured GaAs shells around InAs nanowire cores" *Nanoscale Res. Lett.*, vol. 4, pp. 846–849, 2009.

21. H. J. Joyce, J. Wong-Leung, Q. Gao, H. Hoe Tan, C. Jagadish, "Phase perfection in zinc-blende and wurtzite III–V nanowires using basic growth parameters," *Nano Lett.*, vol. 10, pp. 908–915, 2010.

22. H. J. Joyce, Q. Gao, H. Hoe Tan, C. Jagadish, Y. Kim, J. Zou, L. M. Smith, H. E. Jackson, J. M. Yarrison-Rice, P. Parkinson and M. B. Johnston, "III–V semiconductor nanowires for optoelectronic device applications," Invited and submitted to *Prog. Quantum Electron.*

List of acronyms and common symbols

AsH_3	arsine
CBE	chemical beam epitaxy
DAP	donor–acceptor pair
DI	deionised
DMGa	dimethylgallium
DPSS	diode-pumped solid state
EBL	electron beam lithography
EDS	energy dispersive X-ray spectroscopy
FESEM	field emission scanning electron microscopy
HRTEM	high resolution transmission electron microscopy
LO	longitudinal optical
MBE	molecular beam epitaxy
MMGa	monomethylgallium
MO	metalorganic
MOCVD	metalorganic chemical vapour deposition
PH_3	phosphine
PL	photoluminescence
PLL	poly-L-lysine
SADP	selected area diffraction pattern
SEM	scanning electron microscopy

TCS	terahertz conductivity spectroscopy
TEM	transmission electron microscopy
TMAl	trimethylaluminium, $Al(CH_3)_3$
TMGa	trimethylgallium, $Ga(CH_3)_3$
TMIn	trimethylindium, $In(CH_3)_3$
TMSb	trimethylantimony, $Sb(CH_3)_3$
TRPL	time-resolved photoluminescence
WZ	wurtzite
ZB	zinc-blende
$\mathbf{III}_0$	standard group III precursor flow rate, 1.2×10^{-5} mol/min
$\mathbf{V}_0$	standard group V precursor flow rate, 5.4×10^{-4} mol/min
A	average cross-sectional area of nucleus
$A_{available}$	available diffusion area
a	area per III–V pair on the growth interface
a_0	lattice constant
D	nanowire diameter
E_A	activation energy
h	nucleus height
k_B	Boltzmann constant, 1.381×10^{-23} JK^{-1}
l	nanowire length
L	total nanowire length from base to tip (Au nanoparticle–nanowire interface)
P_{twin}	probability of twin formation
r	nanowire radius
r_b	radius at nanowire base

r_t	radius at nanowire tip (Au nanoparticle–nanowire interface)
R	universal gas constant, 8.314 $JK^{-1}mol^{-1}$
R_g	growth rate
R_{axial}	axial growth rate
R_{radial}	radial growth rate
T	temperature
T_n	nucleation temperature
T_g	growth temperature
T_{50}	temperature at which precursor decomposition is 50% complete
t	growth time
t_g	total growth time
$x_{v,In}$	vapour phase In composition
$x_{s,In}$	solid phase In composition
$x_{s,Ga}$	solid phase Ga composition

Contents

Certificate v

Acknowledgements viii

Abstract xiii

Publications xvi

List of acronyms and common symbols xx

List of figures xxix

List of tables xxxi

1 Introduction 1

1.1 Significance of III–V nanowires . . . 1

1.2 Techniques for III–V nanowire growth . . . 2

1.2.1 Template-directed nanowire growth . . . 3

1.2.2 Free-standing nanowire growth . . . 3

1.3 Au-assisted nanowire growth using MOCVD . . . 4

1.4 Challenges in III–V nanowire growth and design . . . 6

1.5 Thesis synopsis . . . 7

2 Experimental techniques 9

2.1 Introduction . . . 9

2.2 Epitaxial growth . . . 9

2.2.1 Metalorganic chemical vapour deposition . . . 9

2.2.2 Substrate preparation . . . 11

2.2.3 Growth procedure . . . 13

2.3 Electron microscopy . . . 13

2.3.1 Scanning electron microscopy . . . 15

2.3.2 Transmission electron microscopy . . . 17

2.4 Photoluminescence spectroscopy . . . 19
2.4.1 Standard low temperature PL spectroscopy (ANU) . . . 20
2.4.2 Room temperature micro-PL imaging (ANU) . . . 21
2.4.3 Low temperature micro-PL spectroscopy (ANU) . . . 21
2.4.4 Time-integrated micro-PL spectroscopy (UC) . . . 21
2.4.5 Time-resolved photoluminescence spectroscopy (UC) . . . 22
2.5 Summary . . . 23

3 Fundamental principles of III–V nanowire growth and properties 25
3.1 Introduction . . . 25
3.2 Growth thermodynamics . . . 26
3.3 Precursor decomposition and reaction kinetics . . . 26
3.4 Alloy formation between Au and III–V materials . . . 28
3.5 Growth direction . . . 32
3.6 Surface diffusion effects . . . 33
3.7 Axial and radial growth modes . . . 33
3.8 The Au-assisted nanowire growth mechanism, and proposed alternative models . . . 35
3.9 Alternative substrate preparation techniques . . . 35
3.10 Nanowire crystal structure . . . 37
3.11 Nanowire side-facets . . . 38
3.12 Axial and radial heterostructures . . . 40
3.13 Photoluminescence of GaAs nanowires . . . 42
3.13.1 GaAs/AlGaAs core–shell nanowires for PL measurements . . . 42
3.13.2 GaAs nanowire PL spectra . . . 43
3.14 Summary . . . 47

4 A two-temperature growth procedure for GaAs nanowires 49
4.1 Introduction . . . 49
4.2 Experiments . . . 50
4.3 Morphology . . . 51
4.4 Crystal structure . . . 54
4.5 Photoluminescence . . . 56
4.5.1 Donor–acceptor pair recombination and carbon impurities . . . 56
4.5.2 Room temperature photoluminescence . . . 58
4.5.3 Exciton lifetime . . . 59
4.6 Role of the nucleation step . . . 60
4.7 Summary . . . 63

5 Choice of V/III ratio for GaAs nanowire growth **65**
5.1 Introduction . . . 65
5.2 Experiments . . . 66
5.3 Morphology . . . 66
5.4 Crystal structure . . . 71
5.5 Photoluminescence . . . 72
5.5.1 Donor–acceptor pair recombination and carbon impurities . . . 72
5.5.2 Exciton lifetime . . . 73
5.6 An intermediate V/III ratio . . . 74
5.7 Summary . . . 74

6 Unexpected benefits of rapid growth rate for GaAs nanowires **77**
6.1 Introduction . . . 77
6.2 Experiments . . . 78
6.3 Morphology . . . 78
6.4 Crystal structure . . . 81
6.5 Photoluminescence . . . 83
6.5.1 Donor–acceptor pair recombination and carbon impurities . . . 83
6.5.2 Exciton lifetime . . . 85
6.6 Summary . . . 87

7 Growth and structural properties of InAs nanowires **89**
7.1 Introduction . . . 89
7.2 Experiments . . . 89
7.3 Effect of nanowire density on nanowire morphology . . . 90
7.4 Effect of V/III ratio on nanowire morphology . . . 92
7.5 Effect of growth temperature on nanowire morphology . . . 94
7.6 Growth window . . . 97
7.7 Effect of total precursor flow rate on nanowire morphology . . . 98
7.8 Summary . . . 100

8 Ternary InGaAs nanowire growth **103**
8.1 Introduction . . . 103
8.2 Experiments . . . 104
8.3 Morphology . . . 104
8.4 Crystal structure and elemental composition . . . 109
8.5 Photoluminescence . . . 111
8.6 Summary . . . 112

9 Phase perfection in zinc-blende and wurtzite III–V nanowires 115
9.1 Introduction . . . 115
9.2 Experiments . . . 116
9.3 Zinc-blende and wurtzite InAs nanowires . . . 117
9.4 Zinc-blende and wurtzite GaAs nanowires . . . 122
9.5 Sidewall facets of zinc-blende and wurtzite InAs nanowires . . . 124
9.6 Sidewall facets of zinc-blende and wurtzite GaAs nanowires . . . 124
9.7 Phase and composition of the alloyed Au nanoparticles of InAs and GaAs nanowires . . . 125
9.8 Summary . . . 126

10 Theoretical modelling of zinc-blende and wurtzite nanowire growth 129
10.1 Introduction . . . 129
10.2 Model derivation . . . 130
10.2.1 Modelling the Au alloy nanoparticle . . . 130
10.2.2 Modelling the nucleus . . . 131
10.2.3 Nucleus formation energy, ΔG . . . 131
10.2.4 The increment in vapour–liquid nanoparticle area, B . . . 133
10.2.5 Modelling nucleus side-facets, x . . . 135
10.2.6 Modelling pre-existing side-facets, y . . . 137
10.2.7 Possible nuclei, x, on pre-existing sidewalls, y . . . 137
10.2.8 Probabilities . . . 138
10.3 Parameters for InAs nanowire growth . . . 138
10.4 Results of the model . . . 139
10.4.1 Critical nucleus size . . . 139
10.4.2 Effect of contact angle, β . . . 139
10.4.3 Effect of contact angle under high μ_{As} growth conditions . . . 140
10.4.4 Effect of contact angle under low μ_{As} growth conditions . . . 143
10.4.5 Effects of vapour–liquid and liquid–solid surface energies, γ_{vl} and γ_{ls} . . . 143
10.4.6 Effect of supersaturation, $\Delta\mu$ . . . 144
10.4.7 Effect of vapour–nucleus surface energy, γ_{vn} . . . 146
10.5 Relationship between theoretical and experimental results . . . 146
10.5.1 Growth parameters and supersaturation . . . 146
10.5.2 Growth parameters, and vapour–liquid and liquid–solid surface energies . . . 146
10.5.3 Growth parameters and vapour–nucleus surface energy . . . 147

10.6 Model limitations and suggested future improvements 149
10.6.1 Possible mechanism based on surface and interface tensions . . . 150
10.6.2 Possible mechanism based on random fluctuations 150
10.7 Summary 151

11 Conclusion **153**
11.1 Outcomes 153
11.2 Recommendations and future directions 155

References **157**

List of figures

1.1 Schematic illustration of VLS growth of Si nanowires 5
1.2 Schematic illustration of III–V nanowire growth 6

2.1 Schematic illustration of the Aixtron 200/4 MOCVD reactor 10
2.2 Illustration of electron beam interactions with a specimen 14
2.3 Illustration of the escape volume of secondary electrons with respect to surface topography 15
2.4 Ray diagram of a SEM 16
2.5 Ray diagram of a TEM 18
2.6 Schematic illustration of the standard low temperature PL configuration at ANU 20
2.7 Schematic illustration of the room temperature micro-PL configuration at ANU 21
2.8 Schematic illustration of the time-integrated micro-PL configuration at UC 22
2.9 Schematic illustration of the time-resolved micro-PL configuration at UC 23

3.1 FESEM images of typical GaAs and InAs nanowires 26
3.2 Au–Ga binary phase diagram 29
3.3 Au–In binary phase diagram 30
3.4 Au–As binary phase diagram 30
3.5 Au–Ga–As and Au–In–As ternary phase diagrams 31
3.6 Schematic illustration of axial and radial growth 34
3.7 Effect of substrate preparation on GaAs nanowire morphology 37
3.8 Illustration of the bilayers forming III–V crystals 39
3.9 Schematic illustration of III–V nanowire morphologies 40
3.10 Schematic illustration of axial heterostructure nanowire growth 41
3.11 Schematic illustration of radial heterostructure nanowire growth 41
3.12 FESEM images of bare GaAs nanowires and GaAs/AlGaAs core–shell nanowires 43
3.13 Excitation power dependence of PL spectra 44

3.14 Donor–acceptor pair PL spectra 45

4.1 Effect of growth temperature on GaAs nanowire morphology 51
4.2 Effect of the two-temperature procedure on GaAs nanowire morphology . 52
4.3 Effect of growth temperature on GaAs nanowire tapering 54
4.4 Effect of growth temperature on GaAs nanowire crystal structure 55
4.5 Effect of growth temperature on GaAs nanowire PL spectra 59
4.6 Effect of growth temperature on GaAs nanowire exciton lifetime 60

5.1 Effect of V/III ratio on GaAs nanowire morphology 67
5.2 Effect of V/III ratio on GaAs nanowire tapering 68
5.3 Effect of V/III ratio on GaAs nanowire axial growth rate 69
5.4 GaAs nanowires kinked to ⟨112⟩B directions 70
5.5 Effect of V/III ratio on GaAs nanowire crystal structure 71
5.6 Effect of V/III ratio on GaAs nanowire PL spectra 73
5.7 Effect of V/III ratio on GaAs nanowire exciton lifetime 73

6.1 Effect of growth rate on GaAs nanowire morphology 79
6.2 Effect of III flow rate on GaAs nanowire axial growth rate 80
6.3 Effect of growth rate on GaAs nanowire tapering 81
6.4 Effect of growth rate on GaAs nanowire crystal structure 82
6.5 Effect of growth rate on GaAs nanowire PL spectra (constant V/III ratio) . 84
6.6 Effect of growth rate on GaAs nanowire PL spectra (constant V flow) . . 85
6.7 GaAs nanowire PL spectra at discrete time intervals after excitation . . . 86
6.8 Effect of growth rate on GaAs nanowire exciton lifetime 87

7.1 Effect of growth temperature on InAs nanowire density dependencies . . 91
7.2 Schematic illustration of InAs nanowire density dependencies 92
7.3 Effect of V/III ratio on InAs nanowire morphology 93
7.4 Effect of growth temperature on InAs nanowire morphology 95
7.5 InAs nanowire growth window 97
7.6 Effect of growth rate on InAs nanowire morphology 98
7.7 Effect of III flow rate on InAs nanowire axial growth rate 99
7.8 Effect of growth rate on InAs nanowire density dependencies 100

8.1 Effect of density on InGaAs nanowire morphology 105
8.2 Effect of vapour In composition on InGaAs nanowire height 107
8.3 Effect of density on InGaAs nanowire base structure 108
8.4 Effect of density on InGaAs nanowire height and base diameter 110

8.5 InGaAs nanowire crystal structure and elemental composition 111
8.6 Effect of density on InGaAs nanowire PL 113

9.1 FESEM images illustrating typical InAs nanowire morphology 118
9.2 TEM images of zinc-blende and wurtzite InAs nanowires 119
9.3 Effect of growth temperature and V/III ratio on twin density in InAs nanowires 120
9.4 TEM images of zinc-blende and wurtzite InAs nanowires of different diameters 121
9.5 FESEM images illustrating typical GaAs nanowire morphology 122
9.6 TEM images of zinc-blende and wurtzite GaAs nanowires 123
9.7 TEM images of InAs nanowire facets 125
9.8 FESEM images of GaAs nanowire facets 126

10.1 Schematic illustration of the nucleus geometry 131
10.2 Schematic illustration exhibiting parameters r, C and β 134
10.3 Schematic illustration of the low index microfacets of the model 136
10.4 Schematic illustration of the possible nuclei at each type of side-facet . . 137
10.5 Probabilities of nucleus formation at high μ_{As} 141
10.6 Probabilities of nucleus formation at low μ_{As} 142
10.7 Effect of supersaturation on twin formation 145

List of tables

2.1 Nanoparticle size, density and contact time for the different colliodal Au nanoparticle solutions 12

3.1 Homogeneous decomposition temperatures of TMGa, TMIn and TMSb in H_2 carrier gas. 28

3.2 Heterogeneous decomposition temperatures of AsH_3 and PH_3 on III–V substrates. 28

4.1 Summary of nanowire morphology for single- and two-temperature procedures 52

10.1 Surface energies of external vapour–nucleus facets 139

CHAPTER 1

Introduction

1.1 Significance of III–V nanowires

Semiconductor nanowires hold outstanding potential as key components of future devices and systems. Offering reduced dimensionality, outstanding materials properties and the capability for bottom-up assembly, these nanostructures are highly promising nano-building blocks. Consequently, semiconductor nanowires have attracted intense research interest within the past decade. A wide range of nanowire-based electronic and photonic devices have already been developed, including nanowire solar cells,[1–4] photodetectors,[5–7] waveguides,[8] light emitting diodes,[9,10] lasers,[11–16] single photon sources,[17] resonant tunnelling diodes,[18] single-electron transistors and memory devices,[19–23] field-emission electron sources,[24] field-effect transistors for ultrahigh density logic and memory devices[25–28] integrated photonic circuits,[29,30] and highly sensitive biological and chemical sensors.[31,32]

Nanowires can be defined as quasi-one dimensional nanostructures, with diameters typically less than 100 nm and lengths greater than 1 μm. Their unique geometry confers significant advantages over conventional planar structures. If the nanowire diameter is sufficiently small, these structures can exhibit quantum confinement in two dimensions. Their high surface-to-volume ratio makes nanowires ideal for a number of applications, especially sensing applications. Nanowires can function as interconnects, in addition to their function as active device elements. Device architectures of vertical-standing nanowires will allow ultrahigh density device integration into a single chip.[26,28]

Furthermore, nanowires can be tailored into unique axial and radial heterostructures, which greatly expands the range of device possibilities.[33–36] In axial heterostructures, the narrow nanowire diameter allows the nanowire lattice to radially expand or contract. This relaxation mechanism can relieve strain without necessitating misfit dislocations, and hence permits high quality coherent heterointerfaces between even highly lattice

mismatched materials.[37–39] Thus, nanowires present a major advantage over planar and bulk materials, where lattice-mismatched heterostructures can only be grown provided the strained layer is thin and below the critical layer thickness. Nanowire heterostructures involving a wide range of combinations of binary III–V materials, ternary III–V materials, and IV materials such as Si and Ge, have been demonstrated.[40–45] Despite the large thermal, chemical, and structural mismatch between these highly dissimilar materials, high crystallographic and optical qualities have been reported.[40,42,43,46]

Amongst semiconductor nanowires, III–V nanowires show particular promise. Several of the above-mentioned devices were created using III–V nanowires.[3–5,7,9,10,14–24,26,27] The superior electrical and optical properties of III–V materials, including their direct bandgap and high electron mobility, make III–V nanowires ideal for electronic and optoelectronic device applications.[47] GaAs nanowires have significant merits associated with the direct bandgap and high electron mobility of the GaAs material system. The GaAs material system is used extensively in the electronics and optoelectronics industries, and accordingly GaAs nanowires are prime candidates for electrically and optically active nanowire devices such as lasers, solar cells and photodetectors.[3,25,48–50] InAs features a narrow bandgap and very high electron mobility, which makes InAs nanowires highly promising, particularly for use in future high-frequency electronic devices. InGaAs nanowires have significant potential due to the paramount importance of the InGaAs material system for applications in long wavelength optical transmission and integrated photonics. Furthermore, III–V nanowires can be grown epitaxially on Si without antiphase defects or misfit dislocations, which will enable monolithic integration of III–V nanowire optoelectronic devices with established Si microelectronics technology.[40,42,43,46,51–53]

1.2 Techniques for III–V nanowire growth

III–V nanowires can be fabricated via a number of approaches. These are classified into two broad categories: top-down and bottom-up. Top-down methods begin with bulk material, from which nanowires are patterned via a combination of lithography and etching, for example using electron beam lithography or focused ion beam milling. Top-down methods have underpinned the microelectronics industry to date, but as the length scales of devices shrink according to Moore's law, top-down methods become increasingly problematic. The lithographic and etching techniques are resolution limited, which makes it difficult to define smaller features, and the quality of the nanostructures diminishes. The etching and patterning processes introduce surface defects, which adversely affect nanostructure properties. Furthermore, the process is intrinsically wasteful, and there are large challenges to overcome before these technologies become high-throughput, cost-effective means of nanowire fabrication.

Bottom-up methods, on the other hand, involve the chemical synthesis of nanowires whose properties can be carefully controlled and tuned during growth. These nanowires themselves are building blocks, which can subsequently be assembled into more complex nanoscale devices and architectures. This bottom-up paradigm offers opportunities for the fabrication of atomically precise, complex devices not possible with conventional top-down technologies. Consequently, this paradigm is expected to lead the next generation of nanoscale electronics. In many ways, bottom-up methods mimic the growth of living organisms, whereby macro-molecules are assembled into larger, more complex structures. A detailed discussion of the wide variety of nanowire fabrication methods is given in the review by Xia *et al.*[54]. Within the bottom-up fabrication regime, there are two sub-categories of nanowire growth techniques: template-directed and free-standing.

1.2.1 Template-directed nanowire growth

Template directed methods use a template to confine the crystal growth to a one-dimensional nanowire shape, allowing elongation in only one-dimension while physically restraining growth in other directions. Examples of templates are porous anodised alumina, diblock copolymers, V-grooves and step edges. These templates give reasonable control over the diameter and length of nanowires, are scalable, and produce structures which can be readily integrated with existing devices. The success of these techniques is, however, entirely dependent on the ability to fabricate a suitable template. The quality of the template directly influences the quality of the grown nanowires. In cases where growth is epitaxial with the template, as with V-groove templates, the template materials limit the types of nanowire material which can be grown epitaxially. Also, the nanowires remain embedded on the substrate which precludes their assembly into complex device architectures. Finally, control of nanowire size is limited by the resolution of the technique used to pattern the template.

1.2.2 Free-standing nanowire growth

The free-standing nanowire growth method relies on anisotropy of growth rates. Generally, nanowires nucleate at a single point and elongate in the growth direction with the highest growth rate. The slower growth rates of other directions constrain the nanowire to a one-dimensional shape. Numerous techniques exist for free-standing nanowire growth, including self-catalysed growth, oxide-assisted growth, vapour–liquid–solid (VLS) growth, and solution–liquid–solid growth, to name a few. Nanowires can be grown from a solution or vapour phases, and may be suspended in the growth medium, or in contact with a substrate.

The VLS mechanism is the most widely cited growth method. The VLS mechanism was originally proposed by Wagner and Ellis in 1964, to explain the anisotropic growth of

Si wires catalysed by metallic Au particles.[55] The VLS mechanism, so-called due to the vapour, liquid and solid phases involved, is schematically illustrated in Figure 1.1. The Si precursor species were supplied in the vapour phase. At growth temperature, the metallic Au particle formed a liquid eutectic alloy with the Si. With further supply of Si this Au–Si alloy particle became supersaturated with Si, and the Si precipitated at the particle–semiconductor interface to form a solid crystalline Si wire. Wagner and Ellis proposed two possibilities to explain nanowire growth. First, that due to the high accommodation coefficient of the liquid phase, the liquid particles are favourable collection sites for the vapour phase reaction species, and thus assist nanowire growth. The second possibility is that the metallic particle is a chemical catalyst which lowers the activation energy barriers to enhance the decomposition of the gas-phase precursors.[56] Following this work on Si wires, the VLS mechanism was then applied to III–V nanowire growth, using Au nanoparticles.[57]

For III–V nanowires, the VLS principle lends itself to a number of standard industrial and laboratory growth systems, including laser-assisted catalytic growth,[48,58] molecular beam epitaxy (MBE),[59,60] chemical beam epitaxy (CBE),[61–63] and metalorganic chemical vapour deposition (MOCVD).[57,64,65] Of all these techniques, the most promising and most common technique for III–V nanowire growth is MOCVD, using Au nanoparticles to direct nanowire growth via a VLS-like mechanism. The approach achieves epitaxial nanowires that are free-standing on the growth substrate, offers great flexibility and high accuracy in nanowire design, and is readily scalable for industrial mass fabrication. Furthermore, MOCVD is the method of choice for many applications in electronics and optoelectronics.[66–69] This dissertation examines the growth of III–V nanowires using this highly promising growth technique.

1.3 Au-assisted nanowire growth using MOCVD

All III–V nanowires presented in this dissertation were grown by MOCVD, using Au nanoparticles to drive nanowire growth. The underlying nanowire growth mechanism is closely related to, if not identical to, the VLS wire growth mechanism discussed above. The fundamental Au nanoparticle-assisted mechanism of III–V nanowire growth is explained here with reference to the schematic illustration of Figure 1.2. Initially, Au nanoparticles are deposited on a semiconductor substrate surface, as in Figure 1.2a. To initiate growth, vapour phase group III and group V precursors are provided to the reaction chamber. The Au nanoparticles alloy with specific reactant elements to form a liquid or solid alloy, for instance Au–Ga (Figure 1.2b). Deposition of III–V material occurs preferentially at the nanoparticle-substrate interface, so that nanowire nucleation takes place (Figure 1.2c). With continual supply of group III and V reactants, deposition of

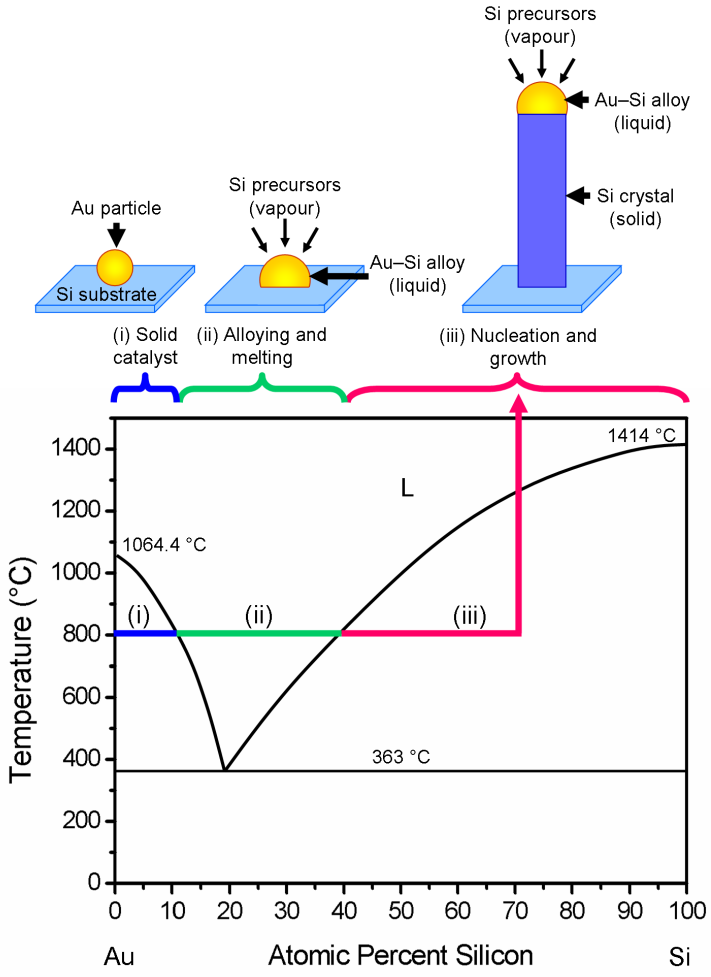

Figure 1.1: Schematic illustration of the VLS growth of Si wires using a Au catalyst particle. The Au–Si binary phase diagram illustrated in the lower portion indicates the various phases the Au–Si particle can adopt under different temperatures and in different composition ranges. Labels (i), (ii) and (iii) illustrate the different stages of nanowire growth for a growth temperature of 800 °C, and the corresponding state of the Au–Si particle.

III–V material continues at the nanoparticle–nanowire interface. Thus the nanoparticle, located at the growing tip of the nanowire, drives highly anisotropic nanowire growth (Figure 1.2d). The diameter at the tip of the grown nanowire is defined by the diameter of the Au nanoparticle. This is essentially a bottom-up fabrication technique, which offers high controllability in nanoscale dimensions not possible by top-down techniques.

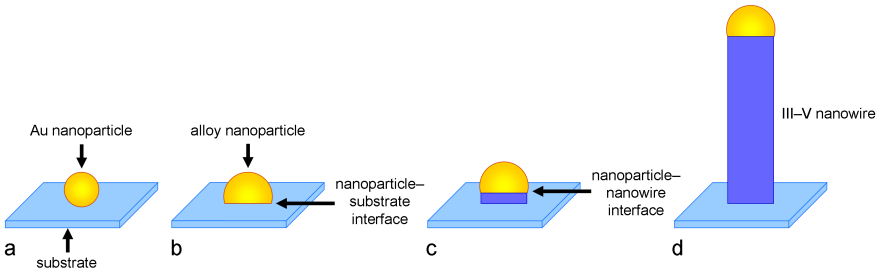

Figure 1.2: Schematic illustration of the nanowire growth mechanism. (a) Au nanoparticles are deposited on the semiconductor substrate. (b) Vapour phase reactants are supplied and the nanoparticle alloys with specific reactant elements. (c) Nucleation takes place at the nanoparticle–substrate interface. (d) Growth continues at the nanoparticle–nanowire interface.

1.4 Challenges in III–V nanowire growth and design

The development of III–V nanowire based devices depends on the ability to fabricate nanowires with tight control over properties such as morphology, orientation, crystal structure, optical properties and chemical composition. Integrated device architectures generally demand straight, vertical nanowires epitaxial with the substrate.[25,50] For this reason, it is unacceptable for nanowires to follow irregular growth directions or kink unpredictably during growth. Nanowire size and shape are crucial: in the nanoscale regime, even small variations in size can have a large effect on overall device performance. Nanowire dimensions can determine the degree of confinement, and consequently the behaviour of charge carriers in quantum electronic devices. Most device applications require a uniform nanowire diameter. For example, in proposed nanowire lasers, a uniform diameter is critical for a nanowire's performance as a resonant cavity. Unintentional radial growth, whereby material deposits on the nanowire sidewalls, can be problematic for nanowire devices. This radial growth can produce undesirable nanowire tapering, unintentional shell structures coating axial heterostructure nanowires, and compositional non-uniformity along the length of ternary nanowires.[70] Control over chemical composition, for instance to achieve intrinsic and doped nanowires, and nanowire heterostructures, is also essential for emerging nanowire device technologies.

Another important consideration is phase purity. Controlling the crystallographic

phase purity of III–V nanowires is notoriously difficult, yet this is essential for future nanowire devices. The crystallographic phase, whether zinc-blende (ZB)[71–73] or wurtzite (WZ),[74] directly affects the bandgap and electronic properties of the nanowires.[75–78] In addition, twin planes, stacking faults and ZB–WZ polytypism are commonly reported crystallographic defects in III–V nanowires.[71–73] Several studies have demonstrated that these imperfections adversely impact the optical and electronic properties of III–V nanowires, for instance by reducing the quantum efficiency, carrier lifetime and carrier mobility.[79–81] Thus, these crystallographic imperfections can drastically limit the performance of nanowire devices. Reported methods for controlling nanowire phase require dopant addition, or a restricted choice of nanowire diameter, and only rarely yield a defect-free phase.[82–84] Arguably, the nanowire diameter and doping can change nanowire properties as dramatically as the crystallographic phase itself, which makes these methods of controlling crystal phase unsuitable for device fabrication.

Finally, because III–V nanowires offer such impressive potential in optoelectronics, their optical properties are of great importance. Optoelectronic device applications usually require a long carrier lifetime and high quantum efficiency. It is therefore important to minimise non-radiative recombination centres which would adversely affect nanowire device performance. Additionally, the unintentional incorporation of dopant impurities such as carbon gives rise to electronic energy levels within the bandgap, which can adversely affect the optical and electronic properties of these nanowires. In the current literature, there are only limited reports on intrinsic dopant incorporation in nanowires, and these found that carbon is the major impurity in MOCVD-grown GaAs nanowires.[85,86] Controlling this intrinsic doping to produce high purity nanowires is a major concern in III–V nanowire growth.

The great challenge is to fabricate III–V nanowires with well-controlled orientation, minimal radial growth and tapering, a defect-free crystal phase, minimal impurity incorporation and long carrier lifetime. Fortunately, the chosen growth technique of MOCVD using Au nanoparticles offers a number of growth parameters that can be tightly controlled to achieve the desired nanowire properties. These parameters include the growth temperature, the input V/III ratio and the absolute flow rates of group III and group V precursor species. This dissertation examines how these parameters control nanowire growth, and how they can be tailored to achieve exceptionally high quality GaAs, InAs and InGaAs nanowires suitable for future applications in electronics and optoelectronics.

1.5 Thesis synopsis

This dissertation presents a detailed investigation into the Au-assisted growth of GaAs, InAs and InGaAs nanowires by MOCVD. Details of the experimental techniques and their

underlying theory are given in Chapter 2. In Chapter 3 the fundamental properties of III–V nanowires are introduced, including the nanowire growth mechanisms, structural properties and crystallographic properties. In addition, the optical properties of GaAs nanowires are discussed, and carbon is identified as the major impurity in GaAs nanowires.

GaAs nanowire growth, structure, crystal phase and optical properties are examined in Chapters 4, 5 and 6. The effects of growth temperature, and a novel two-temperature procedure, are presented in Chapter 4. The effects of V/III ratio and growth rate are presented in Chapters 5 and 6, respectively. Significantly, by tailoring these growth parameters, exceptionally high quality twin-free ZB GaAs nanowires were obtained with minimal tapering, minimal intrinsic carbon doping and nearly intrinsic exciton lifetimes.

In Chapter 7, the growth and structural properties of InAs nanowires are investigated. Unlike GaAs nanowires, InAs nanowire height and tapering is strongly influenced by the diffusion of reaction species adsorbed on the substrate surface. As a result, InAs nanowire growth shows a marked dependence on nanowire density.

The growth, structure, crystallographic properties and optical properties of InGaAs nanowires are investigated in Chapter 8. Similar to InAs nanowires, InGaAs nanowire growth exhibited a strong dependence on nanowire density. This is attributed to the large diffusion length of In species compared to Ga species. These nanowires also exhibited compositional non-uniformity along the length of each nanowire.

Chapter 9 further examines the crystal phase of GaAs and InAs nanowires. It demonstrates that phase-perfect nanowires, of arbitrary diameter, can be achieved simply by tailoring basic growth parameters: temperature and V/III ratio. Pure ZB nanowires, free of twin defects, were achieved using a low growth temperature coupled with a high V/III ratio. Conversely, a high growth temperature coupled with a low V/III ratio produced pure WZ nanowires free of stacking faults. Chapter 10 presents a comprehensive nucleation model to explain the formation of these markedly different crystal phases under these growth conditions. Critical to achieving phase purity are changes in surface energy of the nanowire side-facets, which in turn are controlled by the basic growth parameters of temperature and V/III ratio.

Finally, conclusions and suggestions for future work are given in Chapter 11.

CHAPTER 2

Experimental techniques

2.1 Introduction

This chapter describes the operation and principles of the key experimental techniques used to fabricate and characterise III–V nanowires in this thesis, namely MOCVD, electron microscopy and photoluminescence (PL). These techniques are highly complex, so the discussion is restricted to the basic principles and issues relevant to this work. Further details can be found in the cited references provided for each technique. The text is arranged as follows. Section 2.2 outlines the central technique of MOCVD, which was used to grow all the III–V nanowires in this thesis. The major characterisation techniques, electron microscopy and photoluminescence, are then discussed in Sections 2.3 and 2.4. Two microscopy techniques were pivotal to this research: scanning electron microscopy (SEM) and transmission electron microscopy (TEM).

2.2 Epitaxial growth

2.2.1 Metalorganic chemical vapour deposition

All nanowire samples studied in this dissertation were grown at the Australian National University by MOCVD. This technique, also known as metalorganic vapour phase epitaxy (MOVPE) is a vapour phase deposition process capable of producing atomically abrupt interfaces and high purity materials. MOCVD underwent rapid development in the early 1970s, led by the pioneering work of Manasevit and coworkers.[87,88] This versatile technique can produce almost all III–V and II–V semiconductor compounds and alloys. MOCVD is flexible, accurate and readily scalable for industrial mass production, and is the most economical technique for large-scale commercial production.[89] Therefore, MOCVD is the technique of choice for III–V nanowire growth. A more comprehensive description of MOCVD is found in the book by Stringfellow.[89]

In this work, all nanowire samples were grown using an AIXTRON 200/4 horizontal

flow MOCVD reactor. Figure 2.1 is a schematic illustration of the system. In this system, group III atoms, Ga, In and Al, are provided by metalorganic (organometallic or metal alkyl) precursors trimethylgallium ($Ga(CH_3)_3$, TMGa), trimethylindium ($In(CH_3)_3$, TMIn), and trimethylaluminium ($Al(CH_3)_3$, TMAl), respectively. Group V atoms, As, P and Sb are provided by the hydride precursors arsine (AsH_3) and phosphine (PH_3), and the metal alkyl precursor trimethylantimony ($(CH_3)_3Sb$, TMSb), respectively. The hydrides, AsH_3 and PH_3, are stored in high pressure cylinders and directly supplied to the reactor chamber. Unlike the hydrides, TMGa, TMAl and TMSb are volatile liquids and TMIn is a solid. These volatile organometallic sources are stored at constant temperature and pressure in sealed stainless steel cylinders, called bubblers, immersed in temperature-controlled baths.

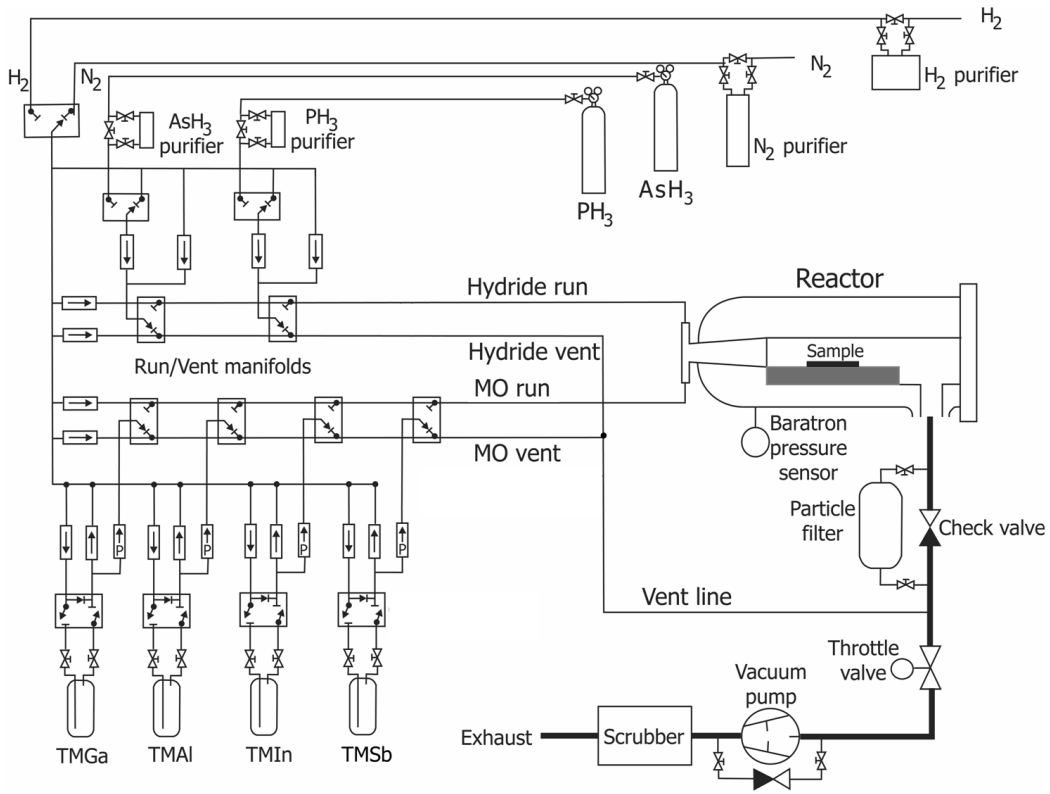

Figure 2.1: Schematic illustration of the Aixtron 200/4 MOCVD reactor.

The carrier gas, H_2, is filtered through a palladium–silver alloy membrane. The metalorganic compounds are then transported by flowing this ultra-high purity H_2 carrier gas, through the bubblers. As the pressure and temperature of the bubblers are fixed, the amount of metalorganic precursor entering the reactor is determined by the hydrogen flow, which is precisely regulated and controlled by electronic mass flow controllers.

The hydrides are also mixed with H_2 carrier gas and regulated by electronic mass flow controllers. The metalorganic and hydride precursors are transported to the reactor via separate metalorganic (labelled MO) and hydride supply lines, to avoid pre-reaction before entering the reactor. Each supply line follows a vent–run configuration. The run lines transport the source flows to the reaction chamber, whereas the vent lines transport the source flows to the exhaust. This configuration allows the source flow rates to be stabilised; the source flows are opened into the vent line to stabilise, prior to being injected into the run line. The total gas flow rates through the hydride and metalorganic lines are kept constant, at 10 standard litres per minute (slm) and 5 slm, respectively. This maintains a total gas flow rate of 15 slm through the reactor. All growths were performed at a reactor pressure of 100 mbar.

In the reaction chamber, the semiconductor substrate is held on a silicon carbide-coated graphite susceptor. The susceptor accommodates three two-inch wafers on gas foil rotation plates, for both planetary and satellite rotation to achieve highly uniform deposition. The substrate temperature is maintained using a three-zone infrared lamp arrangement surrounding the reaction chamber, and is measured by a thermocouple inserted into the susceptor. The growth reaction involves the pyrolysis of the organometallic and hydride sources over the heated substrate. The reaction between metalorganic and hydride precursors can be expressed as

$$Ga(CH_3)_3 + AsH_3 \longrightarrow GaAs + 3CH_4$$
$$In(CH_3)_3 + AsH_3 \longrightarrow InAs + 3CH_4$$
$$Al(CH_3)_3 + AsH_3 \longrightarrow AlAs + 3CH_4$$
$$Ga(CH_3)_3 + PH_3 \longrightarrow GaP + 3CH_4$$
$$In(CH_3)_3 + PH_3 \longrightarrow InP + 3CH_4$$

for the growth of GaAs, InAs, GaP and InP materials, respectively. By selecting different precursors and adjusting their flows, different materials can be deposited, including ternary materials such as InGaAs and AlGaAs.

The exhaust gas mixture, containing the unreacted precursors and the byproducts from the reaction chamber and the vent line, is then passed through an activated charcoal scrubber, which filters the toxic compounds and releases H_2 to the atmosphere.

2.2.2 Substrate preparation

GaAs and InGaAs nanowires were grown on semi-insulating GaAs $(\bar{1}\,\bar{1}\,\bar{1})$B substrates (American Xtal Technology). InAs nanowires were grown on undoped InAs $(\bar{1}\,\bar{1}\,\bar{1})$B substrates (Semiconductor Wafer, Inc). Before growth, Au nanoparticles were deposited on the substrate surface. Nanowire growth was then catalysed by these Au nanoparticles. These Au nanoparticles were obtained as colloidal solutions from British Biocell

Table 2.1: The colloidal Au nanoparticle solutions used for nanowire growth. The table lists the nanoparticle sizes and densities of each colloidal solution. The contact time is the time the colloidal Au solution was left in contact with the PLL-functionalised substrate, before rinsing.

Diameter (nm)	Concentration (Particles/ml)	Contact Time (s)
10	5.7×10^{12}	2
20	7.0×10^{11}	5
30	2.0×10^{11}	10
50	4.5×10^{10}	20
100	5.6×10^{9}	60
150	1.7×10^{9}	60
200	7.0×10^{8}	60
250	3.6×10^{8}	60

International–Ted Pella, Inc. Each solution contains monodisperse Au nanoparticles of a given diameter and density, as listed in Table 2.1.

The Au nanoparticles are citrate-stabilised and carry a net negative surface charge, so that Coulombic repulsion prevents nanoparticle agglomeration. Due to their negative charge, the nanoparticles do not naturally adhere to III–V substrates. Nanoparticle deposition was achieved by functionalising the substrate with poly-L-lysine (PLL) before applying colloidal Au, as follows. First, the substrate was immersed in 0.1% PLL solution for 60 s, then rinsed with deionised (DI) water, and dried with a nitrogen (N_2) gas gun. Then, a 100 μL droplet of undiluted Au colloidal solution was dispersed on the substrate, and rinsed away with DI water after a contact time of 2 to 60 s, and the substrate was again dried with N_2. A longer contact time was used for lower density Au colloidal solutions, to achieve a sufficient density of Au nanoparticles adhering to the substrate. Table 2.1 lists the contact times for each solution.

PLL is a positively charged polyelectrolyte which attracts the negatively charged Au nanoparticles and immobilises them on the substrate surface.[90,91] Treatment with polyamines, such as PLL, is widely used in the life sciences to immobilise cells on slides, and also has been used to immobilise nanoparticles to create standard samples for atomic force microscope calibration.[92] The PLL functionalisation–Au nanoparticle deposition method described above prevents agglomeration of nanoparticles during deposition and achieves an even nanoparticle distribution on the substrate. A discussion of alternative nanoparticle deposition techniques is given in Section 3.9. With the exception of Section 3.9, all nanowire samples discussed in this report were prepared by this PLL functionalisation technique. Throughout this dissertation, results are presented for nanowire samples prepared with 50 nm diameter nanoparticles, except where stated otherwise.

2.2.3 Growth procedure

Prior to growth, Au nanoparticles were deposited on the substrate surface, as described above. The prepared substrate, hosting deposited Au nanoparticles, was placed into the reactor on a graphite susceptor. The substrate was heated to 600 °C and annealed in situ for 10 minutes to desorb surface contaminants, including the surface oxide. Annealing of GaAs and InAs substrates was performed under group V overpressure, to prevent decomposition of the substrate. This group V overpressure was provided by an AsH_3 flow of 1.3×10^{-3} mol/min.

After annealing, the substrate was cooled to growth temperature, typically between 350 °C and 550 °C. The group V flow rate was adjusted for growth. Then group III precursors were fed to the reaction chamber to initiate growth. Growth times were generally between 30 s and 120 minutes, chosen according to the growth rate and the desired nanowire length. Upon completion of growth, each sample was cooled under group V overpressure (AsH_3 flow).

2.3 Electron microscopy

An electron microscope uses a beam of electrons to illuminate a specimen and create a highly magnified image. Electron microscopes can achieve atomic resolution, and thus have much better resolution than optical microscopes which are limited to resolutions of approximately 200 nm. Due to these resolution limits, optical microscopy cannot image nanowires with sufficient resolution, whereas electron microscopy can. Electron microscopy has established itself as an essential technique for characterising the structure, crystallinity and composition of nanowires.[93]

In electron microscopy, a high energy electron beam is directed onto the sample. The electrons interact with the sample and generate a number of signals, some of which are schematically summarised in Figure 2.2. If the sample is sufficiently thin, a fraction of electrons pass through the specimen without any interaction, as a transmitted beam. Other electrons scatter at the surface of the specimen, or during their transit through the specimen. Those that scatter backwards at the surface of the specimen without loss of their energy are known as back-scattered electrons. Those that forward-scatter during transmission through the specimen can be classified as either elastically scattered or inelastically scattered. The former are scattered without loss of their energy, whereas the latter are scattered with measureable loss of energy. If the incident electron beam is coherent, that is, the electrons are in phase to each other, elastically scattered electrons maintain this coherence, whereas inelastically scattered electrons have no phase relationship with each other.

In addition to transmitted and scattered electrons, other signals are generated from

the specimen, including secondary electrons, Auger electrons and characteristic X-rays. During electron beam bombardment, kinetic energy is transferred from incident electrons to outer-shell electrons of the specimen atoms. The outer-shell electrons are ejected as secondary electrons.

Characteristic X-rays are emitted when kinetic energy from the electron beam is transferred to the inner shell electrons of specimen atoms. The inner shell electrons are ejected from their orbitals, leaving empty states. As electrons from an outer shell relax to fill the empty states in the inner-shell, X-ray photons are emitted with energy equal to the energy difference between the two shells. These characteristic X-rays have unique wavelengths for each element in the periodic table, which allows the detection of the elements present in a specimen. These X-rays are measured in a technique called energy dispersive X-ray spectroscopy (EDS) to identify chemical composition of a sample.

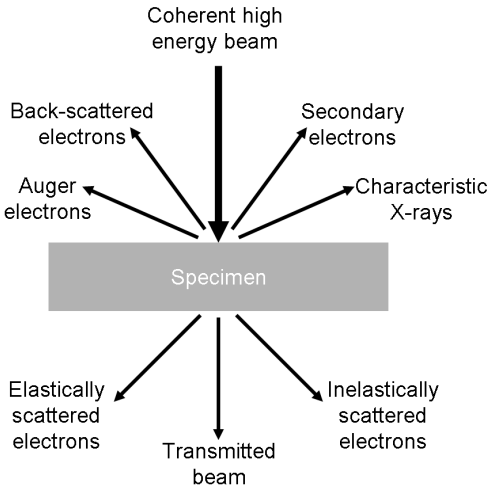

Figure 2.2: Schematic illustration of the interaction of an electron beam with a specimen.

Transmission electron microscopy (TEM) and scanning electron microscopy (SEM), each an important technique for nanowire characterisation, are complementary techniques. They use different beam energies, different signals for image formation, and are appropriate for different types of samples. TEM uses a very high energy electron beam, whereas SEM uses a lower energy electron beam. TEM images are constructed from transmitted and diffracted electrons passing through an electron-transparent sample. Thus, TEM provides information on the internal crystal structure of a specimen. TEM is only possible for thin electron-transparent specimens, typically less than a few hundred nanometres in thickness, so it is suitable for imaging individual nanowires with diameters less than 300 nm. SEM is appropriate for thicker samples, such as nanowires on their growth substrates, as SEM relies on secondary or back-scattered electrons for image

formation. Thus, SEM provides information about nanowire surface morphology.

2.3.1 Scanning electron microscopy

In SEM, a focused beam of electrons raster scans across the sample surface, and the signals generated are used for imaging. Typically, the sample is thick and the electron beam is not transmitted through the sample.

A SEM uses secondary electrons and back-scattered electrons for imaging. All SEM images presented in this dissertation were obtained using secondary electron mode. Secondary electrons have low energies, less than 50 eV. Most secondary electrons are re-absorbed by the sample. Only the electrons produced near the surface (at a depth of less than 5 to 50 nm) can escape from the specimen and participate in image formation. Therefore, secondary electrons provide details of the sample surface topography. The number of secondary electrons emitted from the surface region varies with the topography of the surface. This number is lowest when the incident electron beam is perpendicular to the sample surface. This number increases with increasing angle between the surface normal and the incident electron beam. This phenomenon is schematically illustrated in Figure 2.3, where the surface is not planar. The escape depth of secondary electrons is indicated by the dotted line and the escape volume is shown by the shaded areas. As the electron beam is scanned over the protrusion in Figure 2.3, the escape volume of secondary electrons is much higher than that of the flat surface. Thus, protrusions produce higher counts of secondary electrons, which makes these features brighter.

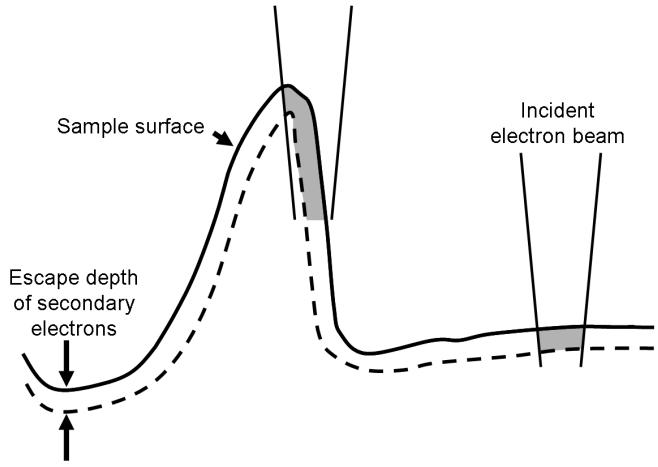

Figure 2.3: Diagram illustrating the influence of surface topography on the escape volume of secondary electrons. The dotted line represents the escape depth and the shaded area represents the escape volume.

Figure 2.4 is a schematic diagram of a SEM. Electrons are extracted from a filament

or field emission tip with a moderate accelerating voltage, typically between 1 and 50 kV. The incident electron beam (also known as electron probe) has a diameter of 1 to 10 nm, depending upon the electron source. For example, a field emission gun, as used in a field emission scanning electron microscope (FESEM), can produce an electron beam that is narrower in diameter and has greater current density than can be achieved with conventional thermionic emitters. The condenser lens controls the spot size by demagnifying the electron beam from the gun. The objective lens focuses the electron beam into a small probe, which controls the focus of the final image. The aperture diameter controls the electron beam convergence angle (α).

When imaging nanowires, the major parameters are the beam diameter, the depth of field and the signal strength. The beam diameter determines the image resolution. A smaller beam diameter can be achieved by decreasing the working distance, which can provide better resolution. Another important parameter, the depth of field, can be defined as the depth of sample which is in acceptably sharp focus. Depth of field is important for nanowire imaging, because nanowires protrude several microns above the substrate plane. Depth of field can be increased by narrowing the aperture, and consequently reducing α. It can also be increased by increasing the working distance. However, narrowing the aperture limits the signal strength, and increasing the working distance reduces the image resolution. Therefore, when imaging nanowires, a compromise must be made between signal strength, depth of field and resolution.

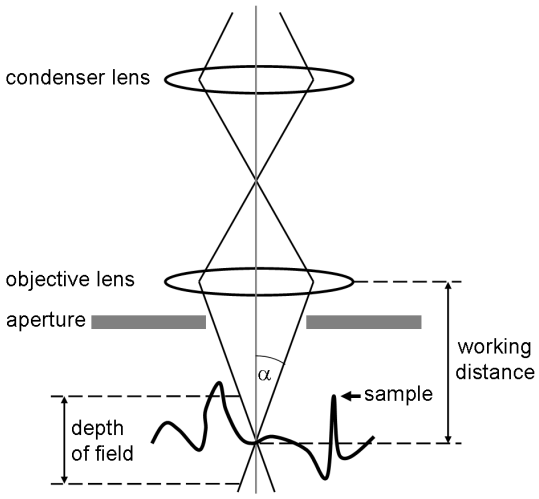

Figure 2.4: A ray diagram of a SEM, showing the working distance and the depth of field.

All SEM images presented in this work, with the exception of Figure 9.8, were obtained on a Hitachi S4500 field emission scanning electron microscope (FESEM) operated at an accelerating voltage of 3 kV. Figure 9.8 was obtained with a Zeiss UltraPlus

field emission microscope operated at an accelerating voltage of 3 kV. FESEM was used to identify nanowire structure and morphology, including height, diameter, degree of tapering, growth direction, facet planes and density.

2.3.2 Transmission electron microscopy

TEM is a well-established technique for studying the crystallinity and microstructure of materials. TEM requires a high energy electron beam, and a thin specimen, up to a few hundred nanometres in thickness, so that the specimen is transparent to the electron beam.

Figure 2.5 is a simplified schematic diagram of a typical TEM. Electrons are extracted from a filament or a field emission tip with a large accelerating voltage ranging from 100 to 1000 kV. The electrons pass through the condensor lens system where the electron beam is condensed to a smaller size. The condenser lenses are fitted with apertures, which control the intensity of the electron beam and convergence angle. The condensed electron beam is incident on the sample, through which electrons are transmitted and scattered. The transmitted and scattered electrons pass through the objective lens and form two planes of interest: the image plane and the back focal plane, as labelled in Figure 2.5. An image of the specimen forms on the image plane. The diffraction pattern forms at the back focal plane. The image and diffraction pattern can be viewed on the viewing screen below. The strength of the intermediate lens is adjusted, to project either the image or the diffraction pattern onto the screen. To view the image of the sample, the intermediate lens strength is chosen so that the image plane of the objective lens becomes the object plane of the intermediate lens. To view the diffraction pattern, the intermediate lens uses the back focal plane as its object plane. Figure 2.5a and b show ray diagrams for imaging and diffraction modes, respectively.

If the sample is crystalline, the elastically scattered electrons generate electron diffraction patterns. The generated diffraction pattern depends on the interplanar spacing of the atomic planes and the angle at which the electron beam is incident on the crystal planes. In a diffraction pattern, each diffraction spot represents the interplanar spacing of a unique set of planes. The axis orthogonal to all the diffraction spots and parallel to the electron beam is termed the zone axis. Diffraction patterns are particularly useful for determining the crystal phases, ZB or WZ, in the nanowires studied.

The two major imaging modes are bright field and dark field. Bright field images are formed using the transmitted beam, whereas dark field images are formed using one diffracted beam.

TEM and EDS investigations were carried out on three separate instruments. In Chapters 4, 5, 6 and 8 TEM was performed on the FEI Technai F30 at the University of Queensland by Prof. Jin Zou, Dr. Xin Zhang and co-workers. In Chapter 8, EDS was

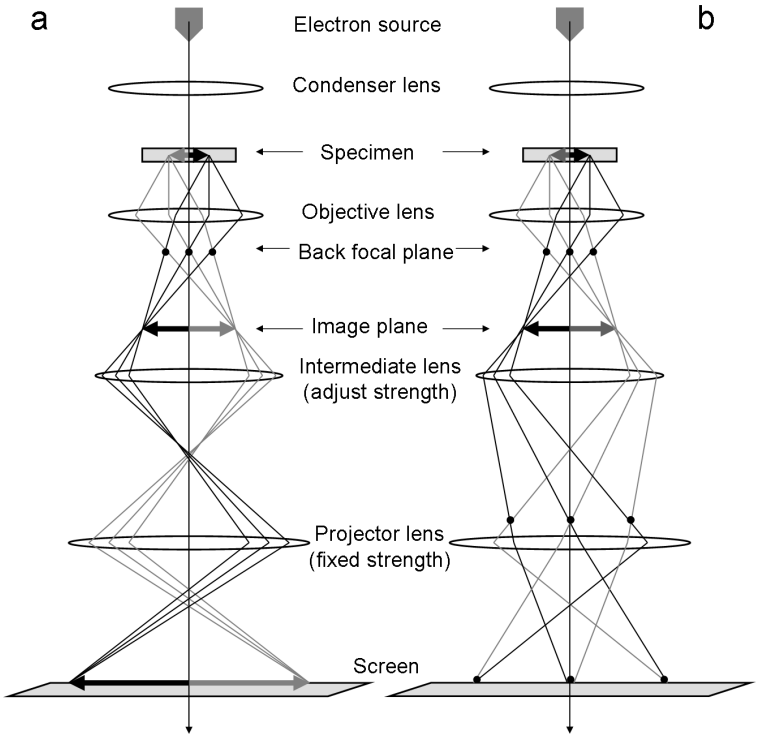

Figure 2.5: Ray diagram of a TEM for (a) imaging mode, where the image is projected onto the viewing screen and (b) diffraction mode, where the diffraction pattern is projected onto the viewing screen. In each case the intermediate lens selects either the image plane or the back focal plane of the objective lens as its object.

performed at the University of Western Australia by Dr. Alexandra Suvorova, using a JEOL 3000F field emission gun TEM equipped with an Oxford Instruments INCA 200 EDS system. In Chapter 9, TEM and EDS were performed on a Phillips CM300 at the Australian National University (ANU) by Dr. Jennifer Wong-Leung. All microscopes were operated at an accelerating voltage of 300 kV.

All nanowires examined had diameters less than 300 nm, and consequently met requirements for electron transparency without requiring thinning or polishing. Nanowire samples were prepared by one of two methods: (i) ultrasonication and (ii) direct mechanical transfer. For the ultrasonication method, pieces of as-grown nanowire samples were cleaved and placed in a beaker with a small amount (approximately 10 mL) of ethanol. The beaker was then placed in an ultrasonic agitator for approximately 20 minutes to break the nanowires from the underlying substrate and disperse the nanowires in the ethanol. A few drops of the nanowire-containing ethanol were dispensed onto a holey carbon-coated copper TEM grid, and the nanowires remained adhered to the grid once the ethanol had evaporated. The direct mechanical transfer method involved gently wiping the holey carbon-coated copper grid over the piece of as-grown nanowire sample. This action transfers the nanowires from the host substrate to the grid.

Conventional bright field and dark field TEM imaging of the nanowires along the $[1\bar{1}0]/[11\bar{2}0]$ zone axis was used to identify the crystal structures (ZB or WZ), twin phase boundaries and stacking faults, in combination with selected area diffraction and high resolution TEM (HRTEM) lattice imaging.

2.4 Photoluminescence spectroscopy

PL spectroscopy is a convenient, contact-free, non-destructive technique of determining the electronic and impurity states in bulk III–V materials,[94] and in semiconductor nanostructures such as III–V nanowires.[95–97] This technique requires only a small quantity of material, as small as a single nanowire. In PL spectroscopy, photons (with energies greater than the semiconductor bandgap) are used to excite electrons to the conduction band, leaving holes in the valence band. These photoexcited carriers diffuse, and either recombine non-radiatively by emitting phonons or transferring energy to other particles, or recombine radiatively to generate photons, known as luminescence. In PL spectroscopy, the emitted photons are detected, from which information about the electron energy levels and carrier lifetimes can be extracted. A clear and thorough description of PL spectroscopy can be found in the review by Gilliland.[98].

Micro-photoluminescence (micro-PL) is a variant of PL, whereby the excitation illumination is focused to a small spot size, and the resulting PL imaged by optical microscopy. This provides high spatial resolution which allows the excitation and

measurement of individual nanowires. In this work both conventional PL and micro-PL were employed.

For PL measurements, InGaAs nanowire samples were characterised as-grown on their original substrates. GaAs nanowires, on the other hand, were transferred to Si substrates for PL characterisation. These were transferred from the as-grown host substrate to the Si substrate by gently touching the two substrates together.

PL measurements were performed at the ANU and the University of Cincinnati (UC). At the ANU, three configurations were used: (i) standard low temperature PL, (ii) room temperature micro-PL and (iii) low temperature micro-PL. The micro-PL system at the University of Cincinnati was used in two different configurations: (iv) time-integrated and (v) time-resolved. These systems are described below.

2.4.1 Standard low temperature PL spectroscopy (ANU)

The spectra presented in Chapter 8 were obtained using the system illustrated in Figure 2.6. The nanowire sample was placed in a closed cycle He cryostat, and cooled to 10 K. The 532 nm line of a frequency-doubled diode-pumped solid state (DPSS) laser was used to excite ensembles of nanowires. The excitation laser spot was approximately 100 μm in diameter. The resulting PL was dispersed through a 0.5 m monochromator, which was scanned through the wavelength range and the PL intensity at each wavelength step was detected by a thermoelectrically cooled InGaAs photodetector. The laser radiation was chopped at a frequency of 300 Hz and the PL signal was detected at the same frequency using a lock-in amplifier.

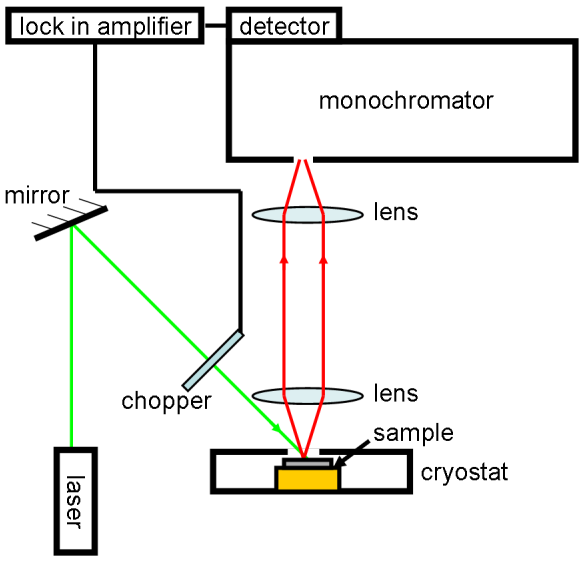

Figure 2.6: Schematic illustration of the standard low temperature PL system (ANU).

2.4.2 Room temperature micro-PL imaging (ANU)

All micro-PL images presented in this dissertation were obtained at the ANU using the system illustrated in Figure 2.7. Individual nanowires were excited through a 100×0.9 numerical aperture (NA) objective (Nikon CFI LU Plan Epi) of an epifluorescence microscope (Nikon Eclipse L150) using the 532 nm line of a DPSS laser. The excitation laser spot was approximately 10 μm in diameter. The resulting PL was collected through this objective and imaged onto a Peltier-cooled CCD camera (Nikon DS-5Mc).

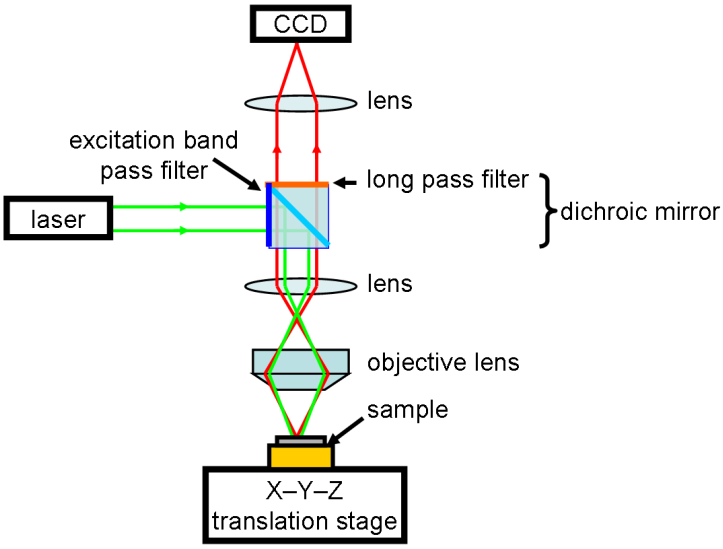

Figure 2.7: Schematic illustration of the room temperature micro-PL system (ANU).

2.4.3 Low temperature micro-PL spectroscopy (ANU)

The Si substrate hosting the nanowires was placed in a continuous flow He cryostat (Janis ST-500 Microscopy Cryostat) and cooled to 4 K. Individual nanowires, or ensembles of nanowires were excited through a 100×0.7 NA super long working distance (6.5 mm) objective (MUE30900 CFI L Plan Epi SLWD 100x) of an epifluorescence microscope (Nikon Eclipse L150). The excitation laser spot was approximately 10 μm in diameter. The resulting PL was collected through this objective and imaged onto a Peltier-cooled CCD camera (Nikon DS-5Mc).

2.4.4 Time-integrated micro-PL spectroscopy (UC)

The Si substrate with dispersed nanowires was placed onto the cold finger of a variable temperature continuous flow helium cryostat. Measurements were conducted at 18 K using slit confocal micro-photoluminescence spectroscopy.[80] Single nanowires or nanowire ensembles were excited at 780 nm with a continuous wave Ti:Sapphire laser defocused to

an approximately 10 μm diameter spot. The laser was focused onto the sample through a 50 $\times$ /0.5 NA long working distance (10.6 mm) microscope objective. Nanowire PL emission was collected by the same microscope objective, spatially filtered by a pinhole, and focused on the entrance slit of the spectrometer. The PL was dispersed by the spectometer and detected by a 2000 $\times$ 800 pixel liquid nitrogen cooled CCD detector. Figure 2.8 is a schematic illustration of the system.

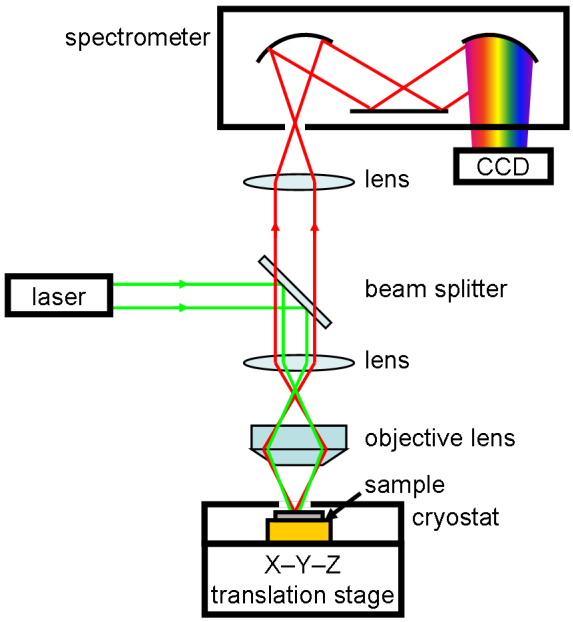

Figure 2.8: Schematic illustration of the time-integrated micro-PL system (UC).

2.4.5 Time-resolved photoluminescence spectroscopy (UC)

Time-resolved PL spectroscopy (TRPL) is a variant of PL spectroscopy used to study carrier dynamics. In TRPL, photons from a short laser pulse are used to excite electrons and holes. As these carriers recombine to emit photons, TRPL measures the rate of photon emission with respect to time after the laser pulse. Thus TRPL measures the carrier lifetime, that is, the time between creation and annihilation of the carrier.

TRPL measurements were performed using time-correlated single photon counting at the University of Cincinnati. Figure 2.9 illustrates the TRPL system. Single, isolated nanowires were excited using pulsed laser excitation (780 nm, 800 μW) from a Ti:Sapphire laser defocused to an approximately 10 μm diameter spot, with 200 fs pulses at a 76 MHz repetition rate. The emitted photons were analysed by a spectrometer and detected by a silicon avalanche photodiode detector (APD).

The APD has its own amplifier and discriminator, and provides logic pulses as its output. The output pulse from the APD serves as the “stop” signal for the time-to-

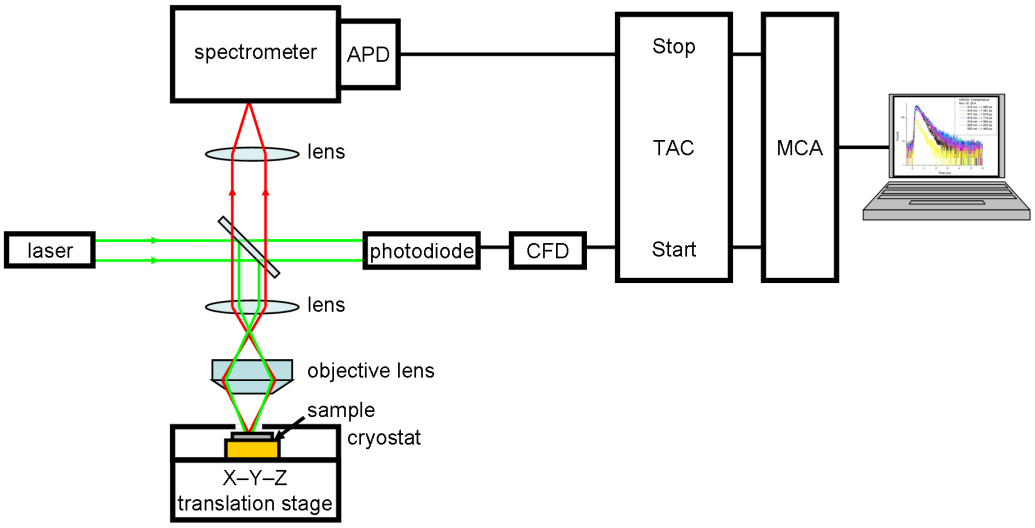

Figure 2.9: Schematic illustration of the time-resolved micro-PL spectroscopy system (UC).

amplitude converter (TAC). Pulses from the laser beam are detected by a fast photodiode and sent to a constant fractional discriminator (CFD), which converts the current pulse to a logic pulse. The output pulse of the CFD serves as the "start" signal for the TAC. The TAC produces a pulse with a voltage proportional to the time between "start" and "stop" pulses. The multichannel analyser (MCA) bins the output pulse voltages from the TAC into channels; each channel corresponds to a different time interval. Thus, the MCA records each photon arriving at the APD at a particular time. The number of output pulses from the MCA is directly proportional to the number of incident photons. By averaging millions of photons, the system creates a histogram which shows how long the photoexcited carriers exist before recombining.

The temporal system response was measured to be 80 ps.

2.5 Summary

This chapter has outlined the operation and principles of the experimental techniques employed in this research project. These include MOCVD, used to grow III–V nanowires, and SEM, TEM and PL, used to characterise the properties of these nanowires. For further information, the reader is referred to the cited references.

CHAPTER 3

Fundamental principles of III–V nanowire growth and properties

3.1 Introduction

The concepts introduced in this chapter will provide the background for the results and discussion presented in the following chapters. This chapter will review previous theoretical and experimental work on nanowires, and present new work which underpins the results presented in the following chapters.

Some of these fundamental concepts are illustrated in Figure 3.1, which shows FESEM images of typical GaAs and InAs nanowires grown via Au-assisted MOCVD. The nanowires are vertically aligned on their $(\bar{1}\,\bar{1}\,\bar{1})$B terminated substrates indicating their epitaxial relationship with the substrate. Some nanowires are tapered, with narrow tips and wider bases. At the tip of each nanowire lies a Au alloy nanoparticle, which drives growth. The diameter at the nanowire tip is governed by the diameter of the Au nanoparticle. The basic Au-assisted nanowire growth mechanism was described in Section 1.3, and following sections describe the growth process in further detail. Sections 3.2 and 3.3 then outline the growth thermodynamics and decomposition kinetics occuring in the MOCVD growth system. Section 3.4 describes the alloy formation and composition of the Au nanoparticle driving nanowire growth. Section 3.5 discusses the $[\bar{1}\,\bar{1}\,\bar{1}]$B growth direction, the energetically preferred growth direction. Surface diffusion, axial growth, radial growth and nanowire tapering will be described in Sections 3.6 and 3.7. Section 3.8 discusses recent debate about the Au-assisted nanowire growth mechanism. Section 3.9 evaluates alternative methods of Au nanoparticle deposition and compares these with the routinely-used PLL functionalisation method used for Au nanoparticle deposition.

Nanowire heterostructures are briefly discussed in Section 3.12. Finally, Section 3.13

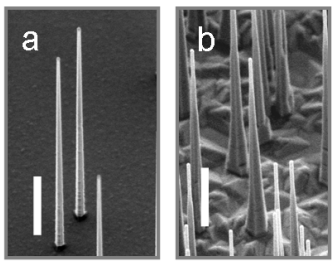

Figure 3.1: FESEM images of (a) GaAs and (b) InAs nanowires catalysed by 50 nm diameter nanoparticles. Samples are tilted at 40°. Scale bars are 1 μm.

describes PL spectroscopy of GaAs/AlGaAs core–shell nanowires, including interpretation of their PL spectra and the characterisation of the donor–acceptor pair peak. Carbon is identified as the dominant acceptor impurity in GaAs nanowires.

3.2 Growth thermodynamics

Epitaxial growth can be described as a tightly-controlled phase transition driven by thermodynamics. Epitaxial growth takes place under non-equilibrium conditions. The difference in chemical potential, $\Delta\mu$, between the reactants and the products, drives the reaction. This is given by

$$\begin{aligned} \Delta\mu &= \mu_{III} + \mu_V - \mu_{III-V} \\ &= k_B T \ln \frac{p_{III} p_V}{p_{III,eq} p_{V,eq}} \end{aligned} \tag{3.1}$$

In this formula, μ_{III} and μ_V are the chemical potentials of the group III and group V reactants, respectively, and μ_{III-V} is the chemical potential of the III–V bulk material. On the bottom line, k_B is the Boltzmann constant 1.381×10^{-23} JK^{-1}, T is the growth temperature, and p_x and $p_{x,eq}$ are the partial pressures of reactant x during growth and at equilibrium with the III–V crystal, respectively. If the group III and group V species are precipitating from a liquid or solid phase, for instance from the Au alloy nanoparticle (liquid or solid), the pressures can be replaced by concentrations, C_x and $C_{x,eq}$.

The non-equilibrium conditions, which drive nanowire growth, are maintained by the continuous supply of gas phase reactants.

3.3 Precursor decomposition and reaction kinetics

In order to understand nanowire growth by MOCVD, it is important to understand the pyrolysis (decomposition) behaviour of the gas phase precursors supplying the group III and V elements. The decomposition kinetics have been studied in detail for bulk GaAs and

InP growth, and the same basic mechanisms are believed to extend to InAs and GaP materials. Decomposition of organometallic compounds proceeds by the stepwise removal of methyl radicals (CH_3), from trimethyl- to dimethyl- to monomethyl-. For instance, TMGa decomposes to dimethylgallium ($Ga(CH_3)_2$, DMGa) to monomethylgallium($GaCH_3$, MMGa) to gallium. Hydrides decompose via the removal of H atoms. The rate limiting steps are the removal of the first methyl group from the organometallic compounds, and the removal of the first H atom from the hydride compounds.[99]

In MOCVD, both homogeneous and heterogeneous decomposition reactions must be considered. Homogeneous reactions are those which take place in the vapour, whereas heterogeneous reactions take place on the substrate, once the precursors have been adsorbed. Whether homogeneous or heterogenous reactions are dominant depends on the growth temperature and the precursor species. These reactions will be discussed considering typical nanowire growth conditions: with H_2 ambient, the presence of a III–V substrate, and growth temperature between 350 °C and 550 °C.

Within this temperature range, homogeneous decomposition is significant for organometallic precursors. The percentage decomposition follows an approximately sigmoidal relation, ranging from the temperature at which decomposition begins, to a higher temperature at which decomposition is complete. Table 3.1 summarises the approximate homogeneous decomposition temperatures of TMGa, TMIn and TMSb in H_2 carrier gas. Heterogeneous pyrolysis of organometallics also takes place. Due to the catalytic action of the III–V substrates, heterogeneous pyrolysis has lower decomposition temperatures and lower activation energies than homogeneous pyrolysis.

Unlike the organometallics, hydride precursors do not undergo homogeneous decomposition within this temperature range. For hydride precursors, heterogeneous decomposition is dominant, as their pyrolysis is strongly catalysed by the presence of III–V substrates. Table 3.2 summarises the heterogeneous decomposition temperatures, including the temperature at which decomposition is 50% complete (T_{50}).

The above discussion has centred on the independent decomposition of each individual precursor species. When both group III organometallic and group V hydride precursors are supplied, these precursors react in concert. In these reactions, the CH_3 and H groups are eliminated via stepwise release of CH_4, such that the group III and group V precursors decompose in a 1:1 ratio.[100–102] There are two main mechanisms by which group III and group V precursors can interact. In one mechanism, undecomposed group III (e.g. TMIn) and group V (e.g. PH_3) precursors form a gas phase adduct (e.g. TMIn:PH_3), homogeneously decompose to release CH_4, and later adsorb on the substrate. In the other mechanism precursors (e.g. MMGa and AsH_2) adsorb independently, then interact on the substrate, possibly as a surface adduct (e.g. MMGa:AsH), and

Table 3.1: Homogeneous decomposition temperatures of TMGa, TMIn and TMSb in H_2 carrier gas.

Precursor	Decomposition range 0% → 100% (°C)	Reference
TMGa	375 → 475	106
TMIn	300 → 400	101
TMSb	350 → 450	107

Table 3.2: Heterogeneous decomposition temperatures of AsH_3 and PH_3 on III–V substrates.

Precursor	Substrate	Decomposition range 0% → 100% (°C)	T_{50}	Reference
AsH_3	GaAs	375 → 525	476	102,108
PH_3	InP	400 → 575	520	99,108,109

then heterogeneously react to eliminate CH_4.[103] By either mechanism, the interaction between group III and group V precursors weakens the group III–methyl (e.g. Ga–CH_3 in TMGa) and group V–H (e.g. As–H in AsH_3) bonds. This reduces the pyrolysis temperature of each precursor involved, and gives a lower activation energy than that of independent decomposition.[101,102] The adduct binding energies are low, so if an adduct is involved, it is only short-lived at the temperatures used for growth. Accordingly, the adduct is thought to release a CH_4 molecule and then dissociate. This means that, once adsorbed on the substrate, the (partially decomposed) group III and group V species diffuse independently. Indeed group III and group V species have very different surface diffusion properties. Group III species are thought to diffuse in a monomethyl- form (e.g. monomethylgallium), and can diffuse a distance of the order of micrometres.[104] Group V species have significantly lower diffusivity, and are believed to incorporate close to the position of adsorption.

In nanowire growth, both independent decomposition, and reactions between group III and group V precursors should be taken into account.[105] If chemical reactions, that is, precursor decomposition reactions, limit nanowire growth, then the growth rate, R_g, follows the relation

$$R_g \propto \exp -\frac{E_A}{RT} \tag{3.2}$$

where E_A is the activation energy of the reaction and R is the gas constant $8.314\ \mathrm{JK^{-1}mol^{-1}}$.

3.4 Alloy formation between Au and III–V materials

During the annealing and growth processes, the Au nanoparticle can interact significantly with the substrate and precursor species. The situation for III–V nanowires is significantly

more complex than for Au-assisted Si wires (as described in Section 1.2.2), because at least three different elements are involved: Au, a group III and a group V. This warrants its detailed discussion here.

The binary and ternary phase diagrams are indispensable in determining the composition and phase of the nanoparticle, and in understanding the growth mechanism. Binary phase diagrams[110–118] indicate which phases are stable at room temperature, during annealing and at growth temperature. Three binary phase diagrams are relevant: (i) Au–group III, (ii) Au–group V, and (iii) III–V. For instance, (i) Au–Ga, (ii) Au–As and (iii) Ga–As binary phase diagrams are each employed to study the Au-assisted growth of GaAs nanowires. Au–Ga, Au–In and Au–As binary phase diagrams are shown in Figures 3.2, 3.3 and 3.4. At typical nanowire growth temperatures (between 350 and 500 °C), the Au–Ga phase diagram indicates that Ga can form a liquid or solid alloy with the Au nanoparticle. If solid, it may assume a number of possible stable intermetallic solid phases, for instance the β or β' phase (Au_7Ga_2), depending on growth temperature. Similarly, the Au–In phase diagram indicates that above 454.3 °C a liquid eutectic Au–In can form. The non-metal As has very different behaviour: it has very low solid solubility in Au, the Au–As phase diagram does not include any intermetallic solid phases, and typical nanowire growth temperatures are too low to form a eutectic liquid Au–As alloy.

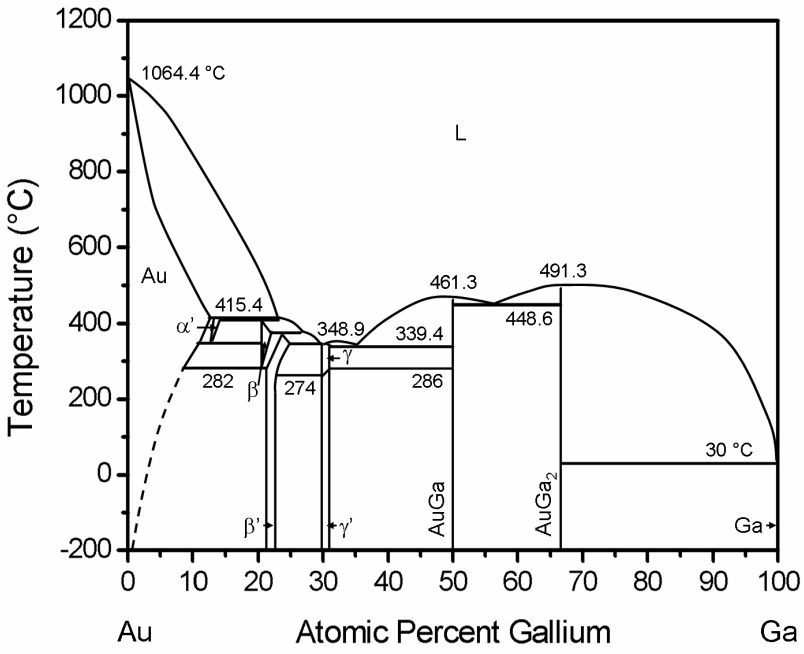

Figure 3.2: Binary phase diagram of the Au–Ga system. Reproduced from Elliot and Shunk.[112]

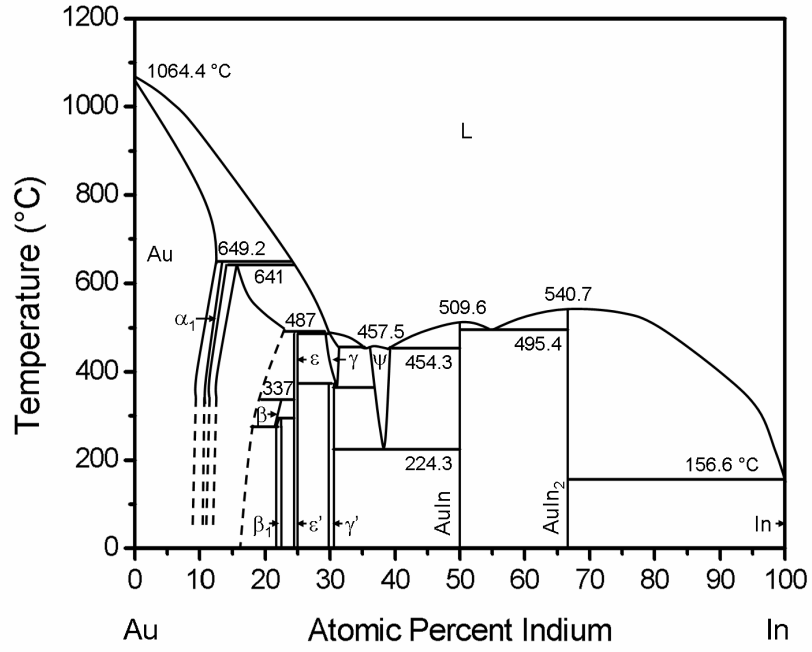

Figure 3.3: Binary phase diagram of the Au–In system. Reproduced from Hiscocks and Hume–Rothery.[110]

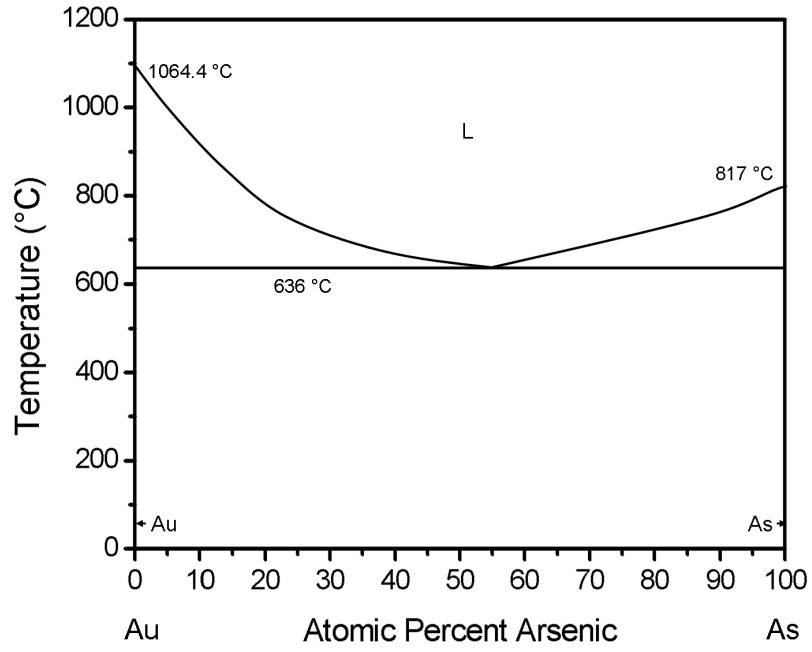

Figure 3.4: Binary phase diagram of the Au–As system. Reproduced from Okamoto and Massalski.[113]

Binary phase data cannot completely describe the interaction between Au and III–V materials, but paired with ternary phase diagrams gives much useful information. Tsai and Williams[119,120] have developed phase diagrams for these ternary Au–III–V interactions. In these ternary phase diagrams, tie lines define pseudobinary systems. Pseudobinary systems are pairs of phases which can exist in equilibrium with one another, and do not react with one another to form products. For example, in the Au–Ga–As ternary phase diagram (Figure 3.5a), the Au–GaAs pseudobinary tie line indicates that Au does not react with the GaAs substrate at equilibrium. On the other hand, in the Au–In–As ternary phase diagram (Figure 3.5b), there is no Au–InAs pseudobinary tie line, indicating that Au reacts with InAs substrates. During growth, supply of group III species (e.g. as decomposed TMGa) and group V species (e.g. as decomposed AsH_3) shifts the elemental composition of the Au–III–V system, moving it out of equilibrium. As a result, the composition of the Au nanoparticle can change, and the III–V phase precipitates. Thus, pairing the binary and ternary phase diagrams gives information on the phases existing under different growth conditions, and the nanowire growth mechanism. Ultimately, the composition and phase of the alloy depends on several factors, particularly the temperature, group III and V flow rates, and the type of III–V material. Dick *et al.* have published a thorough account of the possible alloy phases of the nanoparticle during growth.[47]

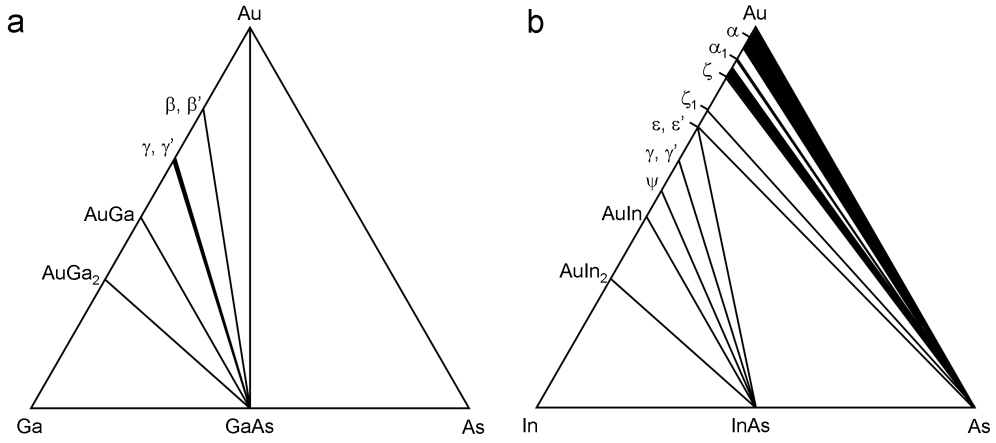

Figure 3.5: Ternary phase diagrams of the (a) Au–Ga–As and (b) Au–In–As systems. Reproduced from Tsai and Williams.[119]

Even with the assistance of ternary phase diagrams, it is difficult to ascertain the exact phase, solid or liquid, of the nanoparticle during growth. Firstly, size dependent melting effects limit the applicability of bulk phase diagrams. The small scale of the alloyed

Au nanoparticles makes them subject to size dependent melting effects, according to the Gibbs–Thomson relation. Therefore, the melting point of the alloy nanoparticles may be depressed relative to the bulk melting points, so eutectic melting may occur at a lower temperature than the bulk phase diagrams predict.

Secondly, the composition of the particle, when analysed post-growth, is generally different to that during growth. After growth is complete, the group III flow is ceased and the sample is cooled under group V overpressure. This high group V vapour supersaturation continues to drive the III–V growth reaction, which consumes group III species alloyed within the nanoparticle. Thus, during cooling, III–V material continues to deposit at the nanoparticle–nanowire interface and group III species in the Au nanoparticle are depleted.

A further factor is melting–freezing hysteresis. In many cases, the Au nanoparticles are thought to form a eutectic liquid alloy with the group III element, either during high temperature pre-growth annealing, or during a high temperature nucleation step. Upon cooling to the growth temperature, the Au alloy nanoparticle may retain its liquid state, even at a temperature below its melting point, due to melting–freezing hysteresis.

In situ TEM growth[121,122] has been used to further elucidate the phase of the nanoparticle during growth. According to these studies, nanowire growth is possible from a solid nanoparticle, and more rapid when the nanoparticle is liquid.[122] Several studies have compared the nanoparticle composition after different cooling procedures, to determine the nanoparticle phase during growth.[121,123]

3.5 Growth direction

Generally, Au-assisted nanowire growth takes place in the group V-terminated $[\bar{1}\,\bar{1}\,\bar{1}]$B crystallographic direction. The nanoparticle–nanowire interface forms at a $\{\bar{1}\,\bar{1}\,\bar{1}\}$B plane of the growing nanowire; this plane is perpendicular to the $[\bar{1}\,\bar{1}\,\bar{1}]$B growth direction. This growth direction is favoured because atoms precipitating on the $\{\bar{1}\,\bar{1}\,\bar{1}\}$B surface produce the largest decrease in Gibbs free energy. The $\{\bar{1}\,\bar{1}\,\bar{1}\}$ planes have the smallest separation and the largest density of surface atoms. The $\{\bar{1}\,\bar{1}\,\bar{1}\}$B growth plane has the lowest interfacial energy, and consequently the $[\bar{1}\,\bar{1}\,\bar{1}]$B growth direction minimises the interfacial energy of the nanoparticle–nanowire interface. In III–V materials, there are 4 equivalent $\langle\bar{1}\,\bar{1}\,\bar{1}\rangle$B directions in total. On a $(\bar{1}\,\bar{1}\,\bar{1})$B surface there is only one $\langle\bar{1}\,\bar{1}\,\bar{1}\rangle$B direction possible, which is directed outward perpendicular to the substrate surface. This means that when nanowires are grown on $\{\bar{1}\,\bar{1}\,\bar{1}\}$B substrates, the nanowires grow vertical to the substrate surface.

3.6 Surface diffusion effects

Axial growth is the term describing the Au-assisted elongating growth of the nanowire. There are two major contributions to axial nanowire growth, as illustrated in Figure 3.6a. The first contribution is from reaction species which directly impinge on the nanoparticle. The second contribution arises from species adsorbed on the substrate or nanowire sidewalls. These adatoms (adsorbed atoms) diffuse along the concentration gradient towards the Au nanoparticle, where they are incorporated into axial growth. As discussed in Section 3.3, surface diffusion is more significant for group III adatoms, which have large diffusion lengths (λ), whereas group V adatoms have much smaller diffusion lengths. Johansson *et al.*[124] have developed a theoretical model describing the dependence of the axial growth rate on surface diffusion.

In regions of high nanowire density, adjacent nanowires spaced within a diffusion length, λ, compete for diffusing adatoms. As a result, nanowires in high density regions have slower axial growth rates than those in low density regions. These density effects are further examined in Chapters 7 and 8.

3.7 Axial and radial growth modes

There are two major growth modes taking place during Au-assisted nanowire growth by MOCVD: axial growth and radial growth. The axial growth rate is the incremental increase in nanowire length, l, per growth time interval, t:

$$R_{axial} = \frac{dl}{dt} \tag{3.3}$$

This can be approximated as

$$R_{axial} = \frac{L}{t_g} \tag{3.4}$$

where L is the total nanowire length (μm) from the base to the Au nanoparticle–nanowire interface, and t_g is the total growth time.

Radial growth, also known as lateral or conformal growth, is the deposition of material on the nanowire sidewalls. It follows a simple vapour–solid growth mechanism, and does not directly involve the Au nanoparticle. As illustrated in Figure 3.6b, radial growth occurs when species adsorbed on the substrate and nanowire sidewalls, diffuse and incorporate on the nanowire sidewalls. In this manner, radial growth competes with axial growth.

Tapered nanowire morphologies, whereby nanowires exhibit wider bases and taper to narrower Au-capped tips, are a consequence of radial growth, as explained here.

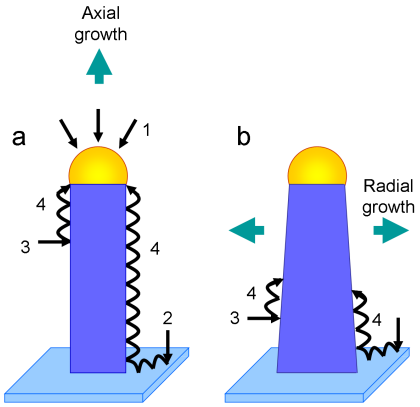

Figure 3.6: Schematic illustration of adatom contributions to (a) axial growth and (b) radial growth. The adatom contributions include those (1) directly impinging on the Au nanoparticle and those adsorbed on the (2) substrate and (3) nanowire sidewalls which (4) diffuse along the concentration gradient toward the nanoparticle–nanowire interface.

Nanowire bases are grown first, and hence are exposed to reactants for longer than the more recently grown Au nanoparticle-capped tip. Also, owing to their proximity to the substrate, the nanowire bases receive a greater fraction of precursor materials collected on and diffusing from the substrate.[125] Thus, lower sections of the nanowire experience more radial growth, which leads to tapered nanowire morphologies with wider bases and narrower tips as illustrated in Figure 3.6b. The radial growth rate is calculated as the increase in nanowire radius, r, per time interval t

$$R_{radial} = \frac{dr}{dt} \tag{3.5}$$

This can be approximated as

$$R_{radial} = \frac{r_b - r_t}{t_g} \tag{3.6}$$

where r_b is the radius at the nanowire base and r_t is the radius at the nanowire tip (the Au nanoparticle–nanowire interface).

In this dissertation, the "tapering parameter" is used to quantify the degree of tapering. The tapering parameter (nm/μm) is defined as the increase in nanowire radius (nm) per unit nanowire length (μm) from the Au nanoparticle–nanowire interface, l. This is equivalent to the ratio of radial to axial growth rates.

$$Tapering\ Parameter = \frac{R_{radial}}{R_{axial}} = \frac{dr}{dl} \tag{3.7}$$

The tapering parameter is thus a figure of merit, with a low tapering parameter signifying

less undesirable tapering.

A further growth process is the deposition of planar layers on the substrate surface. This occurs when adatoms incorporate onto the substrate, rather than onto the nanowire sidewalls or nanowire tip.

3.8 The Au-assisted nanowire growth mechanism, and proposed alternative models

While VLS is the most commonly cited nanowire growth mechanism, other variations exist,[62,121,126–128] including the vapour–solid–solid (VSS) mechanism in which the nanoparticle is solid.[121,127] Both VLS and VSS mechanisms have been observed via in-situ TEM growth studies of Ge nanowires.[122] The nature and role of the metallic particle has long been in question. A further question is the process of reactant diffusion to the growth interface. According to the conventional VLS mechanism, reactant species dissolve into the supersaturated liquid-phase nanoparticle, and then readily diffuse through the liquid nanoparticle to the growth interface. The VSS mechanism, in contrast, proposes solid-phase diffusion, involving dissolution of reactants into the solid Au nanoparticle, followed by their diffusion through the solid nanoparticle to the growth interface.[121] According to these two mechanisms, reaction species are transported to the growth interface via bulk diffusion, either through a liquid or a solid nanoparticle. Alternatively, Cheyssac *et al.*[129] propose that surface diffusion, rather than bulk diffusion, is the main transport mechanism. According to their model, the reactants adsorb and diffuse along the outer surface of the nanoparticle, instead of penetrating it.

Recently, the theory of preferential interface nucleation (PIN) has been proposed as the unifying mechanism of nanowire growth, and the fundamental mechanism underpinning the VLS mechanism and variations such as the VSS mechanism.[130] According to the PIN theory, the probability of nucleation is highest at the nanoparticle–semiconductor interface, whereas nucleation at other interfaces in the system is thermodynamically unfavourable. Preferential nucleation at the nanoparticle–semiconductor interface drives nanowire growth. A comprehensive review article by Dick[105] describes recent progress toward understanding the mechanism of Au-assisted nanowire growth.

Despite these controversies, the general principle of Au-assisted nanowire growth remains: the nucleation rate is highest at the Au nanoparticle–semiconductor interface, which drives nanowire growth.

3.9 Alternative substrate preparation techniques

The PLL functionalisation technique, discussed in Section 2.2.2, gives reliable and reproducible deposition of Au nanopartices on the substrate. Figure 3.7a shows FESEM

images of typical nanowires grown on a substrate prepared by this technique. A number of other techniques were also trialled to obtain Au nanoparticles on the substrate, namely (i) thermal evaporation and annealing of a thin Au layer, (ii) direct evaporation of colloidal solution, and (iii) hydrochloric acid (HCl). The discussion below compares these different methods of substrate preparation.

Method (i) involved depositing a thin, 1 to 10 nm, layer of Au on the substrate via thermal evaporation. Upon annealing, the layer breaks apart into small Au droplets whose size depends on the annealing temperature and whose density depends on the layer thickness. This method is simple but it is difficult to obtain a uniform nanoparticle size or distribution.

Method (ii) utilised colloidal Au nanoparticles. A 100 μL droplet of diluted Au colloidal solution was applied to the substrate, and allowed to evaporate. To obtain a reasonable density of deposited Au, the colloid was diluted to approximately 10^9 nanoparticles/ml. This method is problematic, because during droplet evaporation the Au nanoparticles tend to agglomerate and deposit non-uniformly.

Method (iii) also utilised colloidal Au nanoparticles. A 100 μl droplet of Au colloidal solution was dispensed on the substrate. Then, a 50 μL of 0.03 M HCl was added to the Au colloid droplet and allowed to mix on the substrate for 10 s. The resulting HCl concentration was 0.01 M. The substrate was rinsed with DI water and dried with N_2. This method was developed Woodruff *et al.*[131] for deposition of Au colloidal nanoparticles on Si substrates. As discussed in Section 2.2.2, the colloidal Au nanoparticles are negatively charged at neutral pH. The negative charge hinders deposition on bare GaAs and InAs substrates. When the acid is added to the Au colloid droplet, the solution pH changes, the charge on the Au nanoparticles is neutralised, and the nanoparticles can attach to the substrates. Substrates prepared by this method, with grown nanowires are shown in Figure 3.7b.

The optimum method, which affords control over both nanoparticle size and distribution, is patterning of Au nanoparticles using electron beam lithography (EBL). This technique is time consuming, however, and requires a complex EBL processing. The PLL–Au colloid deposition process, used routinely in this work, is suitable for most device applications and ideal for research into nanowire growth processes.

Before growth, the substrates were annealed in situ, as described in Section 2.2.3. The annealing step removes the surface oxide and other contaminants. In Figure 3.7, the effect of the annealing step is clear from comparing parts a and b, where growth was performed with a pre-growth annealing, against parts c and d, where growth was performed without a pre-growth annealing step. Nanowire growth is more irregular in parts c and d, due to the roughness of the unannealed surface, which hinders the nucleation of straight epitaxial

nanowires. The similarity between the PLL and HCl treated samples indicates that PLL-functionalisation does not interfere significantly with nanowire growth.

This annealing step means that the III–V substrates do not require etching or cleaning before growth. Etching to remove the surface oxide, prior to Au nanoparticle deposition, was performed for the sample of Figure 3.7e. To etch the substrate, it was immersed in 1 M HCl for 2 minutes, rinsed with DI water and dried with N_2. These experiments revealed that etching did not have any measurable effect on the properties of the grown nanowires. As seen in Figure 3.7 by comparing part a (or b) with part e, the resulting nanowire structural properties are comparable, regardless of etching.

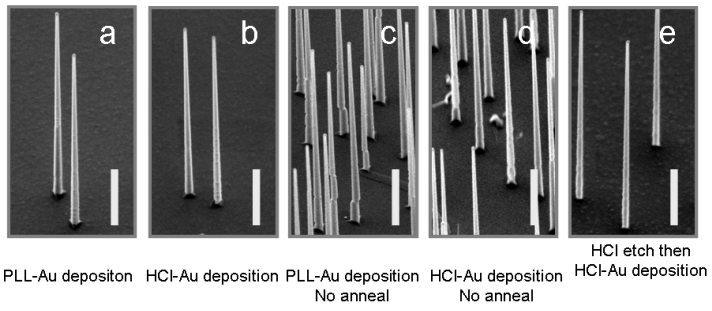

Figure 3.7: FESEM images of GaAs nanowires grown on substates prepared by different methods. (a) Substrate prepared by PLL functionalisation followed by colloidal Au deposition, followed by an in situ annealing step prior to nanowire growth. (b) Substrate prepared by method (iii), involving deposition of HCl and Au colloidal solutions, followed by an in situ annealing step prior to nanowire growth. (c) Substrate prepared using PLL but without any in situ annealing step. (d) Substrate prepared by method (iii) but without any in situ annealing step. (e) Substrate etched in 1 M HCl, prior to treatment by method (iii), and followed by in situ annealing step prior to nanowire growth.

3.10 Nanowire crystal structure

TEM studies have revealed that III–V nanowires can adopt a range of crystal structures. The two main crystal structures are the cubic ZB structure and the hexagonal WZ structure. The WZ structure has been reported, for instance, in MOCVD-grown InP nanowires[97] and in MBE-grown GaAs nanowires.[132] The ZB structure is common in MOCVD-grown GaAs and GaP nanowires.[71,72]

ZB and WZ crystal structures can have very different optical and electrical properties, so the distinction is significant. The difference between ZB and WZ crystals lies in the stacking of the bilayers composing the crystal. Figure 3.8 illustrates the bilayers forming III–V crystals. Each bilayer consists of a row of group V atoms denoted by uppercase letters A, B and C, and a row of group III atoms denoted by lowercase letters a, b and

c. Thus, ZB structures consist of an AaBbCcAaBbCc stacking sequence whereas WZ structures consist of an AaBbAaBb sequence. For brevity, it is common to simply use the capital letters A, B and C to represent bilayers. The lowercase letters can be omitted, because they can be inferred from the stacking sequence. Thus ZB lattices follow an ABCABC stacking sequence and WZ lattices follow an ABABAB stacking sequence, where each letter represents a bilayer of III–V pairs.

There are certain types of planar defects which commonly occur in nanowires: twin planes and stacking faults. Twin planes occur when a single bilayer is faultily stacked in a ZB crystal, which reverses the stacking sequence from ABC to CBA. For instance, the sequence ABCA*C*BA, *C* is the faultily stacked bilayer which creates the twin plane. The crystal on one side of *C* is rotated 60° about the $[\bar{1}\,\bar{1}\,\bar{1}]$ growth axis relative to the crystal on the opposite side. Stacking faults in WZ structures occur when a single bilayer is misplaced, for instance the sequence ABA*C*ACA, contains a stacking fault at bilayer *C*. A WZ structure is equivalent to a ZB structure with a twin plane every bilayer. The crystal structure of the nanowires, including the density of planar crystallographic defects, is determined by the growth parameters, as will be discussed later.

Nanowire crystal structure is routinely determined by tilting the nanowire to the $\langle 1\bar{1}0 \rangle$ zone axis. This allows ZB phases, WZ phases, twin defects and stacking faults to be distinguished. All TEM images and diffraction patterns presented in this thesis were taken along the $\langle 1\bar{1}0 \rangle$ zone axis.

3.11 Nanowire side-facets

III–V nanowires also exhibit side-facets of different orientations. WZ nanowires form a hexagonal prism with either six $\{11\bar{2}0\}$ side-facets, or six $\{1\bar{1}00\}$ side-facets, as shown in Figure 3.9a and b. The $\{11\bar{2}0\}$ and $\{1\bar{1}00\}$ surfaces are non-polar, and consequently the nanowire cross-section is hexagonal with six faces of equal length. ZB nanowires can exhibit a wider range of morphologies. ZB nanowires can be composed of truncated octahedral segments, each with three $\{1\bar{1}\,\bar{1}\}$A and three $\{\bar{1}11\}$B side-facets.[71] Each octahedral segment is bounded by a twin plane above and a twin plane below, such that each octahedral segment has a crystal structure rotated 60° about the $[\bar{1}\,\bar{1}\,\bar{1}]$ growth axis compared to the adjacent segments. This structure is illustrated in Figure 3.9c. Like WZ nanowires, ZB nanowires can have hexagonal cross-sections with either six $\{1\bar{1}0\}$ or six $\{11\bar{2}\}$ side-facets, as shown in Figure 3.9a and b. Note that the $\{1\bar{1}0\}$ ZB and $\{11\bar{2}0\}$ WZ families are crystallographically parallel, and the $\{11\bar{2}\}$ ZB and $\{1\bar{1}00\}$ WZ families are crystallographically parallel.

The $\{11\bar{2}0\}/\{1\bar{1}0\}$ and $\{1\bar{1}00\}$ faces are non-polar, whereas the six $\{11\bar{2}\}$ facets are not all equivalent, and can be subdivided into three $\{\bar{1}\,\bar{1}2\}$A and three $\{11\bar{2}\}$B faces.

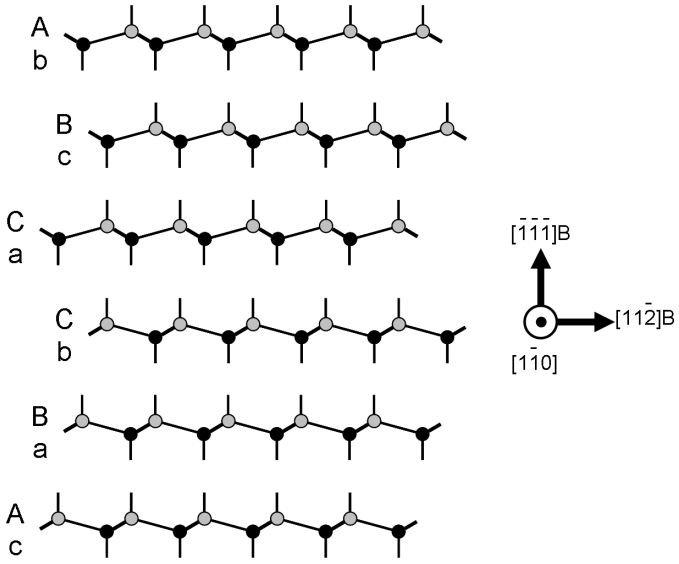

Figure 3.8: Illustration of the bilayers forming III–V crystals. Dark circles represent group III atoms and light circles represent group V atoms. Uppercase letters represent planes of group V atoms and lowercase letters represent planes of group III atoms.

The {$\bar{1}\,\bar{1}$2}A faces consist of two threefold coordinated group III surface atoms and one twofold coordinated group V surface atom in each surface unit cell, and the {11$\bar{2}$}B faces consist of two threefold coordinated group V surface and one twofold coordinated group III surface atom in each surface unit cell. Due to the differences in surface stoichiometry, group III atoms attach preferentially to {$\bar{1}\,\bar{1}$2}A surfaces.[72] Under growth conditions of high group V overpressure, the {11$\bar{2}$}B facets are more stable, with a lower surface energy and a slower growth rate than the {$\bar{1}\,\bar{1}$2}A facets.[133] Radial growth occurs preferentially on the {$\bar{1}\,\bar{1}$2}A surfaces, and the remaining {11$\bar{2}$}B facets become elongated as the {$\bar{1}\,\bar{1}$2}A surfaces grow out. Consequently, the cross-section adopts a truncated triangular shape with elongated {11$\bar{2}$}B side-facets and shorter {$\bar{1}\,\bar{1}$2}A side-facets, as illustrated in Figure 3.9d.[72,133]

In the case of these {112} faceted triangular nanowires, the overall morphology is further modified by the presence of twin planes. When a twin plane forms, the crystal structure is rotated 60° about the [$\bar{1}\,\bar{1}\,\bar{1}$] growth axis. This means that the section of nanowire below the twin exhibits a triangular cross-section oriented one way, and the section of nanowire above the twin can exhibit a triangular cross-section oriented the opposite way, as illustrated in Figure 3.9e. Finally, if a thin twinned segment is inserted into a perfect crystal region, it creates a groove between the {$\bar{1}\,\bar{1}$2}A sidewalls flanking the twin, as illustrated in Figure 3.9f. The groove forms there, because there the twinned segment presents a slow-growing {11$\bar{2}$}B sidewall, not a {$\bar{1}\,\bar{1}$2}A sidewall like those

flanking the twin. As a result the nanowire structure resembles a stack of truncated triangles.[72]

The above discussion has focused the formation of elongated {11$\bar{2}$}B facets under high group V overpressure. Under growth conditions of low group V overpressure, the situation can potentially reverse so that {$\bar{1}$ $\bar{1}$2}A facets become more elongated.[133]

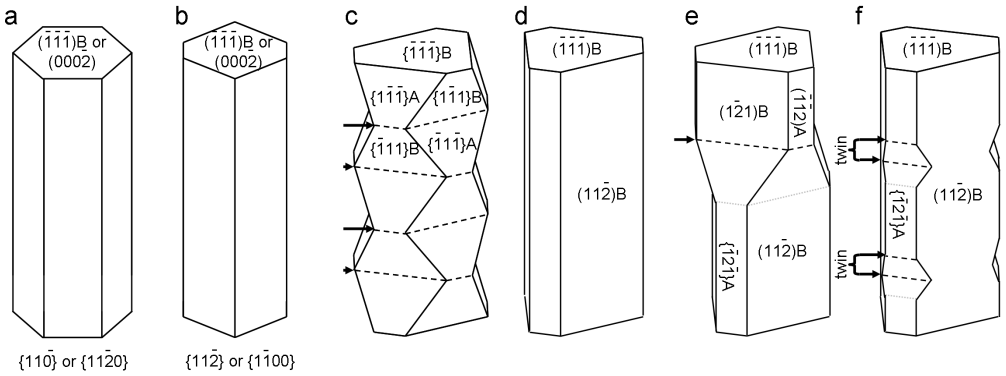

Figure 3.9: Schematic illustration of possible nanowire morphologies. (a) Hexagonal cross-section with six {1$\bar{1}$0}/{11$\bar{2}$0} side-facets. (b) Hexagonal cross-section with six {11$\bar{2}$}/{1$\bar{1}$00} side-facets. (c) Octahedral segments with {111}A and B faces. The dotted lines with arrows indicate twin planes. (d) Near triangular cross-section with three dominant {11$\bar{2}$}B facets and three smaller {$\bar{1}$ $\bar{1}$2}A facets. (e) Effect of a single twin plane on nanowire morphology. The triangular segment above the twin plane is rotated 60° about the growth axis, relative to the triangular segment below the twin. (f) Effect of a thin twinned segment on nanowire morphology. The twinned segment is bounded by the curly braces. The twinned segment creates a groove flanked by the adjacent {$\bar{1}$ $\bar{1}$2}A facets.

3.12 Axial and radial heterostructures

The cylindrical symmetry of nanowires permits two types of heterostructure: axial and radial.

Axial nanowire heterostructures are achieved by switching precursor gases during Au nanoparticle-assisted growth, resulting in compositional modulation along the nanowire growth axis. Figure 3.10 illustrates the growth of an axial heterostructure nanowire. Periodically changing the vapour species produces superlattice nanowires.

Unintentional concurrent radial growth is one limitation in axial heterostructure growth. Consider the growth of a segment of material B on a lower segment of material A (Figure 3.10(iv)-b). During the axial growth of the upper B segment, some material B may incorporate radially onto the sidewalls of the lower A segment. This radial growth creates a shell of material B around the lower segment of material A. This unintentional shell can adversely affect nanowire device function. Minimising radial growth is therefore

important for the development of axial heterostructures.

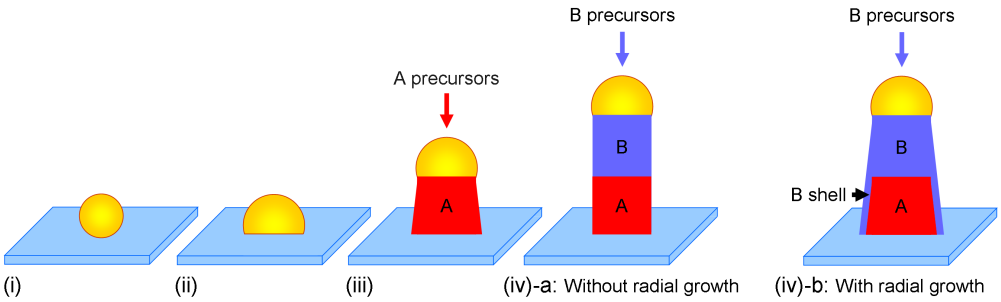

Figure 3.10: (i) to (iv)–a: A schematic diagram illustrating the growth process of an axial heterostructure nanowire. (iv)–b: A schematic diagram of how radial growth results in unintentional shell growth around the axial heterostructure nanowire.

Radial heterostructure nanowires are also known as core–shell nanowires. The nanowire core is grown first, by the Au nanoparticle-assisted mechanism. Then the precursor gases are changed and growth conditions are changed to promote radial growth and hinder axial growth. By this latter step, material is deposited laterally around the nanowire as a shell. This process is illustrated in Figure 3.11. Multiple shell layers can be deposited, to create core–multishell nanowires.

Typically, core growth is achieved at low growth temperature conducive to axial Au-assisted growth, whereas shell growth is achieved at a higher temperature conducive to radial growth. An example is the growth of GaAs/AlGaAs core–shell nanowires. The GaAs core is grown at a low temperature, for instance, 450 °C. The AlGaAs shell is grown at a higher temperature, typically 650 °C.

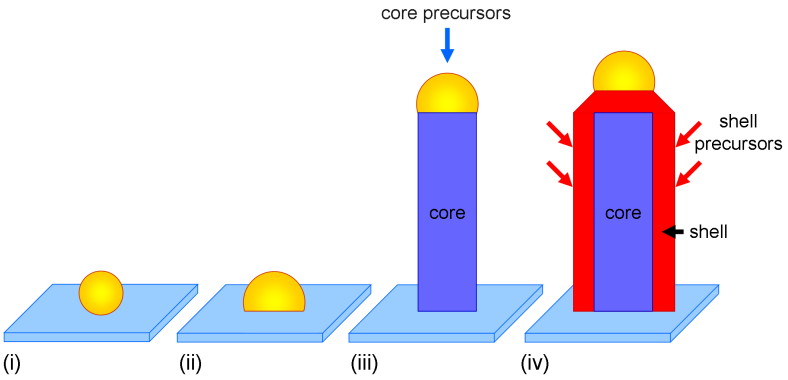

Figure 3.11: A schematic diagram illustrating the growth process of a radial heterostructure nanowire, with axial core growth followed by radial shell growth.

Dick *et al.*[44] and Paladugu *et al.*[134–140] give further details of the principles and limitations of axial and radial heterostructure growth.

3.13 Photoluminescence of GaAs nanowires

In this dissertation, PL is routinely used to characterise the optical properties of GaAs nanowires. Bare GaAs nanowires, however, emit only very weak PL, even at low temperatures of 10 K.[95] This is due to their high density of surface states which act as non-radiative carrier traps. These surface states not only quench GaAs nanowire PL, but also adversely affect optoelectronic device performance.

The problem can be overcome by cladding the GaAs nanowires in a shell of wider bandgap material, such as AlGaAs, creating a core–shell structure.[95,141,142] The shell spatially separates the electronic states of the GaAs core from the surface, and thus reduces the influence of surface states. An AlGaAs shell passivates these surface states to markedly enhance the PL from the GaAs core.[95,141] In addition, a large bandgap shell can act as a carrier reservoir for the inner core.[142]

On top of the AlGaAs shell, a thin GaAs capping layer is routinely grown. This GaAs cap prevents oxidation of the underlying AlGaAs shell. This GaAs core–AlGaAs shell–GaAs cap nanowire structure is hereafter simply referred to as a GaAs/AlGaAs core–shell nanowire. All PL measurements presented in this dissertation were performed on such GaAs/AlGaAs core–shell nanowires, rather than on bare GaAs cores.

3.13.1 GaAs/AlGaAs core–shell nanowires for PL measurements

For PL measurements, GaAs/AlGaAs core–shell nanowires were grown as follows. GaAs nanowires were grown at low temperatures (350 to 500 °C) using TMGa and AsH_3 precursors. After completion of core growth, the TMGa flow was switched off and the temperature was ramped up to 650 °C under an AsH_3 flow of 5.4×10^{-4} mol/min. Then, at 650 °C, TMGa and TMAl were introduced to the reactor for 20 minutes of AlGaAs shell growth. TMGa and TMAl flows were 1.2×10^{-5} mol/min and 4.1×10^{-6} mol/min, respectively, giving a vapour Al composition of 26%. Following AlGaAs growth, the core–shell nanowires were clad in a thin final shell of GaAs. This final GaAs capping layer is grown at 650 °C for 5 minutes with TMGa (1.6×10^{-5} mol/min) and AsH_3 (5.4×10^{-4} mol/min). Figure 3.12 compares FESEM images of bare GaAs nanowires, and GaAs nanowires clad in an AlGaAs shell and GaAs cap layer. This growth procedure gives an AlGaAs shell thickness of approximately 60 nm and a GaAs cap thickness of approximately 5 nm.

Without the GaAs capping layer, AlGaAs oxidises rapidly. This would allow oxygen species to diffuse to the GaAs core. Oxygen is known to create deep levels near the GaAs/AlGaAs interface, which can reduce the recombination lifetime and quantum effi-

ciency significantly.[143,144] Thus, oxidation of the AlGaAs shell reduces the effectiveness of the core–shell structure. The final GaAs capping layer is essential to prevent this oxidation. The GaAs cap layer itself does not contribute to the observed PL, due to its small surface-to-volume ratio coupled with the high non-radiative surface recombination rate, which quenches PL from this thin layer.

Time-resolved PL measurements have supported the effectiveness of this GaAs core–AlGaAs shell–GaAs cap structure. Bare GaAs nanowires, and core–shell GaAs nanowires lacking the final GaAs cap layer, both exhibit very short exciton recombination lifetimes of less than 80 ps, the response time of the experimental system.[95] When clad in the AlGaAs shell plus the thin GaAs capping layer, the exciton lifetime increases significantly.[80] Furthermore, terahertz conductivity spectroscopy (TCS) measurements have demonstrated that overcoating the GaAs core with AlGaAs reduces the density of surface traps by 82%.[81]

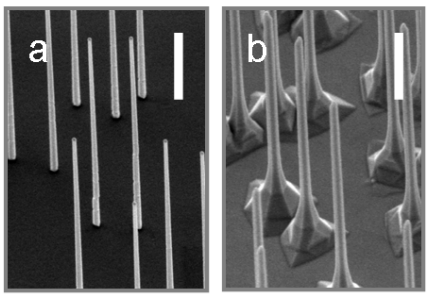

Figure 3.12: FESEM images of (a) bare GaAs nanowires and (b) GaAs nanowires clad in an AlGaAs shell and GaAs cap layer.

Note that the high temperature AlGaAs shell growth step effectively subjects the GaAs core to an annealing stage. All PL samples were subject to the same annealing treatment, so that valid comparisons can be made between different nanowire samples.

3.13.2 GaAs nanowire PL spectra

Two samples, Samples A and B, are discussed here to identify the main peaks arising from the GaAs core. For both samples the GaAs core was grown at 450 °C. The core of Sample A was grown for 30 minutes with TMGa and AsH_3 flows of 1.2×10^{-5} mol/min and 5.4×10^{-4} mol/min, respectively, giving a V/III ratio of 46. The core of Sample B was grown for 120 minutes with TMGa and AsH_3 flows of 2.9×10^{-6} mol/min and 1.3×10^{-4} mol/min, respectively, also giving a V/III ratio of 46. The AlGaAs shell and GaAs cap were grown as described above. Continuous-wave and time-resolved PL measurements were then performed using the systems described in Sections 2.4.4 and 2.4.5.

PL spectra of Figure 3.13 were measured from an ensemble of Sample A nanowires under different excitation intensities. These spectra feature two major peaks. The peak at approximately 1.517 eV is characteristic of free exciton recombination in bulk GaAs.[95,145] The other, lower energy peak (between 1.48 and 1.50 eV) is an impurity-related band.

With increasing excitation power the exciton peak broadens and undergoes a slight blue-shift. This is suggestive of the formation of an electron–hole plasma at higher excitation powers, a phenomenon recently observed in InP nanowires.[146] Also, with increasing excitation intensity the impurity peak saturates and the exciton peak becomes more intense.

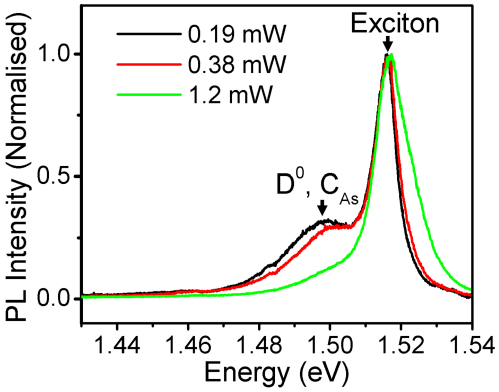

Figure 3.13: Normalised continuous-wave PL spectra from an ensemble of Sample A nanowires under different excitation intensities (indicated in legend). This illustrates the blue-shift and saturation of the impurity peak, and blue-shift with broadening of the exciton line, as excitation intensity increases.

The impurity related peak is assigned to donor–acceptor pair (DAP) recombination.[147] Figure 3.14 supports this assignment by examining nanowire sample B, for which the impurity peak dominates the exciton peak. Figure 3.14a illustrates spectra for several excitation powers under continuous-wave excitation. Figure 3.14b and c, respectively, illustrate time-resolved spectra at discrete time intervals after the excitation pulse, and time decays with corresponding lifetimes (τ) at various photon emission energies. According to Figure 3.14a the impurity emission band blue-shifts and narrows with increasing excitation power. This behaviour is typical of DAP recombination.[148,149] Similar behaviour is evident in the impurity emission peak of Figure 3.13. Further, time-resolved measurements are consistent with DAP recombination:[150] the peak red-shifts with time after the excitation pulse (Figure 3.14b) and accordingly, higher emission energies have shorter lifetimes (Figure 3.14c).

The DAP peak position closely corresponds to the position of neutral donor to neutral carbon acceptor (D^0, C_{As}) emission, reported at approximately 1.49 eV.[151,152] The PL

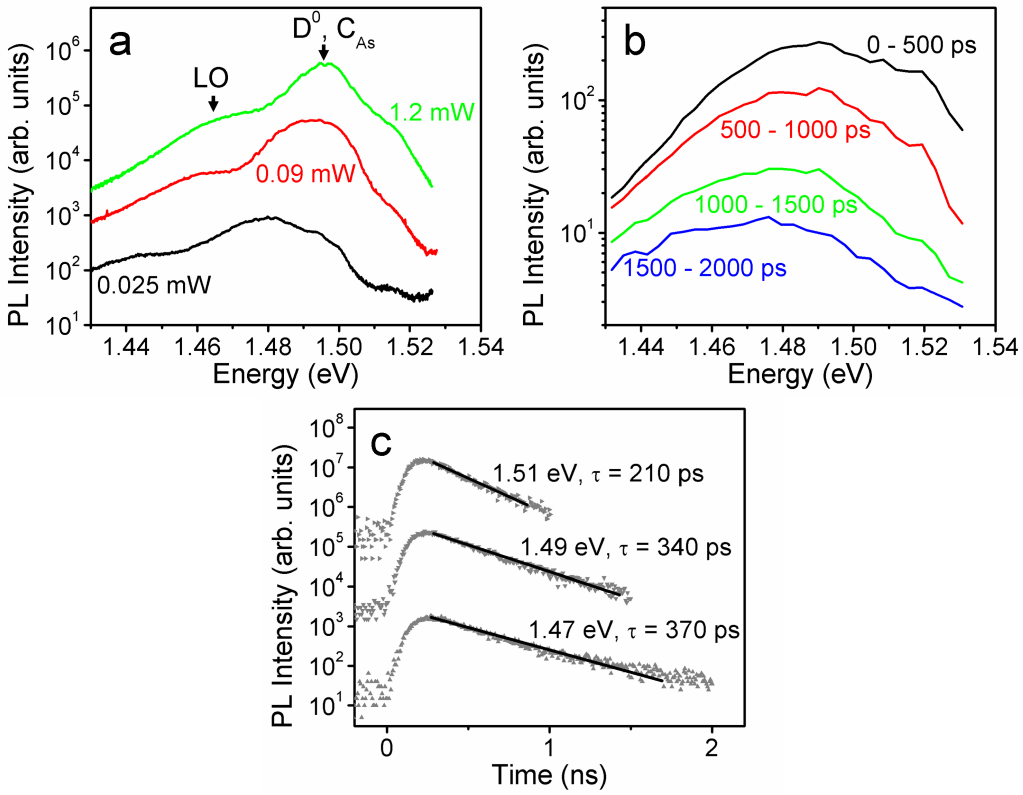

Figure 3.14: PL results obtained from a nanowire sample B with dominant impurity peak (a) Time-integrated PL spectra of a nanowire ensemble on semi-logarithmic axes illustrating blue-shift and narrowing of impurity peak with increasing excitation intensity. (b, c) Time-resolved measurements of a single nanowire. (b) PL spectra at consecutive 500 ps intervals after the excitation laser pulse. PL spectra red-shift with increasing time. (c) Time decays at various emission energies. Time decays are offset for clarity and lifetimes (τ) are indicated.

studies, therefore, identify carbon as the dominant acceptor impurity in these GaAs nanowires. This is consistent with previous studies of MOCVD grown planar epitaxial GaAs layers[145,153] and GaAs nanowires.[85,86] Also note that, in studies of conventional planar epitaxy, the $(\bar{1}\,\bar{1}\,\bar{1})$B surface orientation exhibits the highest rate of carbon incorporation.[154] It is not unexpected, therefore, that these $[\bar{1}\,\bar{1}\,\bar{1}]$B-oriented nanowires exhibit carbon impurity incorporation.

Carbon has previously been identified as the dominant impurity in GaAs nanowires.[85,86] Generally, carbon incorporates on arsenic lattice sites as an acceptor, C_{As}.[155,156] Carbon is particularly problematic because it arises as a decomposition product of the organometallic precursors, for example TMGa.[153,154,157] Other contaminants, such as Si and Zn, are eliminated through the use of high purity precursor sources. The carbon diffusion coefficient is low so carbon contaminants are not easily removed by annealing.[158] For these reasons it is important to choose growth parameters that minimise intrinsic carbon doping.

The relative intensity of the DAP peak to the exciton peak can be used to gauge the degree of carbon impurity content, as has been reported in previous studies of carbon-doped GaAs.[154,159,160] Chapters 4, 5 and 6 use the relative magnitudes of the DAP and exciton peaks to compare intrinsic carbon doping between different nanowire samples. These chapters then identify the growth conditions which minimise carbon impurity incorporation.

Each spectrum of Figure 3.14a features a smaller peak at lower energy than the main DAP peak. At all excitation intensities, this smaller peak maintains an approximately 36 meV energy separation below the DAP peak. This indicates the peak is a phonon replica of the DAP peak,[148] consistent with the 36 meV longitudinal optical (LO) phonon energy.[161]

The exciton peak also gives a LO phonon replica at approximately 1.482 eV, as illustrated in Figure 3.13. The phonon replica is weaker for the exciton peak than for the DAP peak, possibly because the interaction between bound DAP charges and phonons may be enhanced relative to the interaction between free excitons and phonons. The relative intensity of the LO phonon replica, compared with the DAP peak, decreases with excitation intensity. This is consistent with the lower Huang-Rhys parameter for more closely spaced donor-acceptor pairs.[162,163]

In some spectra a broad high-energy shoulder is observed above 1.52 eV. This is attributed to radiative recombination within AlGaAs portions of the nanowire. Its energy and broadness indicate a non-uniform Al distribution, with a lower Al composition than predicted from the vapour Al:Ga composition. This is in agreement with previous observations of AlGaAs nanowires and shells.[141,164]

Finally, note that quantum confinement effects are not observed in these studies. Quantum confinement is insignificant because the exciton Bohr radius (24 nm) is smaller than the size of the GaAs core.[95] Quantum effects are expected to become important for nanowires with diameters smaller than approximately 20 nm.[165]

3.14 Summary

This chapter has provided the background for the following chapters. This chapter has introduced several important subjects, including the growth thermodynamics and kinetics, alloy formation, surface diffusion, axial and radial growth, and nanowire tapering. Nanowire crystal structure and faceting were introduced. Axial and radial heterostructures were discussed, with emphasis on the deleterious effect of unintentional radial growth over axial heterostructure nanowires. Finally, the chapter described the GaAs/AlGaAs core–shell structures routinely used for PL characterisation of the GaAs nanowire core, and the PL signature which indicates carbon impurity incorporation in GaAs nanowires.

CHAPTER 4

A two-temperature growth procedure for GaAs nanowires

4.1 Introduction

MOCVD is a highly accurate and flexible growth technique, in which a number of parameters can be controlled independently to achieve the desired properties in the grown sample. Growth temperature is one of the most critical MOCVD growth parameters.[89,166]

Indeed, growth temperature exerts a significant influence on III–V nanowire growth.[56,167]. Higher temperatures induce significant radial overgrowth, manifested as nanowire tapering,[57,167] undesirable shell structures in axial heterostructure nanowires,[64] and compositional non-uniformity within ternary nanowires.[70] Furthermore, recent studies have shown that the density of crystallographic defects increases with growth temperature.[71] At lower temperatures, however, nanowire growth becomes unstable and prone to kinking, and does not exhibit perfect epitaxy with the substrate.[168,169] Choosing the optimum temperature would involve a compromise, between kinking at lower temperatures, and the radial growth and twin defects at higher temperatures. This compromise is, however, unacceptable for device applications, which demand straight, well-oriented nanowires with uniform diameters, controllable composition, and excellent crystallographic and optical properties.

In this chapter, a novel two-temperature growth procedure is devised to overcome these problems. This achieves vertically-aligned epitaxial GaAs nanowires of excellent crystallographic quality and optimal morphology. The two-temperature procedure consists of a brief initial high-temperature "nucleation" step followed by a prolonged "growth" step at a lower temperature. A similar procedure has previously been investigated for Ge nanowires.[169,170] The initial high-temperature step is essential for the nucleation and growth of straight, vertically-aligned epitaxial GaAs nanowires on the

$(\bar{1}\,\bar{1}\,\bar{1})$B GaAs substrate. The lower temperature employed for subsequent growth imparts superior nanowire morphology by minimising radial growth and tapering. Without the prior nucleation step, such a low growth temperature would produce non-vertical, kinked and irregular nanowires. Two mechanisms are proposed to explain the success of this two-temperature growth process, one involving Au nanoparticle–GaAs interface conditions, and the other involving melting–solidification temperature hysteresis of the Au–Ga nanoparticle alloy.

Significantly, TEM studies reveal that two-temperature growth yields nanowires that are completely free of planar crystallographic defects, in marked contrast to the high density of twin defects found in nanowires grown at higher temperatures. Continuous-wave and time-resolved PL measurements reveal the excellent optical and electronic quality of nanowires obtained by this two-temperature procedure. The low temperature-grown nanowires exhibit minimal carbon impurity incorporation and a nearly intrinsic exciton lifetime approaching 1.1 ns. They emit strong PL, even at room temperature.

4.2 Experiments

Au nanoparticles, 50 nm in diameter, were deposited on semi-insulating GaAs $(\bar{1}\,\bar{1}\,\bar{1})$B substrates using the PLL method described in Section 2.2.2. Prior to growth initiation, the substrate was annealed in situ at 600 °C under AsH_3 ambient to desorb surface contaminants. After cooling to the desired temperature, TMGa was introduced to initiate nanowire growth by either a single-temperature or two-temperature procedure.

The single-temperature procedure involved 15 minutes of growth at a constant temperature, T_g, between 350 °C and 500 °C. For the two-temperature procedure, growth initiated with a 1 minute "nucleation" step at the nucleation temperature, T_n, of 450 °C. The temperature was then rapidly cooled to the subsequent growth temperature, T_g, between 330 °C and 400 °C. This cooling step was typically between 2.5 and 6.5 minutes in duration. The total growth time was typically 15 minutes, including the nucleation and cooling steps. Source flows of TMGa and AsH_3 were 1.2×10^{-5} mol/min and 5.4×10^{-4} mol/min, respectively.

Adjunct growths, using other nucleation temperatures, T_n, of 410 °C to 500 °C, were also performed. To screen for possible effects of PLL on growth direction,[65,171,172] substrates were also prepared without PLL, using method (ii) as described in Section 3.9. Apart from these growths, all data presented in this chapter were obtained from PLL-treated samples, because PLL treatment gave a more uniform and monodisperse distribution of Au nanoparticles on the substrate.

Nanowires were then characterised by FESEM, TEM and PL measurements. TEM was carried out with collaborators at the University of Queensland.

For PL measurements, GaAs nanowire cores were grown as described above, then clad in an AlGaAs shell to passivate the GaAs surface.[95,141] Growth was terminated with a thin GaAs capping layer, to prevent oxidation of the AlGaAs shell. The AlGaAs shell and GaAs cap growth procedures were detailed in Section 3.13. These nanowires were then transferred from the as-grown GaAs substrate to Si substrates by gently touching the two substrates together. PL spectra of nanowire ensembles were obtained using the system described in Section 2.4.3. Micro-PL images were obtained at room temperature using the configuration described in Section 2.4.2. Time-resolved PL measurements were performed on single nanowires as described in Section 2.4.5.

4.3 Morphology

Nanowires grew within the entire temperature range investigated, even at the lowest T_g of 330 °C. Within this temperature range, however, nanowire morphology varied significantly, between kinked, straight, uniform and tapered morphologies.

Before describing results from the two-temperature procedure, the conventional single-temperature procedure is examined. Figure 4.1 illustrates FESEM images of nanowires grown by the single-temperature procedure. When grown at T_g of 410 °C and above, these nanowires were generally straight and epitaxially aligned in the vertical $[\bar{1}\,\bar{1}\,\bar{1}]$B direction, but suffer severe tapering with increasing temperature (parts c–f). At T_g of 400 °C and below (parts a and b), nanowire growth rarely initiated in the vertical $[\bar{1}\,\bar{1}\,\bar{1}]$B direction, and subsequent kinking was common: the initial and final nanowire orientations exhibit no apparent relationship with the substrate.

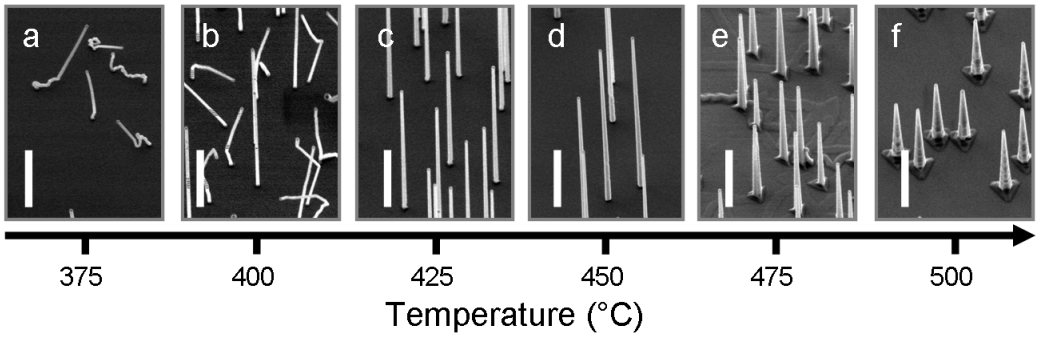

Figure 4.1: FESEM images of GaAs nanowires grown by the single-temperature procedure at temperatures, T_g, of (a) 375 °C, (b) 400 °C, (c) 425 °C, (d) 450 °C, (e) 475 °C and (f) 500 °C. Samples are tilted at 40°. Scale bars are 1 μm.

The two-temperature procedure produced very different results. Figure 4.2 illustrates FESEM images of nanowires grown by the two-temperature procedure. Notably, the two-temperature procedure allowed the growth of straight, vertical $[\bar{1}\,\bar{1}\,\bar{1}]$B-oriented

Table 4.1: Summary of nanowire morphology for single- and two-temperature procedures with various growth temperatures (T_g). Tapering is calculated for straight nanowires only.

Procedure	T_n (°C)	T_g (°C)	Straight [$\bar{1}\,\bar{1}\,\bar{1}$]B nanowires (% of total)	Tapering Parameter (nm/μm)
1-temperature	-	450	98	8.5
1-temperature	-	390	6	-
1-temperature	-	350	0	-
2-temperature	450	390	99	1.5
2-temperature	450	350	88	1
2-temperature	450	330	0	-

nanowires at T_g as low as 350 °C. Thus, the two-temperature procedure achieved straight [$\bar{1}\,\bar{1}\,\bar{1}$]B nanowire growth at temperatures significantly lower than the single-temperature procedure, and significantly lower than previously reported for nanowire growth.[47,57]

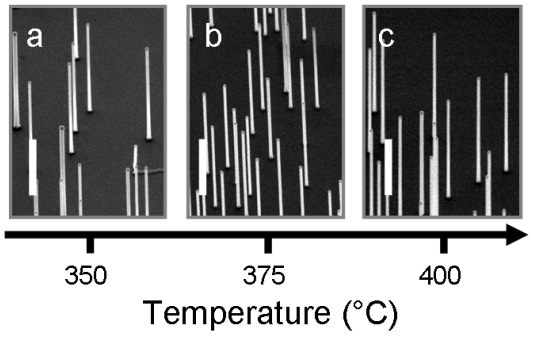

Figure 4.2: FESEM images of GaAs nanowires grown by the two-temperature procedure with nucleation temperature, T_n, of 450 °C and growth temperature, T_g, of (a) 350 °C, (b) 375 °C and (c) 400 °C. (a) was grown for 30 minutes whereas (b) and (c) were grown for 15 minutes. Samples are tilted at 40°. Scale bars are 1 μm.

Table 4.1 summarises key samples, their growth parameters, and the proportions of vertical [$\bar{1}\,\bar{1}\,\bar{1}$]B-oriented nanowires as determined from counts of over 500 nanowires per sample. Using the two-temperature procedure, a minimum T_g of 350 °C was required for straight epitaxial [$\bar{1}\,\bar{1}\,\bar{1}$]B-oriented nanowire growth.

The adjunct studies revealed that the two-temperature procedure is equally effective for nucleation temperatures in the range 410 °C $< T_n <$ 500 °C. A minimum T_n of 410 °C, was required to produce straight, [$\bar{1}\,\bar{1}\,\bar{1}$]B-oriented nanowires. This minimum T_n is the same as the minimum T_g of single-temperature procedure. There was no advantage in increasing T_n above this minimum. Thus, the experiments determined a minimum T_n of 410 °C and a minimum T_g of 350 °C were required for straight, [$\bar{1}\,\bar{1}\,\bar{1}$]B-oriented nanowires.

The nanowire samples prepared with PLL and without PLL were compared post-growth. This clarified that PLL did not affect the minimum T_n (410 °C) and T_g (350 °C) required for straight [$\bar{1}\,\bar{1}\,\bar{1}$]B-oriented growth. It is likely that PLL is removed during the pre-growth annealing step, and consequently does not affect the nanowire growth direction.

Straight [$\bar{1}\,\bar{1}\,\bar{1}$]B-oriented nanowires obtained at low growth temperature, made possible by the two-temperature procedure, were minimally tapered. The reduction in tapering is quantified in Figure 4.3a, which plots nanowire diameter, D, measured at various distances from the Au-capped nanowire tip, l, for various T_g. To obtain these measurements, the GaAs nanowires were first transferred from their as-grown substrates to Si substrates by gently rubbing the substrates together. High resolution FESEM images were obtained of the GaAs nanowires lying horizontally on the Si substrates. These FESEM images allowed more accurate measurement of D and l than images of vertical as-grown nanowires such as Figure 4.1. Ten nanowires were examined for each growth temperature. For nanowires grown by the two-temperature procedure, the lower 500 nm of each nanowire was excluded from the quantitative analysis because nanowire base growth is influenced, albeit minimally, by the brief high-temperature nucleation and cooling steps. The nanowire tapering parameter (see Section 3.7) is expressed in Table 4.1 as the increase in nanowire radius [nm] per unit nanowire length [μm] from the Au nanoparticle-nanowire interface: dr/dl [nm/μm]. These data were calculated from the slopes of straight lines fitted to the data of Figure 4.3a, via equation 4.1:

$$Tapering\ Parameter = \frac{dr}{dl} = \frac{1}{2}\frac{dD}{dl} \tag{4.1}$$

The temperature-dependent reduction in tapering is explained with reference to the axial and radial growth mechanisms[167,173] illustrated schematically in Figure 4.3b. Reaction species which impinge directly upon the nanoparticle contribute to axial growth. Additionally, Ga adatoms are adsorbed on the substrate and nanowire sidewalls and diffuse along the concentration gradient towards the growing nanoparticle–nanowire interface. These diffusing adatoms contribute to both radial and axial growth, hence radial growth competes with axial growth. Radial growth is kinetically limited, so at lower growth temperatures, diffusing adatoms are less likely to be incorporated into nanowire sidewalls. Furthermore, the adatom diffusion length decreases with decreasing growth temperature. This reduces the flux of adatoms diffusing from the substrate, limiting radial growth and tapering.

Previous publications have examined the dependence of axial growth rate on temperature,[65] so it is only briefly discussed here. Between 350 °C and 450 °C, the nanowire

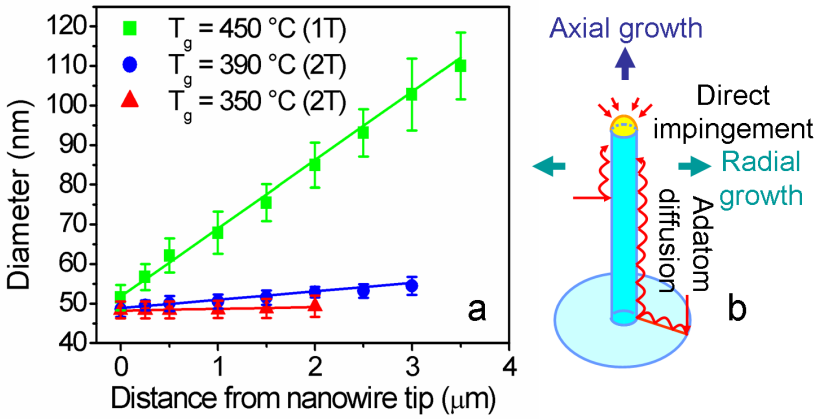

Figure 4.3: (a) Plot of nanowire diameter measured at distances from the Au nanoparticle–nanowire interface, for three T_g. Nanowires were grown by either a single-temperature (1T) or a two-temperature (2T) procedure, at the indicated T_g. For the two-temperature procedure, the nucleation step was performed at T_n of 450 °C. For each data point, ten nanowires were examined. Error bars represent standard deviations over these ten nanowires, at each point. (b) Schematic illustrating axial and radial nanowire growth, fed by direct impingement of precursor species on the nanoparticle and Ga adatom diffusion from the substrate and along nanowire sidewalls.

axial growth rate increases with temperature (Figure 4.2b and c, and Figure 4.1c and d). This increase is attributed to the increase in TMGa and AsH_3 decomposition with temperature. Above 450 °C, however, the axial growth rate decreases with temperature (Figure 4.1d to f). This decrease occurs due to the onset of significant radial growth at higher temperatures, which is observed as strong tapering. This radial growth competes with axial growth for diffusing reaction species, and consequently hinders axial growth.

4.4 Crystal structure

The nanowire crystallographic quality, as examined by TEM, also exhibits a marked dependency on growth temperature. For each sample, at least 10 nanowires were examined in detail by TEM. All nanowires were of ZB structure. It has been well documented that crystallographic twins are common lattice defects in GaAs nanowires,[174] possibly because very little energy is required for twin formation.[175] Extensive TEM investigation confirmed that twins, indeed, exist in the nanowires grown at a high T_g of 450 °C by the single-temperature procedure. Typical images of nanowire tip and base are shown in Figure 4.4a and b, respectively. Nanowires grown at higher temperatures, for example 500 °C, showed an even higher density of twin defects.

In marked contrast, no twins or other planar defects could be found in nanowires grown at the lower T_g of 390 °C by the two-temperature procedure. Figure 4.4c and d show nanowire tip and base respectively, and Figure 4.4e illustrates an entire nanowire

grown under these low-temperature conditions. Likewise, nanowires grown at T_g of 375 °C and 400 °C, via the two-temperature procedure, were completely twin-free.

Clearly, the low growth temperature has eliminated twin defects. This result is consistent with recent TEM studies of ZB GaP nanowires, which showed a distinct reduction in twin density with decreasing growth temperature.[71] Figure 4.4f shows high-resolution TEM (HRTEM) images, detailing the high crystallographic quality of a nanowire segment grown at the lower T_g of 390 °C by the two-temperature procedure. GaAs nanowires free of planar defects have previously been achieved by growing in the [111]A direction on (111)A substrates, however, these [111]A-nanowires showed significant tapering and their growth orientation was less well-controlled than the nanowires reported here.[172]

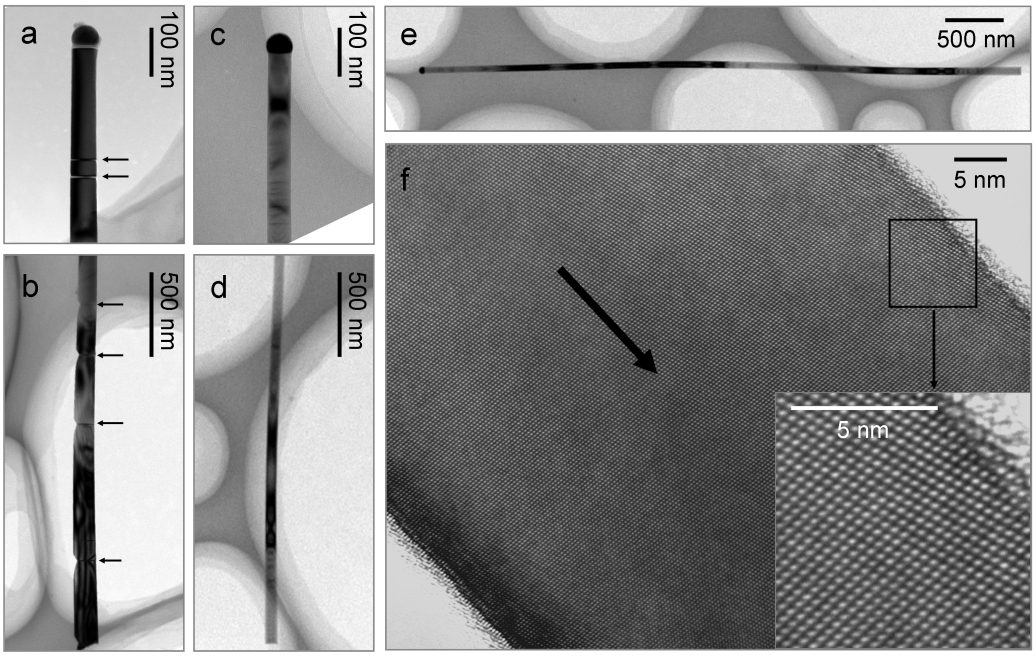

Figure 4.4: (a-e) Bright-field TEM and (f) HRTEM images showing morphologies and crystallographic quality of GaAs nanowires. (a, b) Nanowires grown at a high T_g of 450 °C by the single-temperature procedure, showing Au nanoparticle-capped nanowire tip with arrows labelling twin defects (a), and surface faceting towards the nanowire base (b). (c-f) Nanowires grown at a low T_g of 390 °C by the two-temperature procedure (T_n of 450 °C), showing (c) nanowire tip, (d) nanowire base, (e) an entire nanowire, and (f) a section of a nanowire. There are no lattice defects in (c) and (d), where the contrast in GaAs sections is due to bend contours and thickness effects. The thick arrow in (f) indicates the nanowire growth direction.

Twin defects are closely associated with the sidewall faceting behaviour of both ZB GaP[71] and GaAs nanowires.[72,176] Figure 4.4b illustrates the non-periodic saw-tooth faceted sidewalls, and segmented appearance, typical of nanowires grown at high T_g (by the single-temperature procedure). The faceting occurs in association with the high

density of twins in these nanowires: at least one twin defect is associated with the concave facet of each saw-tooth, and with each boundary between adjacent segments.[72] Radial growth augments the appearance of sidewall facets.[72] Nanowires grown at lower T_g, (by the two-temperature procedure) as illustrated in Figure 4.4c-f, exhibit substantially smoother sidewalls. This is related to the elimination of twins, and also to the reduction of radial growth.

Chapter 10 will give further discussion of the effects of growth temperature on twin formation, and will develop a theoretical model to explain the reduction in twin defects with decreasing growth temperature.

4.5 Photoluminescence

4.5.1 Donor–acceptor pair recombination and carbon impurities

Low temperature (4.2 K) continuous-wave PL measurements were performed on nanowire ensembles of 5 to 10 nanowires using the system desribed in Section 2.4.3. PL spectra are plotted in Figure 4.5a for several different T_g. For T_g of 450 °C and above, GaAs nanowire cores were grown by the single-temperature procedure. For T_g below 450 °C, GaAs nanowire cores were grown by the two-temperature procedure with a T_n of 450 °C.

Samples exhibit the same single broad PL peak at approximately 1.518 eV, which corresponds to excitonic emission in bulk GaAs.[95] The lower energy (D^0, C_{As}) DAP peak is also observed. PL spectra were strongly dependent upon excitation intensity, as observed in Section 3.13. The exciton peak increased in intensity, broadened and underwent a slight blue-shift with increasing excitation power. The DAP peak band increased in intensity, blue-shifted, narrowed, and ultimately saturated, with increasing excitation power. Each spectrum of Figure 4.5a was obtained under an excitation power of approximately 45 μW. This relatively low excitation power avoided saturation of the DAP peak.

The DAP intensity, relative to the exciton peak intensity, indicates the level of intrinsic carbon doping.[154,159,160]. Figure 4.5a illustrates that the DAP peak intensity, and consequently the degree of carbon impurity incorporation, is higher for higher growth temperatures. Therefore, a low growth temperature minimises carbon impurity incorporation. For the lowest growth temperature of 375 °C, the DAP peak could barely be detected in any of the spectra taken.

Carbon incorporation is inherent to GaAs growth, as it is a byproduct of TMGa decomposition. A number of studies of planar MOCVD GaAs growth have demonstrated that a higher growth temperature increases carbon incorporation[153,154,177], which is consistent with this current work on GaAs nanowires. Originally, it was believed

that carbon impurities arise from the adsorption of methyl (CH_3) radicals formed during the dissociation of TMGa.[154,157] According to this model, AsH_3 adsorbed at the growth front suppresses the adsorption of these CH_3 radicals: AsH_3 pyrolysis produces atomic hydrogen, which bonds with adsorbed CH_3 radicals to produce the volatile methane (CH_4) reaction product. The CH_4 reaction product then leaves the reactor and removes the carbon-bearing radical from the growth surface. Kuech *et al.*[154] proposed that a higher growth temperature increases carbon incorporation by (i) increasing the rate of hydrocarbon decomposition, and (ii) increasing decomposition of AsH_3 in the gas phase. Effect (i) would directly increase the concentration of carbon species available for incorporation. Effect (ii) would decrease the amount of AsH_3 adsorbed on the growth front, and thereby inhibit the AsH_3-mediated removal of carbon-bearing radicals from the surface.

Later experiments indicated that carbon is incorporated via a gallium carbene (Ga-bound CH_2) intermediate.[177–179]. In this process, adsorbed MMGa ($GaCH_3$) undergoes a surface reaction to produce gallium carbene ($GaCH_2$). The gallium carbene adsorbs from both ends, with the gallium atom attaching onto a Ga lattice site and the carbon atom attaching onto an As lattice site. This carbon incorporation pathway takes place entirely on the surface.[179].

Formation of the gallium carbene likely involves methyl (CH_3) radicals. Specifically, TMGa decomposition produces CH_3 radicals. These CH_3 radicals then abstract an H atom from the Ga–hydrocarbon reaction species (adsorbed MMGa, and possibly unreacted TMGa or DMGa).[180] This produces volatile CH_4, which leaves the reactor, and highly reactive gallium carbene, which decomposes to incorporate carbon in the growing GaAs.

Experiments have demonstrated that a higher surface concentration of As–H_x increases the desorption of carbon-containing species from the surface.[178,181] It is thought that the highly reactive carbene reacts with adsorbed As–H_x to form GaAs and a desorbing methyl radical.[179] This may explain the temperature dependence observed in the current studies: if gas phase AsH_3 decomposition is increased at higher temperatures,[154] then less As–H_x is available at the surface to remove carbon-containing species. Conseqently, at higher temperatures carbon incorporation is increased. As an alternative explanation, Mountziaris *et al.*[177] proposed that higher temperatures increase the decomposition of TMGa, thus increasing the production of methyl radicals. These methyl radicals attack Ga–hydrocarbon reaction species (unreacted TMGa and its decomposition products, including MMGa) to produce gallium carbene, resulting in higher carbon incorporation at higher temperatures.

Although several studies[153,154,177] corroborate the observation that carbon incorporation decreases with decreasing growth temperature, some studies of planar GaAs

epitaxy have observed the opposite effect.[178,179] As noted in one of those studies,[178] any explanation is necessarily complex, because all homogeneous and heterogeneous reaction rate constants change with temperature. The amount of carbon incorporation is influenced by multiple factors, including the gas phase decomposition rate of TMGa, the desorption rate of methyl radicals, and the adsorption rate of AsH_3. The current study demonstrates that intrinsic carbon doping of GaAs nanowires consistently decreases with decreasing temperature. Considering the above discussion, this result can be explained physically and is consistent with previous work.

Another consideration is the interaction between carbon and the alloyed Au–Ga nanoparticle. Carbon has only limited solubility in Au,[182,183] and studies of gallium-mediated carbon nanotube growth suggest that carbon does not alloy significantly with Ga.[184] Therefore, only a small amount of carbon is likely to be incorporated into the nanowire interior via Au-assisted axial growth. It is more likely that carbon incorporates preferentially via radial growth on the nanowire sidewalls. Thus, nanowires with a greater proportion of radial growth (more tapered nanowires) would be expected to show a greater degree of carbon incorporation. This would explain the present experimental observations of higher carbon incorporation in the more tapered nanowires grown at higher temperature. A similar mechanism has been used to explain the formation of a boron or phosphorus rich shell in deliberately B- or P-doped Ge nanowires.[185–187] The dominant incorporation mechanism for B and P atoms is via radial growth on the nanowire sidewalls, and not via the Au nanoparticle-assisted mechanism. This mechanism of radial growth-mediated carbon incorporation is further discussed in Chapter 6, to explain the growth rate-dependent incorporation of carbon species.

Alternatively, considering the phase diagram of Okamoto *et al.*,[182] it is possible that an increase in growth temperature increases the solubility of carbon species in the nanoparticle. This temperature-dependent change in carbon–nanoparticle interaction could increase carbon incorporation into the nanowire during nanoparticle-driven axial growth. This in turn could account for the increase in intrinsic carbon doping observed for high growth temperatures.

4.5.2 Room temperature photoluminescence

Figure 4.5b shows a room temperature micro-PL image of an individual two-temperature grown nanowire (T_g of 390 °C). PL from high temperature-grown (T_g of 450 °C) nanowires was too weak to be imaged at room temperature. This indicates that nanowires grown at low temperatures, made possible by the two-temperature process, have superior optical properties to their high temperature-grown counterparts.

Improved PL emission is unexpected considering the smaller GaAs volume of the

thin untapered low temperature-grown nanowire. Three factors could contribute to the observed PL enhancement. Firstly, the low growth temperature eliminates twin defects, which are believed to adversely affect the optical and electronic properties of the high temperature-grown nanowires.[79,95] Secondly, the low growth temperature reduces radial overgrowth. This radial overgrowth occurs by a conventional vapour–solid mechanism, unlike Au-assisted axial growth. In the temperature range typically used for nanowire growth (350 to 500 °C), conventional vapour–solid growth is known to be of poor optical quality.[188] Therefore, radial growth is suspected to quench nanowire PL, so minimising radial growth by using a low growth temperature should enhance PL. Finally, the irregular facetted sidewalls of nanowires grown at high temperatures (Figure 4.4b) may cause roughness at the interface between the GaAs core and AlGaAs shell, resulting in a non-radiative recombination pathway. In contrast, the two-temperature grown nanowires exhibit very smooth sidewalls, leading to a smooth GaAs/AlGaAs interface which reduces non-radiative recombination.

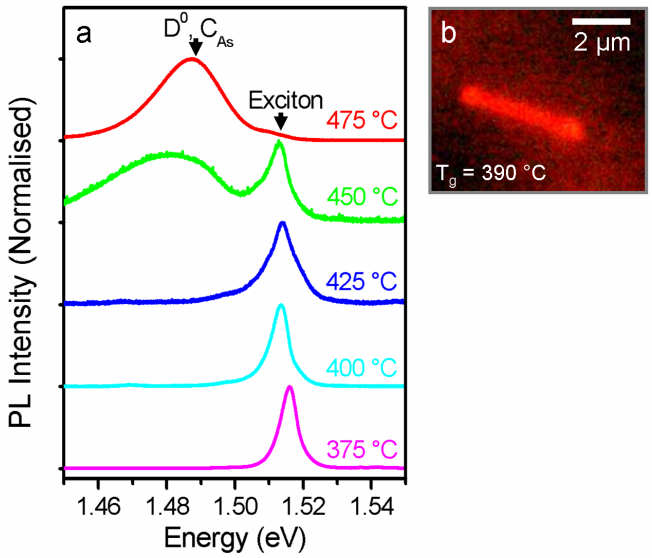

Figure 4.5: (a) Normalised 4.2 K PL spectra of nanowires grown at different T_g. For T_g of 450 °C and above, GaAs cores were grown by the single-temperature procedure. For T_g below 450 °C, GaAs cores were grown by the two-temperature procedure with a T_n of 450 °C. Spectra are offset for clarity. (b) Room-temperature micro-PL image of a nanowire grown via the two-temperature procedure with T_n of 450 °C and T_g of 390 °C.

4.5.3 Exciton lifetime

Time-resolved PL measurements of single nanowires were performed at 18 K using the system described in Section 2.4.5. Figure 4.6 plots time decays of the exciton (at 1.518 eV), for nanowires grown with low (375 °C) and high (450 °C) temperatures.

Exciton lifetimes, τ, are measured from the time decays and are presented alongside. The low-temperature sample was grown using the two-temperature procedure, with T_n of 450 °C, whereas the high-temperature sample was grown using the single-temperature procedure.

Exciton lifetimes indicate the quality of the crystal and the presence of non-radiative recombination centres. As shown in Figure 4.6, the exciton lifetime is only 200 ps for high temperature-grown nanowires. The low temperature-grown nanowires exhibit a significantly longer exciton lifetime of up to 1.1 ns. This lifetime is consistent with intrinsic exciton radiative recombination, and is comparable to very high quality two-dimensional GaAs/AlGaAs heterostructures.[189] Time-resolved measurements of these low temperature-grown nanowires also revealed the formation of an electron–hole plasma at high photoexcited carrier concentrations.[80]

Clearly, the low growth temperature gives a marked increase in exciton lifetime. As discussed in Section 4.5.2, low growth temperatures minimise non-radiative recombination centres, possibly by reducing twin defects, radial overgrowth and roughness at the GaAs core–AlGaAs shell interface. These low temperature-grown nanowires are therefore very promising for optoelectronic device applications, which require a long carrier lifetime and excellent optical properties.

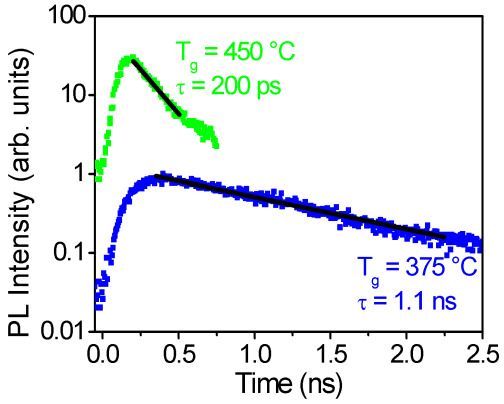

Figure 4.6: Time decays of the exciton (at 1.518 eV) taken from nanowires grown at different growth temperatures, 450 °C by the single-temperature procedure and 375 °C by the two-temperature procedure. Spectra are offset for clarity. Ordinate scale is logarithmic.

4.6 Role of the nucleation step

The final question is why a high temperature (T_n > 410 °C) is necessary to initiate straight epitaxial [$\bar{1}\,\bar{1}\,\bar{1}$]B-oriented growth, which may then be maintained at a lower temperature (T_g > 350 °C). The reasons are unclear, especially in light of recent debate regarding the

state of the nanoparticle during growth, liquid or solid,[47,121,122,127] and whether adatoms are transported across the nanoparticle to the nanoparticle–nanowire interface by a liquid-phase, solid-phase, or surface diffusion mechanism.[121,129] Adhikari *et al.*,[169] in studies of two-temperature growth of Ge nanowires, propose a mechanism which assumes a liquid nanoparticle is necessary for epitaxial growth. According to this mechanism, Gibbs–Thomson pressure acts on the Ge nanowire due to its surface curvature, but not on the Ge bulk, so that the nanoparticle–nanowire eutectic temperature is lower than the nanoparticle–bulk eutectic temperature. If this mechanism is correct, then higher initial temperatures serve to melt the nanoparticle in contact with the substrate and promote epitaxial nucleation. Once nanowire growth has initiated, a lower temperature can maintain the liquid nanoparticle and epitaxial growth.

A simple experiment was devised, to test the applicability of this Gibbs–Thomson pressure argument to the Au–GaAs system under study. Nanowire growth was initiated as described earlier, by the two-temperature procedure with T_n of 450 °C and T_g between 350 °C and 390 °C. After several minutes of growth at T_g, TMGa was removed, the sample was cooled to 200 °C, then reheated to the initial T_g, and TMGa reintroduced to resume growth. This growth interruption is not expected to change the curvatures of the nanoparticle and nanowire significantly, so according to Gibbs–Thomson pressure argument, epitaxial [$\bar{1}\,\bar{1}\,\bar{1}$]B-oriented nanowire growth should resume. In contrast, nanowire growth consistently reinitiated in a kinked and irregular fashion, at the point corresponding to the growth interrupt. Therefore, although the Gibbs–Thomson effect may contribute, it cannot completely describe this Au–GaAs system. Instead, two alternative mechanisms are proposed below. The two mechanisms are not mutually exclusive, and both may play a role.

The first mechanism does not require any assumptions about the liquid or solid nature of the nanoparticle. This mechanism concerns the specific nanoparticle–GaAs interface conditions that are required for the nucleation and continuation of [$\bar{1}\,\bar{1}\,\bar{1}$]B-oriented nanowire growth. It proposes that the pre-growth annealing step is not sufficient to create these interface conditions. Instead, the interface is established at growth initiation when Ga adatoms are supplied, at or above the minimum T_n. This is reasonable given the sensitivity of GaAs ($\bar{1}\,\bar{1}\,\bar{1}$)B surface reconstructions to temperature, Ga fluxes and As fluxes.[190] Compositional changes within the nanoparticle, which occur when Ga adatoms are supplied, could also affect this interface. The minimum T_n represents the critical temperature required to reorder the substrate surface to remove surface roughness, and to establish a planar nanoparticle–substrate interface. Once this interface is established, it is continuously regenerated as nanowire growth continues. Thus, the necessary interface conditions may be subsequently maintained at a lower temperature, down to the minimum

T_g of 350 °C. Unless the interface conditions are established at the beginning of growth, the nanowires will not initiate in the [$\bar{1}\,\bar{1}\,\bar{1}$]B direction. It is unlikely that these interface conditions will be established later on, explaining why nanowires that initially grow in non-vertical directions tend to undergo further kinking.

The second mechanism relates to the physical state of the nanoparticle. In the temperature range studied, the Au–Ga nanoparticle may be homogeneously liquid, homogeneously solid,[47] or may be inhomogeneous with Au–Ga crystalline phases existing in equilibrium with the liquid phase.[191] The presence of a solid phase could cause unstable kinked growth,[191] possibly because it hinders adatom diffusion and uniform deposition at the growing interface. This mechanism proposes that a liquid nanoparticle is necessary for the initiation and continuation of epitaxial nanowire growth, and that the nanoparticle experiences a temperature hysteresis between melting and solidification. This hysteresis has been observed by Tchernycheva *et al.* in reflection high-energy electron diffraction studies of the Au nanoparticle–GaAs bulk system,[191] and Kofman *et al.* in studies of other metallic nanoparticles.[192] Further, the high AsH_3 pressure provided during pre-growth annealing is thought to limit the decomposition of the GaAs surface in contact with the Au nanoparticle,[47] comparable to a closed Au–GaAs system.[119] Thus, the Ga-rich eutectic liquid nanoparticle forms when TMG is supplied at growth initiation,[47] rather than during annealing, and the minimum T_n (410 °C) corresponds to the melting temperature. After melting, the liquid nanoparticle can be supercooled below this melting temperature until solidification at the minimum T_g (350 °C). Interestingly, the experiments demonstrate a 60 °C difference between the minimum T_n and the minimum T_g. This 60 °C difference is very similar to the difference between melting and solidification temperatures observed by Tchernycheva *et al.*[191] Here, inferences are not made about the true nanoparticle temperature, because the nominal thermocouple readings are a few tens of degrees above the true substrate temperature.

Both mechanisms state that the conditions (interface conditions, surface conditions or liquid nanoparticle state) for stable [$\bar{1}\,\bar{1}\,\bar{1}$]B-oriented growth are established at growth initiation, rather than during pre-growth annealing. Additional growth experiments, which omitted this pre-growth annealing step, were performed to test this proposition. Straight [$\bar{1}\,\bar{1}\,\bar{1}$]B-oriented nanowires were obtained with the same minimum T_n and T_g, regardless of whether annealing was performed or omitted. This supports the proposition that growth initiation above T_n, not annealing, produces the conditions required for epitaxial [$\bar{1}\,\bar{1}\,\bar{1}$]B-oriented nanowires.

4.7 Summary

In summary, the two-temperature growth procedure produced straight, epitaxial [$\bar{1}\,\bar{1}\,\bar{1}$]B-oriented GaAs nanowires, at significantly lower growth temperatures than achieved previously. The lower growth temperature had significant advantages, namely the minimisation of undesirable radial growth and the elimination of twin defects. Furthermore, lower growth temperatures produced a marked enhancement of nanowire optical and electronic properties, by minimising intrinsic carbon doping and reducing non-radiative recombination centres to give a nearly intrinsic exciton recombination lifetime of up to 1.1 ns. By minimising radial overgrowth, this procedure should enable the development of ternary nanowires with uniform composition, and axial nanowire heterostructures free of undesirable shell overgrowth. Following this work on GaAs nanowires, another group applied the two-temperature procedure to grow minimally tapered GaP nanowires on Si substrates.[193] The procedure is clearly beneficial not only for GaAs nanowires, but also for other III–V nanowires.

CHAPTER 5

Choice of V/III ratio for GaAs nanowire growth

5.1 Introduction

If GaAs nanowires are to be useful in optoelectronic devices, they require excellent structural, crystallographic, electronic and optical qualities. As described in Chapter 4, extremely high quality GaAs nanowires can be achieved by controlling growth temperature. This chapter explores another key growth parameter: the flow rate of the group V precursor species, arsine. This is equivalent to studying the ratio of group V precursor flow rate to group III precursor flow rate, that is, the V/III ratio. For planar III–V growth, the effect of V/III ratio has been well-characterised, and V/III ratio is acknowledged as a crucial factor.[89] Yet, in the present literature there are only limited reports of the effects of this important growth parameter on III–V nanowire growth.[56,57,194]

This chapter discusses how V/III ratio affords precise control over nanowire crystallographic defect density and impurity incorporation. A high V/III ratio imparts significant advantages. TEM studies reveal that a high V/III ratio can achieve purely ZB nanowires that are free of planar crystallographic defects. These nanowires also exhibit excitonic emission with minimal carbon impurity-related emission, indicating their high purity. The highest V/III ratios, however, produce nanowires with undesirable kinked and tapered morphologies, and reduce the exciton lifetime. This places an upper limit on the range of useful V/III ratios. Accordingly, an intermediate V/III ratio is chosen as a compromise. This achieves uniform, vertically aligned GaAs nanowires, with few planar crystallographic defects and relatively high purity. Furthermore, these effects of V/III ratio yield important information on the mechanisms of kinking, twin formation and carbon impurity incorporation. These findings will greatly assist the development of future GaAs nanowire-based electronic and optoelectronic devices, and are expected to be more broadly relevant to the rational synthesis of other III–V nanowires.

5.2 Experiments

Semi-insulating GaAs ($\bar{1}\,\bar{1}\,\bar{1}$)B substrates were treated with poly-L-lysine (PLL) solution and a solution of colloidal 50 nm diameter Au nanoparticles, as described in Section 2.2.2 The group III and group V precursors were TMGa and AsH_3, respectively. Prior to growth the substrate was annealed in situ at 600 °C under AsH_3 ambient to desorb surface contaminants. After cooling to a growth temperature of 450 °C TMGa was introduced to initiate nanowire growth.

The V/III ratio was controlled by varying the group V (AsH_3) flow rate, while holding the group III (TMGa) flow rate constant. The control TMGa flow rate, denoted III_0, was 1.2×10^{-5} mol/min and AsH_3 flow rates were chosen between 1.3×10^{-4} and 2.1×10^{-3} mol/min to attain V/III ratios of 12, 23, 46, 93 and 190, varying in binary orders of magnitude.

Adjunct studies were performed with other TMG flow rates: III = $\frac{1}{4}$ III_0, $\frac{1}{2}$ III_0, 2 III_0 and 4 III_0 spanning TMGa flow rates of 2.9×10^{-6} to 4.6×10^{-5} mol/min. In each study, TMGa was held constant and AsH_3 was varied to achieve a given V/III ratio. For nanowire samples grown with III = III_0, the growth time, t_g, was 15 minutes. For the adjunct samples, growth time was scaled inversely with TMG flow. This was to achieve nanowires of reasonable height, at least 1 μm long and generally approximately 4 μm long, across all samples.

GaAs nanowires grown under various V/III conditions were characterised by FESEM, TEM and low temperature time-integrated and time-resolved PL measurements. TEM investigations were carried out at the University of Queensland. For PL measurements, GaAs nanowire cores were grown as described above, then clad in an AlGaAs shell and GaAs cap, as described in Section 3.13, to passivate the GaAs surface and hence improve PL emission.[95,141]. These nanowires were then transferred from the as-grown GaAs substrate to Si substrates by gently touching the two substrates together.

5.3 Morphology

The V/III ratio has a profound effect on nanowire morphology, particularly nanowire growth direction. Figure 5.1 illustrates nanowires grown with III = III_0 and various V/III ratios. At low V/III ratios, illustrated in parts a-c, nanowire growth initiates in the vertical [$\bar{1}\,\bar{1}\,\bar{1}$]B direction and epitaxial growth continues in this direction to create straight vertically oriented nanowires. At a critical V/III ratio of approximately 90 (part d), however, a small proportion of nanowires kink to a non-vertical orientation during growth. At even higher V/III ratio (part e) the proportion of kinked nanowires increases. Dayeh *et al.*[195] have made similar observations, reporting InAs nanowires growing at various angles to the substrate normal at high V/III ratios.

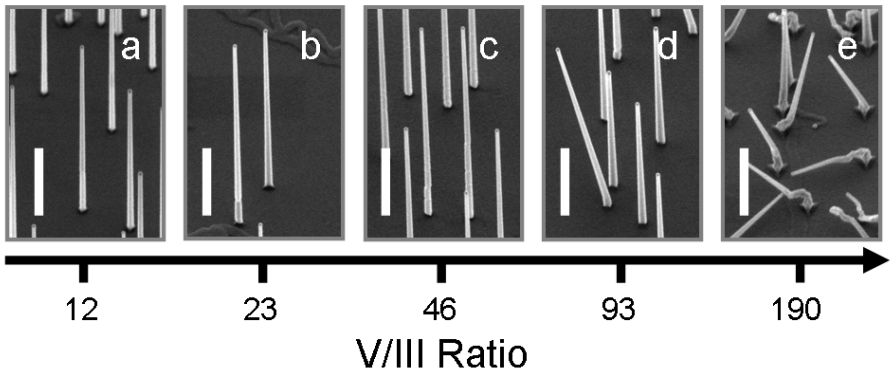

Figure 5.1: FESEM images of nanowires grown at constant III = III_0 and indicated V/III ratios: (a) 12 (b) 23, (c) 46, (d) 93 and (e) 190. Axis is logarithmic. Scale bars are 1 μm. Samples are tilted at 40°.

Nanowire tapering, whereby nanowires exhibit a larger diameter at the nanowire base and a narrower diameter at the Au-capped nanowire tip, is another morphological feature of significance for device applications. With increasing V/III ratio, nanowire tapering increases as seen in Figure 5.1. To quantify tapering, the tapering parameter is used. The tapering parameter is defined as the increment in nanowire radius, Δr, per increment in nanowire length, Δl. This is equivalent to the ratio of radial (R_{radial}) to axial (R_{axial}) growth rates.

$$Tapering\ Parameter = \frac{\Delta r}{\Delta l} \tag{5.1}$$

To obtain these measurements of Δr and Δl, the GaAs nanowires were first transferred from their as-grown substrates to Si substrates by gently rubbing the substrates together. High resolution FESEM images were obtained of the GaAs nanowires lying horizontally on the Si substrates. These FESEM images allowed more accurate measurements than images of vertical as-grown nanowires. Measurements of Δr and Δl were taken at consecutive intervals, of approximately 1 μm in length, along each nanowire from the Au-nanoparticle–nanowire interface to the base. That is, the change in nanowire radius Δr was measured over each nanowire length interval of $\Delta l \approx 1$ μm. For each interval the tapering parameter, $\Delta r/\Delta l$, was determined. This was then averaged for each nanowire. At least 5 nanowires were examined for each sample. In Figure 5.2, the tapering parameter is plotted versus V/III ratio. The figure includes data from the adjunct studies, each performed at a different group III flow rate. Clearly, a high V/III ratio increases nanowire tapering.

This is consistent with previous reports and is explained as follows.[43,195] In this temperature range, two dimensional radial growth is kinetically limited,[124,167] and its activation energy is known to decrease with increasing V/III ratio.[196] Consequently, the

radial growth rate increases with V/III ratio,[43,195] resulting in more tapered nanowires.

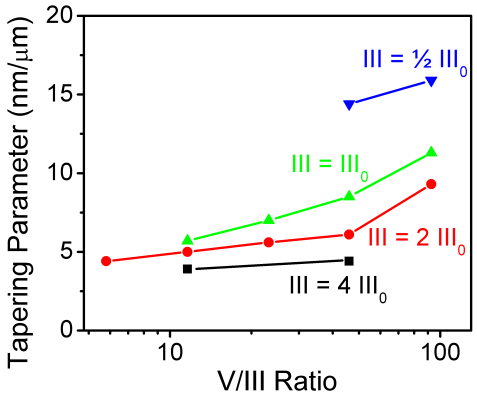

Figure 5.2: Tapering parameter versus V/III ratio. Straight lines group data sets for a constant group III flow rate: III = 4 III_0, III = 2 III_0, III = III_0 and III = $\frac{1}{2}$ III_0. Abscissa scale is logarithmic. The tapering parameter, $\Delta r/\Delta l$, was determined at approximately 1 μm intervals along the length of each nanowire, then averaged for each nanowire. Each data point represents an overall average from at least 5 nanowires. For each data point, the standard deviation is less than 3 nm/μm.

Nanowire lengths, too, vary with V/III ratio, in agreement with previous reports.[56,57,195,197,198] In the range of low V/III ratios, approximately 46 and below (Figure 5.1a-c), the axial growth rate is observed to increase marginally with increasing V/III ratio. The tallest nanowires occur at a V/III ratio of 46. In the range of high V/III ratios, approximately 46 and above (Figure 5.1c-d), the opposite effect is observed. Here the vertical growth rate decreases dramatically with increasing V/III ratio, and shorter nanowires result.

To quantify the axial growth rate for each nanowire sample, nanowire heights, L, were measured from FESEM images of as-grown nanowires, and these heights were divided by growth time, t_g (following equation 3.4). At least 20 nanowires were examined for each sample. In Figure 5.3a, the axial growth rate, R_{axial} is plotted against group V flow rate. Each set of data corresponds to a constant group III flow rate. At lower group V flows there is a weak trend: raising the group V flow increases the growth rate marginally. The growth rate reaches a maximum at an intermediate group V flow rate. Beyond this, the growth rate drops significantly. To further elucidate this phenomenon, growth rate is plotted against V/III ratio in Figure 5.3b. This figure clarifies that, for all III flows investigated, the maximum growth rate occurs at V/III ratio of approximately 46. Above this V/III ratio, the growth rate decreases markedly.

In the low V/III ratio range, the weak dependency on AsH_3 flow rate is typical of the diffusion-limited growth regime, as described by Reep and Ghandhi.[166] In this regime,

the growth rate is predominantly controlled by the diffusion of the group III precursor species. A marginal increase in growth rate is observed because AsH_3 reaction species enhance the decomposition of TMGa.[166] This leads to a slightly higher axial growth rate and taller nanowires with increasing AsH_3 flow rate.[56] In the high V/III ratio range, there are two factors which may contribute to the observation of decreasing axial growth rate with increasing V/III ratio. First, at higher V/III ratios, the radial growth rate increases as described above. Ga adatoms, diffusing from the substrate and along the nanowire sidewalls towards the growing Au-capped nanowire tip, are consumed by this radial growth. These Ga adatoms would otherwise diffuse to the nanowire tip and contribute to axial growth. In short, radial growth competes with axial growth for these Ga adatoms.[167] Therefore, with increasing V/III ratio, the increase in radial growth rate produces a decrease in axial growth rate.[195] Second, at high AsH_3 flows, stable As trimers are known to form on As-terminated $(\bar{1}\,\bar{1}\,\bar{1})$B surfaces.[199] Ikejiri *et al.*[198] have proposed, in the case of catalyst-free GaAs nanowires, that this surface reconstruction hinders growth on the $(\bar{1}\,\bar{1}\,\bar{1})$B nanowire surface.[200] The growth rate in the vertical $[\bar{1}\,\bar{1}\,\bar{1}]$B direction therefore becomes low with increasing AsH_3 flow rate.[198]

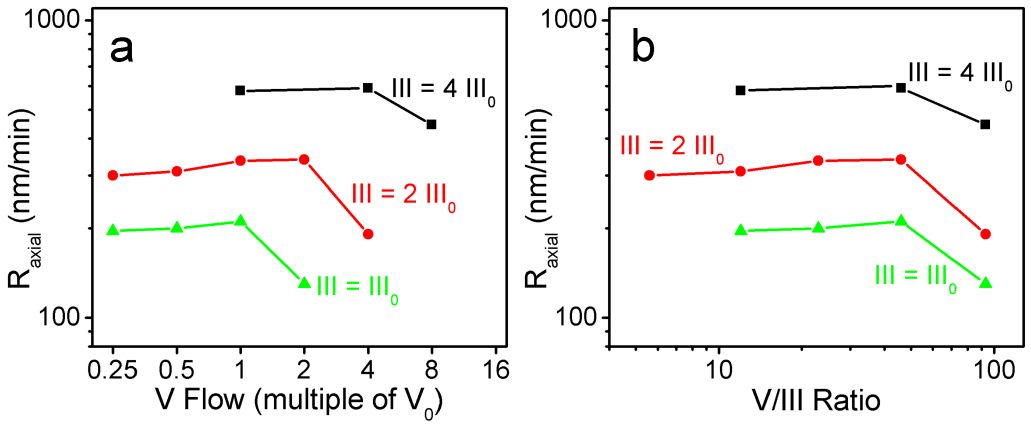

Figure 5.3: Axial growth rate versus (a) group V flow and (b) V/III ratio. Straight lines group data sets for a constant group III flow rate: III = 1, 2 and 4 III_0. Group III and V flows are expressed as multiples of III_0 and V_0 respectively. Axes are logarithmic. Each data point represents an average from at least 20 nanowires. For each data point, the standard deviation is less than 10%.

Perhaps most interesting is the observation of kinking. For all III flows investigated, the onset of kinking occurred at a critical V/III ratio of approximately 90. The dependence of kinking on V/III ratio indicates that TMGa counteracts the kink-producing effects of AsH_3.

One possible reason behind nanowire kinking, is that high V/III ratios change the surface energies to favour other growth directions. As discussed above, at high AsH_3

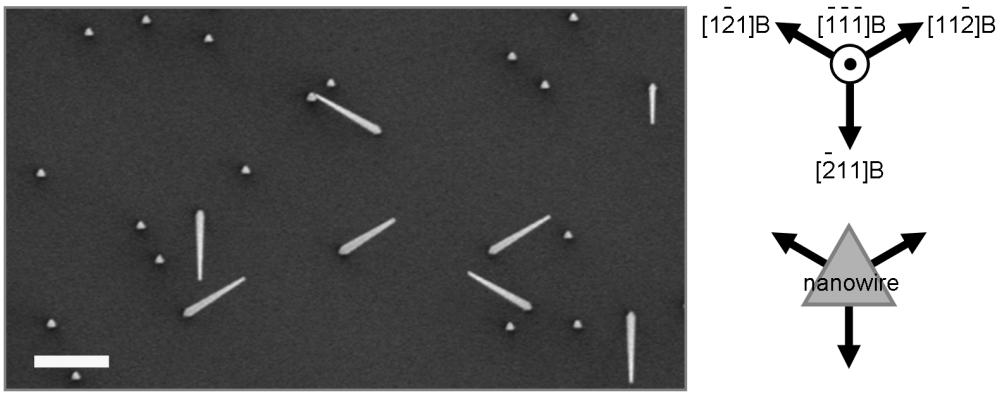

Figure 5.4: Plan-view FESEM image of [$\bar{1}\,\bar{1}\,\bar{1}$]B and ⟨112⟩B-oriented nanowires grown at III = III_0 and a V/III ratio of 93. Scale bar is 1 μm. The illustrations on the right indicate the three dominant {112}B sidewalls, and the three ⟨112⟩B growth directions

flows, stable As trimers form on As-terminated ($\bar{1}\,\bar{1}\,\bar{1}$)B surfaces. In our case of Au-assisted nanowire growth, this surface reconstruction could not only decrease the [$\bar{1}\,\bar{1}\,\bar{1}$]B growth rate, but could also favour a growth direction other than [$\bar{1}\,\bar{1}\,\bar{1}$]B, causing nanowire growth to kink to a non-[$\bar{1}\,\bar{1}\,\bar{1}$]B direction.

A second possible factor is that complete or partial solidification of the Au nanoparticle drives kinked irregular growth, as suggested previously in Chapter 4. Under this suggestion, Ga supplied from TMGa decomposition dissolves into the Au nanoparticle and promotes the liquid eutectic state of the Au nanoparticle.[201] As discussed above, a high V/III ratio promotes radial growth. Radial growth consumes Ga adatoms which would otherwise reach the Au nanoparticle-capped nanowire tip, and consequently depletes the nanoparticle of Ga.[195] This in turn can prevent the formation of the eutectic liquid nanoparticle, and can instead favour a solid nanoparticle at high V/III ratios. With a solid nanoparticle, a decrease in growth rate is expected,[122] leading to shorter nanowires. Indeed, the vertical nanowires of Figure 5.1d, grown at high V/III ratio, are shorter than those of Figure 5.1a-c.

The two kinking mechanisms discussed above may both play a role, and neither mechanism precludes the other. Interestingly, at a moderately high V/III ratio of 93, the nanowires either initiate in and maintain their [$\bar{1}\,\bar{1}\,\bar{1}$]B-growth direction, initiate in and maintain a ⟨112⟩B growth direction, or initiate in a [$\bar{1}\,\bar{1}\,\bar{1}$]B direction and later kink to a ⟨112⟩B direction. This was determined from plan-view FESEM images of these (incidently, twin-free) nanowires, by indexing the growth direction against the dominant {112}B nanowire side-facets. Figure 5.4 shows such an image. In this case, the kinking direction is a well-defined crystallographic direction. At the highest V/III ratios,

however, the nanowires are randomly oriented and do not appear to follow a defined crystallographic direction (Figure 5.1e). It is possible that different kinking mechanisms take place at moderately high, and at very high V/III ratios, accounting for these two different kinking regimes.

Furthermore, these results suggest that a high V/III ratio can be used to select the ⟨112⟩B growth direction rather than [$\bar{1}\,\bar{1}\,\bar{1}$]B. This would offer a novel and simple means of creating branched nanowires[202] and three-dimensional networks of interconnected nanowires,[203] without requiring more complex sequential seeding methods.[202]

Irregular nanowire kinking and tapering, induced by the highest V/III ratios, are potentially deleterious for practical nanowire applications. Consequently, the onset of kinking and severe tapering places an upper limit on the range of useful V/III ratios.

5.4 Crystal structure

Nanowire crystallographic properties also vary as a function of V/III ratio. All nanowires were of ZB crystal structure. Twins are common lattice defects in GaAs and other ZB III–V nanowires,[71,72] and can degrade the performance of optoelectronic nanowire devices. Indeed, non-periodic twin defects are apparent in Figure 5.5a, which shows a TEM image of a nanowire grown with a low V/III ratio of 12. Figure 5.5b, on the other hand, illustrates a twin-free nanowire grown with a high V/III ratio of 93.

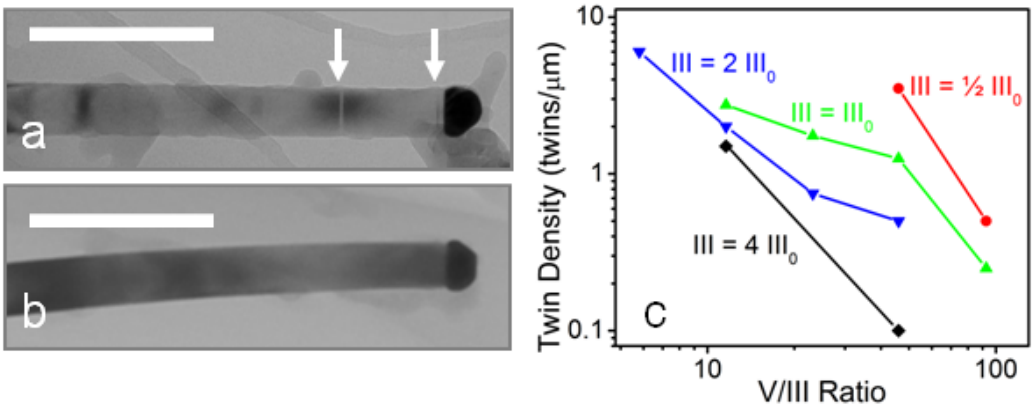

Figure 5.5: (a, b) Bright field TEM images of nanowires. (a) Highly twinned nanowire grown at low V/III = 12 and III = III_0. Arrows indicate twin defects. (b) Twin-free nanowire grown at high V/III = 93 and III = III_0. Scale bars are 250 nm. (c) Twin density versus V/III ratio. Axes are logarithmic. Straight lines group data sets for a constant group III flow rate: III = $\frac{1}{2}$ III_0, III = III_0, III = 2 III_0 and III = 4 III_0.

Twin density is defined as the average number of twins per unit length of nanowire, and is plotted versus V/III ratio in Figure 5.5c. Each data point was determined by averaging the twin density of at least 3 nanowires. This plot contains 4 data sets each

corresponding to a constant III flow. For each III flow, increasing the AsH_3 flow, and hence increasing the V/III ratio, decreased the twin density. This sensitivity to the V/III ratio is likely related to how AsH_3 changes the surface and interfacial energies of the Au nanoparticle–nanowire system. The mechanism of AsH_3-mediated twin reduction will be further discussed in Chapter 10.

Clearly, a dramatic decrease in twin density can be achieved using a high AsH_3 flow rate, that is, a high V/III ratio, as for the twin-free nanowire of Figure 5.5b. This is in marked contrast to the nanowire of Figure 5.5a grown at a low V/III ratio of 12, where a high twin density greater than 2 twins/μm is observed. It is noteworthy that the incidence of nanowire kinking (discussed in Section 5.3), unlike twin defects, increases with V/III ratio. This indicates that nanowire kinking and twin defects are unrelated and independent processes.

5.5 Photoluminescence

5.5.1 Donor–acceptor pair recombination and carbon impurities

Low temperature (18 K) micro-PL spectroscopy was performed on ensembles of 5 to 10 nanowires, as described in Section 2.4.4. PL spectra generally exhibited two peaks: the exciton peak at approximately 1.517 eV,[95,145] and the lower energy (D^0, C_{As}) DAP peak.[151,152] Figure 5.6 compares PL spectra for nanowires grown with various V/III ratios. These spectra were obtained under low excitation power (90 μW) to avoid saturation of the DAP peak. Spectra are normalised to the exciton peak.

The relative intensity of the DAP peak to the exciton peak indicates the degree of carbon impurity content.[154,159,160] In Figure 5.6, the DAP peak intensity decreases with increasing V/III ratio, suggesting that carbon impurity incorporation decreases with increasing V/III ratio. This result parallels previous studies of background impurities in MOCVD grown planar epitaxial GaAs, which show that carbon incorporation decreases with increasing V/III ratio.[145,154,177,179,204,205] Recall from the previous chapter, that carbon incorporates into GaAs via a gallium carbene intermediate. Adsorbed arsine species (As–H_x) are thought to remove carbon-bearing species from the surface.[178,181,206] One explanation is that adsorbed As–H_x reacts with the highly reactive carbene to form GaAs and a desorbing methyl radical, thus eliminating carbon from the growing surface.[179] Another possibility is that surface As–H_x reacts with methyl radicals, to produce the volatile methane (CH_4) reaction product, and thus eliminates methyl radicals from the surface. This prevents the methyl radicals from attacking the Ga–hydrocarbon reaction species (MMGa, DMGa and TMGa) and from producing gallium carbene.[177]

Higher AsH_3 flows, that is, higher V/III ratios, produce a higher adsorbed As–H_x surface concentration, and thus reduce carbon incorporation in nanowires. Consequently,

nanowires of superior purity can be achieved simply by choosing a high V/III ratio.

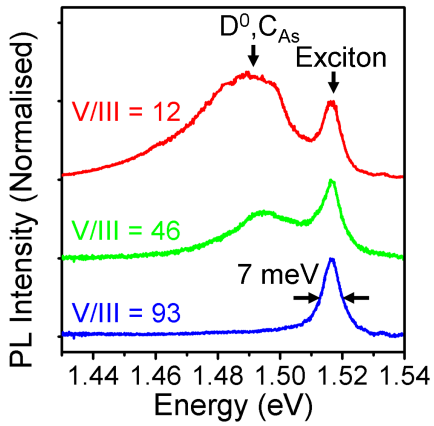

Figure 5.6: Normalised 18 K PL spectra comparing the relative intensities of DAP and exciton emission from nanowire ensembles with varying V/III ratios with constant III flow (III = III_0). The bottom-most spectrum features a FWHM of only 7 meV. Spectra are normalised to the exciton peak at 1.517 eV. Spectra are offset for clarity.

5.5.2 Exciton lifetime

Time-resolved PL measurements were performed on single nanowires as described in Section 2.4.5. Time decays of the exciton, for nanowires grown with different V/III ratios, are plotted in Figure 5.7. Exciton lifetimes, τ, are presented alongside.

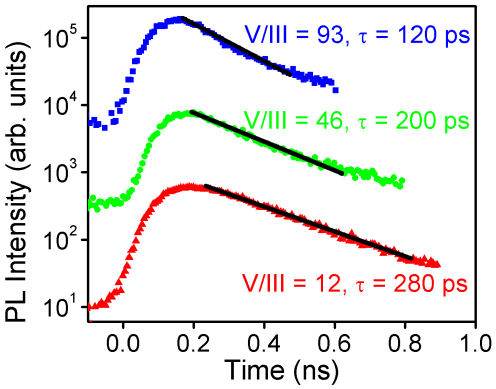

Figure 5.7: Time decays of the exciton (at 1.517 eV) taken from nanowires grown at different V/III ratios (12, 46 and 93) and constant III flow of III_0. Spectra are offset for clarity. Ordinate scale is logarithmic.

Nanowires grown at a high V/III ratio of 93 have an exciton lifetime over 50% shorter than nanowires grown at a low V/III ratio of 11. The short exciton lifetime for nanowires

grown at higher V/III ratios, is attributed to an increase in excess arsenic-related defects at high V/III ratios.[207–209] The defect is most likely the EL2 defect. The EL2 defect is believed to be the isolated arsenic antisite (As_{Ga}) defect.[210,211] It creates a deep donor level in GaAs near midgap and acts as an electron trap.[211,212] Arsenic interstitials (As_i) and Ga vacancies (V_{Ga}) are also possible defects. These As_{Ga}, As_i and V_{Ga} defects are the dominant defects in GaAs material grown by conventional growth techniques.[207,213] These defects create deep levels which rapidly trap free carriers, and act as a non-radiative recombination centers, thereby reducing the radiative lifetime.[208,209,213–216] A high V/III ratio does impart some significant advantages to nanowires, but the associated decrease in radiative lifetime is undesirable for most optoelectronic device applications which require a longer carrier lifetime.

It is interesting to note that the nanowires grown with a high V/III ratio feature a very low twin density, yet have very short exciton lifetimes. This strongly suggests that excess arsenic-related defects (EL2, As_{Ga}, As_i or V_{Ga}) are more detrimental to carrier lifetime than twin defects. This will be further discussed in Chapter 6.

5.6 An intermediate V/III ratio

The bottom spectrum of Figure 5.6, taken from an ensemble of nanowires grown at a high V/III ratio of 93, shows little evidence of carbon-related emission. The spectrum is dominated by excitonic emission with a relatively narrow linewidth with a full width at half maximum of only 7 meV. Such a narrow linewidth is comparable to linewidths observed in high quality single InP nanowires.[42] The GaAs nanowires giving the bottom spectrum were predominantly free of twin defects, occasionally featuring one twin defect per nanowire of 3 μm total length. Images of the corresponding nanowire cores are displayed in Figures 5.1d and 5.5b. This demonstrates that a high V/III ratio not only reduces carbon impurity incorporation, but also minimises twin defects. However, the carrier lifetime of these nanowires is relatively short, and increasing the V/III ratio further instigates severe nanowire kinking and tapering. Therefore an intermediate V/III ratio of approximately 46 is chosen as a reasonable compromise, and achieves nanowires with reasonable structural, crystallographic and optical properties.

5.7 Summary

The development of nanowire based devices and systems depends on the ability to fabricate nanowires with tight control over properties such as morphology, crystal structure, optical properties and composition. This chapter has demonstrated that GaAs nanowires of high optical and crystallographic quality may be achieved by choosing an appropriate group V precursor flow. A high V/III ratio markedly reduces the formation of twin defects

and minimises carbon impurity incorporation. The onset of nanowire kinking at the highest V/III ratios, together with the more significant nanowire tapering occurring at high V/III ratios, place an upper limit on the useful V/III ratio. An intermediate V/III ratio is chosen as a compromise, and achieves straight, [$\bar{1}\,\bar{1}\,\bar{1}$]B-oriented epitaxial nanowires with few crystallographic defects and relatively low impurity incorporation. These findings will greatly assist the development of optoelectronic devices based on GaAs nanowires and associated nanowire heterostructures. Further, many of these results should translate to related nanowire materials systems such as InGaAs and AlGaAs.

CHAPTER 6

Unexpected benefits of rapid growth rate for GaAs nanowires

6.1 Introduction

MOCVD offers a number of growth parameters, which can be independently controlled for optimal nanowire growth. Two of these, growth temperature and input V/III ratio, have already been discussed in Chapters 4 and 5, respectively. Another parameter is the absolute flow rate of group III and group V precursor species. Increasing the absolute group III and group V flow rates directly increases the nanowire growth rate.[56,125] There are however, only limited reports of the effects of III and V flow rates on essential nanowire properties, such as crystallographic quality, optical properties and compositional purity. This chapter investigates how absolute precursor flow rates, or equivalently, the nanowire growth rate, can be chosen to tailor nanowire properties.

In conventional planar epitaxy of bulk III–V materials, a slow growth rate favours high crystallographic quality, optical quality and purity of the resulting material. A rapid growth rate is associated with lower quality material. The same would be assumed for nanowires.[217] Surprisingly, exactly the opposite is observed for GaAs nanowire growth: a rapid nanowire growth rate can significantly improve nanowire properties. This chapter details the advantages of employing a rapid growth rate. SEM studies demonstrate that nanowires grown at a rapid rate exhibit very uniform, minimally tapered morphologies. TEM investigations reveal that a high growth rate eliminates planar crystallographic defects to produce twin-free ZB nanowires. PL measurements on these nanowires reveal strong excitonic emission with minimal impurity-related emission, indicating their high purity. Significantly, increasing the nanowire growth rate had no adverse effect on exciton lifetime, and consequently nanowire quantum efficiency was not compromised. For these reasons, rapid growth rates are recommended for high quality III–V nanowires. These

unexpected results are explained with reference to previous studies of nanowire and bulk epitaxy.

6.2 Experiments

In this study GaAs nanowires were grown on semi-insulating GaAs ($\bar{1}\,\bar{1}\,\bar{1}$)B substrates using TMGa and AsH_3 precursors. GaAs ($\bar{1}\,\bar{1}\,\bar{1}$)B substrates were treated with poly-L-lysine (PLL) solution and a solution of colloidal 50 nm diameter Au nanoparticles, as described in Section 2.2.2. Prior to growth the substrate was annealed in situ at 600 °C under AsH_3 ambient to desorb surface contaminants. After cooling to a growth temperature of 450 °C, TMGa was introduced to initiate nanowire growth.

The control, or standard, group III (TMGa) and group V (AsH_3) flow rates were III_0 = 1.2×10^{-5} mol/min and $V_0 = 5.4 \times 10^{-4}$ mol/min, respectively, corresponding to a V/III ratio of 46. For other growths, III_0 and V_0 were scaled by factors of $\frac{1}{4}$, $\frac{1}{2}$, 1, 2, 4, 8 and 16 to span flow ranges of III = 2.9×10^{-6} to 1.9×10^{-4} mol/min and V = 1.3×10^{-4} to 8.6×10^{-3} mol/min. Group III and group V flows were scaled equally, so that V/III ratio remained at 46. Throughout this chapter, III and V flows will be expressed as multiples of III_0 and V_0, respectively. For nanowire samples grown with III = III_0, the growth time, t_g, was 15 minutes. For other samples, growth time was scaled inversely with group III flow. This was to achieve nanowires of reasonable height, between 1 and 5 μm, across all samples.

Adjunct studies were performed at different V/III ratios of 12, 23 and 93.

GaAs nanowires grown at various growth rates were characterised by FESEM, TEM and low temperature time-integrated and time-resolved PL measurements. TEM investigations were carried out at the University of Queensland. For PL measurements, GaAs nanowire cores were grown as described above, then clad in an AlGaAs shell and GaAs cap, as described in Section 3.13, to passivate the GaAs surface and hence improve PL emission.[95,141]. These nanowires were then transferred from the as-grown GaAs substrate to Si substrates by gently touching the two substrates together.

6.3 Morphology

Precursor flow rates have profound effects on nanowire morphology. Figure 6.1 illustrates FESEM images of GaAs nanowires grown at different growth rates and a V/III ratio of 46. The nanowires grow epitaxially in the [$\bar{1}\,\bar{1}\,\bar{1}$]B direction normal to the substrate surface. Broadly speaking, the axial nanowire growth rate increases with increasing III and V flow, although the relationship is not perfectly linear. This is consistent with previous work,[56,57,125] and is addressed below.

To quantify the axial growth rate for each nanowire sample, nanowire heights, L, were

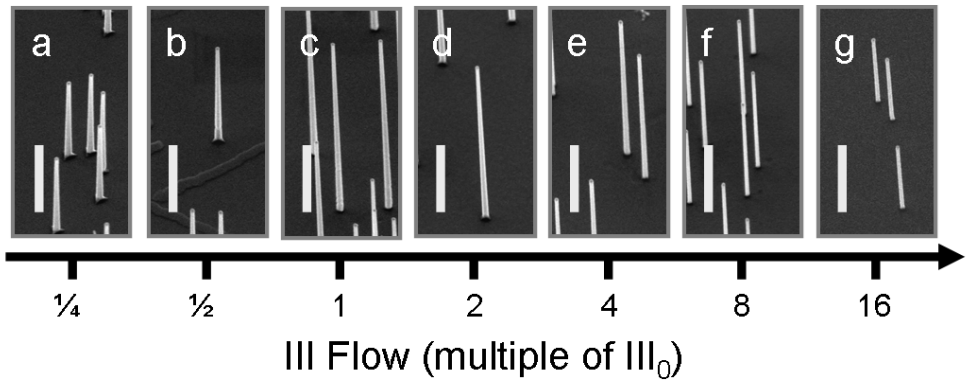

Figure 6.1: FESEM images of nanowires grown at constant V/III ratio of 46 and the indicated group III flows: (a) III = $\frac{1}{4}$ III_0, t_g = 60 minutes, (b) III = $\frac{1}{2}$ III_0, t_g = 30 minutes, (c) III = III_0, t_g = 15 minutes, (d) III = 2 III_0, t_g = 7.5 minutes, (e) III = 4 III_0, t_g = 225 s (f) III = 8 III_0, t_g = 112.5 s and (g) III = 16 III_0, t_g = 56.25 s. Axis is logarithmic. Samples are tilted at 40°. Scale bars are 1 μm.

measured from FESEM images of as-grown nanowires, and these heights were divided by growth time, t_g (following equation 3.4). At least 20 nanowires were examined for each sample. Figure 6.2a plots axial growth rate, R_{axial}, against group III flow rate, under conditions of constant group V flow. The axial growth rate strongly increases with group III flow rate. This indicates that axial nanowire growth falls in the diffusion-limited regime, where the growth rate is predominantly controlled by the diffusion of the group III precursor species.[166] Similar results have been reported by Verheijen *et al.*[56] in their detailed analysis of the nanowire growth rate dependence on TMGa and AsH_3 precursor flow rates.

Figure 6.2b plots R_{axial} against group III flow rate, under conditions of constant V/III ratio. Between III = $\frac{1}{4}$ III_0 and III_0, R_{axial} increases superlinearly with a simultaneous increase of III and V flow rates. The superlinear increase in growth rate with III and V flows indicates that the presence of one of the precursors (TMGa or AsH_3) enhances the decomposition of the other. Indeed, there are reports that AsH_3 enhances the decomposition of TMGa and vice versa.[56,102,218,219] Above III = III_0, R_{axial} increases less steeply and gradually levels off. This is consistent with previous reports[56] and indicates eventual saturation of the growth rate. Conceivably, the decomposition enhancement effect may no longer be significant when AsH_3 and TMGa flow rates are already high. This could explain the growth rate saturation effect observed at the highest flow rates. Alternatively, it is possible that the amount of Ga or As species adsorbed on the Au nanoparticle saturates at these high flow rates, which would account for the saturation of R_{axial}.

Like the axial growth rate, the radial growth rate also has been reported to increase

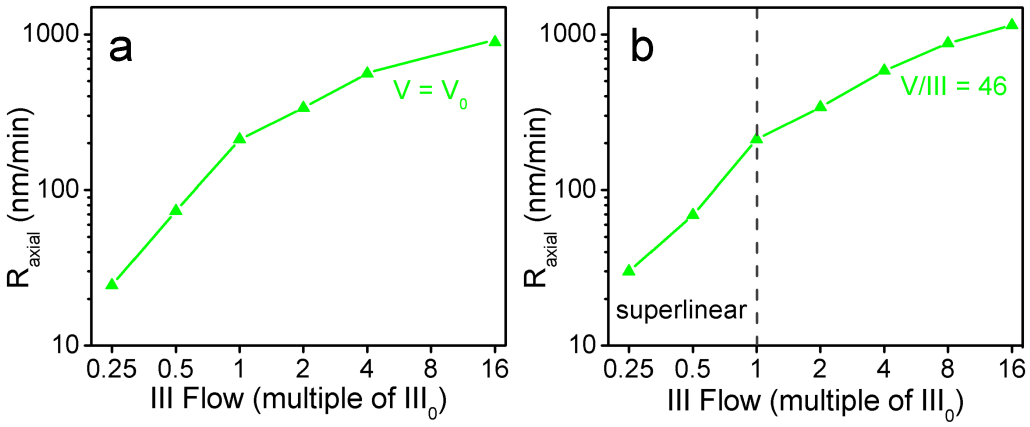

Figure 6.2: Axial growth rate versus group III flow under conditions of (a) constant group V flow of V = V_0 and (b) constant V/III ratio of 46. Group III and V flows are expressed as multiples of III_0 and V_0 respectively. Axes are logarithmic. Each data point represents an average from at least 20 nanowires. For each data point, the standard deviation is less than 10%.

with III and V flow.[125] Yet, inspecting Figure 6.1, the nanowires grown at high III and V flow rates appear least tapered. The tapering parameter, defined as the increment in nanowire radius, Δr, per increment in nanowire length, Δl, is used to quantify tapering.

$$Tapering\ Parameter = \frac{\Delta r}{\Delta l} \tag{6.1}$$

To obtain these measurements of Δr and Δl, the GaAs nanowires were first transferred from their as-grown substrates to Si substrates by gently rubbing the substrates together. High resolution FESEM images were obtained of the GaAs nanowires lying horizontally on the Si substrates. These FESEM images allowed more accurate measurements than images of vertical as-grown nanowires. Measurements of Δr and Δl were taken at consecutive intervals, of approximately 1 μm in length, along each nanowire from the Au-nanoparticle–nanowire interface to the base. That is, the change in nanowire radius Δr was measured over each nanowire length interval of $\Delta l \approx 1$ μm. For each interval the tapering parameter, $\Delta r/\Delta l$, was determined. This was then averaged for each nanowire. At least 5 nanowires were examined for each sample. In Figure 6.3, the tapering parameter is plotted versus group III precursor flow rate. The figure includes data from the adjunct studies, each performed at a constant V/III ratio. Undoubtedly, tapering is reduced by increasing precursor flow.

To explain this finding, note that axial growth is mass transport limited.[56,124] Therefore R_{axial} increases significantly with increasing precursor flow rates.[166] In contrast, radial growth is a thermally activated process, that is, kinetically limited.[124,167] Reep and Ghandhi[166] demonstrated that in the kinetically limited regime, planar growth rates are

strongly dependent on growth temperature, but show only weak, sublinear dependencies on TMGa and AsH_3 flow rates. Therefore, R_{radial} is strongly affected by growth temperature, and is affected less significantly by precursor flow rates. Because R_{axial} increases significantly and R_{radial} increases only marginally, high precursor flow rates reduce nanowire tapering.

Therefore high V and III flows, which accordingly allow a short growth time to achieve a given nanowire length, produce minimally tapered nanowires. This is a great advantage for laser applications which require uniform nanowire diameters. This is also potentially advantageous for ternary nanowires such as InGaAs[220] and AlGaAs.[70] One problem facing ternary nanowire growth is the spontaneous formation of a core–shell structure, where radial growth forms a shell of a different composition to the axially-grown nanowire core.[70] By reducing the amount of radial growth, high precursor flows coupled with short growth times may prevent spontaneous shell structures and achieve compositional uniformity in ternary nanowires.

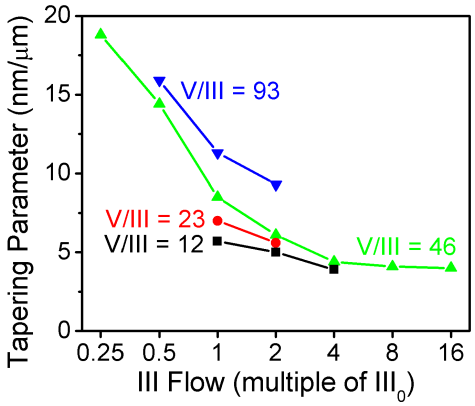

Figure 6.3: Tapering parameter versus group III precursor flow rate. Straight lines group data sets for a constant V/III ratio: 12, 23, 46 and 93. Abscissa scale is logarithmic. The tapering parameter, $\Delta r/\Delta l$, was determined at approximately 1 μm intervals along the length of each nanowire, then averaged for each nanowire. Each data point represents an overall average from at least 5 nanowires. Standard deviations for each data point were less than 3 nm/μm.

6.4 Crystal structure

Nanowire crystallographic properties also depend on the III and V flow rates. To simplify discussion the phrase "increasing (decreasing) growth rate" is occasionally used to describe increasing (decreasing) III and V flow rate whilst keeping V/III ratio constant.

In this study, all GaAs nanowires were of ZB crystal structure, the stable bulk phase. Figure 6.4a illustrates a TEM image of a twinned nanowire grown at a slow growth rate

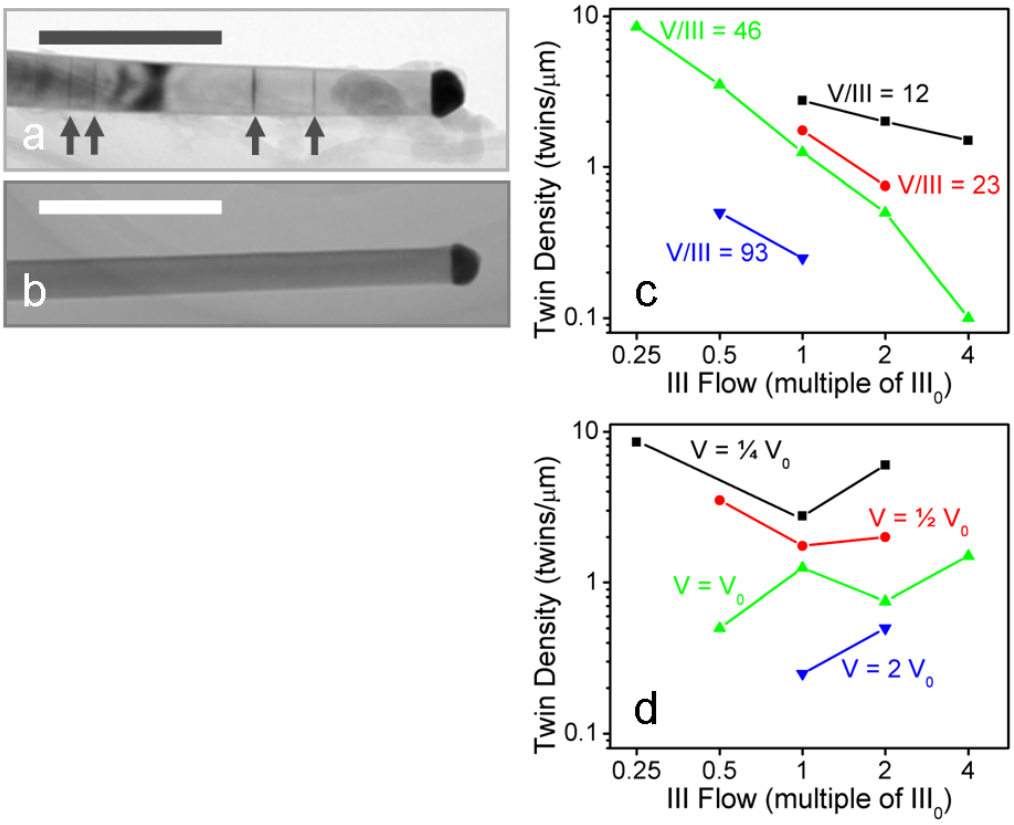

Figure 6.4: (a, b) TEM images of (a) a twinned nanowire grown with a slow growth rate (III = $\frac{1}{4}$ III$_0$, V = $\frac{1}{4}$ V$_0$) and (b) a twin-free nanowire grown at a rapid growth rate (III = 4 III$_0$, V = 4 V$_0$). Arrows indicate twin defects. Scale bars are 250 nm. (c) Twin density versus III flow, for constant V/III ratios. Straight lines group data sets for a constant V/III ratio: 12, 23, 46 and 93. (d) Twin density versus III flow, for constant V flow rate. Straight lines group data sets for a constant V flow: V = $\frac{1}{4}$ V$_0$, V = $\frac{1}{2}$ V$_0$, V = V$_0$ and V = 2 V$_0$. Group III flows are expressed as multiples of III$_0$. Axes are logarithmic.

(III = $\frac{1}{4}$ III_0, V = $\frac{1}{4}$ V_0). Intriguingly, the nanowire of Figure 6.4b, grown at a high growth rate (III = 4 III_0, V = 4 V_0) is completely twin free. Figure 6.4c plots twin density against precursor flow rate. The twin density is defined as the number of twin defects per unit (μm) of nanowire length. Each data point of Figure 6.4c is averaged over at least 3 nanowires. At the higher growth rates (above III = 4 III_0, V = 4 V_0), all nanowires examined were twin free and this data could not be plotted on the logarithmic axis of Figure 6.4c. Clearly, increasing both precursor flows, and consequently increasing growth rate, decreases the twin density.

This is an unexpected result, because increasing precursor flows increases the supersaturation of the vapour and liquid phases. According to previous theoretical and experimental studies of both planar and nanowire growth, a higher supersaturation (or supercooling) causes twin defects,[175,221,222] and can even drive WZ nanowire growth.[132,222,223] Figure 6.4 illustrates the opposite trend to these previous studies. Chapter 10 will examine possible explanations for this intriguing result.

Figure 6.4c has plotted lines connecting data points with common V/III ratios. Figure 6.4d again plots the same data, but this time plots lines to connect data points with common group V flow rates, rather than common V/III ratios. Interestingly, there is no clear trend in Figure 6.4d. Increasing group III flow, whilst keeping group V flow constant, neither consistently promotes nor consistently hinders twin formation. Clearly, increasing group III flow alone is not sufficient to prevent twin formation. Group V flows must also be scaled up to significantly reduce twin density. An explanation will be presented in Chapter 10, along with theoretical modelling studies.

6.5 Photoluminescence

6.5.1 Donor–acceptor pair recombination and carbon impurities

Low temperature (18 K) micro-PL spectroscopy was performed on ensembles of 5 to 10 nanowires, as described in Section 2.4.4. Figures 6.5 and 6.6 plot normalised PL spectra from different nanowire samples. The peak at approximately 1.517 eV is attributed to free exciton recombination, as observed in bulk GaAs.[95,145] The lower energy peak between 1.48 and 1.50 eV is attributed to DAP recombination involving a neutral donor and a carbon acceptor (D^0, C_{As}).[151,152] Note that the exciton peak is not evident in spectrum of the $\frac{1}{4}$ III_0 sample in Figure 6.5, because this time integrated spectrum is dominated by the DAP peak. The time-resolved spectrum of this sample (Figure 6.7), on the other hand, clearly shows the exciton peak at early times.

The relative intensity of the DAP peak to the exciton peak indicates the degree of carbon impurity content.[154,159,160] Figure 6.5 compares the exciton and DAP peaks for nanowires grown with various growth rates (III = $\frac{1}{4}$ III_0, III_0 and 4 III_0) and a constant

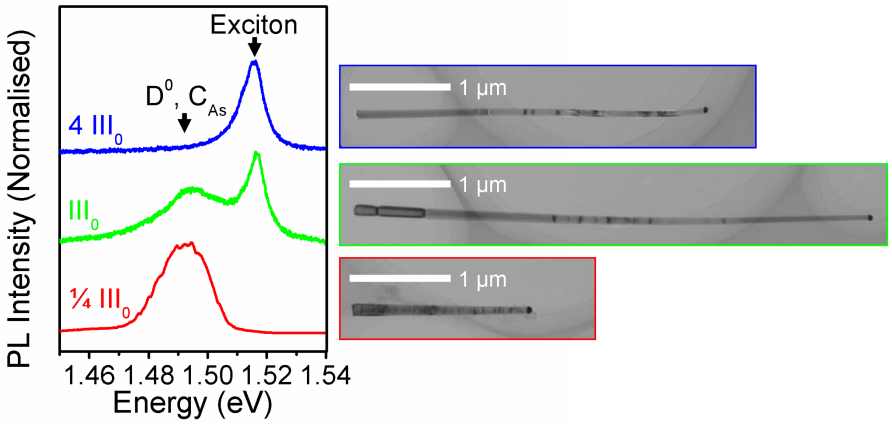

Figure 6.5: Normalised PL spectra comparing the relative magnitudes of DAP and exciton emission from nanowire ensembles grown with various III flows and a constant V/III ratio of 46. Spectra are offset for clarity. TEM images of the corresponding GaAs cores are illustrated alongside each spectrum.

V/III ratio. These spectra were obtained under low excitation power (90 μW) to avoid saturation of the DAP peak. Clearly, the DAP peak intensity decreases with increasing growth rate. This indicates that the carbon impurity concentration decreases as growth rate increases.

Figure 6.6 plots normalised PL spectra from two different nanowire samples, one grown at a slow growth rate (III = $\frac{1}{4}$ III_0) and the other grown at a more rapid rate (III = III_0). Both samples were grown with the same group V flow (V = $\frac{1}{4}$ V_0). This differs from Figure 6.5, in which samples were grown with constant V/III ratio, rather than constant group V flow. These spectra were obtained under low excitation power (90 μW), as for Figure 6.5. Examination of Figure 6.6 shows that the DAP peak intensity decreases with increasing growth rate. This indicates that the carbon impurity concentration decreases as growth rate increases, even when group V flow rate is held constant.

Apparently, a high growth rate favours high purity nanowires with minimal carbon contamination. This results holds under conditions of constant V/III ratio (Figure 6.5), and under conditions of constant group V flow (Figure 6.6). This, again, is surprising. A high growth rate is generally associated with lower quality growth and greater impurity incorporation.[224,225] In studies of planar GaAs growth by MOCVD, Hanna *et al.*[205] observed that (i) carbon incorporation is independent of growth rate provided the V/III ratio is held constant and (ii) carbon incorporation increases with increasing growth rate if the AsH_3 flow rate is held constant.

Correlating these observations with TEM images provides an explanation for the

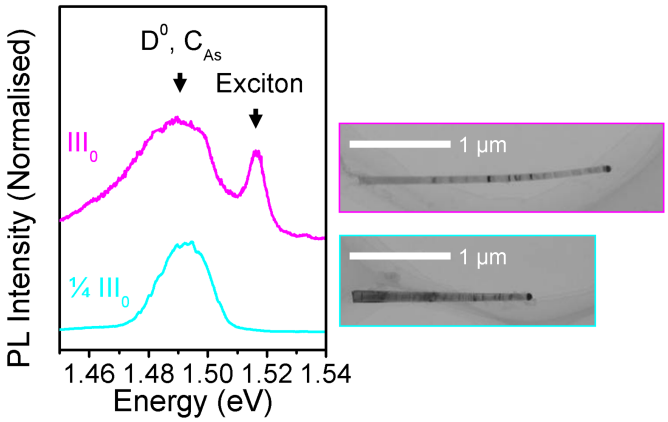

Figure 6.6: Normalised PL spectra comparing the relative magnitudes of DAP and exciton emission from nanowire ensembles grown with various III flows under constant V flow of $\frac{1}{4}$ V_0. Spectra are offset for clarity. TEM images of the corresponding GaAs cores are illustrated alongside each spectrum.

growth rate dependence of carbon incorporation. The TEM images of Figure 6.5 illustrate the large change in nanowire morphology concomitant with the change in carbon incorporation. With lower growth rates nanowires are more tapered, and have more carbon impurity incorporation. A likely explanation is that carbon incorporates preferentially via radial growth on the nanowire sidewalls. Carbon has low solubility in Au,[182,183] so only a small amount of carbon is likely to be incorporated into the nanowire interior via Au-assisted axial growth. In contrast, carbon can be readily incorporated onto the nanowire sidewalls via the vapour–solid radial growth mechanism, likely involving a gallium carbene intermediate species. Thus, nanowires with a greater proportion of radial growth (more tapered nanowires) have a greater degree of carbon incorporation. This mechanism explains the current experimental results, where nanowires grown at a slower growth rate, which feature more radial growth, exhibit more carbon incorporation. This same mechanism has been used to explain the formation of a boron or phosphorus rich shell in deliberately B- or P-doped Ge nanowires,[185–187] and in Chapter 4 where an increase in carbon incorporation was observed for more highly tapered nanowires.

6.5.2 Exciton lifetime

To probe the dynamics of photoexcited carriers in nanowires, time-resolved PL measurements were performed on single nanowires as described in Section 2.4.5. Under the pulsed excitation used for the time resolved measurements, all samples exhibited an exciton peak. Consider the sample (III = $\frac{1}{4}$ III_0) corresponding to the bottommost time-integrated spectrum of Figure 6.5. Figure 6.7 illustrates time-resolved PL spectra from this sample displayed for consecutive 200 ps intervals after the excitation laser pulse. The

exciton peak is clearly observed at early times after the excitation pulse (spectra at 100 and 300 ps), when the electron–hole density is highest. As the carriers recombine, the exciton peak rapidly decreases in intensity, leaving the lower energy DAP peak at later times (spectra at 500, 700 and 900 ps).

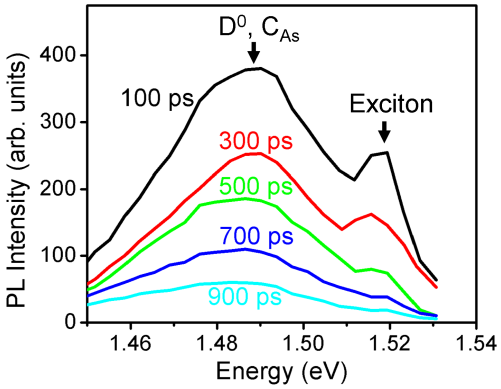

Figure 6.7: PL spectra at 100, 300, 500, 700 and 900 ps after the excitation laser pulse. Each spectrum is integrated over a 200 ps time window.

Time decays of the exciton, for nanowires grown with slow, intermediate and rapid growth rates, are plotted in Figure 6.8. Exciton lifetimes, τ, are presented alongside. The exciton lifetimes are approximately 200 ps regardless of the growth rate. Increasing growth rate had no appreciable effect on exciton lifetime.

This is contrasted with the pronounced effect seen upon increasing V/III ratio (Figure 5.7). As mentioned in Chapter 5, a high V/III ratio does impart some significant advantages to nanowires, but the associated decrease in radiative lifetime is undesirable for optoelectronics applications which require a longer carrier lifetime. In contrast, increasing the growth rate is a superior means of obtaining excellent quality nanowires without compromising the exciton lifetime.

These time-resolved measurements point to a further unexpected phenomenon. One might expect that twin defects are the primary non-radiative recombination centers.[79,80] Indeed, the low temperature grown twin-free nanowires of Chapter 4 exhibit very long, nearly intrinsic exciton lifetimes.[80] Yet, the current study suggests that a rapid growth rate minimises twin defects, but does not enhance the exciton lifetime (Figure 6.8). In addition, nanowires grown with a high V/III ratio feature a very low twin density, yet have short exciton lifetimes (Chapter 5). This indicated that excess arsenic-related defects (EL2, As_{Ga}, As_i or V_{Ga}) are primary non-radiative recombination centers. These studies strongly suggest that both twin defects and point defects must be eliminated to significantly improve nanowire optical properties.

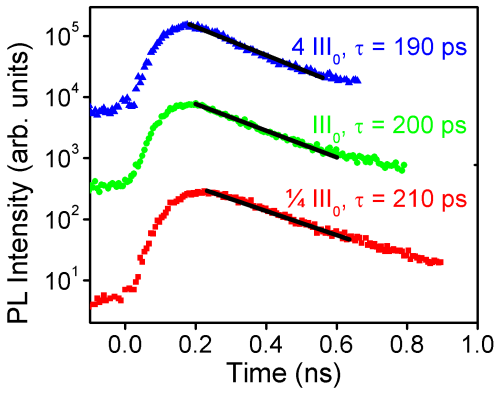

Figure 6.8: Time decays of the exciton (at 1.517 eV) taken from nanowires grown at different growth rates: slow (III = $\frac{1}{4}$ III$_0$), intermediate (III = III$_0$) and rapid (III = 4 III$_0$), and constant V/III ratio. Spectra are offset for clarity. Ordinate scale is logarithmic.

6.6 Summary

In conclusion, a high growth rate has unexpected, yet clear advantages for III–V nanowires. A high growth rate is achieved by scaling up both group III and group V precursor flows. Nanowires grown with fast growth rates were minimally tapered with very uniform diameters. Surprisingly, twin defects were markedly reduced by employing a rapid growth rate. In addition, a rapid growth rate minimised intrinsic carbon doping. Carbon impurities are thought to be incorporated preferentially into radial growth on the nanowire sidewalls, rather than via Au-assisted axial growth. A rapid growth rate had no significant effect on carrier lifetimes. Clearly, high growth rates impart excellent crystallographic and optical nanowire properties. These results should translate to other important III–V nanowire materials systems, and assist in producing high quality binary and ternary nanowires with device accessible properties. Combined with the results of Chapters 4 and 5, these findings represent a significant advance towards the rational growth of GaAs nanowires for device applications.

CHAPTER 7

Growth and structural properties of InAs nanowires

7.1 Introduction

The narrow bandgap (0.35 eV) and very high electron mobility (30 000 $cm^2V^{-1}s^{-1}$) of InAs make InAs nanowires highly promising, particularly for use in future high-frequency electronic devices. A number of InAs nanowire-based electronic devices have already been demonstrated, including infrared photodetectors,[7] single-electron transistors and memory devices,[19,21,22] resonant tunnelling diodes,[18] few-electron quantum dots,[20] and field-effect transistors.[26,27] Controlling InAs nanowire growth is essential if high quality InAs nanowire-based devices are to be realised. Furthermore, understanding the differences between GaAs and InAs nanowire growth is crucial for future fabrication of high quality ternary InGaAs nanowires. Thus, the impressive potential of both InAs and InGaAs nanowires for future devices motivates investigation of InAs nanowire growth.

This chapter examines how the growth parameters of temperature, V/III ratio and growth rate affect InAs nanowire morphology. In some respects, InAs nanowire growth behaviour parallels that of GaAs nanowires, as detailed in previous chapters. Growth rate and growth temperature, however, are found to affect InAs nanowires quite differently to GaAs nanowires. This chapter explores these intriguing differences, and reveals that an important factor in the unique growth behaviour of InAs nanowires is the relatively large growth contribution arising from In species adsorbed on the substrate and diffusing to the Au nanoparticle–InAs nanowire interface.

7.2 Experiments

InAs $(\bar{1}\,\bar{1}\,\bar{1})$B substrates were treated with poly-L-lysine solution followed by a solution of colloidal Au nanoparticles 50 nm in diameter, as described in Section 2.2.2. Prior

to growth, each substrate was annealed in situ at 600 °C under AsH_3 ambient to desorb surface contaminants. After cooling to growth temperature (375 ° to 550 °C), the AsH_3 flow was adjusted and TMIn was introduced to initiate nanowire growth.

Various combinations of growth temperature and V/III ratio were investigated. For these studies, the control group III (TMIn) flow rate was 1.2×10^{-5} mol/min. Growth temperatures between 375 °C and 550 °C and V/III ratios between 1.4 and 370, varying in binary orders of magnitude, were studied. To attain each V/III ratio, the AsH_3 flow rate was chosen between 1.7×10^{-5} and 4.1×10^{-3} mol/min. The growth time was 30 minutes for each sample.

Growths were also performed to study effect of the absolute flow rates of group III and group V precursors. This is equivalent to studying "growth rate" as for GaAs nanowires in Chapter 6. Here, the control, or standard, group III (TMIn) and group V (AsH_3) flow rates were $III_0 = 1.2 \times 10^{-5}$ mol/min and $V_0 = 5.4 \times 10^{-4}$ mol/min, respectively and the V/III ratio was 46. For other growths, III_0 and V_0 were scaled by factors of $\frac{1}{4}$, $\frac{1}{2}$, 1, 2 and 4 to span flow ranges of III = 2.9×10^{-6} to 4.6×10^{-5} mol/min and V = 1.3×10^{-4} to 2.1×10^{-3} mol/min. Group III and group V flows were scaled equally, so that V/III ratio remained at 46. Throughout this chapter, III and V flows will be expressed as multiples of III_0 and V_0, respectively. For nanowire samples grown with III = III_0, the growth time, t_g, was 30 minutes. For other samples, growth time was scaled inversely with group III flow. This was to achieve nanowires of reasonable height, between 1 and 5 μm, across all samples.

FESEM analysis was then used to identify the general morphology of the nanowires, including height and diameter. Images were taken across the samples in regions of low and high nanowire density, to assess the effect of density on nanowire morphology.

7.3 Effect of nanowire density on nanowire morphology

The first major difference between GaAs and InAs nanowire growth, is the sensitivity of InAs nanowire growth to the density of nanowires on the substrate. This is clearly exemplified parts c and d of Figure 7.1. In part d, nanowires are more sparsely distributed than in part c. The low density nanowires of part d are also significantly taller and have much wider bases than their high density counterparts of part c. This can be explained with reference to the schematic illustrations of Figure 7.2.

As discussed in previous chapters, there are three major contributions of reaction species to axial nanowire growth. The first is from the species directly impinging on the Au nanoparticle residing on the top of nanowire. The second arises from the species which arrive at the nanowire sidewalls and subsequently diffuse along the sidewalls toward Au nanoparticle. The third contribution arises from the species that initially arrive at

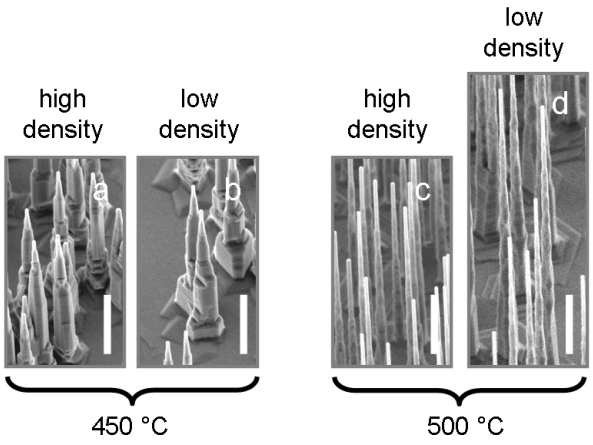

Figure 7.1: FESEM images of InAs nanowires grown at (a, b) 450 °C and (c, d) 500 °C. The areas feature high nanowire density in (a) and (c), and low nanowire density in (b) and (d). Both samples were grown with group III and group V flow rates of $III_0 = 1.2 \times 10^{-5}$ mol/min and $V_0 = 5.4 \times 10^{-4}$ mol/min, respectively and the V/III ratio was 46. Samples are tilted at 40°. Scale bars are 1 μm.

the $(\bar{1}\,\bar{1}\,\bar{1})$B substrate surface, travel on the surface and finally diffuse toward the Au nanoparticle. This third contribution is important for explaining the observed results. If nanowires are spaced within a diffusion length, λ of one another, then these adjacent nanowires compete for reaction species adsorbed on and diffusing from the substrate. In low density regions, on the other hand, there is minimal competition for diffusing species so the axial growth rate is maximum. These diffusing reaction species also contribute to radial growth. Therefore, if nanowires are spaced within a diffusion length, the radial growth too is diminished due to consumption of diffusing adatoms by neighbouring nanowires. Consequently, in Figure 7.1, the low density nanowires of part d are taller with wider bases than the high density nanowires of part c.

The degree of density dependence depends on the diffusion length. If the diffusion length is long, as in the upper part of Figure 7.2, then a significant fraction of axial growth arises from these diffusing species. In this case, the density dependence is marked. If the diffusion length is short, as in the lower part of the figure, then the density dependence is more marginal, because nanowires must be very closely spaced to compete for diffusing reaction species. This explains why, in Figure 7.1, the nanowires of parts a and b do not exhibit such a marked density dependence as those of parts c and d. The nanowires of parts a and b were grown at a lower temperature, which gives a shorter diffusion length, [125,226,227] and consequently a less significant density dependence.

In the previous chapters, none of the GaAs nanowire samples studied showed any

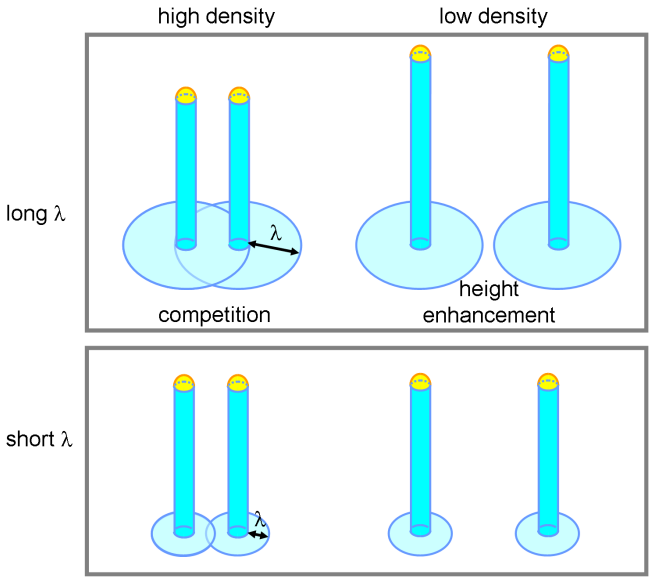

Figure 7.2: Schematic illustration of the competition between adjacent nanowires for adatoms adsorbed on the substrate. This illustrates high and low density nanowire regions, and the effects of diffusion length, λ. When λ is high the density dependencies are more significant: significant competition occurs in high density regions whereas significant height enhancement occurs in low density regions.

significant dependence on density. This is consistent with previous work, in which In species demonstrated a significantly longer diffusion length than Ga species.[220,228–230] Because InAs nanowire growth is much more sensitive to diffusion and nanowire density, the following studies of V/III ratio, temperature and growth rate take great care to compare samples with approximately equal nanowire densities.

7.4 Effect of V/III ratio on nanowire morphology

The V/III ratio has a profound effect on nanowire growth, and the growth behaviour parallels that of GaAs nanowires (Chapter 5). Figure 7.3 illustrates nanowires grown at various V/III ratios. Importantly, nanowires grow only within a finite range of V/III ratios (parts b to e). At the lowest V/III ratios, as illustrated in part a, an irregular planar layer has grown, and the Au nanoparticles failed to nucleate nanowires. Clearly, nanowire growth is limited by insufficient group V species. Pits in the substrate surface evidence decomposition of the InAs substrate, occurring due to the low group V overpressure. Nanoparticles have been observed in these pits, suggesting the Au nanoparticles themselves enhance substrate decomposition.

As V/III ratio is increased, there are sufficient group V species to promote nanowire growth and the nanowire growth rate increases sharply.[125] In the range of low V/III ratios,

approximately 23 and below, the axial growth rate increases with increasing V/III ratio. This is analogous to the case of GaAs nanowires, and is expected because group V flow enhances the pyrolysis of group III species, and hence increases the growth rate. The radial growth rate increases too, causing growth on the nanowire sidewalls and nanowire tapering.

The axial growth rate reaches a maximum at an intermediate V/III ratio of 23 (part c). Beyond this point, the axial growth rate decreases with increasing V/III ratio. Unlike axial growth, the radial continues to increase with V/III ratio, leading to increasingly tapered nanowires. Such effects were also observed for GaAs nanowires in Chapter 5, and can be explained as follows. A high V/III ratio lowers the activation energy for two dimensional planar growth,[196] and causes a reduction in adatom diffusion length.[231] Consequently, a greater proportion of adsorbed In crystallises at the substrate surface and nanowire sidewalls, rather than diffusing to the Au nanoparticle-capped nanowire tip where axial nanowire growth would take place. In this manner, lateral (planar and radial) growth competes with axial growth for In species. Tapering increases whereas the nanowire height decreases. Accordingly, at the highest V/III ratios (part f), lateral growth dominates, and the Au-assisted structures appear island-like rather than nanowire-like.

Some of the nanostructures in part f grow in directions other than the [$\bar{1}\,\bar{1}\,\bar{1}$]B direction, as for GaAs nanostructures in Chapter 5. InAs ($\bar{1}\,\bar{1}\,\bar{1}$)B surfaces, like GaAs ($\bar{1}\,\bar{1}\,\bar{1}$)B surfaces, form an As-trimer surface reconstruction under high As-pressure conditions.[232] This surface reconstruction can decrease the [$\bar{1}\,\bar{1}\,\bar{1}$]B growth rate[198] and also favour a growth direction other than [$\bar{1}\,\bar{1}\,\bar{1}$]B. For each growth temperature examined, V/III ratio had a similar effect on nanowire growth.

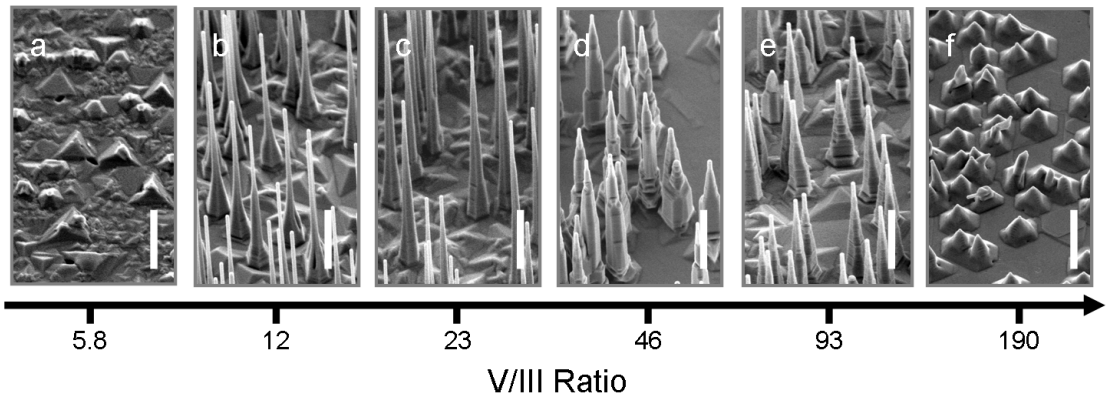

Figure 7.3: FESEM images of InAs nanowires grown with different V/III ratios, as indicated. The growth temperature was 450 °C and the group III flow rate was 1.2×10^{-5} mol/min for all samples. Axis is logarithmic. Scale bars are 1 μm. Samples are tilted at 40°.

7.5 Effect of growth temperature on nanowire morphology

Figure 7.4 compares nanowires grown at different growth temperatures. At the very low growth temperature of 375 °C (part a), the Au nanoparticles have catalysed the growth of irregular and kinked nanostructures, rather than nanowires. Similar observations have been made for GaAs nanowires in Chapter 4. The temperature of 375 °C is below the bulk Au–In eutectic temperature of 454.3 °C. This nominal thermocouple reading of 375 °C is a few tens of degrees higher than the true substrate temperature. Even taking into account melting point depression due to the small nanoparticle size, and melting point hysteresis, it is likely that at a nominal growth temperature of 375 °C, the nanoparticle is partially or completely solid, rather than liquid. The presence of a solid phase within the nanoparticle might be responsible for irregular kinked growth, as discussed in Chapter 4. Occasionally, ultrathin nanowires of approximately 5 nm in diameter are observed. These nanowires are catalysed by In, which is derived from TMIn precursors and has segregated into pure In droplets on the growth surfaces. Pure In is liquid at 375 °C, and these In droplets can drive vapour–liquid–solid nanowire growth.

Between 400 °C and 500 °C, the growth rate shows an interesting dependence on growth temperature. Nanowires are tallest at the highest and lowest temperatures of the growth window (400 °C and 500 °C), and shorter at the intermediate temperatures. This is very different to previous studies of nanowire growth, for example Chapter 4 and other published works.[65,167].

The present results can be explained by considering the relative decomposition efficiencies of TMIn and AsH_3 at the various temperatures. The thermal decomposition of AsH_3 increases markedly between 375 ° and 525 °C.[102,108] TMIn decomposition takes place above 300 °C, and is complete at 400 °C.[101] Note that the decomposition temperatures cited above do not directly translate to the experimental MOCVD system, in which the nominal thermocouple readings are a few tens of degrees higher than the true substrate temperature. Thus, the cited TMIn decomposition temperature (400 °C) translates to a nominal temperature of approximately 450 °C. In other words, TMIn decomposition reaches completion at a nominal temperature of approximately 450 °C. Unlike TMIn, the decomposition of AsH_3 is incomplete, and increases over the growth temperature range (375 to 550 °C).

Due to these temperature-dependent differences in the decomposition efficiencies of TMIn and AsH_3, the *effective* V/III ratio can be markedly different from the *nominal* V/III ratio of 46. Another important factor is the diffusion length of In species, which in turn depends on temperature and effective V/III ratio.

At the low growth temperature of 400 °C (part b), nanowires are tall, straight and

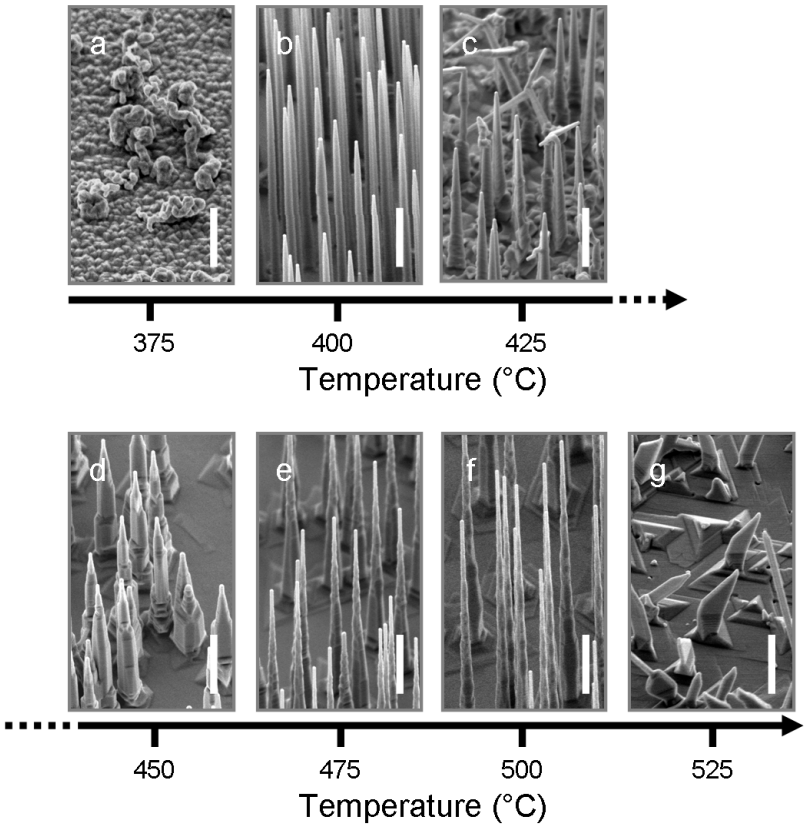

Figure 7.4: FESEM images of InAs nanowires grown at (a) 375 °C (b) 400 °C, (c) 425 °C, (d) 450 °C, (e) 475 °C, (f) 500 °C and (g) 525 °C. The V/III ratio was 46 and the group III flow rate was 1.2×10^{-5} mol/min for all samples. Scale bars are 1 μm. Samples are tilted at 40°.

minimally tapered. Tapering is relatively low because radial growth is kinetically limited at this low temperature.[167] In addition, AsH_3 decomposition is low at this low temperature, which creates a low effective V/III ratio. This low effective V/III ratio is another factor contributing to the low radial growth rate.

At the higher temperatures of 425 °C (part c), the nanowires are shorter, more tapered, and occasionally kinked. These features are the hallmarks of a high V/III ratio, as discussed above. Therefore, it can be inferred that at 425 °C, the *effective* V/III ratio is high. This is reasonable because, as discussed above, TMIn decomposition is not yet complete at the nominal temperature of 425 °C, and AsH_3 decomposition efficiency increases markedly between 400 °C and 425 °C. The growth window, discussed later, gives further evidence for a high effective V/III ratio at 425 °C. Additionally, the irregular surface features in part c indicate that significant crystallisation occurs on the substrate surface. In turn, this indicates that the diffusion length of TMIn species is short, as expected for low temperatures and high V/III ratios. The reduced diffusion length could further decrease the supply of adsorbed TMIn species to the Au nanoparticle and raise the local V/III ratio at the growing nanowire tip.

Between 450 °C and 500 °C (parts d to f) nanowires are straight, with height increasing with temperature, the base diameter and radial growth rate remaining approximately constant, and overall tapering ($\Delta r/\Delta l$) decreasing with temperature. In this temperature range it is expected that TMIn is completely decomposed. The increase in nanowire height, and concomitant decrease in tapering, are attributed to the increase in In adatom diffusion length with temperature.[125,226,227] At higher temperatures, the larger diffusion length means that a greater proportion of adsorbed adatoms can diffuse down the concentration gradient towards the nanowire tip, where they are incorporated in axial growth. Figure 7.1 supports this explanation. This figure compares FESEM images of regions of high and low nanowire density, for temperatures of 450 °C and 500 °C. The nanowires grown at 450 °C exhibit a weak density dependence with marginally taller heights and wider bases in areas of low nanowire density. For nanowires grown at 500 °C, the density dependence is more marked with significantly taller heights and wider bases in areas of low nanowire density. This density dependence confirms that the diffusion length is greater for the higher growth temperature of 500 °C.

Finally, at the highest growth temperature of 525 °C (Figure 7.4g), the nanowire growth rate drops sharply, consistent with previous reports.[195] Most Au nanoparticles fail to nucleate nanowires, and instead catalyse island-like structures or remain on the sample surface while planar growth occurs on the substrate beneath. Only a small proportion of Au nanoparticles nucleate nanowires, and these nanowires are often misoriented from the $[\bar{1}\,\bar{1}\,\bar{1}]$B direction. The nanowire nucleation rate and growth rate drop because of the

increase in competitive lateral growth at these high temperatures and high effective V/III ratios.[195] At such high temperatures, a greater proportion of group III and V reaction species can overcome the activation energy barrier for lateral growth. At 550 °C, nanowire growth ceases completely and only lateral and island-like growth takes place.

7.6 Growth window

The above discussion is corroborated by the growth window plotted in Figure 7.5. This is the window of temperatures and V/III ratios which promote nanowire growth. Points A–I are labelled for discussion.

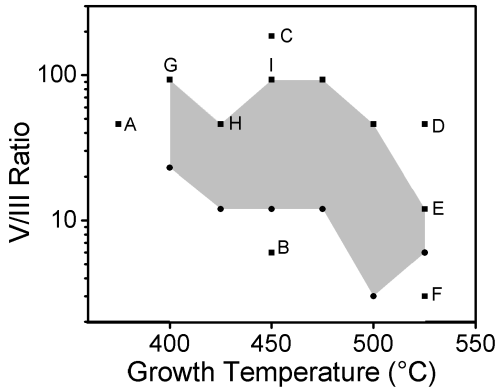

Figure 7.5: The shaded area plots the InAs nanowire growth window: the range of V/III ratio and growth temperature combinations which achieve nanowire growth.

In the low temperature regime, for instance point A at 375 °C (corresponding to Figure 7.4a), nanowire growth is inhibited. Regardless of V/III ratio, 400 °C was the minimum temperature for nanowire growth, presumably due to partial or complete solidification of the Au nanoparticle at temperatures below 400 °C.

In the mid-temperature regime, nanowire growth depends on the V/III ratio. At point B (corresponding to Figure 7.3a), the V/III ratio is too low to support nanowire growth and substrate decomposition takes place. At point C (corresponding to Figure 7.3f), the high V/III ratio means that the lateral growth rate is significant. Lateral growth competes with axial nanowire growth, resulting in a drop in the nanowire growth rate.

In the high temperature regime, nanowire growth too depends on the V/III ratio. The maximum growth temperature for nanowire growth decreases with V/III ratio, because both high temperature and high V/III ratio favour lateral growth over axial nanowire growth.[195] At 525 °C (point D, corresponding to Figure 7.4g) nanowire growth is hindered due to the combination of high temperature and moderate V/III ratio. At high temperatures, nanowire growth is only possible at a relatively low V/III ratio (e.g. point

E), which allows lateral growth to be minimised. At the lowest V/III ratios (e.g. point F), substrate decomposition becomes significant and nanowire growth does not take place.

Finally a dip is observed between points G–H–I. This dip in the maximum input V/III ratio, indicates that, although the nominal V/III ratio at point H is lower than at points G and I, the effective V/III ratio is comparable at points G, H and I. At 425 °C (point H, corresponding to Figure 7.4c) the decomposition of AsH_3 must be relatively high compared with TMIn, to produce this high effective V/III ratio. This is consistent with the earlier discussion of Figure 7.4c.

7.7 Effect of total precursor flow rate on nanowire morphology

Figure 7.6 illustrates FESEM images of nanowires grown with varying group III and V precursor flow rates. Note that the growth time, t_g, was scaled inversely with III and V flow rates. Three observations can be made. Firstly, InAs nanowires appear increasingly tapered with increasing III and V flow rates. Secondly, the substrate surface becomes increasingly irregular. Finally, the axial growth rate increases only marginally with increasing III and V flow rates. This is very different to the behaviour of GaAs nanowires as presented in Chapter 6.

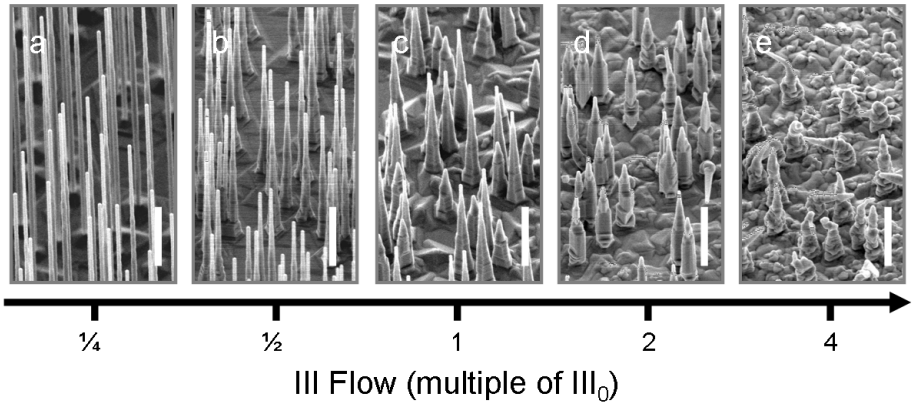

Figure 7.6: FESEM images of InAs nanowires grown at constant V/III ratio of 46 and the indicated III flows: (a) III = $\frac{1}{4}$ III_0, t_g = 120 minutes, (b) III = $\frac{1}{2}$ III_0, t_g = 60 minutes, (c) III = III_0, t_g = 30 minutes, (d) III = 2 III_0, t_g = 15 minutes, (e) III = 4 III_0, t_g = 7.5 minutes. The growth temperature was 450 °C for all samples. Axis is logarithmic. Samples are tilted at 40°. Scale bars are 1 μm.

To quantify the axial growth rate for each nanowire sample, nanowire heights, L, were measured from FESEM images, and these heights were divided by growth time, t_g (following equation 3.4). The analysed FESEM images featured similar nanowire densities, such as those shown in Figure 7.6, so that density effects do not obscure the results. At least 20 nanowires were examined for each sample. The results are plotted

Figure 7.7. In this plot, the weak increase in axial growth rate is clearly observed. The differences between InAs and GaAs nanowire growth behaviour are clear when comparing Figure 7.7 (for InAs nanowires) with Figure 6.2b (for GaAs nanowires). These plots use the same scale so that comparison may be made. The InAs axial growth rate clearly has a weaker dependence on group III flow rate.

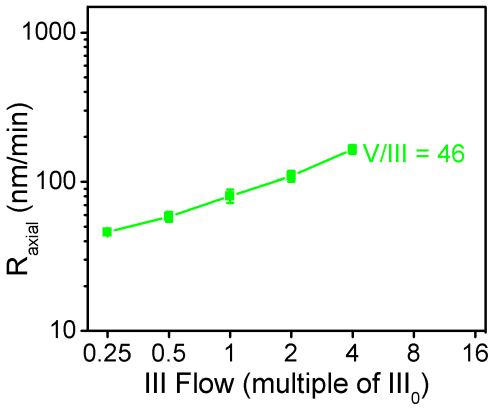

Figure 7.7: Axial growth rate versus group III flow rate under a constant V/III ratio of 46. Group III flows are expressed as multiples of III_0. Axes are logarithmic. Each data point represents an average from at least 20 nanowires. For each data point, the standard deviation is less than 15%.

The three observations mentioned above point to a reduction in adatom diffusion length with increasing growth rate. Indeed, it is well known that at low precursor flow rates, there are fewer adatoms deposited on the surface per unit time, so that the adatoms have more time to migrate on the surface and find energetically favourable sites to incorporate.[231,233,234] Consequently, at low precursor flow rates, In species can diffuse significant distances, and readily diffuse up the nanowire sidewalls to the Au nanoparticle-capped tip, where they are incorporated into axial growth. At high growth rates, adsorbed In species cannot diffuse so far, and are more likely to be incorporated close to the point of adsorption, either on the substrate surface or on the nanowire sidewalls. Thus, radial growth, tapering and substrate growth significantly increase with total precursor flow rate. The axial growth rate, too increases with precursor flow rate, but only marginally due to the onset of significant radial and substrate growth which consumes diffusing In adatoms. At the highest flow rates, the axial, substrate, and sidewall growth is highly irregular, presumably due to the short diffusion length.

This diffusion length argument is supported by Figure 7.8, which compares FESEM images of regions of high and low nanowire density. In parts a and b, the nanowires grown at the lower precursor flow rates exhibit a marked dependence of height and radial growth on density. In areas of high density (part a), nanowires are shorter with less radial growth,

because the closely spaced nanowires compete for diffusing reaction species adsorbed on the substrate surface. This density dependence suggests that the diffusion length is considerable. In contrast, nanowires grown at higher flow rates (parts c and d) do not exhibit this density dependence. This indicates that for high flow rates, even closely spaced nanowires do not compete significantly for diffusing reaction species. Thus, the diffusion length on the substrate is small at high flow rates.

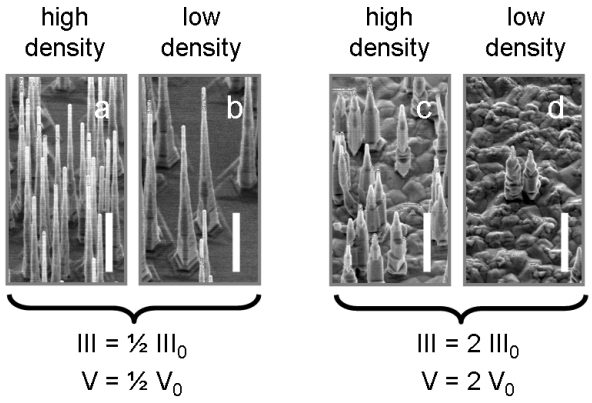

Figure 7.8: FESEM images of InAs nanowires grown at constant V/III ratio of 46 and the indicated III flows: (a, b) III = $\frac{1}{2}$ III_0, t_g = 60 minutes, and (c, d) III = 2 III_0, t_g = 15 minutes. The areas feature high nanowire density in (a) and (c), and low nanowire density in (b) and (d). Samples are tilted at 40°. Scale bars are 1 μm.

These diffusion effects are significant for InAs nanowires, due to the large diffusion length of In species. These effects were not observed for GaAs nanowires, because the diffusion length of Ga species is comparatively small, as will be discussed in Chapter 8.

7.8 Summary

Density, growth temperature, V/III ratio and growth rate each have a significant influence on InAs nanowire morphology. This large sensitivity to growth parameters means great flexibility in designing InAs nanowires with morphologies suitable for device applications. Tapering, for instance, can be minimised by using a very low growth rate, a low V/III ratio, and either a high temperature or a low temperature.

The similarities and differences between InAs and GaAs growth are intriguing. The effect of V/III ratio was similar for both GaAs and InAs nanowires, whereas the effects of density, temperature and growth rate, were remarkably different. Unlike GaAs nanowires, InAs nanowire height and radial growth were dependent on nanowire density, particularly at high temperatures and low precursor flow rates. This dependency is related to the long diffusion length of adsorbed In reaction species on the $(\bar{1}\,\bar{1}\,\bar{1})$B InAs substrate. The effects

of temperature and growth rate were also mediated by variations in the diffusion length of In species. Such effects were not evident in any of the presented studies of GaAs nanowire growth, because the diffusion length of Ga species is significantly shorter than that of In species.

CHAPTER 8

Ternary InGaAs nanowire growth

8.1 Introduction

Recent developments in III–V nanowires have been largely limited to binary nanowires, composed of only two different elements, such as GaAs. Ternary alloy nanowires, such as InGaAs,[142,235,236] AlGaAs,[70,164] InAsP[237] and GaAsSb[238,239] nanowires, and quaternary nanowires such as InGaAsP, offer further advantages. Their energy bandgap can be tuned by adjusting the composition of the alloy. Ternary and quaternary alloy nanowires enable a greater range of axial and radial heterostructures, and thus broaden the application range of nanowires.

The development of ternary and quaternary nanowires is complicated by the different growth behaviours of the different elements comprising the nanowire. The different decomposition, diffusion and incorporation efficiencies of the various precursors determine the final nanowire properties, including composition and compositional uniformity. Systematic studies, with emphasis on the uniform growth of ternary nanowires with device-accessible structural and optical properties, are essential. This chapter focuses on ternary InGaAs nanowires, motivated by the paramount importance of the InGaAs material system for applications in long wavelength optical fibre transmission and integrated photonics. InGaAs nanowires are expected to have significant importance in future photonic and electronic devices. Control of InGaAs nanowire shape, height and composition is studied, in conjunction with their optical properties.

The study reveals a strong influence of nanowire density on nanowire height, tapering, and base shape, specific to the nanowires with high In composition. This dependency is attributed to the large difference of diffusion length on $(\bar{1}\,\bar{1}\,\bar{1})$B surfaces between In and Ga reaction species, with In being the more mobile species. EDS analysis together with high-resolution electron microscopy of individual InGaAs nanowires shows large In/Ga compositional variation along the nanowire, supporting the presented diffusion model.

Photoluminescence spectra exhibit a red-shift with decreasing nanowire density due to the higher degree of In incorporation in more sparsely distributed InGaAs nanowires.

8.2 Experiments

InGaAs nanowires were grown on GaAs ($\bar{1}\,\bar{1}\,\bar{1}$)B substrates using TMIn, TMGa and AsH_3 precursors. GaAs($\bar{1}\,\bar{1}\,\bar{1}$)B substrates were treated with poly-L-lysine (PLL) solution and a solution of colloidal 50 nm diameter Au nanoparticles, as described in Section 2.2.2. Prior to nanowire growth, the substrate was annealed in situ at 600 °C under AsH_3 to desorb surface contaminants. After cooling down to the desired growth temperature, group III source gases were introduced to the reactor to initiate nanowire growth. The molar flow rates of TMGa and AsH_3 were 1.2×10^{-5} and 5.4×10^{-4} mol/min, respectively. The TMIn molar flow rate was selected between 0 and 3.5×10^{-6} mol/min to yield vapour In compositions ($x_{v,In}$) of 0, 0.11, 0.19, and 0.23. GaAs nanowires were grown in the absence of TMIn for reference. Growth temperature and time were 450 °C and 30 min, respectively, for all samples. Because the Au colloidal solution was applied as a droplet, a circular pattern of nanowires on the substrate was obtained after the growth. The colours within this circle changed with viewing angle due to diffraction effects. A non-uniform nanowire distribution within the circle was apparent even by visual inspection. This was further confirmed by optical microscopy. In general, nanowire density was the highest in the circle centre and decreased gradually toward the edge of the circle.

FESEM images of regions between the circle centre and edge were obtained for each sample. Nanowire density and height distribution were measured within each imaged region. TEM measurements were carried out at the University of Queensland. Bright-field and HRTEM imaging were employed to study the nanostructure and nanomorphology of these nanowires. EDS was performed at the University of Western Australia to study compositional variation within the nanowires. For each nanowire, the EDS spectra were taken at three different locations (close to Au catalyst, in the middle and at the base end of a nanowire). The In/Ga ratio at each location was evaluated by comparing In Lα and Ga Kα X-ray peaks using the ISIS software package.[240]

8.3 Morphology

Figure 8.1 shows FESEM images taken with the substrate tilted 45° from the electron beam. Most nanowires grow perpendicular to the substrate surface in the [111]B direction, which is the energetically favourable direction. However, as observed in Figure 8.1c, there are some inclined nanowires with growth directions other than [111]B. These inclined nanowires were generally longer and were excluded from the presented statistical investigation of nanowire density and height. Parts a and b of Figure 8.1 show InGaAs

nanowires grown with a $x_{v,In}$ of 0.11. In part a, the nanowire density is 0.73 μm^{-2}, whereas in part b the density is 0.015 μm^{-2}. Parts c and d are images of InGaAs nanowires grown at a higher $x_{v,In}$ of 0.19. The densities of parts c and d are 0.70 and 0.018 μm^{-2}, respectively. For the nanowires with lower In composition, as shown in parts a and b, there is no significant density dependency of nanowire height. The same trend was observed for GaAs nanowires. In contrast, the nanowires grown at the higher $x_{v,In}$ exhibit drastic height enhancement in the low-density region: the average height in part c was 5.8 ± (0.1) μm, whereas average height in part d was 13 ± (0.8) μm. Thus the height enhancement is more than a factor of 2. A similar height enhancement is observed for InGaAs nanowires with $x_{v,In}$ of 0.23.

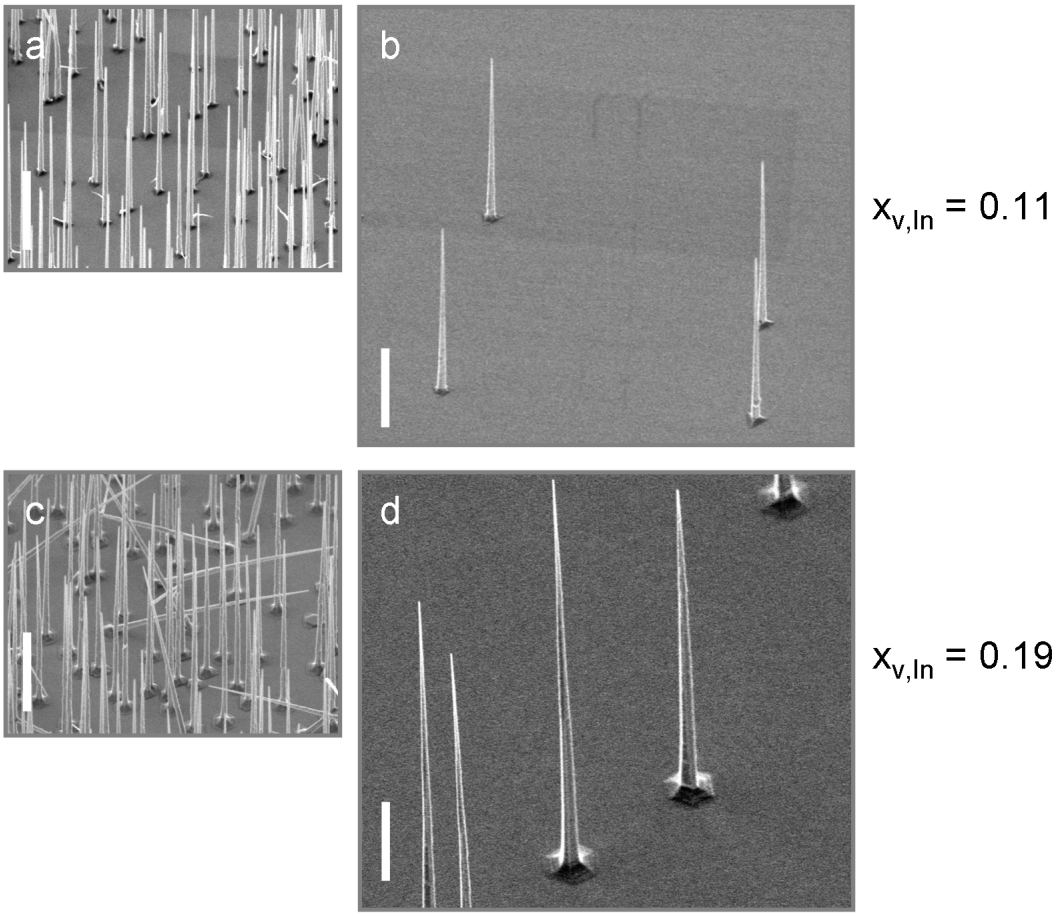

Figure 8.1: FESEM images of InGaAs nanowires. (a, b) InGaAs nanowires with $x_{v,In}$ of 0.11. (c, d) InGaAs nanowires with $x_{v,In}$ of 0.19. The nanowires in parts a and c have almost equal available diffusion areas of approximately 1.4 μm^2. The nanowires in parts b and d have available diffusion areas of approximately 67 μm^2. Samples are tilted at 45°. Scale bars are 2 μm.

As discussed in previous chapters, there are three major contributions of reaction species to axial nanowire growth. The first contribution arises from the species directly

impinging on the Au nanoparticle residing on the top of nanowire. The second comes from the species which arrive at the nanowire sidewalls and subsequently diffuse along the sidewalls toward the Au nanoparticle. The third contribution arises from the species that initially arrive at the $(\bar{1}\,\bar{1}\,\bar{1})$B substrate surface, travel on the surface and finally diffuse toward the Au nanoparticle. This third contribution is important for explaining the observed results. If nanowires are spaced within a diffusion length of one another, then these adjacent nanowires compete for reaction species adsorbed on and diffusing from the substrate. In low density regions, on the other hand, adjacent nanowires are effectively isolated from one another so the growth rate is maximum. In the case of ternary InGaAs nanowires, the diffusion of both In and Ga species must be considered. The results suggest that the diffusion length, which is the average migration distance of reaction species before incorporation, of In species on the $(\bar{1}\,\bar{1}\,\bar{1})$B substrate surface is much larger than that of Ga species. The concept of available diffusion area, $A_{available}$, defined as the inverse of nanowire density, σ, gives much physical insight because its square root value is roughly equivalent to available diffusion distance, $\lambda_{available}$. Thereby, the available diffusion area gives information about the diffusion lengths, λ_{In} and λ_{Ga}, of the two species.

$$A_{available} = \frac{1}{\sigma} \approx \lambda^2_{available} \tag{8.1}$$

Figure 8.2 shows FESEM images of representative nanowires grown with $x_{v,In}$ between 0 and 0.23. Their available diffusion areas are larger than 40 μm^2. As will be discussed later, such a large available diffusion area means these nanowires are effectively isolated and subject to minimal interference from neighbouring nanowires during growth. The nanowires of parts c and d, grown at high $x_{v,In}$, are significantly taller than those of parts a and b, grown at lower $x_{v,In}$. This provides evidence that the observed height enhancement is specific for nanowires of high In composition in regions of low nanowire density. The heights of GaAs nanowires and InGaAs nanowires with a $x_{v,In}$ of 0.11 (parts a and b) appear the same. However, more tapering is observed for the InGaAs nanowire in part b compared to the GaAs nanowire of part a, indicating the incorporation of In species into radial growth following diffusion from the substrate surface. This strongly suggests that the radial growth is In-rich compared with the axial growth. Throughout parts a to d, there is a systematic increase in tapering with increasing In composition. The base shape also evolves with increasing In composition. The GaAs nanowires of part a show a triangular base. With increasing $x_{v,In}$, this triangular base develops to a hexagonal base shape, as in parts c and d, accompanied by widening of the base. Future TEM experiments, focussed on the nanowire–substrate interface, should determine the

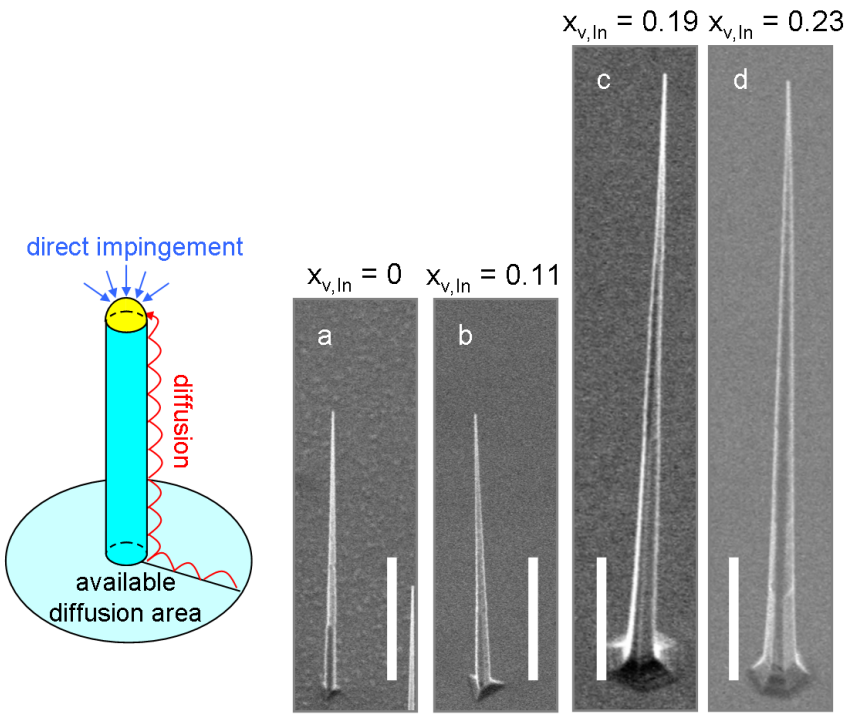

Figure 8.2: FESEM images of representative InGaAs nanowires grown with different $x_{v,In}$ of (a) 0, (b) 0.11, (c) 0.19 and (d) 0.23. All images were taken from regions with available diffusion area larger than 40 μm^2. Therefore, these nanowires are effectively isolated from the influence of neighbouring nanowires during growth. Samples are tilted at 45°. Scale bars are 2 μm. A schematic picture illustrating the concept of available diffusion area is also included.

mechanism for this shape change. The mechanism is probably related to the different faceting behaviour of GaAs and InAs nanowires grown at 450 °C: GaAs nanowires exhibit triangular cross-sections as described by Zou *et al.*[72] whereas InAs nanowires exhibit hexagonal cross-sections (see Figure 7.4d). Therefore, nanowires grown with higher $x_{v,In}$ should tend toward a more hexagonal base shape.

Figure 8.3 shows the evolution of the base for InGaAs nanowires with $x_{v,In}$ of 0.23 with increasing available diffusion area. The elbow at the intersection between a nanowire and the substrate exhibits a higher growth rate with increasing available diffusion area and develops into a base structure.[121] This confirms that base widening is strongly correlated with the surface diffusion of reaction species. In addition, the hexagonal base shape is retained even for nanowires with very low available diffusion area as shown in part a. The shape-determining factor is the In composition. In the case of GaAs nanowires, there was no apparent density-dependent widening of the base in any of the imaged areas.

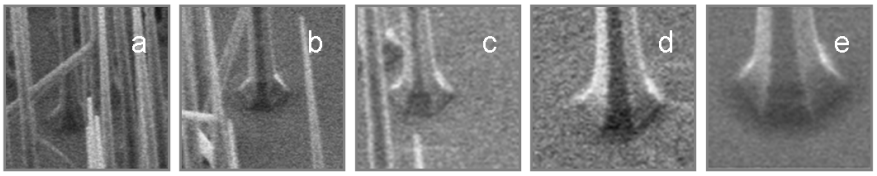

Figure 8.3: FESEM images showing the evolution of the nanowire base with increasing available diffusion area. These nanowires were grown with $x_{v,In}$ of 0.23. The available diffusion areas are (a) 0.65, (b) 1.58, (c) 3.70, (d) 20.8 and (e) 33.3 μm^2. Samples are tilted at 45°. The imaging areas are each 1.5 × 1.5 μm^2.

Figure 8.4a shows the nanowire height variation as a function of available diffusion area. Regardless of $x_{v,In}$, nanowire height increases significantly with available diffusion area provided available diffusion area is less than a few square micrometers. At higher available diffusion area, GaAs nanowires and InGaAs nanowires with $x_{v,In}$ of 0.11 exhibit height saturation. In contrast, the heights of InGaAs nanowires with higher $x_{v,In}$ continue to increase and exhibit height saturation at a larger available diffusion area of approximately 30 to 40 μm^2. The initial increase is believed to be related to Ga diffusion length. When available diffusion area exceeds Ga diffusion length, the heights of GaAs or InGaAs nanowires with low $x_{v,In}$, will saturate. Therefore, the Ga diffusion length is less than 2 μm on the $(\bar{1}\,\bar{1}\,\bar{1})$B GaAs surface.

It is well-known that In species have a larger diffusion length than Ga species. This difference has led to the In content increase near the mask edges during the selective area epitaxy of InGaAs by low-pressure MOCVD growth.[228,229] Recently this difference has been utilized for emission wavelength tuning of InGaAs quantum dots during selective

area epitaxy.[230] From the height saturation behaviour of InGaAs nanowires with higher $x_{v,In}$, the In diffusion length on the surface is estimated at approximately 6 μm. This was determined by taking the square root of the available diffusion area at the height saturation, using equation 8.1. It is noteworthy that the diffusion length is that on the $(\bar{1}\,\bar{1}\,\bar{1})$B GaAs substrate surface. For an estimate of total diffusion length, it would be necessary to add nanowire height. Here, the discussion is limited to the diffusion length difference on $(\bar{1}\,\bar{1}\,\bar{1})$B surfaces, because this alone gives significant insight into height enhancement, tapering and base-shape change.

Figure 8.4b shows the base diameter variation of InGaAs nanowires with a $x_{v,In}$ of 0.23. The base diameter is indicative of the radial growth rate. The base diameter was fairly uniform within each imaged area, although height showed some statistical fluctuation. The base width shows a similar trend to nanowire height with saturation at an available diffusion area of approximately 30 to 40 μm^2. This result again indicates that the main reason for height and tapering enhancement is the incorporation of In species diffusing from substrate surface.

Recent work by Jensen *et al.* investigated the surface diffusion of In species on InAs $(\bar{1}\,\bar{1}\,\bar{1})$B substrates in CBE of InAs nanowires. This showed similar saturation behaviour in nanowire height but at an available diffusion area of approximately 1 μm^2.[241] This is an order of magnitude smaller than the present result. This is expected for two reasons. Firstly, the work of Jensen *et al.* used InAs $(\bar{1}\,\bar{1}\,\bar{1})$B substrates whereas this current work uses GaAs $(\bar{1}\,\bar{1}\,\bar{1})$B substrates. The In diffusion length is believed to be longer on GaAs substrates than on InAs substrates, and also longer on the compressively strained InGaAs layers which might form on GaAs substrates during InGaAs nanowire growth.[242–244] Secondly, CBE uses high vacuum conditions which enhance adatom desorption, so that the diffusion length is typically lower in CBE than in MOCVD.[69] The current estimates of adatom diffusion are consistent with previous studies of MOCVD growth.[245]

8.4 Crystal structure and elemental composition

Figure 8.5a shows a HRTEM image of a nanowire with the catalyst on top of the wire. The nanowires feature a ZB crystal structure together with twin defects. HRTEM also confirmed the growth direction was $[\bar{1}\,\bar{1}\,\bar{1}]$B. Figure 8.5b shows a bright-field TEM image of a typical nanowire. Markers indicate the EDS measurement positions. As observed in the EDS spectra of Figure 8.5c, there is remarkable In/Ga variation along the InGaAs nanowire, with greater In corporation toward the nanowire base. The In/Ga compositional ratio near the tip of the nanowire was 0.27, giving a solid phase In composition of $x_{s,In}$ = 0.21. This value of $x_{s,In}$ is very close to the vapour In composition, $x_{v,In}$, of 0.19. In/Ga compositional variations were measured from several InGaAs nanowires with the same

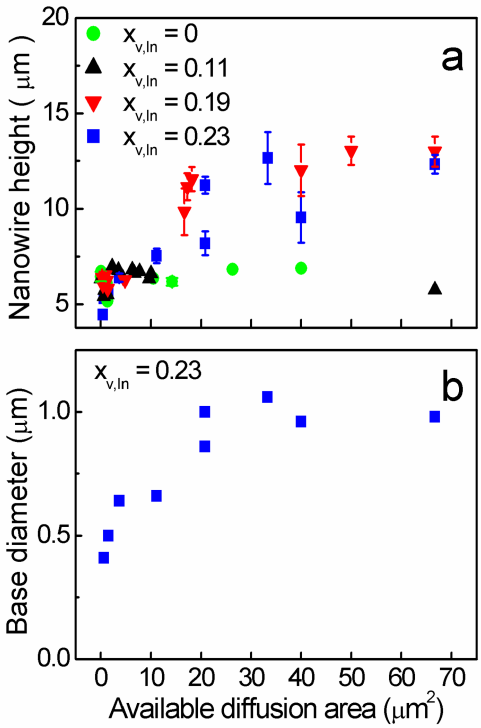

Figure 8.4: (a) Nanowire height versus available diffusion area for InGaAs nanowires with $x_{v,In}$ of 0, 0.11, 0.19 and 0.23. (b) Base diameter versus available diffusion area for InGaAs nanowires with $x_{v,In}$ of 0.23.

$x_{v,In}$ of 0.19. Similar strong In/Ga compositional variations were observed along these nanowires.

These EDS results clearly support the diffusion model introduced previously. This diffusion model would result in a gradual variation in chemical composition along each nanowire, as observed experimentally. In particular, the significant incorporation of diffusing In species into radial growth is believed to give rise to an In-rich shell structure around these tapered nanowires. This would be responsible for the enhanced In content of the nanowire base compared to the tip. Cross-sectional TEM and EDS measurements are currently being performed by collaborators at the University of Queensland, with preliminary results confirming the presence of an In-rich shell which is thickest at the nanowire base.

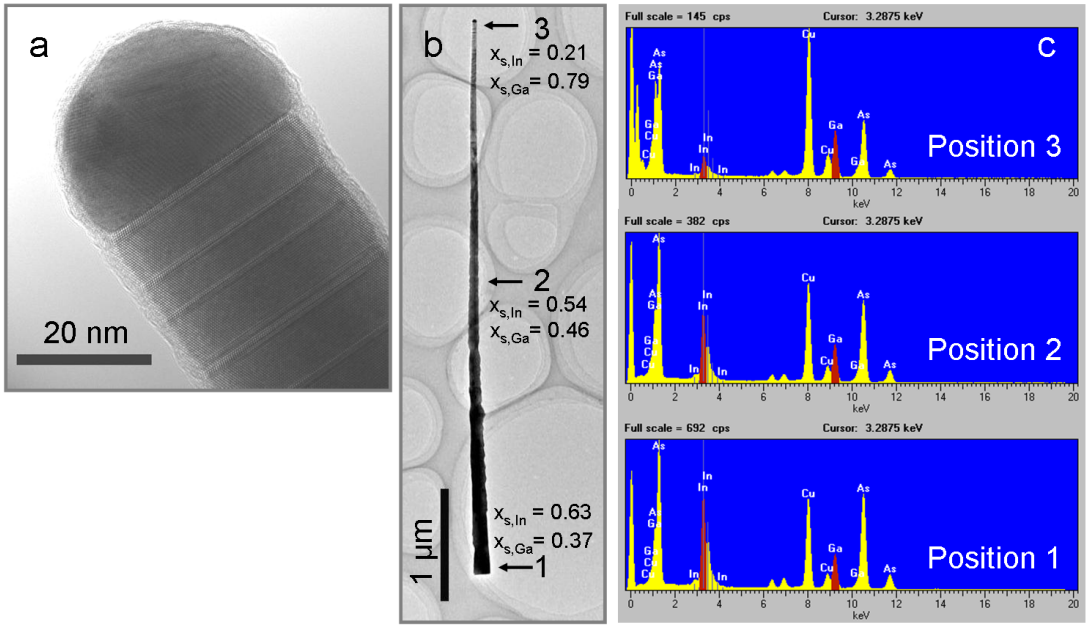

Figure 8.5: (a) HRTEM image of a nanowire ($x_{v,In}$ = 0.19) with the Au catalyst on the top of the nanowire. (b) TEM image of InGaAs nanowire on a holey carbon grid. Markers indicate detection positions for EDS measurements. (c) EDS from various detection positions. From these EDS measurements the solid phase In composition, $x_{s,In}$, and solid phase Ga composition, $x_{s,Ga}$, were determined for each position as displayed in (b).

8.5 Photoluminescence

PL measurements were performed at 10 K using the system described in Section 2.4.1. For each spectrum, the excitation laser was focussed on a particular area of the as-grown sample, to trace PL from regions of high InGaAs nanowire density and regions of low nanowire density. This allowed characterisation of the density-dependent emission energy

shift. Figure 8.6 shows PL spectra of InGaAs nanowires with a $x_{v,In}$ of 0.19 measured at the different positions of the circular pattern. PL intensity is primarily related to nanowire density, with PL peak intensity gradually decreasing as the laser spot is traced from regions of high to low nanowire density. This confirms that the PL in Figure 8.6 arises from nanowires. The broadness of PL spectra is presumably due to a spread in the chemical composition along nanowires, as observed in the EDS analysis of Figure 8.5c.

PL spectra consist of two peaks. As observed in Figure 8.6b, the higher energy PL peak undergoes a red-shift together with a decrease in PL intensity, correlated with the decrease in nanowire density, and the consequent increase in available diffusion area. A higher In composition is generally associated with a red-shift in PL, so the PL results indicate that the average In composition increases with available diffusion area. This is in good agreement with the FESEM observations.

The lower energy PL peak also decreases in intensity, as the photoexcited area is moved from high nanowire density to low nanowire density. It is difficult to draw conclusions from this peak, as the detector sensitivity cuts off dramatically at wavelengths higher than approximately 1.6 μm (0.77 eV). The presence of two peaks suggests that two different compositions may exist in each nanowire. Considering the above discussion of In-rich radial growth, a possible scenario is that the relatively In-rich shell produces the lower energy PL signal and the relatively Ga-rich core is responsible for the higher energy PL peak.

A final possibility is that the low energy PL peak is related to defects. These defects may occur near the base of nanowires, and may be related to the large lattice mismatch between the InGaAs nanowires and underlying GaAs substrate.

Note that two-dimensional growth occurs on the substrate. To test whether the PL arises from this two-dimensional layer, nanowires were removed from the substrates by scraping with a scalpel. FESEM measurements confirmed that the nanowires had been broken at their bases, and had been effectively removed from the substrate. PL measurements were repeated on the same substrates after nanowire removal. These PL measurements gave significantly weaker PL and neither of the two peaks described above were present. It can be concluded with reasonable confidence that the two PL peaks arise from the nanowires.

8.6 Summary

In summary, InGaAs nanowires have been grown successfully by MOCVD. Nanowire density has a strong influence on nanowire height, tapering and base shape. This dependency is attributed to the large difference of diffusion lengths between In and Ga species on the $(\bar{1}\,\bar{1}\,\bar{1})$B GaAs substrate, which determines the degree of In and Ga incorporation

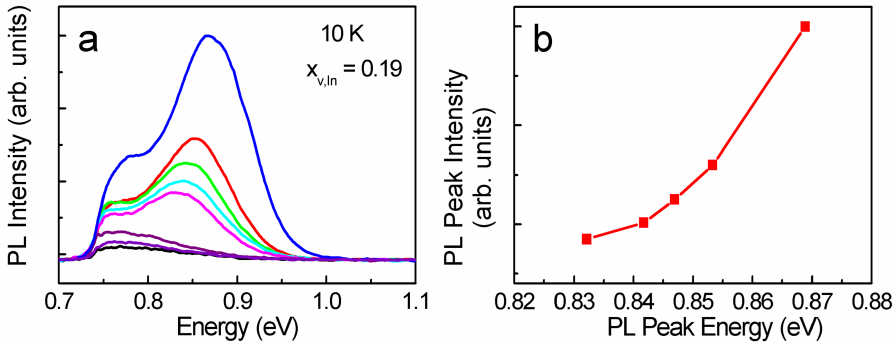

Figure 8.6: Low temperature (10 K) PL measurements of InGaAs nanowires grown with $x_{v,In}$ of 0.19. (a) PL spectra taken from regions of different nanowire densities. The PL intensity is related to nanowire density. A higher intensity corresponds to a higher nanowire density, as confirmed by visual observations and optical microscopy. (b) PL peak intensity as a function of peak energy.

into nanowires. The estimated Ga diffusion length is less than 2 μm whereas the In diffusion length is estimated at approximately 6 μm. Diffusing In species make a significant contribution to radial growth and tapering. EDS analysis of individual InGaAs nanowires shows large In/Ga compositional variation along the nanowire length supporting this diffusion model. With decreasing nanowire density, there was increased In incorporation into nanowires, and this caused a red-shift in the PL peak. These results highlight the difficulty in controlling the composition and uniformity of ternary InGaAs nanowires during MOCVD growth, particularly for nanowires with higher In composition. Similar phenomena would be observed in other ternary nanowire systems with large differences in the diffusion lengths of constituent group III reaction species. Nevertheless, uniform and reliable ternary nanowire synthesis for photonic device fabrication could still be achieved by precise control of inter-nanowire distance. The previous chapters have identified the optimal growth parameters for GaAs and InAs nanowires. It is anticipated that similar principles will apply to InGaAs nanowires, which will deliver significant improvements in InGaAs nanowire growth in future.

CHAPTER 9

Phase perfection in zinc-blende and wurtzite III–V nanowires

9.1 Introduction

Despite significant advances in nanowire growth, the crystallographic quality of nanowires remains difficult to control. The cubic zinc-blende (ZB) phase, which is the stable phase in bulk III–V materials, is not always the dominant phase in nanowires. Instead, nanowires often feature the hexagonal wurtzite (WZ) phase in sections of, or throughout, the nanowire. Twin defects, stacking faults and ZB–WZ polytypism are commonly reported problems. Several studies have demonstrated that these defects adversely impact the optical and electronic properties of III-V nanowires, for instance by reducing the quantum efficiency, carrier lifetime and carrier mobility.[79–81] Device applications demand nanowires with excellent physical properties, and consequently control over the nanowire crystal structure is imperative. On the other hand, controlled twin planes, stacking faults and polytypism offer new possibilities for engineering nanowire band structure, luminescence polarisation and emission energy.[76–78]

Research into controlling nanowire crystal structure has intensified. Several reports address the diameter dependency of nanowire crystal structure, with smaller diameter nanowires tending toward a WZ phase and larger diameter nanowires tending toward a ZB phase.[82–84] Algra *et al.* observed a dramatic transition from a WZ structure to a periodically twinned ZB structure upon the addition of Zn dopants to the InP nanowire growth system.[82] Caroff *et al.* used a combination of nanowire diameter and growth temperature to controllably achieve WZ and periodically twinned ZB nanowires.[83]

The aforementioned methods for controlling crystal phase necessitate a particular choice of nanowire diameter, or the deliberate introduction of dopants. Arguably, nanowire diameter and doping can change nanowire properties as dramatically as the crys-

tallographic phase itself. For device applications, it is desirable to control crystal quality without sacrificing important specifications of diameter and dopant levels. Furthermore, these methods seldom produced truly phase-perfect nanowires free of twin defects and stacking faults.

Fortunately, two basic growth parameters have exhibited potential as means to control crystal phase. These basic parameters are firstly, growth temperature, and secondly, the ratio of the group V precursor flow rate to the group III precursor flow rate, termed the V/III ratio. Increasing the growth temperature is known to promote twin defect formation in GaP[71,246] and GaAs[83] nanowires (see Chapter 4). Increasing the second parameter, V/III ratio, is known to reduce the occurrence of twin defects in GaAs nanowires (see Chapter 5).

In this study, these two basic growth parameters, alone, are used to achieve defect-free III-V nanowires in either perfect WZ or ZB form. This method affords precise control over nanowire crystal structure, without limiting diameter choice or requiring dopant addition. For a given diameter, both WZ and ZB nanowires can be grown without stacking faults or twin defects. Furthermore, to the best of our knowledge, this is the first report of WZ GaAs nanowires by MOCVD, and the first report of twin-free ZB InAs nanowires by any growth method.

9.2 Experiments

InAs nanowires were grown on InAs $(\bar{1}\,\bar{1}\,\bar{1})$B substrates using TMIn as the group III precursor and AsH_3 as the group V precursor. The substrates were treated with poly-L-lysine solution followed by a solution of colloidal Au nanoparticles 50 nm in diameter. Prior to growth, each substrate was annealed in situ at 600 °C under AsH_3 ambient to desorb surface contaminants. After cooling to growth temperature, the AsH_3 flow was adjusted and TMIn was introduced to initiate nanowire growth. The growth time was 30 minutes for each sample. The group III (TMIn) flow rate was 1.2×10^{-5} mol/min for all growths. Growth temperatures between 375 °C and 550 °C were studied. To study V/III ratio, AsH_3 flow rates were chosen between 1.7×10^{-5} and 4.1×10^{-3} mol/min to attain V/III ratios between 1.4 and 370, varying in binary orders of magnitude. InAs nanowires grown under various temperature and V/III conditions were characterised by FESEM and TEM. Adjunct studies using different Au nanoparticle diameters (10, 20, 30 and 100 nm), were performed to demonstrate the applicability of our results to other nanowire diameters.

GaAs nanowires were also grown to demonstrate that the results are also pertinent to III-V materials other than InAs. GaAs nanowires were grown on GaAs $(\bar{1}\,\bar{1}\,\bar{1})$B substrates using TMGa as the group III precursor and AsH_3 as the group V precursor. The

substrates were treated with poly-L-lysine solution followed by a solution of colloidal Au nanoparticles 10, 20, 30, 50 or 100 nm in diameter. Prior to growth, the substrate was annealed in situ at 600 °C under AsH_3 ambient to desorb surface contaminants. After cooling to the desired temperature, TMGa was introduced to initiate nanowire growth by either a single-temperature or two-temperature procedure. Growth temperatures of 425 °C and above were accessed using a single-temperature procedure. This involved 15 minutes of growth at a constant temperature, T_g, between 425 °C and 575 °C. For the two-temperature procedure, growth initiated with a 1 minute "nucleation" step at the nucleation temperature, T_n, of 450 °C. The temperature was then rapidly ramped down to the subsequent growth temperature, T_g, between 375 °C and 400 °C. The total growth time was typically 15 minutes, including the nucleation and cooling steps, and the cooling time was typically between 2.5 and 6.5 minutes. The group III (TMGa) flow rate was 1.2×10^{-5} mol/min for all growths, and AsH_3 flow rates were chosen between 8.4×10^{-6} and 2.1×10^{-3} mol/min to attain V/III ratios between 0.7 and 190, varying in binary orders of magnitude.

TEM investigations were carried out at the Australian National University. To ensure consistency and reproducibility, at least 3 nanowires from each sample were examined in detail. Key growths were duplicated and at least 10 nanowires were examined in such cases. Nanowires were screened for twin defects and stacking faults over their entire length. The composition of the Au nanoparticle was studied by EDX analysis.

Sidewall facets were determined by FESEM and TEM. Using FESEM, the sidewall facets were indexed against the {110} cleavage planes of the substrate. Using TEM, the cross-sections of short (< 500 nm long) sections of nanowire were examined. These cross-sections were imaged along the $[\bar{1}\,\bar{1}\,\bar{1}]/[000\bar{1}]$ zone axis. Full nanowire lengths were also imaged along the $\langle 1\bar{1}0\rangle/\langle 11\bar{2}0\rangle$ and $\langle 112\rangle/\langle 1\bar{1}00\rangle$ zone axes. Sidewall indices were confirmed by indexing these TEM images against their corresponding selected area diffraction patterns (SADP).

9.3 Zinc-blende and wurtzite InAs nanowires

InAs nanowire growth occurred in a limited range of temperatures and V/III ratios, as described in Chapter 7. Nanowire crystal structure was examined throughout this growth window. Figure 9.1 illustrates FESEM images of typical nanowires from key samples. Nanowires generally grew normal to the $(\bar{1}\,\bar{1}\,\bar{1})$B substrate, indicating the nanowires have a $[\bar{1}\,\bar{1}\,\bar{1}]$B or $[000\bar{2}]$ orientation defined by whether they were ZB or WZ respectively.

Figure 9.2 illustrates HRTEM and SADP of InAs nanowires grown at the lower (400 °C), middle (450 °C) and upper (500 °C) temperatures of the growth window. At 400 °C (part a), the nanowires are pure ZB without planar crystallographic defects. The

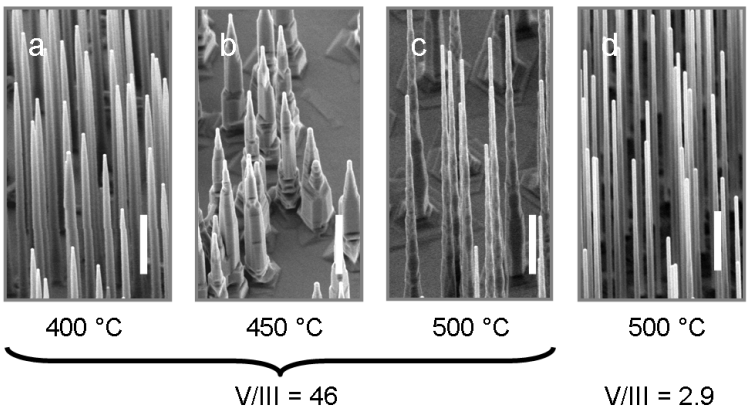

Figure 9.1: FESEM images of key InAs nanowire samples. Nanowires were grown at temperatures between 400 °C and 500 °C, with V/III ratios as indicated. Scale bars are 1μm. Samples are tilted at 40.°

SADP in part e consists of a single set of diffraction spots characteristic of a twin-free ZB crystal. At the higher growth temperature of 450 °C (part b), the nanowires feature a mixture of WZ and ZB segments. The diffraction pattern (part f) is a superposition of WZ and ZB diffraction patterns. Certain ZB diffraction spots appear as doublets, for instance $(00\bar{2})$a and $(\bar{1}\,\bar{1}1)$b. This is indicative of rotational twins (as denoted by a and b) in the $[\bar{1}\,\bar{1}\,\bar{1}]$ growth direction which give superimposed diffraction patterns along the $\langle 1\bar{1}0\rangle$ direction.

At the highest growth temperature, 500 °C, nanowires have a predominantly WZ structure (part c). The diffraction pattern (part g) is characteristic of WZ crystal, and streaks in the [0001] direction indicate the presence of stacking faults along the $(000\bar{1})$ growth plane. HRTEM reveals that thin ZB segments, up to 6 bilayers thick, are also present. Note that the diffraction pattern does not reveal this minority ZB phase due to the high contrast streaks arising from the stacking faults.

Here, it is important to understand the definitions of ZB, WZ, twins and stacking faults. ZB sections follow an ABCABC stacking sequence, whereas WZ sections follow an ABABAB stacking sequence. Each letter represents a bilayer of III-V pairs as described in Chapter 3. In a WZ structure, a stacking fault occurs when a single bilayer is misplaced, locally creating a ZB stacking sequence. For instance, sequence ABAB*C*BCB, growing from left to right, features a faultily placed bilayer at *C*. This creates a minimally thin ZB segment, AB*C*. A twin plane defect occurs when a single bilayer is faultily stacked in a ZB crystal, which reverses the stacking sequence from ABC to CBA. For example, in a section ABCAB*A*CBA, growing from left to right, *A* is the faultily stacked bilayer creating the twin plane. The layer *A* is denoted the "twinned bilayer". This creates

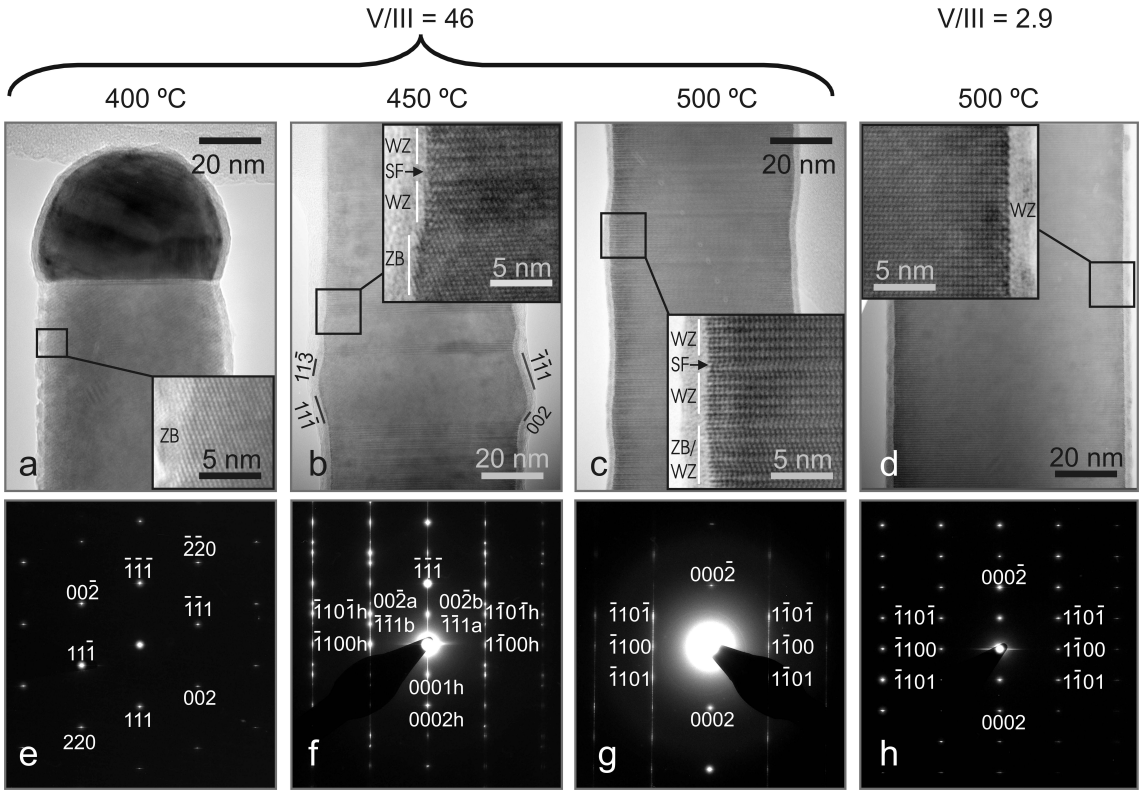

Figure 9.2: TEM results for InAs nanowires. (a-d) HRTEM images of nanowires grown at the indicated temperatures and V/III ratios, and (e-h) their respective SADP. The insets in (a-d) show higher magnification images with ZB and WZ regions, and stacking faults (SF) labelled. The indexed SADP patterns illustrate the nanowires are (e) twin-free ZB, (f) mixed ZB (spots denoted "a" and "b") and WZ (spots denoted "h") with stacking faults and twin defects, (g) WZ with stacking faults and (h) stacking fault-free WZ. From left to right, these nanowires correspond to the FESEM images of Figure 9.1.

a minimally thin WZ segment AB*A*. Sequential twin planes, or equivalently sequential twinned bilayers, create an extended WZ structure. In Figure 9.3a, the proportion of twinned bilayers, as determined from HRTEM images, is quantified for different growth temperatures. As this proportion increases from 0 to 100%, the crystal phase changes from ZB to WZ. The plot clearly illustrates that as growth temperature is increased, the nanowire makes a transition from ZB to WZ.

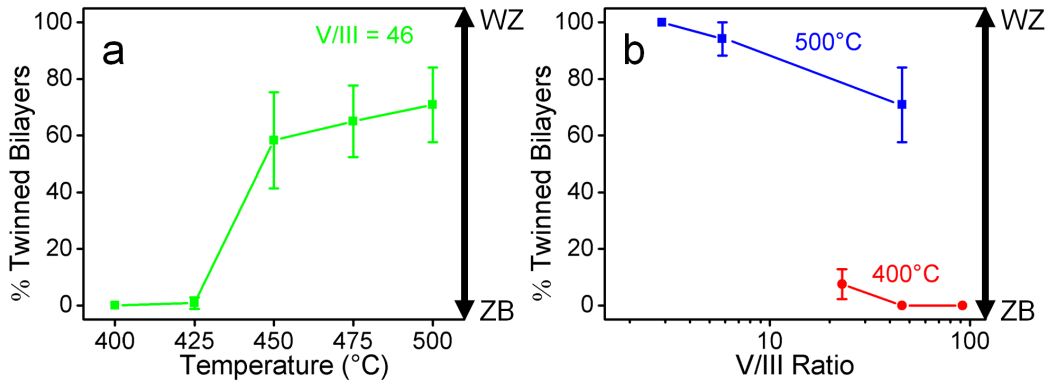

Figure 9.3: Percentage of twinned bilayers. Nanowires were grown at (a) different temperatures and a V/III ratio of 46, and (b) different V/III ratios, with constant growth temperatures of 400 °C and 500 °C. Error bars represent the standard deviation over 10 segments of nanowire, each segment 20 bilayers thick.

Next, V/III ratio is examined, revealing that V/III ratio has a remarkable effect on crystal structure. A high V/III ratio promotes a ZB phase whereas a low V/III ratio promotes a WZ phase. This trend is clear in Figure 9.3b, which plots the proportion of twinned bilayers in nanowires grown at different V/III ratios.

For example, compare the predominantly WZ nanowires of Figure 9.2c and d, with a common growth temperature of 500 °C. The nanowires grown at the higher V/III ratio of 46 (part c) have a high density of stacking faults and some thin ZB sections. The nanowires grown with a significantly lower V/III ratio of 2.9 (part d), in contrast, are pure WZ and free of stacking faults. Clearly, a low V/III ratio reduces stacking faults and promotes a perfect WZ phase. Only a thin, less than 40 nm thick, neck region at the nanowire tip, directly below the nanoparticle, shows any degree of polytypism. The neck region is formed during post-growth cooling,[121] rather than during growth, so it is omitted from the quantitative analyses of Figure 9.3.

By combining a high growth temperature and low V/III ratio, pure WZ nanowires, as in Figure 9.2d, were obtained. These nanowires complement the pure ZB nanowires of Figure 9.2a grown at the low temperature of 400 °C and high V/III ratio of 46. Thus two basic parameters, namely growth temperature and V/III ratio, afford precise control over

the nanowire crystal phase.

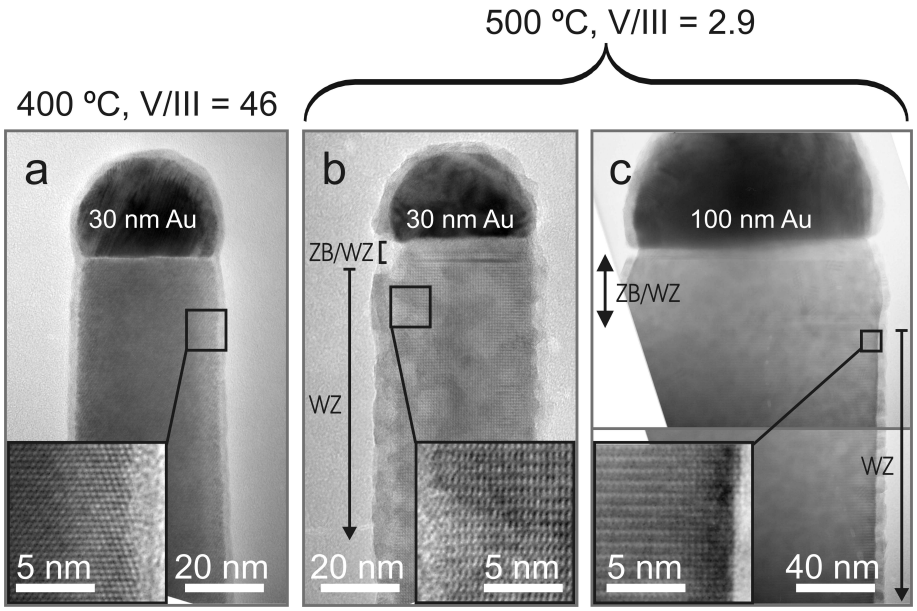

Figure 9.4: HRTEM images of InAs nanowires grown with the indicated Au nanoparticle size, at the indicated temperatures and V/III ratios. The insets show higher magnification images of the pure ZB and WZ regions. The nanowires are (a) pure ZB and (b, c) pure WZ with the exception of the cooling neck region directly below the nanoparticle.

The above discussion has presented results for InAs nanowires catalysed by 50 nm diameter Au nanoparticles. To demonstrate that the same principles apply for other nanowire diameters, InAs nanowires were also grown using Au nanoparticles of diameters between 10 and 100 nm. The size of the Au nanoparticle determines the diameter of the grown nanowire. Figure 9.4 compares HRTEM images of InAs nanowires of different diameters and grown under different conditions. Part a illustrates a narrow diameter pure ZB nanowire, grown with a small 30 nm Au nanoparticle, at a low temperature and high V/III ratio. Parts b and c, respectively, show narrow and wide WZ nanowires obtained with small (30 nm) and large (100 nm) diameter Au nanoparticles. These were grown at high temperature and low V/III ratio, and are pure WZ except for the small neck region. Note that the neck region is formed during cooling,[121] and hence is not representative of nanowire growth. Thus, regardless of nanowire diameter, the same trends were observed: twin-free ZB nanowires were obtained using a low temperature and high V/III ratio, and stacking-fault free WZ nanowires were obtained using a high temperature and low V/III ratio.

9.4 Zinc-blende and wurtzite GaAs nanowires

GaAs nanowires were studied to demonstrate that the results for InAs nanowires translate to other III–V material systems. Chapters 4 and 5 demonstrated that high temperatures and low V/III ratios increase twin density in otherwise purely ZB nanowires. Based on these results, extremely high temperatures (up to 575 °C) and low V/III ratios (down to 0.7) were tested aiming to achieve WZ GaAs. FESEM images of key samples are shown in Figure 9.5. Nanowires generally grew in the $(\bar{1}\,\bar{1}\,\bar{1})$B or $[000\bar{2}]$ direction. The nanowires of part b appear curved because, as the electron beam is scanned across the sample during FESEM imaging, thin nanowires tend to charge and bend towards adjacent nanowires.

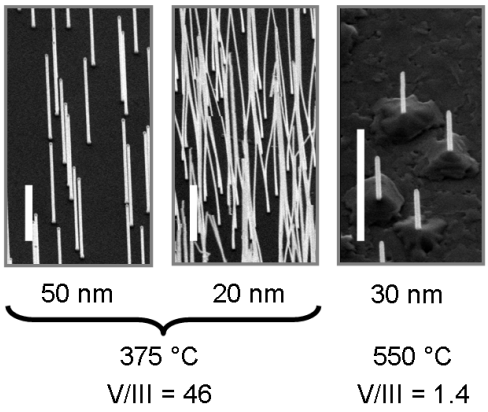

Figure 9.5: FESEM images of key GaAs nanowire samples. Nanowires were grown at temperatures between 375 °C and 575 °C, with V/III ratios as indicated. The nanowires were grown with different Au nanoparticle sizes of (a) 50 nm, (b) 20 nm, and (c) 30 nm. Scale bars are 1μm. Samples are tilted at 40.°

As anticipated, a high temperature (550 °C) and low V/III ratio (1.4) produced stacking-fault free WZ GaAs nanowires. On the other hand, a low temperature (375 °C) and high V/III ratio (46) achieved twin-free ZB GaAs nanowires. Pure ZB and pure WZ GaAs nanowires were achieved over the wide range of nanowire diameters investigated. Figure 9.6 illustrates typical HRTEM images obtained from these GaAs nanowires. In parts a and b, the nanowires are pure ZB. In part c, the nanowire is pure WZ. Thus, the effects of these basic growth parameters on crystal structure are the same for both GaAs and InAs.

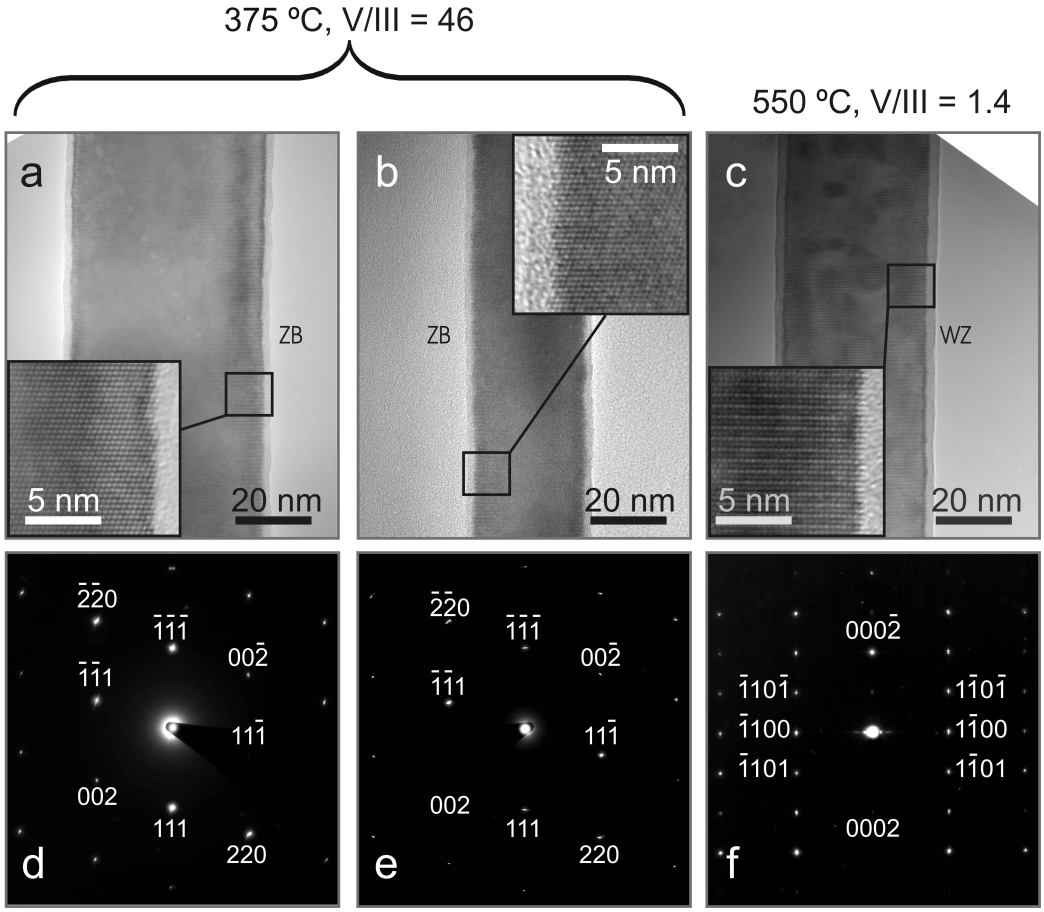

Figure 9.6: TEM results for GaAs nanowires. (a-c) HRTEM images of pure ZB and WZ nanowires, and (d-f) their respective SADP. The insets in (a-c) show higher magnification images of the pure ZB and WZ nanowires. The nanowires were grown with different Au nanoparticle sizes of (a) 50 nm, (b) 20 nm, and (c) 30 nm. From left to right, these nanowires correspond to the FESEM images of Figure 9.5.

9.5 Sidewall facets of zinc-blende and wurtzite InAs nanowires

To develop a physical explanation for the ZB–WZ phase control demonstrated, information is required about the sidewall facets adopted under different growth conditions. Certainly, growth temperature and V/III ratio can have a significant effect on the thermodynamic stability of sidewall facets, as on nanowire crystal phase.[133]

Consistent with previous studies of III–V nanowire faceting, InAs nanowires featured approximately hexagonal cross-sections with six dominant {112}/{1$\bar{1}$00} side-facets (Figure 9.7a, b).[71,72,133,246] The {112} and {1$\bar{1}$00} families are crystallographically parallel. Towards the base of the nanowires, where more significant radial growth has occurred, ZB nanowires frequently have an undulated, or microfacetted appearance as in Figure 9.2. There, alternating {001} and {111}, {111}A and {111}B, or {113} and {111} microfacets comprise overall {112} sidewalls.[133]

The six {112} facets are not all equivalent, and can be subdivided into three {112}A and three {112}B facets.[72,133] The lower surface energy, stable {112}B facets tend to be elongated compared to the {112}A facets (Figure 9.7a), so the nanowire cross-section tends toward a triangular shape rather than a perfect hexagon, as reported previously for GaAs and GaP nanowires.[72,133] This is thought to be a consequence of radial growth: under the high group V overpressure conditions in the growth window, radial growth occurs preferentially on the {112}A facets, which then grow out.[72,133]

For WZ nanowires, the six side-facets are approximately equal in length due to the non-polar nature of {1$\bar{1}$00} surfaces (Figure 9.7b). In a minority of highly tapered WZ nanowires, {11$\bar{2}$0} facets are observed at the nanowire base, although the remainder of the nanowire remains {1$\bar{1}$00}. Figure 9.7d illustrates the facets of such a nanowire. These {11$\bar{2}$0} surfaces are thought to evolve during kinetically limited radial growth on nanowire sidewalls, rather than during axial growth.[3]

9.6 Sidewall facets of zinc-blende and wurtzite GaAs nanowires

All ZB GaAs nanowires examined featured truncated triangular or hexagonal cross-sections with six {11$\bar{2}$} side-facets. At high temperatures, high V/III ratios or low growth rates, radial growth was significant (see Chapters 4, 5 and 6). This radial growth occurred preferentially on {11$\bar{2}$}A facets.[72] Consequently, the three {11$\bar{2}$}B facets were elongated compared to the three {$\bar{1}$ $\bar{1}$2}A facets, and a truncated triangular cross-section was observed.[72] At the lowest temperatures, lowest V/III ratios or rapid growth rates, with minimal radial growth, all six {11$\bar{2}$} facets were of approximately equal length, giving a hexagonal cross-section. This is consistent with the findings of Verheijen *et al.*[133]

The WZ GaAs nanowires featured hexagonal cross-sections with six {1$\bar{1}$00} side-facets of approximately equal length. Figure 9.8 illustrates the characterisation of these

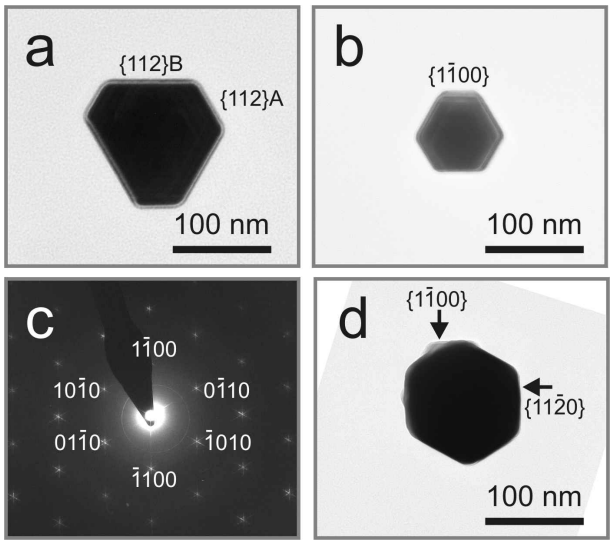

Figure 9.7: Bright field TEM and SADP of nanowire cross-sections taken along the [111] zone axis. (a, b) Mixed ZB/WZ nanowire grown at 450 °C with {112}/{1$\bar{1}$00} facets (c) SADP pattern corresponding to image (b). (d) WZ nanowire grown at 500 °C with {11$\bar{2}$0} facets at the base and {1$\bar{1}$00} facets at the tip.

facets by FESEM.

9.7 Phase and composition of the alloyed Au nanoparticles of InAs and GaAs nanowires

EDX measurements were used to determined post-growth composition of the alloyed Au nanoparticles. For InAs nanowires the post-growth nanoparticles contained only Au and In. The relative intensities of the In and Au peaks were constant, regardless of growth temperature or V/III ratio. This indicates that the post-growth fractions of In and Au are constant, regardless of growth conditions. The nanoparticles were polycrystalline and diffraction patterns showed spots with d-spacings consistent with the γ' phase (Au_7In_3). The polycrystallinity of the nanoparticle, however, makes it difficult to unambiguously index these diffraction patterns. A γ' phase would mean an In composition of approximately 30%, consistent with that determined in previous studies of InAs nanowires.[247,248] Note that after the nanowire growth period, the samples were cooled under AsH_3 ambient, and during this cooling period, In from the nanoparticle was further consumed into the InAs nanowire. The In composition of the nanoparticle during growth, therefore, is expected to be higher than the post-growth In composition determined by TEM and EDX.[121] The observed γ' phase can form by cooling a eutectic Au–In alloy. Therefore, it is probable that during growth the nanoparticle was at, or near, the bulk liquid eutectic composition. The composition, polycrystallinity and hemispherical shape of the nanoparticle, suggest

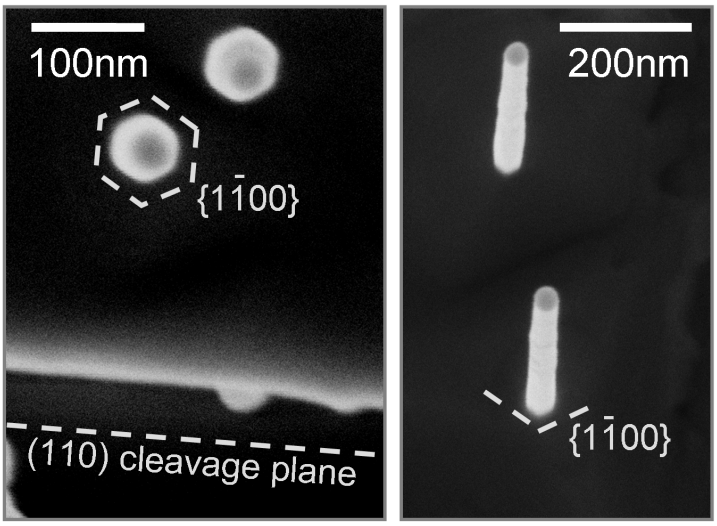

Figure 9.8: FESEM images illustrating the facets of GaAs nanowires. The imaged nanowires correspond to the WZ GaAs nanowires of Figure 9.6c. By indexing the facet edges against the {1$\bar{1}$0} cleavage planes of the substrate, the nanowire facets were determined to be {1$\bar{1}$00}. Image (a) is plan-view with 0° tilt and image (b) was taken with a 5° tilt.

it was liquid during nanowire growth.

For GaAs nanowires, EDS revealed that the post-growth nanoparticles contained only Au and Ga. Similar to InAs nanowire growth, the post-growth fractions of Au and Ga were constant regardless of growth temperature or V/III ratio. The nanoparticles were polycrystalline and the diffraction patterns showed spots with d-spacings consistent with an Au-rich Au–Ga alloy, possibly the β' phase (Au_7Ga_2). Similar to InAs nanowire growth, post-growth cooling under AsH_3 ambient depletes the Au–Ga nanoparticle of Ga, with Ga consumed by the GaAs nanowire neck growth. Therefore, the nanoparticle Ga composition during growth is expected to be higher than the post-growth Ga composition measured by TEM and EDX. As for InAs nanowire growth, these results suggest the nanoparticle was liquid during growth.

Accordingly, the next chapter applies a vapour–liquid–solid mechanism to model GaAs and InAs nanowire growth.

9.8 Summary

In conclusion, simply by tailoring the basic growth parameters of temperature and V/III ratio, pure ZB and pure WZ III–V nanowires were achieved. Thus, complete phase transitions can be achieved without compromising other key nanowire properties, such as diameter and doping. Indeed, the crystal phase could be tightly controlled over a wide range of nanowire diameters. For both narrow and wide nanowire diameters, twin-

free ZB nanowires could be achieved using low temperature and high V/III ratio, and stacking fault-free WZ nanowires could be achieved using the opposite conditions of high temperatures and low V/III ratios.

CHAPTER 10

Theoretical modelling of zinc-blende and wurtzite nanowire growth

10.1 Introduction

Understanding the mechanisms of twin formation, and ZB and WZ phase formation, is crucial for the development of high quality nanowires for device applications. It is a topic of intense research interest. A number of studies indicate that a high supersaturation can promote twin defect nucleation.[60,71,246,249] In effect, the high supersaturation provides enough system energy to overcome the energy barrier for twin formation. Other reports of nanowire[250,251] and bulk systems[221] suggest surface and interfacial tensions drive twin formation. This can be intuitively explained as follows. During nanowire growth, each epitaxial plane nucleates at the three phase contact line where the growing nanowire tip, the Au nanoparticle and the ambient atmosphere meet.[71,132] Accordingly, twin plane nucleation initiates at this triple phase line.[71,132] Several processes take place continuously during nanowire growth: nanowire side facets form, the shape and wettability of the nanoparticle–nanowire interface can change, and the nanoparticle can deform to wet this interface.[71,132,250,252] Fluctuations in mass transport and thermal fluctuations can also occur.[71,253] Consequently, surface and interfacial tensions at the three phase contact line can change dynamically throughout growth. It is possible that twin planes nucleate to relieve these surface and interfacial tensions[250,251], when these tensions exceed critical values.[250,251]

The previous chapters have identified the growth conditions which dictate ZB and WZ growth, and twin formation. Specifically, growth conditions of high V/III ratio and low temperature promoted twin-free ZB growth, whereas growth conditions of low V/III ratio and high temperature promoted twin formation, and even pure WZ growth. In addition, a high growth rate reduced the incidence of twin defects in ZB GaAs nanowires. These

observations alone have given considerable insight into the mechanisms of WZ and ZB nanowire growth and planar defect formation. The aim of this chapter is to enhance this understanding, and support these experimental results, using theoretical modelling of ZB and WZ nanowire growth.

This chapter develops a theoretical model, based on classical nucleation theory, of ZB and WZ nanowire growth. Several studies advocate nucleation theory[71,82,132,221,249] for the study of WZ and ZB formation in nanowire and bulk systems. Glas *et al.*[132] have developed a robust nucleation model which firstly predicts nucleus formation at the vapour–liquid–solid triple-phase boundary, and secondly predicts WZ nanowires at high supersaturation growth conditions. Johansson *et al.*[71,246,249] and Algra *et al.*[82] have developed useful nucleation models to explain the formation of WZ nanowires and periodically twinned ZB nanowires.

The model presented in the chapter builds on these pre-existing models, to describe the effect of temperature and V/III ratio on nanowire crystal structure. Importantly, this theoretical analysis reveals that changes to the surface energy at the nucleus–vapour interface, brought about by changes in growth temperature and V/III ratio, are crucial for the ZB–WZ phase transition.

10.2 Model derivation

This theoretical model builds on pre-existing models[71,82,132,221,249,252] developed by several groups. These have established that III–V nanowires grow by repeated birth and spread of two-dimensional nuclei on the nanoparticle–nanowire interface. That is, once a bilayer nucleus of critical size has formed, bilayer growth propagates over the remainder of the interface. Nucleation occurs at the three phase contact line, where vapour, nanoparticle and nanowire meet,[71,132] as shown in Figure 10.1. Each nucleus is a single bilayer of III–V pairs.

10.2.1 Modelling the Au alloy nanoparticle

According to EDX and TEM analysis, the nanoparticle post-growth is a polycrystalline Au–group III alloy of hemispherical shape, as discussed in detail in Section 9.7. This suggests that during growth, the nanoparticles were liquid. Accordingly, the model is derived for a liquid nanoparticle. The liquid nanoparticle surface makes a contact angle of β with the $(\bar{1}\,\bar{1}\,\bar{1})$B nanowire tip, as shown in Figure 10.1a. The model is, nevertheless, also valid for solid nanoparticles which sinter or distort at the nanoparticle–nanowire interface.[121]

10.2.2 Modelling the nucleus

The nucleus is modelled as illustrated in Figure 10.1. It has average cross-sectional area A, perimeter P, and height $h = a_0\sqrt{3}/3$ (a single bilayer of III–V pairs) where a_0 is the lattice constant. A fraction α of this perimeter is in contact with the vapour, and the remainder of the perimeter is in contact with the liquid nanoparticle.

Each bilayer nucleus creates a new external vapour–nucleus (v–n) facet at the three phase contact line. Each nucleus is named according to its external v–n facet. For instance, a nucleus which forms an external $\{\bar{1}\,\bar{1}1\}$A v–n facet is denoted a "$\{\bar{1}\,\bar{1}1\}$A nucleus". This nomenclature is used to define the nuclei throughout this chapter. The v–n facet makes an angle θ with the vertical, and may be vertical as in Figure 10.1b (e.g. $\{1\bar{1}0\}$, $\{1\bar{1}00\}$ and $\{11\bar{2}0\}$ nuclei), inward-inclined as in Figure 10.1c (e.g. $\{\bar{1}\,\bar{1}\,1\}$A and $\{00\bar{1}\}$ nuclei) or outward-inclined as in Figure 10.1d (e.g. $\{11\bar{1}\}$B and $\{001\}$ nuclei).

The $\{1\bar{1}00\}$ and $\{11\bar{2}0\}$ nuclei form with a twin plane, whereas the other nuclei do not involve a twin plane.

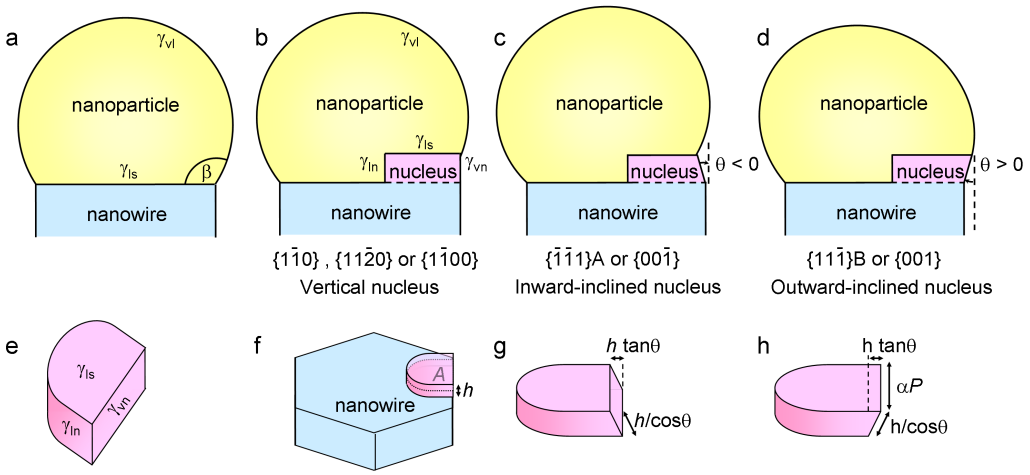

Figure 10.1: Schematic illustrations of the nucleus, liquid nanoparticle and nanowire, indicating key parameters. (a) β is the contact angle of the liquid nanoparticle. (b) γ_{ln}, γ_{vn}, γ_{ls} and γ_{vl} are the energies of the liquid–nucleus sidewall, vapour–nucleus sidewall, liquid–nucleus upper face and vapour–liquid interfaces, respectively. The external nucleus facet is (b) vertical with $\theta = 0$, (c) inward-inclined with $\theta < 0$ and (d) outward-inclined with $\theta > 0$. (e) A nucleus of arbitrary shape, illustrating γ_{ln}, γ_{vn} and γ_{ls}, (f) its geometry on the nanowire tip, with nucleus area A and height h, and the dimensions of (g) inward- and (h) outward-inclined nuclei.

10.2.3 Nucleus formation energy, ΔG

When the nucleus forms, a number of new interfaces are created, as illustrated in Figure 10.1. A vapour–nucleus interface is formed, with areal energy γ_{vn} and area $\alpha Ph/\cos\theta$.

Liquid–nucleus interfaces are formed at the sides of the nucleus. These are modelled as vertical interfaces with areal energy γ_{ln} and area $(1-\alpha)Ph$. The liquid–nanowire interface (areal energy γ_{ls}) is increased or reduced by an area $\alpha Ph\tan\theta$. The formation of the nucleus area A is associated with an areal energy γ_A, which for non-twinned nuclei equals 0, and for twinned nuclei equals γ_{twin}, the twin formation energy. Finally, distortion of the liquid nanoparticle can take place. If θ is positive (Figure 10.1d) the nanowire effectively widens, β decreases, and the droplet is stretched taut.[252] If θ is negative (Figure 10.1c) the nanowire narrows, β increases and the droplet balls up.[252] This distortion creates or removes a portion of vapour–liquid interface, of areal energy γ_{vl} and area B. Including these energy increments, the formation energy of a nucleus is calculated as

$$\Delta G = -\frac{A\Delta\mu}{a} + Ph\left[(1-\alpha)\gamma_{ln} + \alpha\left(\frac{\gamma_{vn}}{\cos\theta} + \gamma_{ls}\tan\theta\right)\right] + A\gamma_A + B\gamma_{vl} \tag{10.1}$$

where $\Delta\mu$ is the change in chemical potential per III–V pair and a is the area per III–V pair on the $(\bar{1}\,\bar{1}\,\bar{1})$B growth interface, with $a = a_0^2\sqrt{3}/2$. Because this is a binary material, calculation of $\Delta\mu$ involves the chemical potentials of both group III (μ_{III}) and group V (μ_V) reactant species, as well as the III–V product (μ_{III-V}). This gives $\Delta\mu = \mu_{III} + \mu_V - \mu_{III-V}$.

The increment in vapour–liquid area, B, will be discussed in Section 10.2.4. It is modelled by equation 10.2:

$$B(\beta) = Ph\alpha\tan\theta\left(\frac{\beta\sin^3\beta - \cos^3\beta + 3\cos\beta - 2}{(\cos\beta - 1)^2}\right) \tag{10.2}$$

where β is the contact angle the liquid nanoparticle surface makes with the $(\bar{1}\,\bar{1}\,\bar{1})$B nanowire tip. Substituting equation 10.2 into equation 10.1 gives

$$\Delta G = -\frac{A\Delta\mu}{a} + Ph\Gamma + A\gamma_A \tag{10.3}$$

where Γ is given by

$$\Gamma = (1-\alpha)\gamma_{ln} + \alpha\left[\frac{\gamma_{vn}}{\cos\theta} + \gamma_{ls}\tan\theta + \gamma_{vl}\tan\theta\left(\frac{\beta\sin^3\beta - \cos^3\beta + 3\cos\beta - 2}{(\cos\beta - 1)^2}\right)\right] \tag{10.4}$$

The term Γ represents the total change in surface and interfacial energy per unit area.

A range of nucleus geometries are possible, including truncated circular, hexagonal or triangular geometries. Nucleus geometries generally follow the relations $A \propto \rho^2$ and $P \propto \rho$ where ρ describes the lateral dimension (e.g. radius or side length) of the nucleus. For an arbitrary nucleus geometry, the perimeter and area can be defined as $P = b\rho$ and $A = c\rho^2/2$, where b and c are constants depending on the geometry of the nucleus. For

instance,

- for a truncated circular nucleus of radius ρ similar to that described by van Enckevort,[254] $A = \rho^2\left(\phi - \frac{1}{2}\sin 2\phi\right)$ and $P = 2\rho\left(\phi + \sin\phi\right)$ where ϕ defines the angle between the liquid–nucleus and vapour–nucleus interfaces.
- for a semicircular nucleus of radius ρ, $A = \frac{\pi}{2}\rho^2$ and $P = (\pi + 2)\,\rho$.
- for a triangular nucleus of side length ρ, $A = \frac{\sqrt{3}}{4}\rho^2$ and $P = 3\rho$.
- for a hexagonal nucleus of side length ρ, $A = \frac{3\sqrt{3}}{2}\rho^2$ and $P = 6\rho$.

The critical nucleus size, ρ^*, is found by differentiating the equation for ΔG, equating to zero and solving:

$$\begin{aligned}\frac{\partial\left(\Delta G\right)}{\partial\rho} &= -c\rho^*\left(\frac{\Delta\mu}{a} - \gamma_A\right) + bh\Gamma \\ &= 0 \\ \therefore \rho^* &= \frac{bh\Gamma}{c\left(\frac{\Delta\mu}{a} - \gamma_A\right)}\end{aligned} \tag{10.5}$$

Accordingly, the formation energy ΔG^*, is given by substituting equation 10.5 into equation 10.3:

$$\Delta G^* = \Delta G|_{\rho^*} = \frac{b^2h^2\Gamma^2}{2c\left(\frac{\Delta\mu}{a} - \gamma_A\right)} \tag{10.6}$$

Therefore, the energy associated with nucleus formation is given by equations 10.7 and 10.8 for nuclei with and without twins, respectively:

$$\Delta G^*_{twin} = \frac{b^2h^2\Gamma^2_{twin}}{2c\left(\frac{\Delta\mu}{a} - \gamma_{twin}\right)} \tag{10.7}$$

$$\Delta G^*_{no\ twin} = \frac{b^2h^2\Gamma^2_{no\ twin}}{2c\frac{\Delta\mu}{a}} \tag{10.8}$$

10.2.4 The increment in vapour–liquid nanoparticle area, *B*

As described above, distortion of the liquid nanoparticle can occur when a nucleus forms at the three phase contact line. This distortion creates or removes a portion of vapour–liquid interface of area B. To calculate this change in area some assumptions and approximations are made, as follows. The liquid nanoparticle is modelled as a truncated sphere. It lies on a cylindrical nanowire of radius r making a contact angle β, as illustrated in Figure 10.2. Throughout growth, the volume of the nanoparticle remains constant, given by

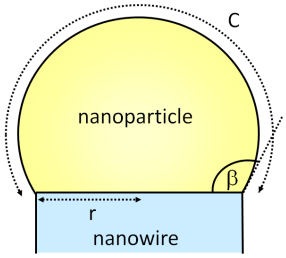

Figure 10.2: Schematic illustration of nanoparticle and nanowire, illustrating the radius r, arc length C and contact angle β.

$$V = \pi r^3 \frac{\cos^3\beta - 3\cos\beta + 2}{3\sin^3\beta} \tag{10.9}$$

Consequently, r and β are interdependent. Rearranging equation 10.9 gives

$$r = \left(\frac{3V}{\pi}\right)^{\frac{1}{3}} \frac{\sin\beta}{(\cos^3\beta - 3\cos\beta + 2)^{\frac{1}{3}}} \tag{10.10}$$

The arc formed at the nanoparticle surface has length given by

$$C = \frac{2\beta r}{\sin\beta} \tag{10.11}$$

When the nucleus forms, r increases by $\Delta r = \frac{1}{2}h\tan\theta$. As a result, at the vapour–liquid–nucleus interface, the droplet contact angle is distorted by $\Delta\beta$, and the arc length between the vapour–liquid–nucleus interface and the opposite side of the nanowire is distorted by ΔC. The increment in droplet surface area is estimated as

$$B = \alpha P \Delta C \tag{10.12}$$

where αP is the perimeter of the nucleus in contact with the triple phase boundary.

To find an expression for ΔC, derivatives of equations 10.10 and 10.11 are taken to give, respectively, equations 10.13 and 10.14 below:

$$\frac{dr}{d\beta} = \frac{-\cos^2\beta + 2\cos\beta - 1}{(\cos^3\beta - 3\cos\beta + 2)^{\frac{4}{3}}} \left(\frac{3V}{\pi}\right)^{\frac{1}{3}} \tag{10.13}$$

$$\frac{dC}{dr} = 2\left(\frac{\beta}{\sin\beta} + r\frac{d\beta}{dr}\frac{\sin\beta - \beta\cos\beta}{\sin^2\beta}\right) \tag{10.14}$$

Then substituting equation 10.13 into equation 10.14 gives

$$\frac{dC}{dr} = 2\frac{\beta\sin^3\beta - \cos^3\beta + 3\cos\beta - 2}{(\cos\beta - 1)^2} \tag{10.15}$$

Therefore

$$\Delta C = \frac{dC}{dr}\Delta r = h\tan\theta\frac{\beta\sin^3\beta - \cos^3\beta + 3\cos\beta - 2}{(\cos\beta - 1)^2} \tag{10.16}$$

Substituting equation 10.16 into equation 10.12 then gives an expression for B

$$B = \alpha Ph\tan\theta\frac{\beta\sin^3\beta - \cos^3\beta + 3\cos\beta - 2}{(\cos\beta - 1)^2} \tag{10.17}$$

This formula is derived for a perfectly cylindrical nanowire, rather than a more realistic nanowire of hexagonal cross-section. Nevertheless, equation 10.17 gives a reasonable approximation for the distortion of the nanoparticle during nanowire growth.

10.2.5 Modelling nucleus side-facets, x

This nucleation model is primarily interested in facets in the vicinity of the nanowire growth front. Note that the faceting behaviour observed experimentally in the previous chapters is partially driven by radial growth. Nevertheless, the previous chapters give an understanding of the possible nucleus facets at the nanoparticle–nanowire interface: the {112}/{1$\bar{1}$00}, {001}, {111} and {113} families. The model also considers other plausible low index facets, namely the {1$\bar{1}$0} and {11$\bar{2}$0} facets, which have been reported for nanowires with significant radial growth, or grown at high temperatures.[3,255]

As described in Section 10.2.2, each nucleus bilayer creates an external v–n facet. The model is restricted to the six low index (singular) v–n facets: {$\bar{1}$ $\bar{1}$ 1}A, {11$\bar{1}$}B, {001}, {1$\bar{1}$0}, {1$\bar{1}$00} and {11$\bar{2}$0}, as listed in Figure 10.1. Thus, each bilayer is assigned a low index external facet, and is named according to its facet, for instance as a {$\bar{1}$ $\bar{1}$ 1}A bilayer. These bilayers are basic building blocks which can be constructed into higher index facets, such as {112} and {113}.[256] Accordingly, {112}A (or B) facets are comprised of a 2:1 ratio of {111}A (or B) and {001} bilayers, and {113}A (or B) facets are composed of alternating {111}A (or B) and {001} bilayers. These facets are illustrated in Figure 10.3. The restriction to low index side-facets prevents any redundancy in the model, yet allows modelling (via construction) of all higher index facets. Moreover, high index facets possess physical and chemical characteristics in between those of their composite low index singular facets,[256] which further justifies this model of only low index facets.

This gives a discrete set of six nuclei, x. In addition, the model takes into account the pre-existing vapour–nanowire side-facet, y, which lies immediately below the nucleating bilayer. This is discussed later in Section 10.2.6.

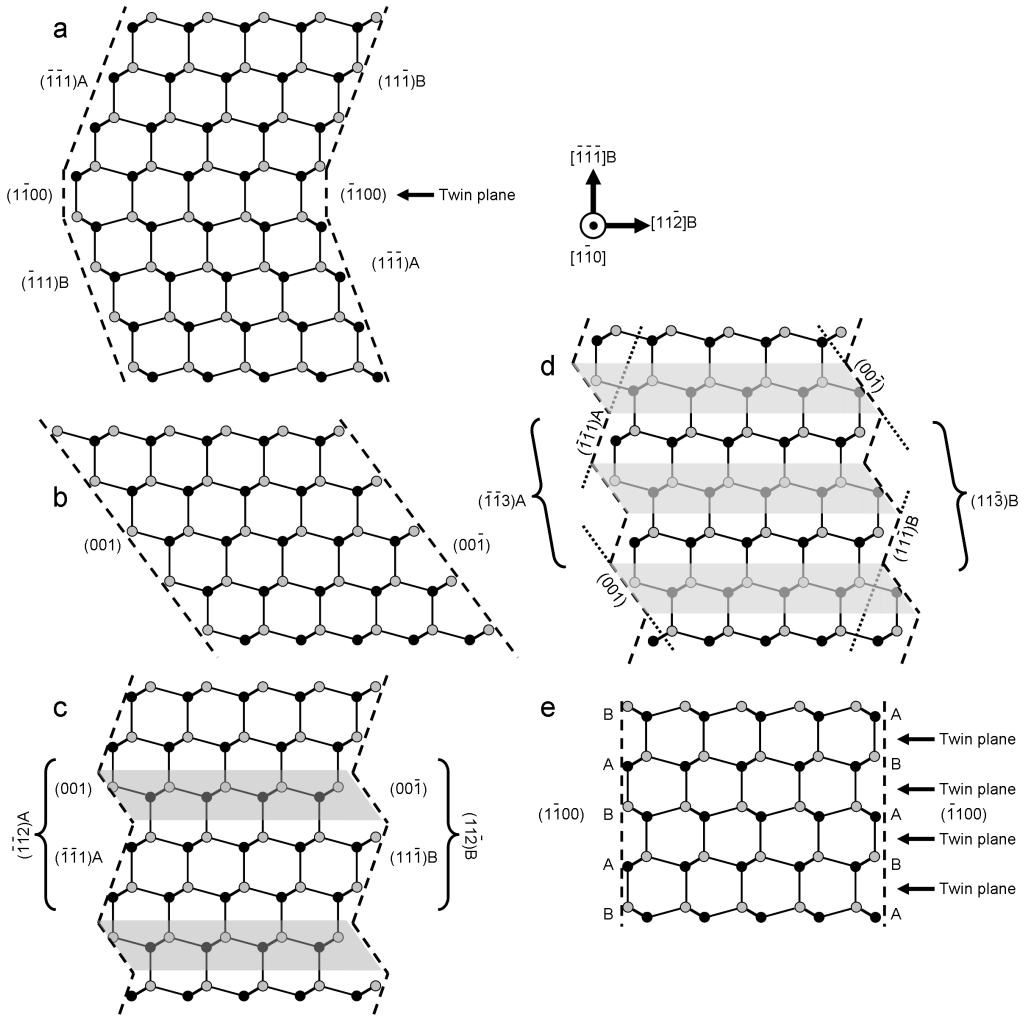

Figure 10.3: Low index (a) {111}A, {111}B, {1$\bar{1}$00} and (b) {001} microfacets. These comprise (c) {112}, and (d) {113} microfacets. (e) Extended {1$\bar{1}$00} facets.

10.2.6 Modelling pre-existing side-facets, *y*

There are three types of pre-existing side-facets, *y*. These are non-equivalent, and are denoted A, B and C. Figures 10.4b and c illustrate y = A, B and C. Pre-existing A side-facets include {112}A, {113}A, {$\bar{1}\,\bar{1}1$}A, {001} and {$1\bar{1}00$}A. Pre-existing B side-facets include {112}B, {113}B, {$11\bar{1}$}B, {$00\bar{1}$} and {$\bar{1}100$}B. Pre-existing C side-facets include {$1\bar{1}0$} and {$11\bar{2}0$}.

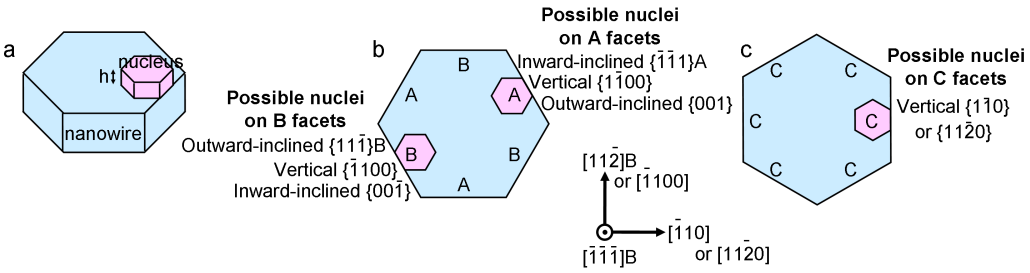

Figure 10.4: Possible nuclei at each type of pre-existing side-facet, exemplified with a hexagonal nucleus. (a) Hexagonal nucleus of bilayer height, *h*. (b) Possible nuclei on pre-existing A and B facets and (c) possible nuclei on pre-existing C facets. The labels A, B and C denote three types of non-equivalent pre-existing side-facets.

Nominally, extended {$1\bar{1}00$} WZ side-facets do not have an A or B face, because every bilayer is twinned such that the overall side-facet is non-polar. However, when considering an individual pre-existing bilayer as a starting point (*y*), there is an 'A' equivalent face and a 'B' equivalent face on the opposite side of the same bilayer. Therefore, the model defines the {$1\bar{1}00$} side-facet of the pre-existing bilayer adjacent to the nucleus, as either 'A' or 'B'. This is illustrated in Figure 10.3, where opposite sides of individual bilayers are labelled A and B.

10.2.7 Possible nuclei, *x*, on pre-existing sidewalls, *y*

Calculations of the probability of a twinned or twin-free nucleus must consider each of the possible pre-existing side-facets, *y*, and all the possible nuclei, *x*, on each of these side-facets.

Figures 10.4b and c illustrate the possible nuclei on each of the non-equivalent pre-existing side-facets, y = A, B and C. For pre-existing A facets, the possible nuclei, *x*, are inward-inclined {$\bar{1}\,\bar{1}1$}A, outward-inclined {001}, and vertical twinned {$1\bar{1}00$} (Figure 10.4b). For pre-existing B facets, the possible nuclei are outward-inclined {$11\bar{1}$}B, inward-inclined {$00\bar{1}$} and vertical twinned {$\bar{1}100$} (Figure 10.4b). For pre-existing C facets, the possible nuclei are both vertical: {$1\bar{1}0$} and twinned {$11\bar{2}0$} (Figure 10.4c).

10.2.8 Probabilities

Following the approach of Johansson *et al.*,[71,249] the nucleation of a facet, x, at the edge of a pre-existing sidewall, y, is governed by an exponential distribution with probability

$$P\left(x|\,y\right) = \frac{\exp\left(-\frac{\Delta G^*_{xy}}{k_B T}\right)}{\sum_i \exp\left(-\frac{\Delta G^*_{iy}}{k_B T}\right)} \tag{10.18}$$

where i represents all possible orientations of nucleating facets, k_B is the Boltzmann constant 1.381×10^{-23} JK^{-1}, T is the growth temperature (K) and G^*_{xy} is the formation energy of nucleus x nucleating at the edge of pre-existing side-facet y.

The probability of a twinned nucleus is then given by

$$P_{twin} = \frac{\exp\left(-\frac{\Delta G^*_{twin}}{k_B T}\right)}{\sum_i \exp\left(-\frac{\Delta G^*_{iy}}{k_B T}\right)} \tag{10.19}$$

Pure ZB growth requires $P_{twin} \to 0$, and pure WZ growth requires $P_{twin} \to 1$.

10.3 Parameters for InAs nanowire growth

The above-described probability model was used to comprehensively study twin formation in InAs nanowires. InAs was chosen because it represents a typical III–V materials system, and is relatively well-characterised.

Calculating the twin formation probability requires knowledge of several parameters: γ_{twin}, γ_{vl}, γ_{ls}, γ_{ln}, γ_{vn} and $\Delta\mu$. Estimates were obtained for these parameters, based on published data for InAs. The twin formation energy, γ_{twin}, takes into account the lattice parameter and ionicity of InAs.[257] This was estimated as approximately half the stacking fault energy,[71] giving $\gamma_{twin} = 0.94$ meV/Å^2.[258] The vapour–liquid surface energy γ_{vl} lies between the surface energies of pure Au and pure In, and depends on the liquid composition.[259] This was modelled as $\gamma_{vl} = 56$ meV/Å^2. At the nanoparticle–nucleus interface, the surface energies γ_{ls} and γ_{ln} were approximated as the surface energy of a $\{\bar{1}\,\bar{1}\,\bar{1}\}$B surface, following Algra *et al.*[82] This gives $\gamma_{ls} = \gamma_{ln} = 36$ meV/Å^2.

Estimating γ_{vn} is more complex. First, γ_{vn} depends on the orientation of the facet, so is different for each type of nucleus. Second, γ_{vn} strongly depends on the surface reconstruction adopted, which in turn depends on the growth conditions. For instance, As-rich surface reconstructions form under growth conditions of high As chemical potential, that is, high μ_{As}. Table 10.1 lists values for γ_{vn}, for each type of nucleus, at both high and low μ_{As} growth conditions.

The chemical potential was estimated as $\Delta\mu = 750$ meV for the MOCVD growth

Table 10.1: External vapour–nucleus facet surface energies of the different nucleating facets, under high and low μ_{As} growth conditions. Twin probability calculations reveal that these high and low μ_{As} growth conditions yield ZB and WZ nanowires, respectively. Surface energies are measured in meV/Å^2. Values are obtained from literature.[232,260–265]

Nucleus facet	{111}A	{111}B	{00$\bar{1}$}	{001}	{110}	{1$\bar{1}$00} with twin	{11$\bar{2}$0} with twin	Resulting crystal structure
θ	-19.5°	19.5°	-35.3°	35.3°	0°	0°	0°	
γ_{vn} at high μ_{As}	42	36	44	44	40	46.5	36	ZB
γ_{vn} at low μ_{As}	46.5	56	54.5	54.5	40	46.5	36	WZ

system, which is the same order as that estimated by Glas *et al.* for MBE nanowire growth.[132] This section presents results for a nucleus of hexagonal shape. Note that the trends presented pertain to all the other nucleus geometries studied, including triangular, semicircular, or truncated circular.[254]

By substituting these estimates into equations 10.4, 10.7, 10.8, 10.18 and 10.19, the probabilities of different nuclei (twinned and twin-free) were calculated.

10.4 Results of the model

10.4.1 Critical nucleus size

In all calculations, the critical nucleus size ρ^* was between 1 and 10 nm. This is smaller than the radius of the nanowire and nanoparticle, which supports the validity of the model.

10.4.2 Effect of contact angle, β

This section individually considers each of the three types of non-equivalent pre-existing side-facets, y = A, B and C. The probability of twin formation is a function of β, and is denoted $P_{twin}(\beta)$.

For a pre-existing C facet, at which vertical nuclei {1$\bar{1}$0} or {11$\bar{2}$0} can form, $\theta = 0$. In this case equation 10.4 simplifies to

$$\Gamma = (1 - \alpha)\,\gamma_{ln} + \alpha\gamma_{vn} \tag{10.20}$$

Thus, for a pre-existing C facet, there is no dependence on β, so $P_{twin}(\beta)$ is constant.

For pre-existing A and B facets, on the other hand, β does influence P_{twin}. This is described qualitatively as follows. On A and B facets, inclined nuclei can form. The formation of an inclined nucleus causes distortion of the nanoparticle, meaning a change in β. The quantity Γ accounts for the amount of distortion. Formation of an outward-inclined nucleus (Figure 10.1d), for example {11$\bar{1}$}B, causes the nanoparticle–nanowire interface to locally expand, the nanoparticle to be pulled taut, and β to decrease.[82] With

continuing nucleation of outward-inclined $\{11\bar{1}\}$B nuclei, β decreases further, until a critical angle β_c where $\Gamma_{\{11\bar{1}\}\mathrm{B}}$ is large and another nucleus is favoured. This nucleus is either an inward-inclined $\{00\bar{1}\}$ nucleus without a twin plane, or a vertical $\{\bar{1}100\}$ nucleus accompanied by a twin plane, which, respectively, relieve the distortion, or prevent further distortion of the nanoparticle. The relative values of $\Gamma_{\{00\bar{1}\}}$ and $\Gamma_{\{\bar{1}100\}}$ determine whether the nucleus is $\{00\bar{1}\}$ or $\{\bar{1}100\}$. On the other hand, inward-inclined nuclei (Figure 10.1c), for example $\{\bar{1}\ \bar{1}\ 1\}$A, cause β to increase,[82] until $\Gamma_{\{\bar{1}\ \bar{1}\ 1\}\mathrm{A}}$ is large and an outward-inclined $\{001\}$ nucleus, or a vertical $\{1\bar{1}00\}$ nucleus accompanied by a twin plane, become more energetically favourable. In short, for pre-existing A and B facets, distortion of the nanoparticle can play an important role in the creation of twin plane defects.

To demonstrate this effect quantitatively, nucleus probabilities were calculated, with respect to β, for both pre-existing A and B side-facets, under both high and low μ_{As} growth conditions. The results are plotted in Figures 10.5 and 10.6, for high and low μ_{As} growth conditions, respectively.

These figures define contact angles $\beta_{c,\mathrm{A}}$ and $\beta_{c,\mathrm{B}}$, at which the probability of $\{\bar{1}\ \bar{1}1\}$A and $\{11\bar{1}\}$B nuclei, respectively, drop to 50%. The probabilities of twinned nuclei, $P(\{1\bar{1}00\}|\mathrm{A})$ or $P(\{\bar{1}100\}|\mathrm{B})$, at $\beta_{c,\mathrm{A}}$ and $\beta_{c,\mathrm{B}}$, are denoted $P_{twin}(\beta_{c,\mathrm{A}})$ and $P_{twin}(\beta_{c,\mathrm{B}})$, respectively. Formation of outward-inclined $\{11\bar{1}\}$B and $\{001\}$ nuclei causes the nanoparticle–nanowire interface to locally expand. The nanoparticle is pulled taut, and β decreases,[82] as indicated by the black arrows in Figures 10.5b and 10.6b, and the blue arrows of Figures 10.5a and 10.6a. Inward-inclined $\{\bar{1}\ \bar{1}1\}$A and $\{00\bar{1}\}$ nuclei cause β to increase,[82] as indicated by the black arrows in Figures 10.5a and 10.6a, and the blue arrows in Figures 10.5b and 10.6b.

10.4.3 Effect of contact angle under high μ_{As} growth conditions

Figure 10.5 illustrates the nucleation scenario for nanowires under high μ_{As} growth conditions. Consider a pre-existing outward-inclined $\{11\bar{1}\}$B facet and the probability plot of Figure 10.5b. With repeated formation of $\{11\bar{1}\}$B facets, the contact angle β decreases until a critical angle $\beta_{c,\mathrm{B}}$, at which further nucleation of $\{11\bar{1}\}$B facets, and the consequent further reduction of β, are energetically costly. Beyond $\beta_{c,\mathrm{B}}$, two other nucleus possibilities become energetically favourable: $\{\bar{1}100\}$ accompanied by twin plane formation, or $\{00\bar{1}\}$ without twin plane formation. The latter, inward-inclined nucleus would increase β to relieve the tautness, as indicated by the blue arrow in Figure 10.5b. Of these two nuclei, one requires twin plane formation and the other does not. In Figure 10.5b, the likelihood of the twinned nucleus, $P_{twin}(\beta_{c,\mathrm{B}})$, is approximately zero.

Figure 10.5a illustrates a typical scenario for original inwards-inclined $\{\bar{1}\ \bar{1}1\}$A facets. Repeated nucleation of $\{\bar{1}\ \bar{1}1\}$A facets causes β to increase until it reaches a critical angle,

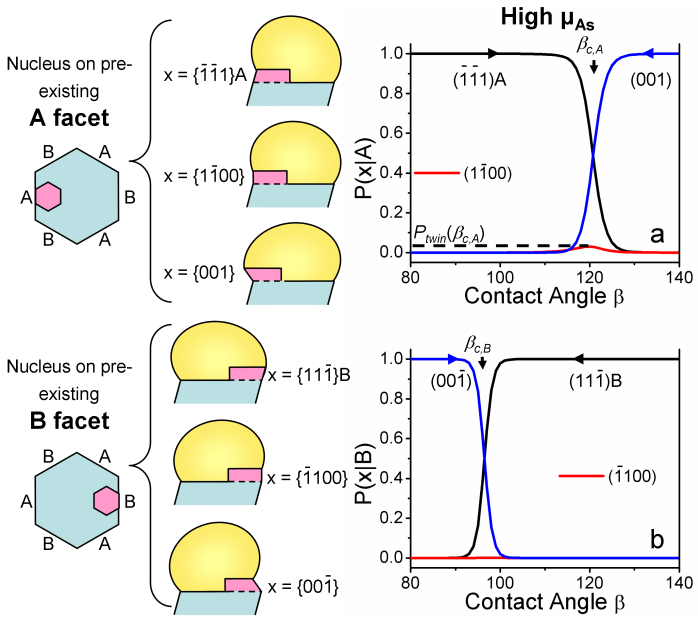

Figure 10.5: The probability of different nuclei according to the model, versus contact angle β. The nuclei, illustrated in pink, are $x = \{\bar{1}\,\bar{1}1\}$A, $\{11\bar{1}\}$B, {001}, $\{00\bar{1}\}$ and $\{1\bar{1}00\}$. (a, b) Typical nucleus probability functions, $P\,(x|\,y)$, expected under high μ_{As} growth conditions, considering pre-existing (a) A and (b) B facets. The arrows indicate the direction of change of contact angle, with the nucleation of nucleus x.

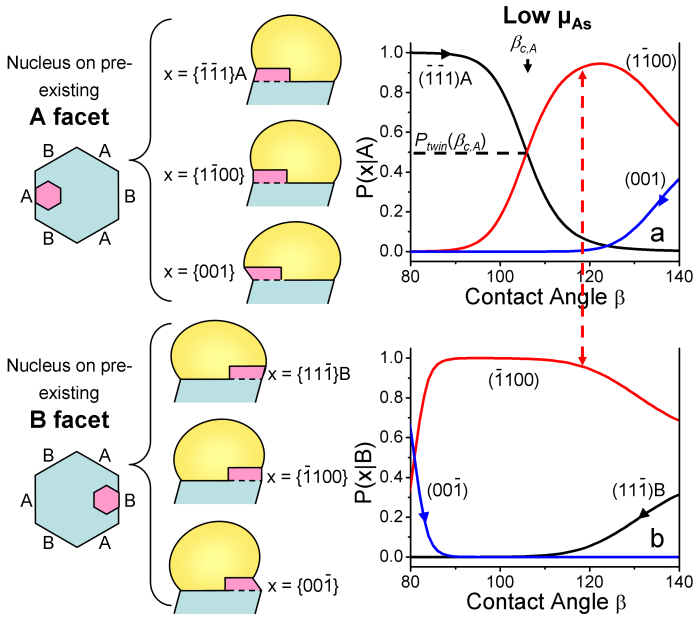

Figure 10.6: The probability of different nuclei according to the model, versus contact angle β. The nuclei, illustrated in pink, are $x = \{\bar{1}\,\bar{1}1\}$A, $\{11\bar{1}\}$B, $\{001\}$, $\{00\bar{1}\}$ and $\{1\bar{1}00\}$. (a, b) Typical nucleus probability functions, $P\,(x|\,y)$, expected under low μ_{As} growth conditions, considering pre-existing (a) A and (b) B facets. The arrows indicate the direction of change of contact angle, with the nucleation of nucleus x. The dashed red line indicates how repeated $\{1\bar{1}00\}$ nucleation, maintaining a constant β, can create a WZ structure.

$\beta_{c,\mathrm{A}}$, beyond which further nucleation of $\{\bar{1}\,\bar{1}1\}$A facets is energetically unfavourable. Vertical or outward-inclined facets become favourable: $\{1\bar{1}00\}$ accompanied by twin plane formation, or {001} without twin plane formation.

The above discussion, in fact, elucidates the requirements for zinc-blende nanowires. For zinc-blende nanowire growth, $\{\bar{1}\,\bar{1}1\}$A, $\{11\bar{1}\}$B, {001} and $\{00\bar{1}\}$ nuclei form in preference to $\{1\bar{1}00\}$ nuclei. Two subtypes of zinc-blende nanowires are twin-free and periodically twinned nanowires. For **twin-free nanowires**, inward- or outward-inclined {001} nuclei form in preference to twinned $\{1\bar{1}00\}$ nuclei at β_c. That is, $P_{twin}\,(\beta_{c,\mathrm{A}})$ and $P_{twin}\,(\beta_{c,\mathrm{B}}) \rightarrow 0$.

For **periodically twinned nanowires**, on the other hand, {001} nuclei are not energetically preferable. Instead, at the critical angle β_c, twinned $\{1\bar{1}00\}$ nuclei are preferable. That is, $P_{twin}\,(\beta_{c,\mathrm{A}}) \rightarrow 0.5$ and/or $P_{twin}\,(\beta_{c,\mathrm{B}}) \rightarrow 0.5$. The evolution of a periodically twinned nanowire is as follows. At A sidewalls, $\{\bar{1}\,\bar{1}1\}$A nuclei form, and as a result, the contact angle β increases.[82] At B sidewalls, $\{11\bar{1}\}$B nuclei form, causing β to decrease.[82] This continues until, at one of the A or B sidewalls, β_c is reached and a twin plane nucleates. After the twin plane, the originally A facets switch to B facets, and vice versa. The process repeats with a twin plane occurring each time β approaches $\beta_{c,\mathrm{A}}$ or $\beta_{c,\mathrm{B}}$, on an A or B facet, respectively.

Thus, the high μ_{As} scenario illustrated in Figure 10.5 would yield zinc-blende nanowires. The low $P_{twin}\,(\beta_{c,\mathrm{A}})$ and $P_{twin}\,(\beta_{c,\mathrm{B}})$ in Figure 10.5, suggest that the nanowires formed under these conditions would have a very low probability of twin formation.

10.4.4 Effect of contact angle under low μ_{As} growth conditions

Figure 10.6 illustrates the nucleation scenario for nanowires under low μ_{As} growth conditions. In this case, $\beta_{c,\mathrm{A}} < \beta_{c,\mathrm{B}}$, the opposite to high μ_{As} growth conditions. For a range of contact angles $\beta_{c,\mathrm{A}} < \beta < \beta_{c,\mathrm{B}}$, $P_{twin} \rightarrow 1$, and $\{1\bar{1}00\}$ nuclei can form in succession, each separated by a twin plane. That is, a wurtzite structure would evolve. Vertical $\{1\bar{1}00\}$ nuclei do not change the contact angle β, as indicated between Figure 10.6a and b by means of a red double arrow. If a non-twinned $\{\bar{1}\,\bar{1}1\}$A (Figure 10.6a) or $\{11\bar{1}\}$B nucleus (Figure 10.6b) forms, this shifts β further within the range $\beta_{c,\mathrm{A}} < \beta < \beta_{c,\mathrm{B}}$, so that $\{1\bar{1}00\}$ nucleation is stable.

Thus, the low μ_{As} scenario illustrated in Figure 10.6 would yield wurtzite nanowires with a very low probability of stacking fault formation.

10.4.5 Effects of vapour–liquid and liquid–solid surface energies, γ_{vl} and γ_{ls}

Our theoretical model revealed that γ_{vl} and γ_{ls} favour certain inclined nuclei. A high γ_{vl} favours outward-inclined nuclei (e.g. $\{11\bar{1}\}$B), which minimise the vapour–liquid interfacial area where γ_{vl} acts. In contrast, a high γ_{ls} favours inward-inclined nuclei (e.g.

$\{\bar{1}\,\bar{1}1\}$A), which minimise the liquid–solid interfacial area where γ_{ls} acts. Consequently, β_c is a decreasing function of γ_{vl} and an increasing function of γ_{ls}.

In addition, $\beta_{c,\mathrm{A}}$ and $\beta_{c,\mathrm{B}}$ converge as γ_{vl} increases, and γ_{ls} decreases. Thus, changes in γ_{ls} and γ_{vl}, can affect the periodicity of periodically twinned nanowires (for which $P_{twin}(\beta_{c,\mathrm{A}}) \rightarrow 0.5$ and/or $P_{twin}(\beta_{c,\mathrm{B}}) \rightarrow 0.5$). If $\beta_{c,\mathrm{A}}$ and $\beta_{c,\mathrm{B}}$ converge, the period of twinned ZB nanowires reduces to one bilayer, which is equivalent to a WZ structure. This is consistent with work by Algra *et al.*,[82] which found that a decrease in γ_{ls} promotes WZ rather than periodically twinned ZB nanowires. Interestingly, γ_{ls} and γ_{vl} have negligible effect on the magnitude of probabilities $P_{twin}(\beta_{c,\mathrm{A}})$ or $P_{twin}(\beta_{c,\mathrm{B}})$. Therefore, changes in γ_{ls} and γ_{vl} can only account for changes in the twin period, but not complete growth transitions from twin-free ZB to pure WZ.

10.4.6 Effect of supersaturation, $\Delta\mu$

The chemical potential, $\Delta\mu$ is a measure of the supersaturation of the growth system, and hence $\Delta\mu$ and supersaturation can be used interchangeably.

According to this theoretical model, the chemical potential, $\Delta\mu$, has a minimal effect on β_c, but a marked effect on P_{twin}, $P_{twin}(\beta_{c,\mathrm{A}})$ and $P_{twin}(\beta_{c,\mathrm{B}})$.

To demonstrate this effect on P_{twin}, consider a simple scenario of a pre-existing C facet, upon which only vertical nuclei, $\{11\bar{2}0\}$ and $\{1\bar{1}0\}$, can form. For these nuclei, there is no β dependency (see equation 10.20). The $\{11\bar{2}0\}$ nucleus requires twin formation whereas the $\{1\bar{1}0\}$ nucleus does not. Figure 10.7 plots the dependence of twin probability, P_{twin}, for the range of $\Delta\mu$ likely to be encountered in the MOCVD growth system.[132]

This plot was calculated using the published value of $\gamma_{vn,\{11\bar{2}0\}} = 36$ meV/Å^2,[263] and arbitrary values of $\gamma_{vn,\{1\bar{1}0\}}$.

The relationship between $\Delta\mu$, growth temperature T, and the flows of group III and group V precursors is given by

$$\Delta\mu = k_B T \ln \frac{C_{In} C_{As}}{C_{In,eq} C_{As,eq}} \tag{10.21}$$

where C_z and $C_{z,eq}$ are the concentrations of reactant z during growth and at equilibrium with the InAs crystal, respectively. Group III species are expected to be supplied from the Au–group III alloy nanoparticle, so C_{In} and $C_{In,eq}$ refer to the In concentrations in the alloy. Group V species, on the other hand, have very low solubility in Au, and are expected to be supplied to the growth interface from the vapour phase, so C_{As} and $C_{As,eq}$ refer to the vapour phase As concentrations.

In Figure 10.7, the top axes plot the ratio of growth and equilibrium concentrations, corresponding to the $\Delta\mu$ on the bottom axis, for T of 400 °C and 500 °C, according to

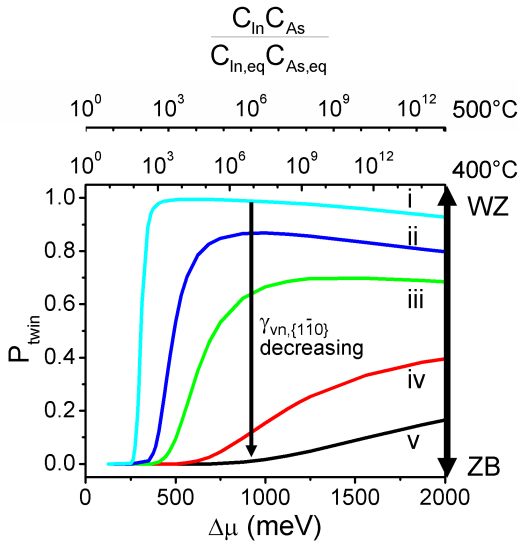

Figure 10.7: Twin probability, P_{twin}, within the range of supersaturation, $\Delta\mu$, relevant to the MOCVD growth system, as calculated by the model. This plot considers only vertical $\{11\bar{2}0\}$ and $\{1\bar{1}0\}$ nuclei. P_{twin} is calculated assuming $\gamma_{vn,\{11\bar{2}0\}} = 36$ meV/Å^2, its published value,[263] and arbitrary values of $\gamma_{vn,\{1\bar{1}0\}}$: (i) 48, (ii) 42, (iii) 40, (iv) 36 and (v) 32 meV/Å^2.

relationship 10.21.

Note that temperature, T, also directly features in equations 10.18 and 10.19, but, between 400 °C and 500 °C this term has a negligible effect on the shape of the P_{twin} curves of Figure 10.7. Therefore, the use of multiple axes for different temperatures, 400 °C and 500 °C, in Figure 10.7 is valid. As illustrated in Figure 10.7, at very low $\Delta\mu$, twin formation is not energetically favourable. The probability P_{twin} increases with $\Delta\mu$, to a maximum that depends on the relative γ_{vn} the twinned and twin-free nuclei. At very high chemical potentials, not considered relevant to our growth conditions, P_{twin} converges to 0.5, regardless of γ_{vn}.

Figure 10.7 indicates that twin nucleation, and consequently a majority proportion of WZ phase, are possible under certain growth conditions. First, Γ_{twin} for the twinned $\{11\bar{2}0\}$ nucleus must be less than $\Gamma_{no\ twin}$ for the non-twinned $\{1\bar{1}0\}$ nucleus. This means the v–n energy of WZ nucleus, $\gamma_{vn,\{11\bar{2}0\}}$, must be lower than that of the ZB nucleus, $\gamma_{vn,\{1\bar{1}0\}}$, as for curves (i), (ii) and (iii). Second, the chemical potential, $\Delta\mu$, must be moderately high. This discussion has considered vertical nuclei (pre-existing C facets), for simplicity. For inclined nuclei (pre-existing A and B facets), the results are analogous: $\Delta\mu$ must be moderately high for twin formation to occur at the critical angle β_c.

10.4.7 Effect of vapour–nucleus surface energy, γ_{vn}

The vapour–nucleus surface energy, γ_{vn}, appears to play a very significant role in the ZB to WZ growth transition. Put simply, a facet with a lower γ_{vn} is generally more favourable than a facet with a higher γ_{vn}.

As discussed in Section 10.3, γ_{vn} is highly dependent upon μ_{As}. In Section 10.4.3, when modelling high μ_{As} growth conditions, $\gamma_{vn,\{\bar{1}\,\bar{1}1\}\mathrm{A}}$, $\gamma_{vn,\{11\bar{1}\}\mathrm{B}}$ and $\gamma_{vn,\{001\}}$ assumed low values. This yielded ZB nanowires with very low twin density. In contrast, in Section 10.4.4, when modelling low μ_{As} growth conditions, $\gamma_{vn,\{\bar{1}\,\bar{1}1\}\mathrm{A}}$, $\gamma_{vn,\{11\bar{1}\}\mathrm{B}}$ and $\gamma_{vn,\{001\}}$ assumed higher values. This yielded WZ nanowires with very low stacking fault density. This indicates that γ_{vn} alone can dictate whether growth is ZB or WZ.

10.5 Relationship between theoretical and experimental results

This section focuses on how growth conditions affect the parameters in equations 10.7 and 10.8, and consequently affect the probability of twin nucleation, which in turn determines the experimentally observed ZB to WZ growth transition.

10.5.1 Growth parameters and supersaturation

First, consider the effect of $\Delta\mu$, and how it is influenced by temperature, V/III ratio and growth rate. According to equation 10.21, an increase in growth temperature, T, increases $\Delta\mu$. This in turn can promote WZ growth, as discussed for Figure 10.7. The experimental results for growth temperature are superficially consistent with this theoretical prediction, and that of Johansson *et al.*: twin defects and WZ growth occur selectively under high temperature, high supersaturation conditions.[71,246,249]

Yet, according to equation 10.21, a high group V flow rate, that is, a high C_{As}, should also increase $\Delta\mu$, and thereby promote a WZ phase. Intriguingly, our experimental results, as discussed earlier, show the exact opposite behaviour: a high V/III ratio promotes a ZB phase. Moreover, Chapter 6 revealed that twin density decreased with a higher growth rate, that is, a higher supersaturation. Clearly, supersaturation alone cannot account for the experimental observations.

10.5.2 Growth parameters, and vapour–liquid and liquid–solid surface energies

Next consider changes in γ_{vl} and γ_{ls} that might occur with changes in growth parameters, and their potential effect on ZB and WZ growth.

Firstly, growth temperature can affect the surface energy of the liquid Au nanoparticle. Higher temperatures are expected to reduce both γ_{vl} and γ_{ls}.[266]

Excess As and Ga species are also believed to change γ_{vl} and γ_{ls}. A high V/III ratio creates an abundance of As species. Increasing both group V and group III flows simultaneously, as in Chapter 6, increases growth rate and creates an abundance of both

As and Ga species.

Arsenic species, with their very low solubility in gold,[113,114] are thought to act as surfactants[267]. For example, when the As species $AsCl_3$ is added during Au-assisted VLS growth of Ge wires, the $AsCl_3$ acts as a surfactant on the Au droplet surface. Thus it decreases both the vapour–liquid and liquid–solid surface energies in the Au droplet–Ge wire system.[253] Furthermore, in melt growth of bulk GaAs material, the addition of excess arsenic is known to lower the surface tension of the melt, and thus suppresses twinning.[221] Arsenic surfactant layers have also been utilised in the epitaxial growth of island-free Si/Ge heterostructures.[267]

Therefore, it is expected that when adsorbed on the Au nanoparticle surface, arsenic species can significatly reduce γ_{vl}. Adsorbed arsenic surfactants on the Au nanoparticle–nanowire interface may also reduce γ_{ls}, but this effect is expected to be less significant due to the rapid consumption of any arsenic surfactant species present at this growth interface, into new nanowire growth.

Gallium, on the other hand, dissolves into the nanoparticle to make it more Ga-rich. Ga has lower surface and interfacial energies than pure Au,[268] so it is expected that a higher Ga concentration would reduce the nanoparticle surface and interfacial tensions, γ_{vl} and γ_{ls}.[132,269] Thus, both excess As and excess Ga species act to reduce surface and interface tensions throughout growth.

Clearly, growth conditions can affect γ_{ls} and γ_{vl}. However, as discussed in Section 10.4.5, γ_{ls} and γ_{vl} merely affect the twin period. These parameters do not change P_{twin} significantly, and hence cannot account for a complete transition from twin-free ZB to pure WZ. This suggests that changes to γ_{ls} or γ_{vl} occuring with temperature, V/III ratio or growth rate, are not the critical factors determining ZB or WZ growth.

10.5.3 Growth parameters and vapour–nucleus surface energy

The model suggests that the critical factor, determining ZB and WZ phase perfection, is the change in γ_{vn} that occurs with temperature and V/III ratio. For many III–V semiconductors, surface energies can change markedly with temperature and V/III ratio.[232,260–262,264,265,270] The surface energy is closely related to the surface reconstruction adopted under the growth conditions. Surface reconstructions consist of a discrete arrangement of surface atoms, into unit cells which periodically repeat over the surface. For instance, under high As overpressure, $\{11\bar{1}\}$B surfaces can form an As trimer reconstruction.[232]

For ZB structures, the surface reconstruction and surface energy of $\{1\bar{1}0\}$, $\{\bar{1}\,\bar{1}1\}$A, $\{11\bar{1}\}$B, and {001} surfaces, can depend strongly on As overpressure, that is, the V/III ratio.[264,270] At higher As flow rates, these surfaces adsorb As atoms onto the surface, to

form energetically favourable surface reconstructions, such as the As trimers mentioned above. Surfaces composed of these low index planes, namely {112} and {113} surfaces, also form low energy surface reconstructions under As-rich conditions.[271,272] These low energy As-stabilised surfaces are also stable at low temperature, where As desorption is minimal.[260,261] In contrast, at low V/III ratios where As coverage is not possible, and at high temperatures where As desorption is significant, these surface reconstructions cannot form and a higher energy surface reconstruction is adopted.

Wurtzite crystal surfaces, $\{11\bar{2}0\}$ and $\{1\bar{1}00\}$, show very different surface behaviour to their ZB counterparts. These WZ surfaces are not believed to form low energy surface reconstructions under high As pressure.[265] The $\{11\bar{2}0\}$ surfaces are unlikely to reconstruct or change surface energy significantly with growth conditions.[263,265] It is possible that $\{1\bar{1}00\}$ surfaces form low energy surface reconstructions under In-rich conditions, similar to GaN $\{1\bar{1}00\}$ surfaces under Ga-rich conditions.[265] These In-rich conditions, that is, high μ_{In} conditions, occur at high growth temperature and low V/III ratio. Under these conditions, In species can readily diffuse from the substrate and along the nanowire sidewalls for incorporation into the alloy nanoparticle, which increases μ_{In}.

The discussion above illustrates a trend, where the γ_{vn} of ZB nuclei ($\{\bar{1}\,\bar{1}1\}$A, $\{11\bar{1}\}$B, $\{001\}$ and $\{1\bar{1}0\}$) are lowest under conditions of high As coverage, that is, high μ_{As}. These conditions correspond to a high V/III ratio, to give excess of As species, and a low growth temperature, to prevent desorption of As species from the surface. The low γ_{vn} of ZB nuclei at low temperature and high V/III ratio, allows the formation of perfect twin-free nanowires. Rather than a twinned $\{1\bar{1}00\}$ nucleus forming in response to nanoparticle deformation, a twin-free $\{001\}$ nucleus, with low γ_{vn}, can form.

On the other hand, under low μ_{As} growth conditions, WZ nuclei ($\{11\bar{2}0\}$ or $\{1\bar{1}00\}$) are likely to have lower γ_{vn} than their ZB counterparts. Low μ_{As} conditions correspond to lower V/III ratios and higher temperatures, at which As species are limited and As desorption from the substrate is significant. Indeed, modelling, within the range of possible γ_{vn} (Table 10.1), reveals that changes in γ_{vn} are largely responsible for ZB and WZ phase formation.

In summary, a low temperature and high V/III ratio lower the γ_{vn} of ZB nuclei to favour ZB nucleation. Conversely, a high temperature and low V/III ratio raise the γ_{vn} of ZB nuclei to favour WZ nucleation with twin formation. This accounts for the observations in Chapter 9 for GaAs and InAs nanowires, where a low temperature and high V/III ratio achieved twin-free ZB nanowires, and a high temperature and low V/III ratio achieved stacking fault-free WZ nanowires. It also explains the results of Chapters 4 and Chapter 5, in which a decrease in temperature, and an increase in V/III ratio, respectively, reduce the twin density in GaAs nanowires.

10.6 Model limitations and suggested future improvements

The model cannot yet account for surface and internal stresses in the nanowire crystal,[273–275] line tension,[276] fluctuations in mass transport and thermal fluctuations.[71,253] Note that, for vapour–liquid and liquid–liquid interfaces, surface stress and surface free energy are same quantity. In a liquid, excess surface stress immediately disappears because extra atoms migrate freely to, or away from the surface.[275] In contrast, for a liquid–solid or vapour–solid interface, surface stress and surface energy are distinct and very different quantities.[273–275]

The role of surface stresses is explained as follows. The contact angle β made by the Au nanoparticle should obey the Young relation:

$$0 = \gamma_{ls} + \gamma_{vs} \sin\theta + \gamma_{lv} \cos\beta \tag{10.22}$$

For a given γ_{ls}, γ_{vs}, γ_{lv} and θ, equation 10.22 is only satisfied for discrete values of β. At other values of β, an unbalanced force, F, will result:

$$F = \gamma_{ls} + \gamma_{vs} \sin\theta + \gamma_{lv} \cos\beta \tag{10.23}$$

Surface stress must work to balance forces in all directions, otherwise the unbalanced force will cause the Au nanoparticle to migrate.[277,278] These stresses exist at the vapour–nanowire or Au nanoparticle–nanowire interface. These surface stresses create internal stresses within the nanowire. Positive surface stress creates tensile stresses in the nanowire, whereas negative surface stress creates compressive stresses. The theoretical model does not yet account for these surface and internal stresses. With further development of the model, these stresses will be taken into accout.

The model has not yet been applied to investigate "compensating" twins observed in ZB GaAs nanowires: in GaAs nanowire growth, twin planes generally form in discrete pairs. The first twin plane rotates the crystal lattice 60° about the $[\bar{1}\,\bar{1}\,\bar{1}]$B axis. The second twin plane forms in close succession. This latter twin plane rotates the crystal back 60°, thereby compensating for the original twin plane. Future modelling studies will examine the formation of the second compensating twin.

In addition, equations 10.18 and 10.19 can be made more accurate by incorporating the Zeldovich coefficients.[279]

The final limitation is found when describing the growth rate dependence of GaAs nanowire growth, as studied in Chapter 6. At present, this is not adequately described by the theoretical model, firstly because it is unclear how growth rate affects μ_{As}, and consequently γ_{vn}. Secondly, the mechanism may involve thermal and mass transport fluctuations which occur unpredictably during growth, or the internal stresses described

above. Two possible explanations for this unexpected result are outlined below.

10.6.1 Possible mechanism based on surface and interface tensions

Unlike the current model, future modelling, which will take into account surface stresses, may reveal that γ_{vl} and γ_{ls} can indeed influence P_{twin}. The mechanism proposed here suggests that γ_{vl} and γ_{ls} influence P_{twin}.

The experimental studies found that twin density decreased when AsH_3 and TMGa flows were simultaneously increased (see Figure 6.4c) to achieve a high growth rate. Under these growth conditions, there is an abundance of As and Ga precursor species. As detailed in Section 10.5.2, As and Ga species act to reduce γ_{vl} and γ_{ls}. This may then decrease P_{twin}. This may be responsible for the observed reduction in twin defects when As and Ga precursor flow rates are high.

The experiments also showed that if the AsH_3 flow rate was held constant, increasing the TMGa flow rate neither consistently promoted nor consistently hindered twin formation (see Figure 6.4d). This suggests there are two opposing mechanisms which contribute to this result. At higher group III flows, the high supersaturation and rapid growth rate may indeed promote twin formation.[71,132,175,221,223] In opposition, the abundance of Ga species would decrease γ_{vl} and γ_{ls} of the nanoparticle–nanowire system, and hence decrease P_{twin}. According to this explanation, increasing TMGa flow alone is not sufficient to prevent twin formation. The AsH_3 flow must also be scaled up, to reduce γ_{vl} and thus significantly reduce twin density.

10.6.2 Possible mechanism based on random fluctuations

This mechanism proposes that a fluctuation perturbs the Au nanoparticle, and this drives twin formation. The fluctation event is random, and the number of such incidents occurring in a given time interval, t_g, obeys a Poisson distribution. The probability of k occurrences is given by

$$f(k, \lambda) = \frac{\lambda^k e^{-\lambda}}{k!} \tag{10.24}$$

where λ is the expected number of occurrences that occur during time interval t_g.

Nanowires grown with a faster growth rate, are grown for a shorter time, t_g. This means that fewer fluctuation events will occur during nanowire growth. Nanowires grown at a slower growth rate for a longer time experience more fluctuation events, and hence feature a higher density of twin defects. This explanation fits well with the data in Figure 6.4c, which show an almost linear decrease in twin density with decreasing growth time.

Figure 6.4d shows that increasing TMGa flow, but not AsH_3 flow, does not consis-

tently increase or decrease twin formation. Two opposing mechanisms would cause this result. On the one hand, the shorter growth time means fewer twin defects. On the other hand, raising the TMGa flow consumes more AsH_3, and thus decreases the amount of excess As species. Depletion of As species would raise the γ_{vn} of ZB nuclei, and hence promote twin formation.

10.7 Summary

This model of nanowire nucleation has established that the orientation and surface energy of the external vapour–nucleus facet plays a significant role in twin formation. Changes to the vapour–nucleus surface energy, which occur with changes in growth conditions, are critical for achieving phase purity. Low temperatures and high V/III ratios create As-rich growth conditions. Under such growth conditions, ZB surfaces can form low energy surface reconstructions, making the nucleation and growth of ZB nanowires more energetically favourable. The low temperature also creates a low supersaturation growth condition, which further hinders twin formation. Consequently, low temperatures and high V/III ratios produce twin-free ZB nanowires, as observed experimentally. In direct contrast, high temperatures and low V/III ratios, produce As-poor growth conditions under which ZB surfaces are less stable. This makes WZ nanowires more favourable. In agreement with the model, growth experiments found that high temperatures and low V/III ratios achieved perfect, stacking fault-free WZ nanowires.

This model can also be extended to other Au-assisted nanowire growth systems, such as MBE and CBE. In these systems, growth takes place under high vacuum conditions. These high vacuum conditions tend to increase the desorption of As species.[280]. According to the nucleation model presented here, this would promote twin formation. In agreement, CBE- and MBE-grown nanowires typically exhibit WZ structure,[132] whereas MOCVD-grown nanowires are more frequently ZB.[72]

Although the current model has limitations, it has proved useful in predicting the twin formation, and ZB and WZ growth. In future, the model will be extended to take into account other growth factors, including growth fluctuations and surface stress.

CHAPTER 11

Conclusion

11.1 Outcomes

Clearly, Au-assisted growth of III–V nanowires by MOCVD is a very viable fabrication technique, which will propel the development of future nanowire-based electronic and optoelectronic devices. This dissertation has investigated the Au-assisted growth of GaAs, InAs and InGaAs nanowires, and how growth parameters can be controlled to achieve exceptionally high quality nanowires suitable for device applications.

Firstly, the growth of GaAs nanowires was studied. The properties of these MOCVD-grown nanowires were highly sensitive to growth temperature, with higher temperatures inducing significant nanowire tapering and lower temperatures producing irregular kinked nanowire growth. To overcome these problems, a two-temperature growth procedure was developed. This consisted of a brief initial high-temperature nucleation step followed by a prolonged growth step at lower temperature. The nucleation step was necessary for the epitaxial nucleation and growth of straight, vertically-aligned nanowires on the (111)B GaAs substrate. The lower temperature employed for subsequent growth imparts superior nanowire morphology and crystallographic quality by minimising radial growth to produce effectively untapered nanowires. The success of the two-temperature procedure points to two possible growth phenomena: sensitivity of the Au nanoparticle–GaAs interface conditions to temperature, and melting–solidification temperature hysteresis of the Au–Ga nanoparticle alloy.

The two-temperature procedure holds further advantages. It eliminated twin defects from these ZB nanowires and these nanowires exhibited strong PL even at room temperature. Low temperature PL measurements revealed these nanowires have minimal carbon impurity incorporation and very long, almost intrinsic exciton lifetimes approaching 1.1 ns. High electron mobility can be expected in these twin-free, high purity nanowires.[81] This represents a significant advance in achieving nanowires with high material quality

suitable for high speed optoelectronic devices.

The input V/III ratio was found to have a significant effect on GaAs nanowire growth. A high V/III ratio dramatically reduced planar crystallographic defects and reduced intrinsic carbon dopant incorporation. Increasing V/III ratio further, however, instigated severe nanowire kinking, increased nanowire tapering and reduced the exciton lifetime. As a compromise, an intermediate V/III ratio was chosen, to achieve epitaxial vertically aligned GaAs nanowires, with few planar crystallographic defects, and reasonable optical properties and purity. This work also revealed that excess As-related defects, such as EL2, can be more detrimental to exciton lifetime than twin defects.

The investigation of GaAs nanowire growth rate revealed very unexpected and unique growth behaviour. Unlike conventional planar growth, in which a rapid growth rate confers lower material quality, a rapid growth rate significantly improved GaAs nanowire properties. A rapid growth rate markedly reduced tapering, eliminated planar crystallographic defects from these ZB nanowires, and minimised intrinsic carbon doping. The exciton lifetime was approximately 200 ps, regardless of growth rate, indicating that increasing the growth rate does not compromise nanowire quantum efficiency. The ability to obtain high quality material using rapid growth rates is advantageous for industrial processes, where a rapid growth rate should increase throughput. The rapid nanowire growth rates accessible by MOCVD (up to 1 μm/min), present a further advantage over MBE and CBE growth methods, which typically can only achieve very slow growth nanowire rates of approximately 25 nm per minute.[33,281]

InAs nanowire growth, too, was strongly influenced by temperature, V/III ratio and growth rate. The growth of InAs nanowires is more complex, however, because it receives a much more significant contribution from species adsorbed on the substrate. Unlike GaAs nanowire growth, InAs is significantly influenced by the relatively long diffusion length of In species on the growth substrate. This long In diffusion length creates density dependencies of InAs nanowire height and radial growth, whereby closely spaced nanowires compete for diffusing reaction species, and consequently show diminished heights and radial growth. Sparsely distributed InAs nanowires, on the other hand, showed markedly enhanced axial and radial growth rates. These density dependencies were most apparent at high growth temperatures and low growth rates, where the In diffusion length is the longest.

Ternary InGaAs nanowires with high In composition also exhibited these density dependencies, due to the long diffusion length of In species. More sparsely distributed InGaAs nanowires exhibited higher axial and radial growth rates, and higher In content, than densely distributed InGaAs nanowires which compete for diffusing In species during growth. These nanowires also exhibited compositional variation along the nanowire

length, with an In-rich base and Ga-rich tip, due to the large diffusion length of In species compared to Ga species.

Significantly, TEM revealed that GaAs and InAs nanowires could be tuned between pure ZB and pure WZ crystal structure. This was achieved using only two growth parameters: temperature and V/III ratio. Thus, phase purity was achieved without sacrificing important specifications of diameter and dopant levels. Low growth temperatures coupled with high V/III ratios produced twin-free ZB nanowires. Pure WZ nanowires, free of stacking faults, were obtained using high growth temperatures paired with low V/III ratios. These phase perfect ZB and WZ nanowires could be achieved over a wide range of nanowire diameters. This ability to tune the crystal structure between defect-free ZB and defect-free WZ will not only enhance the performance of nanowire devices, but also opens new possibilities for engineering nanowire devices, without restrictions on nanowire diameters or dopants. Finally, a theoretical model of nanowire nucleation was developed to elucidate the mechanisms driving ZB and WZ phase formation. This revealed that the changes in vapour–nucleus surface energy that occur with changes in temperature and V/III ratio, can drive the formation of different crystal phases.

11.2 Recommendations and future directions

In this work, the structural, crystallographic and optical properties of GaAs nanowires have been studied in detail. It is clear that the two-temperature growth procedure produces GaAs nanowires of exceptional quality, which are highly suitable for use in future electronic and optoelectronic devices. The next step is to utilise these high quality nanowires in devices, such as nanowire lasers. In addition, it may be possible to further improve selected properties of these nanowires by tailoring other growth parameters, for instance by using a lower V/III ratio to achieve a longer exciton lifetime.

For InAs nanowires, a number of interesting aspects remain to be investigated. Firstly, growth rate is expected to have a significant effect on InAs nanowire crystal structure, much as it did for GaAs nanowires. TEM investigations on the samples presented in Section 7.7 will be performed in the near future, to ascertain whether InAs nanowires too exhibit a reduction in twin density with increasing growth rate. In addition, the optical properties of InAs nanowires have not yet been characterised. Photoluminescence measurements should reveal a wealth of information on the optical properties, dopant incorporation and carrier lifetime of these nanowires. These measurements will require a specialised system for long wavelength detection.

There is significant room for improvement in InGaAs nanowire growth. The observed density dependencies of height, base shape and In composition can potentially cause uniformity problems in nanowire devices. Another significant problem is the axial and

radial compositional variation within individual nanowires, which makes it impossible to tightly control nanowire optical and electronic properties. These problems arise due to the large diffusion length of In species. Accordingly, these problems may be circumvented by choosing growth conditions which minimise this diffusion length. In this respect, a low growth temperature is especially promising. Chapter 7 found that a low growth temperature limits the In adatom diffusion distance along the $(\bar{1}\,\bar{1}\,\bar{1})$B substrate, and minimises radial growth. Thus, low growth temperatures are predicted to minimise any diffusion-mediated density dependencies of nanowire composition and height, and minimise non-uniformity within individual nanowires. The two-temperature procedure, as described for GaAs nanowires in Chapter 4 may be applied to the growth of InGaAs nanowires. The two-temperature procedure may assist in accessing the low temperatures required for the growth of high quality, compositionally-uniform InGaAs nanowires. Another suggestion is a quantitative study of the In diffusion length at different growth temperatures, V/III ratios and growth rates. Such a quantitative study will assist in finding conditions which minimise diffusion length.

The demonstration of both pure ZB and pure WZ nanowires in Chapter 9 creates many avenues for future work. The growth and characterisation of ZB–WZ heterostructures is one obvious extension of this work. PL, Raman spectroscopy and TCS measurements comparing ZB and WZ nanowires will yield much information about the structural, optical and electronic properties of these different phases.[81,282,283] It is anticipated that the same principles used to control GaAs and InAs nanowire phase can be used to control the crystal quality of InGaAs nanowires.

The nucleation model of ZB and WZ nanowire growth can also be further developed. Future work will extend this model to describe the effects of surface and interfacial tensions, the formation of compensating twins and the effects of growth rate on twin formation.

In conclusion, this work has made considerable progress in the growth of GaAs, InAs and InGaAs nanowires. It has demonstrated that nanowire morphology, compositional purity, quantum efficiency and phase purity can be tightly controlled during growth, to produce nanowires suitable for device applications. Noting that the growth of III–V nanowires is governed by common principles,[47] it is anticipated that many of these findings are not specific to GaAs, InAs and InGaAs nanowires, but are more broadly applicable to other III–V nanowire systems, such as InP and AlGaAs. With further advances in III–V nanowire growth, these nanostructures will become crucial nanocomponents of future electronic and optoelectronic devices and systems.

References

[1] M. Law, L. E. Greene, J. C. Johnson, R. Saykally, and P. Yang, "Nanowire dye-sensitized solar cells," *Nature Mater.*, vol. 4, no. 6, pp. 455–459, 2005.

[2] E. C. Garnett and P. Yang, "Silicon nanowire radial p–n junction solar cells," *J. Am. Chem. Soc.*, vol. 130, no. 29, pp. 9224–9225, 2008.

[3] J. A. Czaban, D. A. Thompson, and R. R. LaPierre, "GaAs core-shell nanowires for photovoltaic applications," *Nano Lett.*, vol. 9, no. 1, pp. 148–154, 2009.

[4] Y. Dong, B. Tian, T. J. Kempa, and C. M. Lieber, "Coaxial group III–nitride nanowire photovoltaics," *Nano Lett.*, vol. 9, no. 5, pp. 2183–2187, 2009.

[5] J. Wang, M. S. Gudiksen, X. Duan, Y. Cui, and C. M. Lieber, "Highly polarized photoluminescence and photodetection from single indium phosphide nanowires," *Science*, vol. 293, no. 5534, pp. 1455–7, 2001.

[6] Y. Gu, E.-S. Kwak, J. L. Lensch, J. E. Allen, T. W. Odom, and L. J. Lauhon, "Near-field scanning photocurrent microscopy of a nanowire photodetector," *Appl. Phys. Lett.*, vol. 87, no. 4, p. 043111, 2005.

[7] H. Pettersson, J. Trägårdh, A. I. Persson, L. Landin, D. Hessman, and L. Samuelson, "Infrared photodetectors in heterostructure nanowires," *Nano Lett.*, vol. 6, no. 2, pp. 229–232, 2006.

[8] C. J. Barrelet, A. B. Greytak, and C. M. Lieber, "Nanowire photonic circuit elements," *Nano Lett.*, vol. 4, no. 10, pp. 1981–1985, 2004.

[9] F. Qian, S. Gradecak, Y. Li, C.-Y. Wen, and C. Lieber, "Core/multishell nanowire heterostructures as multicolor, high-efficiency light-emitting diodes," *Nano Lett.*, vol. 5, no. 11, pp. 2287–2291, 2005.

[10] E. D. Minot, F. Kelkensberg, M. van Kouwen, J. A. van Dam, L. P. Kouwenhoven, V. Zwiller, M. T. Borgström, O. Wunnicke, M. A. Verheijen, and E. P. A. M. Bakkers, "Single quantum dot nanowire LEDs," *Nano Lett.*, vol. 7, no. 2, pp. 367–371, 2007.

[11] M. H. Huang, S. Mao, H. Feick, H. Yan, Y. Wu, H. Kind, E. Weber, R. Russo, and P. Yang, "Room-temperature ultraviolet nanowire nanolasers," *Science*, vol. 292, no. 5523, pp. 1897–1899, 2001.

[12] X. F. Duan, Y. Huang, R. Agarwal, and C. M. Lieber, "Single-nanowire electrically driven lasers," *Nature*, vol. 421, no. 6920, pp. 241–245, 2003.

[13] R. Agarwal, C. J. Barrelet, and C. M. Lieber, "Lasing in single cadmium sulfide nanowire optical cavities," *Nano Lett.*, vol. 5, no. 5, pp. 917–920, 2005.

[14] A. H. Chin, S. Vaddiraju, A. V. Maslov, C. Z. Ning, M. K. Sunkara, and M. Meyyappan, "Near-infrared semiconductor subwavelength-wire lasers," *Appl. Phys. Lett.*, vol. 88, no. 16, p. 163115, 2006.

[15] F. Qian, Y. Li, S. Gradecak, H.-G. Park, Y. Dong, Y. Ding, Z. L. Wang, and C. M. Lieber, "Multi-quantum-well nanowire heterostructures for wavelength-controlled lasers," *Nature Mater.*, vol. 7, no. 9, pp. 701–706, 2008.

[16] B. Hua, J. Motohisa, Y. Kobayashi, S. Hara, and T. Fukui, "Single GaAs/GaAsP coaxial core-shell nanowire lasers," *Nano Lett.*, vol. 9, no. 1, pp. 112–116, 2009.

[17] M. T. Borgström, V. Zwiller, E. Muller, and A. Imamoglu, "Optically bright quantum dots in single nanowires," *Nano Lett.*, vol. 5, no. 7, pp. 1439–1443, 2005.

[18] M. T. Björk, B. J. Ohlsson, C. Thelander, A. I. Persson, K. Deppert, L. R. Wallenberg, and L. Samuelson, "Nanowire resonant tunneling diodes," *Appl. Phys. Lett.*, vol. 81, no. 23, pp. 4458–4460, 2002.

[19] C. Thelander, T. Martensson, M. T. Björk, B. J. Ohlsson, M. W. Larsson, L. R. Wallenberg, and L. Samuelson, "Single-electron transistors in heterostructure nanowires," *Appl. Phys. Lett.*, vol. 83, no. 10, pp. 2052–2054, 2003.

[20] M. T. Björk, C. Thelander, A. E. Hansen, L. E. Jensen, M. W. Larsson, L. R. Wallenberg, and L. Samuelson, "Few-electron quantum dots in nanowires," *Nano Lett.*, vol. 4, no. 9, pp. 1621–1625, 2004.

[21] C. Thelander, H. A. Nilsson, L. E. Jensen, and L. Samuelson, "Nanowire single-electron memory," *Nano Lett.*, vol. 5, no. 4, pp. 635–638, 2005.

[22] H. A. Nilsson, C. Thelander, L. E. Fröberg, J. B. Wagner, and L. Samuelson, "Nanowire-based multiple quantum dot memory," *Appl. Phys. Lett.*, vol. 89, no. 16, p. 163101, 2006.

[23] H. A. Nilsson, T. Duty, S. Abay, C. Wilson, J. B. Wagner, C. Thelander, P. Delsing, and L. Samuelson, "A radio frequency single-electron transistor based on an InAs/InP heterostructure nanowire," *Nano Lett.*, vol. 8, no. 3, pp. 872–875, 2008.

[24] E. C. Heeres, E. P. A. M. Bakkers, A. L. Roest, M. Kaiser, T. H. Oosterkamp, and N. de Jonge, "Electron emission from individual indium arsenide semiconductor nanowires," *Nano Lett.*, vol. 7, no. 2, pp. 536–540, 2007.

[25] H. T. Ng, J. Han, T. Yamada, P. Nguyen, Y. P. Chen, and M. Meyyappan, "Single crystal nanowire vertical surround-gate field-effect transistor," *Nano Lett.*, vol. 4, no. 7, pp. 1247–1252, 2004.

[26] T. Bryllert, L.-E. Wernersson, T. Lowgren, and L. Samuelson, "Vertical wrap-gated nanowire transistors," *Nanotechnology*, vol. 17, no. 11, p. S227, 2006.

[27] E. Lind, A. I. Persson, L. Samuelson, and L.-E. Wernersson, "Improved subthreshold slope in an InAs nanowire heterostructure field-effect transistor," *Nano Lett.*, vol. 6, no. 9, pp. 1842–1846, 2006.

[28] M. T. Bjork, O. Hayden, H. Schmid, H. Riel, and W. Riess, "Vertical surround-gated silicon nanowire impact ionization field-effect transistors," *Appl. Phys. Lett.*, vol. 90, no. 14, p. 142110, 2007.

[29] C. J. Barrelet, J. Bao, M. Lončar, H.-G. Park, F. Capasso, and C. M. Lieber, "Hybrid single-nanowire photonic crystal and microresonator structures," *Nano Lett.*, vol. 6, no. 1, pp. 11–15, 2006.

[30] H.-G. Park, C. J. Barrelet, Y. Wu, B. Tian, F. Qian, and C. M. Lieber, "A wavelength-selective photonic-crystal waveguide coupled to a nanowire light source," *Nature Photon.*, vol. 2, no. 10, pp. 622–626, 2008.

[31] Y. Cui, Q. Wei, H. Park, and C. M. Lieber, "Nanowire nanosensors for highly sensitive and selective detection of biological and chemical species," *Science*, vol. 293, no. 5533, pp. 1289–1292, 2001.

[32] J.-I. Hahm and C. M. Lieber, "Direct ultrasensitive electrical detection of DNA and DNA sequence variations using nanowire nanosensors," *Nano Lett.*, vol. 4, no. 1, pp. 51–54, 2004.

[33] M. T. Björk, B. J. Ohlsson, T. Sass, A. I. Persson, C. Thelander, M. H. Magnusson, K. Deppert, L. R. Wallenberg, and L. Samuelson, "One-dimensional heterostructures in semiconductor nanowhiskers," *Appl. Phys. Lett.*, vol. 80, no. 6, pp. 1058–1060, 2002.

[34] M. S. Gudiksen, L. J. Lauhon, J. Wang, D. C. Smith, and C. M. Lieber, "Growth of nanowire superlattice structures for nanoscale photonics and electronics," *Nature*, vol. 415, no. 6872, pp. 617–620, 2002.

[35] C. M. Lieber, "Nanoscale science and technology: Building a big future from small things," *MRS Bulletin*, vol. 28, no. 7, pp. 486–491, 2003.

[36] L. Samuelson, C. Thelander, M. T. Björk, M. Borgström, K. Deppert, K. A. Dick, A. E. Hansen, T. Mårtensson, N. Panev, A. I. Persson, W. Seifert, N. Sköld, M. W. Larsson, and L. R. Wallenberg, "Semiconductor nanowires for 0D and 1D physics and applications," *Physica E*, vol. 25, no. 2-3, pp. 313–318, 2004.

[37] Y. N. Guo, J. Zou, M. Paladugu, H. Wang, Q. Gao, H. H. Tan, and C. Jagadish, "Structural characteristics of GaSb/GaAs nanowire heterostructures grown by metal-organic chemical vapor deposition," *Appl. Phys. Lett.*, vol. 89, no. 23, p. 231917, 2006.

[38] E. Ertekin, P. A. Greaney, D. C. Chrzan, and T. D. Sands, "Equilibrium limits of coherency in strained nanowire heterostructures," *J. Appl. Phys.*, vol. 97, no. 11, p. 114325, 2005.

[39] M. W. Larsson, J. B. Wagner, M. Wallin, P. Håkansson, L. E. Fröberg, L. Samuelson, and L. R. Wallenberg, "Strain mapping in free-standing heterostructured wurtzite InAs/InP nanowires," *Nanotechnology*, vol. 18, no. 1, p. 015504, 2007.

[40] T. Mårtensson, C. P. T. Svensson, B. A. Wacaser, M. W. Larsson, W. Seifert, K. Deppert, A. Gustafsson, L. R. Wallenberg, and L. Samuelson, "Epitaxial III–V nanowires on silicon," *Nano Lett.*, vol. 4, no. 10, pp. 1987–1990, 2004.

[41] E. P. A. M. Bakkers, J. A. van Dam, S. De Franceschi, L. P. Kouwenhoven, M. Kaiser, M. Verheijen, H. Wondergem, and P. van der Sluis, "Epitaxial growth of InP nanowires on germanium," *Nature Mater.*, vol. 3, no. 11, pp. 769–773, 2004.

[42] L. C. Chuang, M. Moewe, C. Chase, N. P. Kobayashi, C. Chang-Hasnain, and S. Crankshaw, "Critical diameter for III–V nanowires grown on lattice-mismatched substrates," *Appl. Phys. Lett.*, vol. 90, no. 4, p. 043115, 2007.

[43] L. C. Chuang, M. Moewe, S. Crankshaw, and C. Chang-Hasnain, "Optical properties of InP nanowires on Si substrates with varied synthesis parameters," *Appl. Phys. Lett.*, vol. 92, no. 1, p. 013121, 2008.

[44] K. A. Dick, S. Kodambaka, M. C. Reuter, K. Deppert, L. Samuelson, W. Seifert, L. R. Wallenberg, and F. M. Ross, "The morphology of axial and branched nanowire heterostructures," *Nano Lett.*, vol. 7, no. 6, pp. 1817–1822, 2007.

[45] M. Moewe, L. C. Chuang, V. G. Dubrovskii, and C. Chang-Hasnain, "Growth mechanisms and crystallographic structure of InP nanowires on lattice-mismatched substrates," *J. Appl. Phys.*, vol. 104, no. 4, p. 044313, 2008.

[46] T. Mårtensson, J. B. Wagner, E. Hilner, A. Mikkelsen, C. Thelander, J. Stangl, B. J. Ohlsson, A. Gustafsson, E. Lundgren, L. Samuelson, and W. Seifert, "Epitaxial growth of indium arsenide nanowires on silicon using nucleation templates formed by self-assembled organic coatings," *Adv. Mater.*, vol. 19, no. 14, pp. 1801–1806, 2007.

[47] K. A. Dick, K. Deppert, L. S. Karlsson, L. R. Wallenberg, L. Samuelson, and W. Seifert, "A new understanding of Au-assisted growth of III–V semiconductor nanowires," *Adv. Funct. Mater.*, vol. 15, no. 10, pp. 1603–1610, 2005.

[48] X. Duan, J. Wang, and C. M. Lieber, "Synthesis and optical properties of gallium arsenide nanowires," *Appl. Phys. Lett.*, vol. 76, no. 9, pp. 1116–1118, 2000.

[49] B. Hua, J. Motohisa, Y. Ding, S. Hara, and T. Fukui, "Characterization of Fabry-Pérot microcavity modes in GaAs nanowires fabricated by selective-area metal organic vapor phase epitaxy," *Appl. Phys. Lett.*, vol. 91, no. 13, p. 131112, 2007.

[50] M. S. Islam, S. Sharma, T. I. Kamins, and R. S. Williams, "Ultrahigh-density silicon nanobridges formed between two vertical silicon surfaces," *Nanotechnology*, vol. 15, no. 5, pp. L5–L8, 2004.

[51] S. S. Yi, G. Girolami, J. Amano, M. S. Islam, S. Sharma, T. I. Kamins, and I. Kimukin, "InP nanobridges epitaxially formed between two vertical Si surfaces by metal-catalyzed chemical vapor deposition," *Appl. Phys. Lett.*, vol. 89, no. 13, p. 133121, 2006.

[52] A. L. Roest, M. A. Verheijen, O. Wunnicke, S. Serafin, H. Wondergem, and E. P. A. M. Bakkers, "Position-controlled epitaxial III–V nanowires on silicon," *Nanotechnology*, vol. 17, no. 11, p. S271, 2006.

[53] K. Tomioka, Y. Kobayashi, J. Motohisa, S. Hara, and T. Fukui, "Selective-area growth of vertically aligned GaAs and GaAs/AlGaAs core–shell nanowires on Si(111) substrate," *Nanotechnology*, vol. 20, no. 14, p. 145302, 2009.

[54] Y. Xia, P. Yang, Y. Sun, Y. Wu, B. Mayers, B. Gates, Y. Yin, F. Kim, and H. Yan, "One-dimensional nanostructures: Synthesis, characterization, and applications," *Adv. Mater.*, vol. 15, no. 5, pp. 353–389, 2003.

[55] R. S. Wagner and W. C. Ellis, "Vapor–liquid–solid mechanism of single crystal growth," *Appl. Phys. Lett.*, vol. 4, no. 5, pp. 89–90, 1964.

[56] M. A. Verheijen, G. Immink, T. de Smet, M. T. Borgström, and E. P. A. M. Bakkers, "Growth kinetics of heterostructured GaP–GaAs nanowires," *J. Am. Chem. Soc.*, vol. 128, no. 4, pp. 1353–1359, 2006.

[57] K. Hiruma, M. Yazawa, K. Haraguchi, K. Ogawa, T. Katsuyama, M. Koguchi, and H. Kakibayashi, "GaAs freestanding quantum-size wires," *J. Appl. Phys.*, vol. 74, no. 5, pp. 3162–3171, 1993.

[58] M. S. Gudiksen, J. Wang, and C. M. Lieber, "Synthetic control of the diameter and length of single crystal semiconductor nanowires," *J. Phys. Chem. B*, vol. 105, no. 19, pp. 4062–4064, 2001.

[59] J. C. Harmand, M. Tchernycheva, G. Patriarche, L. Travers, F. Glas, and G. Cirlin, "GaAs nanowires formed by Au-assisted molecular beam epitaxy: Effect of growth temperature," *J. Crystal Growth*, vol. 301–302, pp. 853–856, 2007.

[60] H. Shtrikman, R. Popovitz-Biro, A. Kretinin, and M. Heiblum, "Stacking-faults-free zinc blende GaAs nanowires," *Nano Lett.*, vol. 9, no. 1, pp. 215–219, 2009.

[61] B. J. Ohlsson, M. T. Bjork, M. H. Magnusson, K. Deppert, L. Samuelson, and L. R. Wallenberg, "Size-, shape-, and position-controlled GaAs nano-whiskers," *Appl. Phys. Lett.*, vol. 79, no. 20, pp. 3335–3337, 2001.

[62] A. Persson, B. Ohlsson, S. Jeppesen, and L. Samuelson, "Growth mechanisms for GaAs nanowires grown in CBE," *J. Crystal Growth*, vol. 272, no. 1–4, pp. 167–174, 2004.

[63] A. I. Persson, L. E. Fröberg, L. Samuelson, and H. Linke, "The fabrication of dense and uniform InAs nanowire arrays," *Nanotechnology*, vol. 20, no. 22, p. 225304, 2009.

[64] K. Hiruma, H. Murakoshi, M. Yazawa, and T. Katsuyama, "Self-organized growth of GaAs/InAs heterostructure nanocylinders by organometallic vapor phase epitaxy," *J. Crystal Growth*, vol. 163, no. 3, pp. 226–231, 1996.

[65] W. Seifert, M. Borgström, K. Deppert, K. A. Dick, J. Johansson, M. W. Larsson, T. Mårtensson, N. Sköld, C. P. T. Svensson, B. A. Wacaser, L. R. Wallenberg, and L. Samuelson, "Growth of one-dimensional nanostructures in MOVPE," *J. Crystal Growth*, vol. 272, no. 1–4, pp. 211–220, 2004.

[66] D. J. Wolford, G. D. Gilliland, T. F. Kuech, J. F. Klem, H. P. Hjalmarson, J. A. Bradley, C. F. Tsang, and J. Martinsen, "Comparison of transport, recombination, and interfacial quality in molecular beam epitaxy and organometallic vapor-phase epitaxy GaAs/$Al_xGa_{1-x}As$ structures," *Appl. Phys. Lett.*, vol. 64, no. 11, pp. 1416–1418, 1994.

[67] M. Behet, R. Hövel, A. Kohl, A. M. Küsters, B. Opitz, and K. Heime, "MOVPE growth of III–V compounds for optoelectronic and electronic applications," *Microelectronics J.*, vol. 27, no. 4-5, pp. 297–334, 1996.

[68] R. L. Moon, "MOVPE: is there any other technology for optoelectronics?," *J. Crystal Growth*, vol. 170, no. 1–4, pp. 1–10, 1997.

[69] M. D. Williams, A. L. Greene, T. Daniels-Race, and R. M. Lum, "Comparison of InGaAs(100) grown by chemical beam epitaxy and metal organic chemical vapor deposition," *Appl. Surf. Sci.*, vol. 157, no. 3, pp. 123–128, 2000.

[70] S. K. Lim, M. J. Tambe, M. M. Brewster, and S. Gradecak, "Controlled growth of ternary alloy nanowires using metalorganic chemical vapor deposition," *Nano Lett.*, vol. 8, no. 5, pp. 1386–1392, 2008.

[71] J. Johansson, L. S. Karlsson, C. P. T. Svensson, T. Mårtensson, B. A. Wacaser, K. Deppert, L. Samuelson, and W. Seifert, "Structural properties of ⟨111⟩B-oriented III–V nanowires," *Nature Mater.*, vol. 5, no. 7, pp. 574–580, 2006.

[72] J. Zou, M. Paladugu, H. Wang, G. J. Auchterlonie, Y. Guo, Y. Kim, Q. Gao, H. J. Joyce, H. H. Tan, and C. Jagadish, "Growth mechanism of truncated triangular III–V nanowires," *Small*, vol. 3, no. 3, pp. 389–393, 2007.

[73] L. S. Karlsson, K. A. Dick, J. B. Wagner, J.-O. Malm, K. Deppert, L. Samuelson, and L. R. Wallenberg, "Understanding the 3D structure of GaAs⟨111⟩b nanowires," *Nanotechnology*, no. 48, p. 485717, 2007.

[74] M. Koguchi, H. Kakibayashi, M. Yazawa, K. Hiruma, and T. Katsuyama, "Crystal structure change of GaAs and InAs whiskers from zinc-blende to wurtzite type," *Jpn. J. Appl. Phys.*, vol. 31, no. 7, pp. 2061–2065, 1992.

[75] M. Murayama and T. Nakayama, "Chemical trend of band offsets at wurtzite/zinc-blende heterocrystalline semiconductor interfaces," *Phys. Rev. B*, vol. 49, no. 7, pp. 4710 – 4724, 1994.

[76] A. Mishra, L. V. Titova, T. B. Hoang, H. E. Jackson, L. M. Smith, J. M. Yarrison-Rice, Y. Kim, H. J. Joyce, Q. Gao, H. H. Tan, and C. Jagadish, "Polarization and temperature dependence of photoluminescence from zincblende and wurtzite InP nanowires," *Appl. Phys. Lett.*, vol. 91, no. 26, p. 263104, 2007.

[77] J. Bao, D. C. Bell, F. Capasso, J. B. Wagner, T. Mårtensson, J. Trägårdh, and L. Samuelson, "Optical properties of rotationally twinned InP nanowire heterostructures," *Nano Lett.*, vol. 8, no. 3, pp. 836–841, 2008.

[78] T. B. Hoang, A. F. Moses, H. L. Zhou, D. L. Dheeraj, B. O. Fimland, and H. Weman, "Observation of free exciton photoluminescence emission from single wurtzite GaAs nanowires," *Appl. Phys. Lett.*, vol. 94, no. 13, p. 133105, 2009.

[79] R. L. Woo, R. Xiao, Y. Kobayashi, L. Gao, N. Goel, M. K. Hudait, T. E. Mallouk, and R. F. Hicks, "Effect of twinning on the photoluminescence and photoelectrochemical properties of indium phosphide nanowires grown on silicon (111)," *Nano Lett.*, vol. 8, no. 12, pp. 4664–4669, 2008.

[80] S. Perera, M. A. Fickenscher, H. E. Jackson, L. M. Smith, J. M. Yarrison-Rice, H. J. Joyce, Q. Gao, H. H. Tan, C. Jagadish, X. Zhang, and J. Zou, "Nearly intrinsic exciton lifetimes in single twin-free GaAs/AlGaAs core–shell nanowire heterostructures," *Appl. Phys. Lett.*, vol. 93, no. 5, p. 053110, 2008.

[81] P. Parkinson, H. J. Joyce, Q. Gao, H. H. Tan, X. Zhang, J. Zou, C. Jagadish, L. M. Herz, and M. B. Johnston, "Carrier lifetime and mobility enhancement in nearly defect-free core–shell nanowires measured using time-resolved terahertz spectroscopy," *Nano Lett.*, vol. 9, no. 9, pp. 3349–3353, 2009.

[82] R. E. Algra, M. A. Verheijen, M. T. Borgström, L.-F. Feiner, G. Immink, W. J. P. van Enckevort, E. Vlieg, and E. P. A. M. Bakkers, "Twinning superlattices in indium phosphide nanowires," *Nature*, vol. 456, no. 7220, pp. 369–372, 2008.

[83] P. Caroff, K. A. Dick, J. Johansson, M. E. Messing, K. Deppert, and L. Samuelson, "Controlled polytypic and twin-plane superlattices in III-V nanowires," *Nature Nanotech.*, vol. 4, no. 1, pp. 50–55, 2009.

[84] H. Shtrikman, R. Popovitz-Biro, A. Kretinin, L. Houben, M. Heiblum, M. Bukala, M. Galicka, R. Buczko, and P. Kacman, "Method for suppression of stacking faults in wurtzite III–V nanowires," *Nano Lett.*, vol. 9, no. 4, pp. 1506–1510, 2009.

[85] K. Hiruma, M. Yazawa, T. Katsuyama, K. Ogawa, K. Haraguchi, M. Koguchi, and H. Kakibayashi, "Growth and optical properties of nanometer-scale GaAs and InAs whiskers," *J. Appl. Phys.*, vol. 77, no. 2, pp. 447–462, 1995.

[86] A. Mikkelsen, N. Sköld, L. Ouattara, and E. Lundgren, "Nanowire growth and dopants studied by cross-sectional scanning tunnelling microscopy," *Nanotechnology*, vol. 17, no. 11, pp. S362–S368, 2006.

[87] H. M. Manasevit, "Single-crystal gallium arsenide on insulating substrates," *Appl. Phys. Lett.*, vol. 12, no. 4, pp. 156–159, 1968.

[88] H. M. Manasevit and W. I. Simpson, "The use of metal-organics in the preparation of semiconductor materials," *J. Electrochem. Soc.*, vol. 116, no. 12, pp. 1725–1732, 1969.

[89] G. B. Stringfellow, *Organometallic vapor-phase epitaxy: theory and practice*. San Diego: Academic Press, 2nd ed., 1999.

[90] Y. Cui, L. J. Lauhon, M. S. Gudiksen, J. Wang, and C. M. Lieber, "Diameter-controlled synthesis of single-crystal silicon nanowires," *Appl. Phys. Lett.*, vol. 78, no. 15, pp. 2214–2216, 2001.

[91] A. I. Hochbaum, R. Fan, R. He, and P. Yang, "Controlled growth of Si nanowire arrays for device integration," *Nano Lett.*, vol. 5, no. 3, pp. 457–460, 2005. .

[92] J. Vesenka, S. Manne, R. Giberson, T. Marsh, and E. Henderson, "Colloidal gold particles as an incompressible atomic force microscope imaging standard for assessing the compressibility of biomolecules," *Biophys. J.*, vol. 65, no. 3, pp. 992–997, 1993.

[93] D. C. Bell, Y. Wu, C. J. Barrelet, S. Gradecak, J. Xiang, B. P. Timko, and C. M. Lieber, "Imaging and analysis of nanowires," *Microsc. Res. Tech.*, vol. 64, no. 5-6, pp. 373–389, 2004.

[94] D. J. Ashen, P. J. Dean, D. T. J. Hurle, J. B. Mullin, A. M. White, and P. D. Greene, "The incorporation and characterisation of acceptors in epitaxial GaAs," *J. Phys. Chem. Solids*, vol. 36, no. 10, pp. 1041–1053, 1975.

[95] L. V. Titova, T. B. Hoang, H. E. Jackson, L. M. Smith, J. M. Yarrison-Rice, Y. Kim, H. J. Joyce, H. H. Tan, and C. Jagadish, "Temperature dependence of photoluminescence from single core–shell GaAs–AlGaAs nanowires," *Appl. Phys. Lett.*, vol. 89, no. 17, p. 173126, 2006.

[96] T. B. Hoang, L. V. Titova, J. M. Yarrison-Rice, H. E. Jackson, A. O. Govorov, Y. Kim, H. J. Joyce, H. H. Tan, C. Jagadish, and L. M. Smith, "Resonant excitation and imaging of nonequilibrium exciton spins in single core-shell GaAs–AlGaAs nanowires," *Nano Lett.*, vol. 7, no. 3, pp. 588–595, 2007.

[97] M. Mattila, T. Hakkarainen, M. Mulot, and H. Lipsanen, "Crystal-structure-dependent photoluminescence from InP nanowires," *Nanotechnology*, vol. 17, no. 6, p. 1580, 2006.

[98] G. Gilliland, "Photoluminescence spectroscopy of crystalline semiconductors," *Mater. Sci. Eng. R: Reports*, vol. 18, no. 3-6, pp. 99–399, 1997.

[99] C. A. Larsen, N. I. Buchan, and G. B. Stringfellow, "Mass spectrometric studies of phosphine pyrolysis and OMVPE growth of InP," *J. Crystal Growth*, vol. 85, no. 1–2, pp. 148–153, 1987.

[100] C. A. Larsen, N. I. Buchan, and G. B. Stringfellow, "Reaction mechanisms in the organometallic vapor phase epitaxial growth of GaAs," *Appl. Phys. Lett.*, vol. 52, no. 6, pp. 480–482, 1988.

[101] N. Buchan, C. Larsen, and G. Stringfellow, "Mass spectrometric studies of trimethylindium pyrolysis," *J. Crystal Growth*, vol. 92, no. 3–4, pp. 591–604, 1988.

[102] C. A. Larsen, S. H. Li, N. I. Buchan, G. B. Stringfellow, and D. W. Brown, "Kinetics of the reaction between trimethylgallium and arsine," *J. Crystal Growth*, vol. 102, no. 1–2, pp. 126–136, 1990.

[103] M. Tirtowidjojo and R. Pollard, "Elementary processes and rate-limiting factors in MOVPE of GaAs," *J. Crystal Growth*, vol. 93, no. 1–4, pp. 108–114, 1988.

[104] M. T. Borgström, G. Immink, B. Ketelaars, R. Algra, and E. P. A. M. Bakkers, "Synergetic nanowire growth," *Nature Nanotech.*, vol. 2, no. 9, pp. 541–544, 2007.

[105] K. A. Dick, "A review of nanowire growth promoted by alloys and non-alloying elements with emphasis on Au-assisted III–V nanowires," *Prog. Cryst. Growth Charact. Mater.*, vol. 54, no. 3-4, pp. 138–173, 2008.

[106] C. A. Larsen, N. I. Buchan, S. H. Li, and G. B. Stringfellow, "Decomposition mechanisms of trimethylgallium," *J. Crystal Growth*, vol. 102, no. 1–2, pp. 103–116, 1990.

[107] C. Larsen, S. H. Li, and G. B. Stringfellow, "Decomposition mechanisms of trimethylantimony and reactions with trimethylindium," *Chem. Mater.*, vol. 3, pp. 39–44, 1991.

[108] R. Lückerath, P. Tommack, A. Hertling, H. J. Koss, P. Balk, K. F. Jensen, and W. Richter, "CARS in situ diagnostics in MOVPE: The thermal decomposition of AsH_3 and PH_3," *J. Crystal Growth*, vol. 93, no. 1–4, pp. 151–158, 1988.

[109] C. A. Larsen and G. B. Stringfellow, "Decomposition kinetics of OMVPE precursors," *J. Crystal Growth*, vol. 75, no. 2, pp. 247–254, 1986.

[110] S. E. R. Hiscocks and W. Hume-Rothery, "The equilibrium diagram of the system gold–indium," *Proc. R. Soc. Lond. A*, vol. 282, no. 1390, pp. 318–330, 1964.

[111] J. Murray, H. Okamoto, and T. Massalski, "The Al-Au (aluminum–gold) system," *J. Phase Equilibria*, vol. 8, no. 1, pp. 20–30, 1987.

[112] R. Elliott and F. Shunk, "The Au–Ga (gold–gallium) system," *J. Phase Equilibria*, vol. 2, no. 3, pp. 356–358, 1981.

[113] H. Okamoto and T. Massalski, "The As–Au (arsenic–gold) system," *J. Phase Equilibria*, vol. 5, no. 1, pp. 56–59, 1984.

[114] H. Okamoto and T. B. Massalski, eds., *Binary Alloy Phase Diagrams*, vol. 1. Metals Park, Ohio: ASM International, 1 ed., 1986.

[115] H. Okamoto and T. Massalski, "The Au–P (gold–phosphorus) system," *J. Phase Equilibria*, vol. 5, no. 5, pp. 490–491, 1984.

[116] H. Okamoto and T. Massalski, "The Au–Sb (gold–antimony) system," *J. Phase Equilibria*, vol. 5, no. 2, pp. 166–171, 1984.

[117] H. S. Liu, Y. Cui, K. Ishida, and Z. P. Jin, "Thermodynamic reassessment of the Au–In binary system," *Calphad*, vol. 27, no. 1, pp. 27–37, 2003.

[118] H. Okamoto, "Au–In (gold-indium)," *J. Phase Equilibria*, vol. 25, no. 2, pp. 197–198, 2004.

[119] C. T. Tsai and R. S. Williams, "Solid phase equilibria in the Au–Ga–As, Au–Ga–Sb, Au–In–As and Au–In–Sb ternaries," *J. Mater. Res.*, vol. 1, no. 2, p. 352, 1986.

[120] C. T. Tsai and R. S. Williams, "Chemical reactions at the Au/InP interface," *J. Mater. Res.*, vol. 1, no. 6, pp. 820–826, 1986.

[121] A. I. Persson, M. W. Larsson, S. Stenström, B. J. Ohlsson, L. Samuelson, and L. R. Wallenberg, "Solid-phase diffusion mechanism for GaAs nanowire growth," *Nature Mater.*, vol. 3, no. 10, pp. 677–681, 2004.

[122] S. Kodambaka, J. Tersoff, M. C. Reuter, and F. M. Ross, "Germanium nanowire growth below the eutectic temperature," *Science*, vol. 316, no. 5825, pp. 729–732, 2007.

[123] J. C. Harmand, G. Patriarche, N. Pere-Laperne, M.-N. Merat-Combes, L. Travers, and F. Glas, "Analysis of vapor–liquid–solid mechanism in Au-assisted GaAs nanowire growth," *Appl. Phys. Lett.*, vol. 87, no. 20, p. 203101, 2005.

[124] J. Johansson, C. Svensson, T. Mårtensson, L. Samuelson, and W. Seifert, "Mass transport model for semiconductor nanowire growth," *J. Phys. Chem. B*, vol. 109, no. 28, pp. 13567–13571, 2005.

[125] K. A. Dick, K. Deppert, L. Samuelson, and W. Seifert, "Optimization of Au-assisted InAs nanowires grown by MOVPE," *J. Crystal Growth*, vol. 297, no. 2, pp. 326–333, 2006.

[126] P. D. Markowitz, M. P. Zach, P. C. Gibbons, R. M. Penner, and W. E. Buhro, "Phase separation in $Al_xGa_{1-x}As$ nanowhiskers grown by the solution–liquid–solid mechanism," *J. Am. Chem. Soc.*, vol. 123, no. 19, pp. 4502–4511, 2001.

[127] K. A. Dick, K. Deppert, T. Mårtensson, B. Mandl, L. Samuelson, and W. Seifert, "Failure of the vapor–liquid–solid mechanism in Au-assisted MOVPE growth of InAs nanowires," *Nano Lett.*, vol. 5, no. 4, pp. 761–764, 2005.

[128] G. A. Bootsma and H. J. Gassen, "A quantitative study on the growth of silicon whiskers from silane and germanium whiskers from germane," *J. Crystal Growth*, vol. 10, no. 3, pp. 223–234, 1971.

[129] P. Cheyssac, M. Sacilotti, and G. Patriarche, "Vapor–liquid–solid mechanisms: Challenges for nanosized quantum cluster/dot/wire materials," *J. Appl. Phys.*, vol. 100, no. 4, p. 044315, 2006.

[130] B. A. Wacaser, K. A. Dick, J. Johansson, M. T. Borgström, K. Deppert, and L. Samuelson, "Preferential interface nucleation: An expansion of the VLS growth mechanism for nanowires," *Adv. Mater.*, vol. 21, no. 2, pp. 153–165, 2009.

[131] J. H. Woodruff, J. B. Ratchford, I. A. Goldthorpe, P. C. McIntyre, and C. E. D. Chidsey, "Vertically oriented germanium nanowires grown from gold colloids on silicon substrates and subsequent gold removal," *Nano Lett.*, vol. 7, no. 6, pp. 1637–1642, 2007.

[132] F. Glas, J. C. Harmand, and G. Patriarche, "Why does wurtzite form in nanowires of III–V zinc blende semiconductors," *Phys. Rev. Lett.*, vol. 99, no. 14, p. 146101, 2007.

[133] M. A. Verheijen, R. E. Algra, M. T. Borgström, G. Immink, E. Sourty, W. J. P. van Enckevort, E. Vlieg, and E. P. A. M. Bakkers, "Three-dimensional morphology of GaP–GaAs nanowires revealed by transmission electron microscopy tomography," *Nano Lett.*, vol. 7, no. 10, pp. 3051–3055, 2007.

[134] M. Paladugu, J. Zou, G. J. Auchterlonie, Y. N. Guo, Y. Kim, H. J. Joyce, Q. Gao, H. H. Tan, and C. Jagadish, "Evolution of InAs branches in InAs/GaAs nanowire heterostructures," *Appl. Phys. Lett.*, vol. 91, no. 13, p. 133115, 2007.

[135] M. Paladugu, J. Zou, Y.-N. Guo, G. Auchterlonie, H. Joyce, Q. Gao, H. H. Tan, C. Jagadish, and Y. Kim, "Novel growth phenomena observed in axial InAs/GaAs nanowire heterostructures," *Small*, vol. 3, no. 11, pp. 1873–1877, 2007.

[136] M. Paladugu, J. Zou, Y.-N. Guo, X. Zhang, H. J. Joyce, Q. Gao, H. H. Tan, C. Jagadish, and Y. Kim, "Polarity driven formation of InAs/GaAs hierarchical nanowire heterostructures," *Appl. Phys. Lett.*, vol. 93, no. 20, p. 201908, 2008.

[137] M. Paladugu, J. Zou, Y.-N. Guo, X. Zhang, Y. Kim, H. J. Joyce, Q. Gao, H. H. Tan, and C. Jagadish, "Nature of heterointerfaces in GaAs/InAs and InAs/GaAs axial nanowire heterostructures," *Appl. Phys. Lett.*, vol. 93, no. 10, p. 101911, 2008.

[138] M. Paladugu, J. Zou, Y. Guo, X. Zhang, H. Joyce, Q. Gao, H. Tan, C. Jagadish, and Y. Kim, "Evolution of wurtzite structured GaAs shells around InAs nanowire cores," *Nanoscale Res. Lett.*, vol. 4, no. 8, pp. 846–849, 2009.

[139] M. Paladugu, J. Zou, Y.-N. Guo, X. Zhang, H. J. Joyce, Q. Gao, H. H. Tan, C. Jagadish, and Y. Kim, "Formation of hierarchical InAs nanoring/GaAs nanowire heterostructures," *Angew. Chem.*, vol. 121, no. 4, pp. 794–797, 2009.

[140] M. Paladugu, J. Zou, Y.-N. Guo, X. Zhang, H. J. Joyce, Q. Gao, H. H. Tan, C. Jagadish, and Y. Kim, "Crystallographically driven Au catalyst movement during growth of InAs/GaAs axial nanowire heterostructures," *J. Appl. Phys.*, vol. 105, no. 7, p. 073503, 2009.

[141] J. Noborisaka, J. Motohisa, S. Hara, and T. Fukui, "Fabrication and characterization of freestanding GaAs/AlGaAs core–shell nanowires and AlGaAs nanotubes by using selective-area metalorganic vapor phase epitaxy," *Appl. Phys. Lett.*, vol. 87, no. 9, p. 093109, 2005.

[142] F. Jabeen, S. Rubini, V. Grillo, L. Felisari, and F. Martelli, "Room temperature luminescent InGaAs/GaAs core–shell nanowires," *Appl. Phys. Lett.*, vol. 93, no. 8, p. 083117, 2008.

[143] J. M. Ryan, J. W. Huang, T. F. Kuech, and K. L. Bray, "The effects of temperature and oxygen concentration on the photoluminescence of epitaxial metalorganic vapor-phase epitaxy GaAs:O," *J. Appl. Phys.*, vol. 76, no. 2, pp. 1175–1179, 1994.

[144] J. W. Orton, P. Dawson, D. E. Lacklison, T. S. Cheng, and C. T. Foxon, "Recombination lifetime measurements in AlGaAs/GaAs quantum well structures," *Semicond. Sci. Technol.*, vol. 9, no. 9, p. 1616, 1994.

[145] V. Swaminathan, D. L. V. Haren, J. L. Zilko, P. Y. Lu, and N. E. Schumaker, "Characterization of GaAs films grown by metalorganic chemical vapor deposition," *J. Appl. Phys.*, vol. 57, no. 12, pp. 5349–5353, 1985.

[146] L. V. Titova, T. B. Hoang, J. M. Yarrison-Rice, H. E. Jackson, Y. Kim, H. J. Joyce, Q. Gao, H. H. Tan, C. Jagadish, X. Zhang, J. Zou, and L. M. Smith, "Dynamics of strongly degenerate electron-hole plasmas and excitons in single InP nanowires," *Nano Lett.*, vol. 7, no. 11, pp. 3383–3387, 2007.

[147] E. H. Bogardus and H. B. Bebb, "Bound-exciton, free-exciton, band–acceptor, donor–acceptor, and auger recombination in GaAs," *Phys. Rev.*, vol. 176, no. 3, pp. 993–1002, 1968.

[148] R. C. C. Leite and A. E. DiGiovanni, "Frequency shift with temperature as evidence for donor–acceptor pair recombination in relatively pure n-type GaAs," *Phys. Rev.*, vol. 153, no. 3, pp. 841–843, 1967.

[149] K. Tanaka, Y. Miyamoto, H. Uchiki, K. Nakazawa, and H. Araki, "Donor–acceptor pair recombination luminescence from Cu_2ZnSnS_4 bulk single crystals," *Phys. Status Solidi A*, vol. 203, no. 11, pp. 2891–2896, 2006.

[150] D. G. Thomas, J. J. Hopfield, and W. M. Augustyniak, "Kinetics of radiative recombination at randomly distributed donors and acceptors," *Phys. Rev.*, vol. 140, no. 1A, pp. A202–A220, 1965.

[151] B. J. Skromme, T. S. Low, T. J. Roth, G. E. Stillman, J. K. Kennedy, and J. K. Abrokwah, "Residual donors and acceptors in high-purity GaAs and InP grown by hydride VPE," *J. Electron. Mater.*, vol. 12, no. 2, pp. 433–457, 1983.

[152] B. J. Skromme and G. E. Stillman, "Excited-state-donor-acceptor transitions in the photoluminescence spectrum of GaAs and InP," *Phys. Rev. B*, vol. 29, no. 4, pp. 1982–1992, 1984.

[153] P. D. Dapkus, H. M. Manasevit, K. L. Hess, T. S. Low, and G. E. Stillman, "High purity GaAs prepared from trimethylgallium and arsine," *J. Crystal Growth*, vol. 55, no. 1, pp. 10–23, 1981.

[154] T. F. Kuech and E. Veuhoff, "Mechanism of carbon incorporation in MOCVD GaAs," *J. Crystal Growth*, vol. 68, no. 1, pp. 148–156, 1984.

[155] M. J. Ashwin, B. R. Davidson, K. Woodhouse, R. C. Newman, T. J. Bullough, T. B. Joyce, R. Nicklin, and R. R. Bradley, "Carbon acceptors passivated with hydrogen and the search for carbon donors in highly doped GaAs:C," *Semicond. Sci. Technol.*, no. 5, p. 625, 1993.

[156] B.-H. Cheong and K. J. Chang, "Compensation and diffusion mechanisms of carbon dopants in GaAs," *Phys. Rev. B*, vol. 49, no. 24, pp. 17436–17439, 1994.

[157] H. Mori and S. Takahashi, "Influence of H_2 overpressure on the properties of GaAs grown by low-pressure MOCVD," *Jpn. J. Appl. Phys.*, vol. 23, no. 12, pp. L877–L879, 1984.

[158] B. T. Cunningham, L. J. Guido, J. E. Baker, J. J. S. Major, J. N. Holonyak, and G. E. Stillman, "Carbon diffusion in undoped, n-type, and p-type GaAs," *Appl. Phys. Lett.*, vol. 55, no. 7, pp. 687–689, 1989.

[159] Z. H. Lu, M. C. Hanna, D. M. Szmyd, E. G. Oh, and A. Majerfeld, "Determination of donor and acceptor densities in high-purity GaAs from photoluminescence analysis," *Appl. Phys. Lett.*, vol. 56, no. 2, pp. 177–179, 1990.

[160] M. Ciorga, L. Bryja, J. Misiewicz, R. Paszkiewicz, M. Panek, B. Paszkiewicz, and M. Tlaczala, "Photoluminescence measurements of GaAs grown by liquid phase epitaxy from Ga-Bi solution," *Adv. Mater. Opt. Electron.*, vol. 8, no. 1, pp. 9–12, 1998.

[161] D. C. Reynolds, D. N. Talwar, M. O. Manasreh, and C. E. Stutz, "Phonon coupling associated with free-to-bound and bound-to-bound transitions in GaAs layers

grown by molecular-beam epitaxy," *Phys. Rev. B*, vol. 47, no. 20, pp. 13304–13308, 1993.

[162] A. L. Gurskii and S. V. Voitikov, "Quantum defect approach for the effect of electron-phonon coupling on impurity recombination in semiconductors," *Solid State Comm.*, vol. 112, no. 6, pp. 339–343, 1999.

[163] U. Woggon, E. Lüthgens, H. Wenisch, and D. Hommel, "Probing the electron–LO-phonon interaction of a single impurity state in a semiconductor," *Phys. Rev. B*, vol. 63, no. 7, p. 073205, 2001.

[164] Z. H. Wu, M. Sun, X. Y. Mei, and H. E. Ruda, "Growth and photoluminescence characteristics of AlGaAs nanowires," *Appl. Phys. Lett.*, vol. 85, no. 4, pp. 657–659, 2004.

[165] M. S. Gudiksen, J. Wang, and C. M. Lieber, "Size-dependent photoluminescence from single indium phosphide nanowires," *J. Phys. Chem. B*, vol. 106, no. 16, pp. 4036–4039, 2002.

[166] D. H. Reep and S. K. Ghandhi, "Deposition of GaAs epitaxial layers by organometallic CVD," *J. Electrochem. Soc.*, vol. 130, no. 3, pp. 675–680, 1983.

[167] M. Borgström, K. Deppert, L. Samuelson, and W. Seifert, "Size- and shape-controlled GaAs nano-whiskers grown by MOVPE: a growth study," *J. Crystal Growth*, vol. 260, no. 1–2, pp. 18–22, 2004.

[168] J. Westwater, D. P. Gosain, S. Tomiya, S. Usui, and H. Ruda, "Growth of silicon nanowires via gold/silane vapor–liquid–solid reaction," *J. Vac. Sci. Tech. B*, vol. 15, no. 3, pp. 554–557, 1997.

[169] H. Adhikari, A. F. Marshall, C. E. D. Chidsey, and P. C. McIntyre, "Germanium nanowire epitaxy: Shape and orientation control," *Nano Lett.*, vol. 6, no. 2, pp. 318–323, 2006.

[170] A. B. Greytak, L. J. Lauhon, M. S. Gudiksen, and C. M. Lieber, "Growth and transport properties of complementary germanium nanowire field-effect transistors," *Appl. Phys. Lett.*, vol. 84, no. 21, pp. 4176–4178, 2004.

[171] A. Mikkelsen, J. Eriksson, E. Lundgren, J. N. Andersen, J. Weissenreider, and W. Seifert, "The influence of lysine on InP(001) surface ordering and nanowire growth," *Nanotechnology*, vol. 16, no. 10, p. 2354, 2005.

[172] B. A. Wacaser, K. Deppert, L. S. Karlsson, L. Samuelson, and W. Seifert, "Growth and characterization of defect free GaAs nanowires," *J. Crystal Growth*, vol. 287, no. 2, pp. 504–508, 2006.

[173] J. Johansson, B. A. Wacaser, K. A. Dick, and W. Seifert, "Growth related aspects of epitaxial nanowires," *Nanotechnology*, vol. 17, no. 11, p. S355, 2006.

[174] A. Mikkelsen, N. Sköld, L. Ouattara, M. Borgström, J. N. Andersen, L. Samuelson, W. Seifert, and E. Lundgren, "Direct imaging of the atomic structure inside a nanowire by scanning tunnelling microscopy," *Nature Mater.*, vol. 3, no. 8, pp. 519–523, 2004.

[175] D. T. J. Hurle and P. Rudolph, "A brief history of defect formation, segregation, faceting, and twinning in melt-grown semiconductors," *J. Crystal Growth*, vol. 264, no. 4, pp. 550–564, 2004.

[176] J. Bauer, V. Gottschalch, H. Paetzelt, G. Wagner, B. Fuhrmann, and H. Leipner, "MOVPE growth and real structure of vertical-aligned GaAs nanowires," *J. Crystal Growth*, vol. 298, pp. 625–630, 2007.

[177] T. J. Mountziaris and K. F. Jensen, "Gas-phase and surface reaction mechanisms in MOCVD of GaAs with trimethyl-gallium and arsine," *J. Electrochem. Soc.*, vol. 138, no. 8, pp. 2426–2439, 1991.

[178] N. I. Buchan, T. F. Kuech, D. Beach, G. Scilla, and F. Cardone, "The use of azo-compounds as probes of carbon incorporation of nominally undoped metalorganic vapor phase epitaxy grown GaAs," *J. Appl. Phys.*, vol. 69, no. 4, pp. 2156–2160, 1991.

[179] M. Masi, H. Simka, K. F. Jensen, T. F. Kuech, and R. Potemski, "Simulation of carbon doping of GaAs during MOVPE," *J. Crystal Growth*, vol. 124, no. 1–4, pp. 483–492, 1992.

[180] K. F. Jensen, "Transport phenomena and chemical reaction issues in OMVPE of compound semiconductors," *J. Crystal Growth*, vol. 98, no. 1–2, pp. 148–166, 1989.

[181] U. Memmert and M. L. Yu, "Pyrolysis of trimethylgallium on GaAs(100) surfaces," *Appl. Phys. Lett.*, vol. 56, no. 19, pp. 1883–1885, 1990.

[182] H. Okamoto and T. Massalski, "The Au–C (gold-carbon) system," *J. Phase Equil.*, vol. 5, no. 4, pp. 378–379, 1984.

[183] D. Takagi, Y. Kobayashi, H. Hibino, S. Suzuki, and Y. Homma, "Mechanism of gold-catalyzed carbon material growth," *Nano Lett.*, vol. 8, no. 3, pp. 832–835, 2008.

[184] Z. W. Pan, S. Dai, D. B. Beach, N. D. Evans, and D. H. Lowndes, "Gallium-mediated growth of multiwall carbon nanotubes," *Appl. Phys. Lett.*, vol. 82, no. 12, pp. 1947–1949, 2003.

[185] E. Tutuc, J. Appenzeller, M. C. Reuter, and S. Guha, "Realization of a linear germanium nanowire p–n junction," *Nano Lett.*, vol. 6, no. 9, pp. 2070–2074, 2006.

[186] E. Tutuc, J. O. Chu, J. A. Ott, and S. Guha, "Doping of germanium nanowires grown in presence of PH_3," *Appl. Phys. Lett.*, vol. 89, no. 26, p. 263101, 2006.

[187] E. Tutuc, S. Guha, and J. O. Chu, "Morphology of germanium nanowires grown in presence of B_2H_6," *Appl. Phys. Lett.*, vol. 88, no. 4, p. 043113, 2006.

[188] H. Sakaguchi, T. Mishima, T. Meguro, and Y. Fujiwara, "Low-temperature growth of GaAs with high quality by metalorganic vapor phase epitaxy," *J. Phys.: Conf. Ser.*, vol. 165, p. 012024, 2009.

[189] D. J. Wolford, G. D. Gilliland, T. F. Kuech, L. M. Smith, J. Martinsen, J. A. Bradley, C. F. Tsang, R. Venkatasubramanian, S. K. Ghandi, and H. P. Hjalmarson, "Intrinsic recombination and interface characterization in "surface-free" GaAs structures," *J. Vac. Sci. Technol. B*, vol. 9, no. 4, pp. 2369–2376, 1991.

[190] A. Y. Cho and I. Hayashi, "Surface structures and photoluminescence of molecular beam epitaxial films of GaAs," *Solid-State Electron.*, vol. 14, no. 2, pp. 125–132, 1971.

[191] M. Tchernycheva, J. C. Harmand, G. Patriarche, L. Travers, and G. E. Cirlin, "Temperature conditions for GaAs nanowire formation by Au-assisted molecular beam epitaxy," *Nanotechnology*, vol. 17, no. 16, p. 4025, 2006.

[192] R. Kofman, P. Cheyssac, Y. Lereah, and A. Stella, "Melting of clusters approaching 0D," *Eur. Phys. J. D*, vol. 9, no. 1, pp. 441–444, 1999.

[193] G. Zhang, K. Tateno, T. Sogawa, and H. Nakano, "Growth and characterization of GaP nanowires on Si substrate," *J. Appl. Phys.*, vol. 103, no. 1, p. 014301, 2008.

[194] S. Paiman, Q. Gao, H. H. Tan, C. Jagadish, K. Pemasiri, M. Montazeri, H. E. Jackson, L. M. Smith, J. M. Yarrison-Rice, X. Zhang, and J. Zou, "The effect of

V/III ratio and catalyst particle size on the crystal structure and optical properties of InP nanowires," *Nanotechnology*, vol. 20, no. 22, p. 225606, 2009.

[195] S. A. Dayeh, E. T. Yu, and D. Wang, "III–V nanowire growth mechanism: V/III ratio and temperature effects," *Nano Lett.*, vol. 7, no. 8, pp. 2486–2490, 2007.

[196] D. H. Reep and S. K. Ghandhi, "Electrical properties of organometallic chemical vapor deposited GaAs epitaxial layers," *J. Electrochem. Soc.*, vol. 131, no. 11, pp. 2697–2702, 1984.

[197] A. M. S. El Ahl, M. He, P. Zhou, G. L. Harris, L. Salamanca-Riba, F. Felt, H. C. Shaw, A. Sharma, M. Jah, D. Lakins, T. Steiner, and S. N. Mohammad, "Systematic study of effects of growth conditions on the (nano-, meso-, micro)size and (one-, two-, three-dimensional) shape of GaN single crystals grown by a direct reaction of Ga with ammonia," *J. Appl. Phys.*, vol. 94, no. 12, pp. 7749–7756, 2003.

[198] K. Ikejiri, J. Noborisaka, S. Hara, J. Motohisa, and T. Fukui, "Mechanism of catalyst-free growth of GaAs nanowires by selective area MOVPE," *J. Crystal Growth*, vol. 298, pp. 616–619, 2007.

[199] D. K. Biegelsen, R. D. Bringans, J. E. Northrup, and L.-E. Swartz, "Reconstructions of GaAs($\bar{1}\,\bar{1}\,\bar{1}$) surfaces observed by scanning tunneling microscopy," *Phys. Rev. Lett.*, vol. 65, no. 4, pp. 452–455, 1990.

[200] T. Hayakawa, M. Morishima, and S. Chen, "Surface reconstruction limited mechanism of molecular-beam epitaxial growth of AlGaAs on (111)B face," *Appl. Phys. Lett.*, vol. 59, no. 25, pp. 3321–3323, 1991.

[201] J. Hu, T. Odom, and C. Lieber, "Chemistry and physics in one dimension: Synthesis and properties of nanowires and nanotubes," *Acc. Chem. Res.*, vol. 32, no. 5, pp. 435–445, 1999.

[202] K. A. Dick, K. Deppert, M. W. Larsson, T. Mårtensson, W. Seifert, L. R. Wallenberg, and L. Samuelson, "Synthesis of branched 'nanotrees' by controlled seeding of multiple branching events," *Nature Mater.*, vol. 3, no. 6, pp. 380–384, 2004.

[203] K. A. Dick, K. Deppert, L. S. Karlsson, W. Seifert, L. R. Wallenberg, and L. Samuelson, "Position-controlled interconnected InAs nanowire networks," *Nano Lett.*, vol. 6, no. 12, pp. 2842–2847, 2006.

[204] T. F. Kuech, M. A. Tischler, P.-J. Wang, G. Scilla, R. Potemski, and F. Cardone, "Controlled carbon doping of GaAs by metalorganic vapor phase epitaxy," *Appl. Phys. Lett.*, vol. 53, no. 14, pp. 1317–1319, 1988.

[205] M. C. Hanna, Z. H. Lu, E. G. Oh, E. Mao, and A. Majerfeld, "Intrinsic carbon incorporation in very high purity MOVPE GaAs," *J. Crystal Growth*, vol. 124, no. 1–4, pp. 443–448, 1992.

[206] B. K. Chadwick, "Equilibrium analysis of the MOCVD $Ga(CH_3)_3$–AsH_3–H_3 system," *J. Crystal Growth*, vol. 96, no. 3, pp. 693–702, 1989.

[207] X. Liu, A. Prasad, J. Nishio, E. R. Weber, Z. Liliental-Weber, and W. Walukiewicz, "Native point defects in low-temperature-grown GaAs," *Appl. Phys. Lett.*, vol. 67, no. 2, pp. 279–281, 1995.

[208] F. Ganikhanov, G.-R. Lin, W.-C. Chen, C.-S. Chang, and C.-L. Pan, "Subpicosecond carrier lifetimes in arsenic-ion-implanted GaAs," *Appl. Phys. Lett.*, vol. 67, no. 23, pp. 3465–3467, 1995.

[209] I. S. Gregory, C. M. Tey, A. G. Cullis, M. J. Evans, H. E. Beere, and I. Farrer, "Two-trap model for carrier lifetime and resistivity behavior in partially annealed GaAs grown at low temperature," *Phys. Rev. B*, vol. 73, no. 19, p. 195201, 2006.

[210] J. C. Bourgoin, H. J. v. Bardeleben, and D. Stiévenard, "Native defects in gallium arsenide," *J. Appl. Phys.*, vol. 64, no. 9, pp. R65–R92, 1988.

[211] J. M. Baranowski and P. Trautman, *Properties of Gallium Arsenide*. The Institution of Electrical Engineers, 3 ed., 1996.

[212] G. Martin, A. Mitonneau, and A. Mircea, "Electron traps in bulk and epitaxial GaAs crystals," *Electron. Lett.*, vol. 13, no. 7, pp. 191–193, 1977.

[213] S. Gupta, M. Y. Frankel, J. A. Valdmanis, J. F. Whitaker, G. A. Mourou, F. W. Smith, and A. R. Calawa, "Subpicosecond carrier lifetime in GaAs grown by molecular beam epitaxy at low temperatures," *Appl. Phys. Lett.*, vol. 59, no. 25, pp. 3276–3278, 1991.

[214] S. Y. Chiang and G. L. Pearson, "Properties of vacancy defects in GaAs single crystals," *J. Appl. Phys.*, vol. 46, no. 7, pp. 2986–2991, 1975.

[215] G. M. Martin, J. P. Farges, G. Jacob, J. P. Hallais, and G. Poiblaud, "Compensation mechanisms in GaAs," *J. Appl. Phys.*, vol. 51, no. 5, pp. 2840–2852, 1980.

[216] M. Eizenberg and H. J. Hovel, "Space-charge-limited current measurements in semi-insulating GaAs," *J. Appl. Phys.*, vol. 69, no. 4, pp. 2256–2263, 1991.

[217] K. Takahashi and T. Moriizumi, "Growth of InAs whiskers in wurtzite structure," *Jpn. J. Appl. Phys.*, vol. 5, no. 8, pp. 657–662, 1966.

[218] S. P. DenBaars, B. Y. Maa, P. D. Dapkus, A. D. Danner, and H. C. Lee, "Homogeneous and heterogeneous thermal decomposition rates of trimethylgallium and arsine and their relevance to the growth of GaAs by MOCVD," *J. Crystal Growth*, vol. 77, no. 1–3, pp. 188–193, 1986.

[219] J. E. Butler, N. Bottka, R. S. Sillmon, and D. K. Gaskill, "In situ, real-time diagnostics of OMVPE using IR-diode laser spectroscopy," *J. Crystal Growth*, vol. 77, no. 1–3, pp. 163–171, 1986.

[220] Y. Kim, H. J. Joyce, Q. Gao, H. H. Tan, C. Jagadish, M. Paladugu, J. Zou, and A. A. Suvorova, "Influence of nanowire density on the shape and optical properties of ternary InGaAs nanowires," *Nano Lett.*, vol. 6, no. 4, pp. 599–604, 2006.

[221] D. T. J. Hurle, "A mechanism for twin formation during Czochralski and encapsulated vertical Bridgman growth of III–V compound semiconductors," *J. Crystal Growth*, vol. 147, no. 3–4, pp. 239–250, 1995.

[222] J. Johansson, L. S. Karlsson, K. A. Dick, J. Bolinsson, B. A. Wacaser, K. Deppert, and L. Samuelson, "Effects of growth conditions on the crystal structure of gold-seeded GaP nanowires," *J. Crystal Growth*, vol. 310, no. 23, pp. 5102–5105, 2008.

[223] B. Mandl, J. Stangl, T. Mårtensson, A. Mikkelsen, J. Eriksson, L. S. Karlsson, G. Bauer, L. Samuelson, and W. Seifert, "Au-free epitaxial growth of InAs nanowires," *Nano Lett.*, vol. 6, no. 8, pp. 1817–1821, 2006.

[224] R. N. Hall, "p–n junctions produced by growth rate variation," *Phys. Rev.*, vol. 88, no. 1, pp. 139 – 139, 1952.

[225] Y. Hayakawa, Y. Saitou, Y. Sugimoto, and M. Kumagawa, "Analysis of impurity concentration distributions in pulled semiconductor crystals," *J. Electron. Mater.*, vol. 19, no. 2, pp. 145–149, 1990.

[226] A. I. Persson, L. E. Fröberg, S. Jeppesen, M. T. Björk, and L. Samuelson, "Surface diffusion effects on growth of nanowires by chemical beam epitaxy," *J. Appl. Phys.*, vol. 101, no. 3, p. 034313, 2007.

[227] M. Tchernycheva, L. Travers, G. Patriarche, F. Glas, J.-C. Harmand, G. E. Cirlin, and V. G. Dubrovskii, "Au-assisted molecular beam epitaxy of InAs nanowires: Growth and theoretical analysis," *J. Appl. Phys.*, vol. 102, no. 9, p. 094313, 2007.

[228] G. Zimmermann, A. Ougazzaden, A. Gloukhian, E. V. K. Rao, D. Delprat, A. Ramdane, and A. Mircea, "Selective area MOVPE growth of InP, InGaAs and InGaAsP using TBAs and TBP at different growth conditions," *J. Crystal Growth*, vol. 170, no. 1–4, pp. 645–649, 1997.

[229] M. Ida, N. Shigekawa, T. Furuta, H. Ito, and T. Kobayashi, "Compositional change near the mask edge in selective InGaAs growth by low-temperature MOCVD," *J. Crystal Growth*, vol. 158, no. 4, pp. 437–442, 1996.

[230] S. Mokkapati, P. Lever, H. H. Tan, C. Jagadish, K. E. McBean, and M. R. Phillips, "Controlling the properties of InGaAs quantum dots by selective-area epitaxy," *Appl. Phys. Lett.*, vol. 86, no. 11, p. 113102, 2005.

[231] Z. H. Zhang, G. W. Pickrell, K. L. Chang, H. C. Lin, K. C. Hsieh, and K. Y. Cheng, "Surface morphology control of InAs nanostructures grown on InGaAs/InP," *Appl. Phys. Lett.*, vol. 82, no. 25, pp. 4555–4557, 2003.

[232] A. Taguchi, "First-principles investigations of surface reconstructions of an InAs(111)B surface," *J. Crystal Growth*, vol. 278, no. 1–4, pp. 468–472, 2005.

[233] S. V. Ghaisas and S. Das Sarma, "Surface diffusion length under kinetic growth conditions," *Phys. Rev. B*, vol. 46, no. 11, pp. 7308–7311, 1992.

[234] F. A. Zhao, J. Wu, P. Jin, B. Xu, Z. G. Wang, and C. L. Zhang, "InAs nanostructure grown with different growth rate in InAlAs matrix on InP (0 0 1) substrate," *Physica E*, vol. 23, no. 1-2, pp. 31–35, 2004.

[235] I. Regolin, V. Khorenko, W. Prost, F.-J. Tegude, D. Sudfeld, J. Kastner, and G. Dumpich, "Composition control in metal-organic vapor-phase epitaxy grown InGaAs nanowhiskers," *J. Appl. Phys.*, vol. 100, no. 7, p. 074321, 2006.

[236] K. Tateno, G. Zhang, and H. Nakano, "Growth of GaInAs/AlInAs heterostructure nanowires for long-wavelength photon emission," *Nano Lett.*, vol. 8, no. 11, pp. 3645–3650, 2008.

[237] M. Tchernycheva, G. E. Cirlin, G. Patriarche, L. Travers, V. Zwiller, U. Perinetti, and J.-C. Harmand, "Growth and characterization of InP nanowires with InAsP insertions," *Nano Lett.*, vol. 7, no. 6, pp. 1500–1504, 2007.

[238] D. L. Dheeraj, G. Patriarche, H. Zhou, T. B. Hoang, A. F. Moses, S. Gronsberg, A. T. J. van Helvoort, B.-O. Fimland, and H. Weman, "Growth and characterization

of wurtzite GaAs nanowires with defect-free zinc blende GaAsSb inserts," *Nano Lett.*, vol. 8, no. 12, pp. 4459–4463, 2008.

[239] D. L. Dheeraj, G. Patriarche, L. Largeau, H. L. Zhou, A. T. J. v. Helvoort, F. Glas, J. C. Harmand, B. O. Fimland, and H. Weman, "Zinc blende GaAsSb nanowires grown by molecular beam epitaxy," *Nanotechnology*, vol. 19, no. 27, p. 275605, 2008.

[240] J. C. Houck and L. A. Denicola, "ISIS: An interactive spectral interpretation system for high resolution X-ray spectroscopy," in *ASP Conf. Proc.* (N. Manset, C. Veillet, and D. Crabtree, eds.), vol. 216, p. 591, Astronomical Society of the Pacific, 2000.

[241] L. E. Jensen, M. T. Bjork, S. Jeppesen, A. I. Persson, B. J. Ohlsson, and L. Samuelson, "Role of surface diffusion in chemical beam epitaxy of InAs nanowires," *Nano Lett.*, vol. 4, no. 10, pp. 1961–1964, 2004.

[242] E. Penev, P. Kratzer, and M. Scheffler, "Effect of strain on surface diffusion in semiconductor heteroepitaxy," *Phys. Rev. B*, vol. 64, no. 8, p. 085401, 2001.

[243] J. Johansson and S. Toxvaerd, "Adatom diffusion on strained (111) surfaces: A molecular dynamics study," *Phys. Rev. B*, vol. 69, no. 23, p. 233401, 2004.

[244] M. Rosini, P. Kratzer, and R. Magri, "In adatom diffusion on $In_xGa_{1-x}As$/GaAs(001): effects of strain, reconstruction and composition," *J. Phys.: Condens. Matter*, no. 35, p. 355007, 2009.

[245] C. Lobo and R. Leon, "InGaAs island shapes and adatom migration behavior on (100), (110), (111), and (311) GaAs surfaces," *J. Appl. Phys.*, vol. 83, no. 8, pp. 4168–4172, 1998.

[246] J. Johansson, L. S. Karlsson, C. P. T. Svensson, T. Mårtensson, B. A. Wacaser, K. Deppert, L. Samuelson, and W. Seifert, "The structure of ⟨111⟩B oriented GaP nanowires," *J. Crystal Growth*, vol. 298, pp. 635–639, 2007.

[247] K. A. Dick, Z. Geretovszky, A. Mikkelsen, L. S. Karlsson, E. Lundgren, J.-O. Malm, J. N. Andersen, L. Samuelson, W. Seifert, B. A. Wacaser, and K. Deppert, "Improving InAs nanotree growth with composition-controlled Au–In nanoparticles," *Nanotechnology*, vol. 17, no. 5, p. 1344, 2006.

[248] L. E. Fröberg, B. A. Wacaser, J. B. Wagner, S. Jeppesen, B. J. Ohlsson, K. Deppert, and L. Samuelson, "Transients in the formation of nanowire heterostructures," *Nano Lett.*, vol. 8, no. 11, pp. 3815–3818, 2008.

[249] J. Johansson, L. S. Karlsson, K. A. Dick, J. Bolinsson, B. A. Wacaser, K. Deppert, and L. Samuelson, "Effects of supersaturation on the crystal structure of gold seeded III–V nanowires," *Cryst. Growth Des.*, vol. 9, no. 2, pp. 766–773, 2009.

[250] Y. Hao, G. Meng, Z. L. Wang, C. Ye, and L. Zhang, "Periodically twinned nanowires and polytypic nanobelts of ZnS: The role of mass diffusion in vapor–liquid–solid growth," *Nano Lett.*, vol. 6, no. 8, pp. 1650–1655, 2006.

[251] Q. Li, X. Gong, C. Wang, J. Wang, K. Ip, and S. Hark, "Size-dependent periodically twinned ZnSe nanowires," *Adv. Mater.*, vol. 16, no. 16, pp. 1436–1440, 2004.

[252] F. M. Ross, J. Tersoff, and M. C. Reuter, "Sawtooth faceting in silicon nanowires," *Phys. Rev. Lett.*, vol. 95, no. 14, p. 146104, 2005.

[253] E. I. Givargizov, "Periodic instability in whisker growth," *J. Crystal Growth*, vol. 20, no. 3, pp. 217–226, 1973.

[254] W. J. P. van Enckevort, "Contact nucleation of steps: theory and Monte Carlo simulation," *J. Crystal Growth*, vol. 259, no. 1–2, pp. 190–207, 2003.

[255] N. Sköld, J. B. Wagner, G. Karlsson, T. Hernan, W. Seifert, M.-E. Pistol, and L. Samuelson, "Phase segregation in AlInP shells on GaAs nanowires," *Nano Lett.*, vol. 6, no. 12, pp. 2743–2747, 2006.

[256] R. Nötzel, L. Däweritz, and K. Ploog, "Topography of high- and low-index GaAs surfaces," *Phys. Rev. B*, vol. 46, no. 8, pp. 4736 – 4743, 1992.

[257] T. Ito, "Simple criterion for wurtzite-zinc-blende polytypism in semiconductors," *Jpn. J. Appl. Phys.*, vol. 37, no. 10B Part 2, pp. L1217–L1220, 1998.

[258] H. Gottschalk, G. Patzer, and H. Alexander, "Stacking fault energy and ionicity of cubic III–V compounds," *Phys. Status Solidi A*, vol. 45, no. 1, pp. 207–217, 1978.

[259] E. J. Schwalbach and P. W. Voorhees, "Phase equilibrium and nucleation in VLS-grown nanowires," *Nano Lett.*, vol. 8, no. 11, pp. 3739–3745, 2008.

[260] J. M. Moison, C. Guille, and M. Bensoussan, "Commensurate and incommensurate phase transitions of the (001) InAs surface under changes of bulk lattice constant, as chemical potential, and temperature," *Phys. Rev. Lett.*, vol. 58, no. 24, pp. 2555 –2558, 1987.

[261] S. Ohkouchi and N. Ikoma, "Straight step edge formation on an InAs(001) vicinal surface by the transition of surface reconstruction," *Jpn. J. Appl. Phys.*, vol. 33, pp. L1700–L1702, 1994.

[262] E. Pehlke, N. Moll, A. Kley, and M. Scheffler, "Shape and stability of quantum dots," *Appl. Phys. A: Mater. Sci. Proc.*, vol. 65, no. 6, pp. 525–534, 1997.

[263] E. Hilner, U. Håkanson, L. E. Fröberg, M. Karlsson, P. Kratzer, E. Lundgren, L. Samuelson, and A. Mikkelsen, "Direct atomic scale imaging of III–V nanowire surfaces," *Nano Lett.*, vol. 8, no. 11, pp. 3978–3982, 2008.

[264] C. Ratsch, W. Barvosa-Carter, F. Grosse, J. H. G. Owen, and J. J. Zinck, "Surface reconstructions for InAs(001) studied with density-functional theory and STM," *Phys. Rev. B*, vol. 62, no. 12, pp. R7719–R7722, 2000.

[265] J. E. Northrup and J. Neugebauer, "Theory of GaN($10\bar{1}0$) and ($11\bar{2}0$) surfaces," *Phys. Rev. B*, vol. 53, no. 16, pp. R10477–R10480, 1996.

[266] I. Egry, G. Lohoefer, and G. Jacobs, "Surface tension of liquid metals: Results from measurements on ground and in space," *Phys. Rev. Lett.*, vol. 75, no. 22, pp. 4043–4046, 1995.

[267] M. Copel, M. C. Reuter, E. Kaxiras, and R. M. Tromp, "Surfactants in epitaxial growth," *Phys. Rev. Lett.*, vol. 63, no. 6, pp. 632–635, 1989.

[268] H. Peng, S. Meister, C. K. Chan, X. F. Zhang, and Y. Cui, "Morphology control of layer-structured gallium selenide nanowires," *Nano Lett.*, vol. 7, no. 1, pp. 199–203, 2007.

[269] M. S. Song, J. H. Jung, Y. Kim, Y. Wang, J. Zou, H. J. Joyce, Q. Gao, H. H. Tan, and C. Jagadish, "Vertically standing Ge nanowires on GaAs(110) substrates," *Nanotechnology*, vol. 19, no. 12, p. 125602, 2008.

[270] R. H. Miwa and G. P. Srivastava, "Structure and electronic states of InAs(001)-(2×4) surfaces," *Phys. Rev. B*, vol. 62, no. 23, pp. 15778–15787, 2000.

[271] M. Kawase, Y. Ishikawa, and T. Fukui, "Atomic structure studies of (113)B GaAs surfaces grown by metalorganic vapor phase epitaxy," *Appl. Surf. Sci.*, vol. 130-132, pp. 457–463, 1998.

[272] K. Jacobi, L. Geelhaar, J. Márquez, J. Platen, and C. Setzer, "The morphology of high-index GaAs surfaces," *Appl. Surf. Sci.*, vol. 166, no. 1-4, pp. 173–178, 2000.

[273] J. Cahn and R. Hanneman, "(111) surface tensions of III–V compounds and their relationship to spontaneous bending of thin crystals," *Surf. Sci.*, vol. 1, no. 4, pp. 387–398, 1964.

[274] J. S. Vermaak, C. W. Mays, and D. Kuhlmann-Wilsdorf, "On surface stress and surface tension: I. theoretical considerations," *Surf. Sci.*, vol. 12, no. 2, pp. 128–133, 1968.

[275] J.-P. Borel and A. Châtelain, "Surface stress and surface tension: Equilibrium and pressure in small particles," *Surf. Sci.*, vol. 156, no. 2, pp. 572–579, 1985.

[276] A. Checco, P. Guenoun, and J. Daillant, "Nonlinear dependence of the contact angle of nanodroplets on contact line curvature," *Phys. Rev. Lett.*, vol. 91, no. 18, p. 186101, 2003.

[277] D. N. McIlroy, D. Zhang, Y. Kranov, and M. G. Norton, "Nanosprings," *Appl. Phys. Lett.*, vol. 79, no. 10, pp. 1540–1542, 2001.

[278] J. Zhang, B. Li, and D. Y. Kwok, "Metastable contact angles and self-propelled drop movement on chemically heterogeneous surfaces by a mean-field lattice Boltzmann model," *Eur. Phys. J. - Special Topics*, vol. 171, no. 1, pp. 73–79, 2009.

[279] D. Kashchiev, *Nucleation: Basic Theory with Applications*. Oxford: Butterworth–Heinemann, 2000.

[280] Y. Kobayashi, K. Uwai, and N. Kobayashi, "Chemical structure of As-stabilized surface during GaAs metalorganic vapor phase epitaxy studied by surface photo-absorption," *Jpn. J. Appl. Phys.*, vol. 34, no. 6A Part 1, pp. 3008–3011, 1995.

[281] L. E. Fröberg, W. Seifert, and J. Johansson, "Diameter-dependent growth rate of InAs nanowires," *Phys. Rev. B*, vol. 76, no. 15, p. 153401, 2007.

[282] P. Parkinson, J. Lloyd-Hughes, Q. Gao, H. H. Tan, C. Jagadish, M. B. Johnston, and L. M. Herz, "Transient terahertz conductivity of GaAs nanowires," *Nano Lett.*, vol. 7, no. 7, pp. 2162–2165, 2007.

[283] N. Begum, M. Piccin, F. Jabeen, G. Bais, S. Rubini, F. Martelli, and A. S. Bhatti, "Structural characterization of GaAs and InAs nanowires by means of Raman spectroscopy," *J. Appl. Phys.*, vol. 104, no. 10, p. 104311, 2008.